technische universität
dortmund

A Tabletop XUV Beamline for Time-Resolved Momentum Microscopy

Commissioning and Applications to Two-Dimensional van der Waals Semiconductors

Karl Jakob Schiller

2026

Dissertation submitted in partial fulfillment of the
requirements for the degree of

Doctor rerum naturalium

to the Faculty of Physics at the
TU Dortmund University, Germany

Accepted by the Faculty of Physics at TU Dortmund University, Germany.

Date of the oral examination: 9 June 2026

Doctoral examination committee:

Prof. Dr. Mirko Cinchetti

Prof. Dr. Christoph Lange

Prof. Dr. Frithjof Anders

Dr. Tim Ruhe

Abstract

Quantum materials often host emergent phases and excitations that arise from interactions between electrons and other quasiparticles. Capturing the ultrafast dynamics of these states requires experimental access to the electronic structure and its evolution in energy, momentum, and time. Time-resolved momentum microscopy provides this access by combining pump–probe photoemission with parallel multidimensional detection, but its performance is fundamentally limited by the trade-off between temporal and energy resolution. In this thesis, a femtosecond high-harmonic-generation-based extreme-ultraviolet beamline is presented that operates in two modes optimized either for energy or for temporal resolution. This dual-mode concept mitigates the time–bandwidth trade-off and enables flexible optimization of spectral and temporal performance. Combined with a momentum microscope for multidimensional detection, the instrument achieves an energy resolution better than 110 meV and a temporal resolution below 50 fs in the respective modes. Using this setup, light-driven dynamics in layered semiconductors and heterostructures are investigated. In bulk WS_2, carrier relaxation across separate valleys of the Brillouin zone is tracked. In a WS_2/WSe_2 heterobilayer, resonant excitation reveals signatures consistent with the formation and decay of excitons. Finally, core-level spectroscopy combined with theoretical modeling identifies chromium interstitials and bromine vacancies as sources of intrinsic *n*-type doping in the van der Waals antiferromagnet CrSBr, while sub-band-gap excitation reveals field-driven photoemission effects.

Kurzfassung

Quantenmaterialien weisen häufig Phasen und Anregungen auf, die aus den Wechselwirkungen zwischen Elektronen und anderen Quasiteilchen entstehen. Das Erfassen der ultraschnellen Dynamik dieser Zustände erfordert einen experimentellen Zugang zur elektronischen Struktur sowie zu ihrer zeitlichen Entwicklung in Energie- und Impulsraum. Die zeitaufgelöste Impulsmikroskopie ermöglicht diesen Zugang, indem sie Pump-Probe Photoemission mit paralleler multidimensionaler Detektion kombiniert, wird jedoch durch die wechselseitige Abhängigkeit von Energie- und Zeitauflösung grundlegend limitiert. In dieser Arbeit wird eine auf Erzeugung hoher Harmonischer basierende Strahlungsquelle mit extrem-ultravioletten Photonen im Femtosekundenbereich vorgestellt, die in zwei Betriebsmodi arbeitet, welche jeweils auf hohe Energie- bzw. Zeitauflösung optimiert sind. Dieses Dual-Mode Konzept mildert die durch das Zeit-Bandbreite Produkt vorgegebene Beschränkung und erlaubt eine flexible Optimierung der spektralen und zeitlichen Auflösung. In Kombination mit einem Impulsmikroskop zur multidimensionalen Datenerfassung erreicht das Instrument eine Energieauflösung unter 110 meV und eine Zeitauflösung unter 50 fs in den jeweiligen Betriebsmodi. Mit diesem Aufbau werden lichtinduzierte Dynamiken in geschichteten Halbleitern und Heterostrukturen untersucht. In Volumenkristall WS_2 wird die Relaxation angeregter Ladungsträger zwischen verschiedenen Tälern der Brillouin-Zone verfolgt. In einer WS_2/WSe_2-Doppelschicht zeigt resonante Anregung Signaturen, die auf die Bildung und den Zerfall von Exzitonen hinweisen. Abschließend werden intrinsische Punktdefekte im van-der-Waals-Antiferromagneten CrSBr untersucht: Die Kombination aus Kernlevel-Spektroskopie und theoretischer Modellierung identifiziert Chrom-Zwischengitterplätze und Brom-Fehlstellen als Quellen der intrinsischen *n*-Dotierung, während Anregung unterhalb der Bandlücke feldinduzierte Photoemissionseffekte offenbart.

Abbreviations

AFM	antiferromagnetic
ARPES	angle-resolved photoemission spectroscopy
BBO	β barium borate
BZ	Brillouin zone
CA	contrast aperture
CBM	conduction band minimum
CW	continuous wave
DFT	density functional theory
DMDS	dimethyl disulfide
EDC	energy distribution curve
EFL	effective focal length
FA	field aperture
FM	ferromagnetic
FROG	frequency-resolved optical gating
FWHM	full width at half maximum
GDD	group delay dispersion
GVD	group velocity dispersion
h-BN	hexagonal boron nitride
HDA	hemispherical deflection analyzer
HHG	high harmonic generation
HOPG	highly oriented pyrolytic graphite
ILX	interlayer exciton
IR	infrared
IRF	instrument response function
LAPE	laser-assisted photoemission
MM	momentum microscope

MPC	multi-pass cell
OPA	optical parametric amplifier
OPCPA	optical parametric chirped-pulse amplification
PEEM	photoemission electron microscopy
PES	photoelectron spectroscopy
PL	photoluminescence
PME	photoemission matrix element
ROC	radius of curvature
ROI	region of interest
SFG	sum-frequency generation
SH	second harmonic
SHG	second harmonic generation
SNR	signal-to-noise ratio
SPM	self-phase modulation
SPV	surface photovoltage
STEM	scanning transmission electron microscopy
STM	scanning tunneling microscopy
TDC	time-to-digital converter
TEM	transverse electromagnetic mode
TMD	transition metal dichalcogenide
TOF	time of flight
trARPES	time- and angle-resolved photoemission spectroscopy
trMM	time-resolved momentum microscopy
UHV	ultra-high vacuum
UV	ultraviolet
VBM	valence band maximum
vdW	van der Waals
XPS	X-ray photoelectron spectroscopy
XUV	extreme ultraviolet

Contents

Abbreviations iii

Table of Contents vi

1 Introduction 1

2 Concepts and Methods 7
2.1 Nonlinear Optics for Ultrafast Photoemission . . . 7
2.1.1 Ultrafast Gaussian Optics . . . 7
2.1.2 Nonlinear Optics . . . 9
2.1.3 High Harmonic Generation . . . 13
2.2 Photoemission Electron Spectroscopy . . . 16
2.2.1 Three-Step Model . . . 16
2.2.2 X-ray Photoemission Spectroscopy . . . 20
2.2.3 Momentum Microscopy . . . 21
2.2.4 Time-Resolved Photoemission . . . 23
2.2.5 Space Charge . . . 26
2.3 Selected Transient Signatures and Artifacts . . . 28
2.3.1 Exciton Fingerprint . . . 29
2.3.2 Laser-Assisted Photoemission . . . 31
2.3.3 Surface Photovoltage Effect . . . 32
2.3.4 Pump-Induced Space Charge . . . 34
2.4 Experimental Instrumentation . . . 37
2.4.1 XPS Setup . . . 37
2.4.2 KREIOS Momentum Microscope . . . 38
2.4.3 METIS Beamline . . . 41

3 Commissioning of a trMM Beamline 43
3.1 Generation of Coherent XUV Photons . . . 45
3.2 Frequency Conversion of Optical Pump Pulses . . . 49
3.3 Beamline Integration . . . 51
3.4 Beamline Modification for OPA Integration . . . 55

4 Materials and Preparation 59
4.1 Gold (111) Surface State . . . 60
4.2 Sample Preparation . . . 60
4.3 Highly Oriented Pyrolytic Graphite . . . 64
4.4 Transition-Metal Dichalcogenides . . . 66
4.5 Chromium Sulfur Bromide . . . 69

5 Ultrafast Dynamics in 2D vdW Semiconductors 73
5.1 Conduction Band Electron Relaxation in WS_2 73
5.1.1 Static Characterization 74
5.1.2 Transient Behavior of Bulk WS_2 76
5.1.3 Comparison to WS_2 Monolayer on Gold 80
5.2 Exciton Formation in Bilayer WS_2/WSe_2 85
5.2.1 Equilibrium Spectrum 85
5.2.2 Transient Behavior of WS_2 / WSe_2 90
5.3 Defect-Driven Phenomena in CrSBr 99
5.3.1 Doping Through Intrinsic Defects 99
5.3.2 Field Effects at Sub-Bandgap Excitation 106

6 Summary and Outlook 113

A Appendix 115

Bibliography 117

List of publications 143

Declaration of the Use of Artificial Intelligence Tools 145

Acknowledgements 147

1 Introduction

A central focus in condensed-matter physics is the study of *quantum materials*, whose macroscopic properties are governed by emergent quantum phenomena such as topology, strong electronic correlations, and collective order [1, 2]. Prominent examples include topological insulators [3, 4], high-temperature superconductors [5], and charge density wave systems [6, 7]. In many of these materials, key observables are controlled by the electronic degrees of freedom, such as spin or orbital order, and by interactions with quasi-particles such as phonons [8]. Experimentally exploring these interaction pathways requires momentum- and energy-resolved access to the electronic excitations, because coupling strengths and relaxation dynamics depend sensitively on the electron momentum and energy, and an unambiguous identification of valley-, band-, or defect-specific processes relies on this resolution.

Among the available experimental techniques, angle-resolved photoemission spectroscopy (ARPES) is a well-established technique that measures the photoemission intensity as a function of energy and momentum, providing access to the occupied electronic structure and many-body renormalizations through the single-particle spectral function. The method is based on the photoelectric effect (discovered by Hertz 1887 [9] and explained by Einstein 1905 [10]), where photons with energy exceeding the work function liberate electrons from a solid. Extending ARPES to a pump–probe geometry in so-called time- and angle-resolved photoemission spectroscopy (trARPES) enables tracking the transient evolution of the electronic structure after ultrafast excitation [11, 12]. Importantly, trARPES accesses states above the Fermi energy as they become transiently occupied. In this way, trARPES can quantify nonequilibrium dynamics such as relaxation times, transient band shifts, linewidth changes, and gap renormalization [8]. Interactions such as electron–electron and electron–phonon scattering can often be distinguished by their characteristic timescale [13, 14] and by their momentum dependence within the Brillouin zone (BZ) [15].

A trARPES experiment combines three essential elements: (i) a light source providing photons above the work function (and, for pump–probe operation, well-defined pulse structure), (ii) a well-prepared sample under controlled environment, and (iii) electron optics and detection that resolve the kinetic energy and emission direction (and optionally spin) of the photoelectrons. Over the past decades, progress has been driven by both advances in light sources [11] and by the development of multichannel electron spectrometers [12].

Modern multichannel detection aims at rapid, parallel acquisition of photoelectron kinetic energy and transverse momentum with high resolution. Momentum mi-

croscopes (MMs), which are closely related to photoemission electron microscopy (PEEM) instruments, use a cathode-lens-based electron-optical column to collect electrons over a wide angular range and to image either the real-space distribution (PEEM mode) or the momentum-space distribution (ARPES mode) onto a detector [16, 17]. Energy selection can be realized, for example, by a hemispherical deflection analyzer (HDA) stage or by time of flight (TOF) detection in a drift region, where the flight time encodes kinetic energy and enables parallel acquisition over a broad energy window [18]. Apertures placed in an intermediate image plane can restrict the field of view to a selected real-space region of the sample, while apertures in a back-focal (angular) plane can select a region in momentum space, enabling dark-field imaging, for example [19].

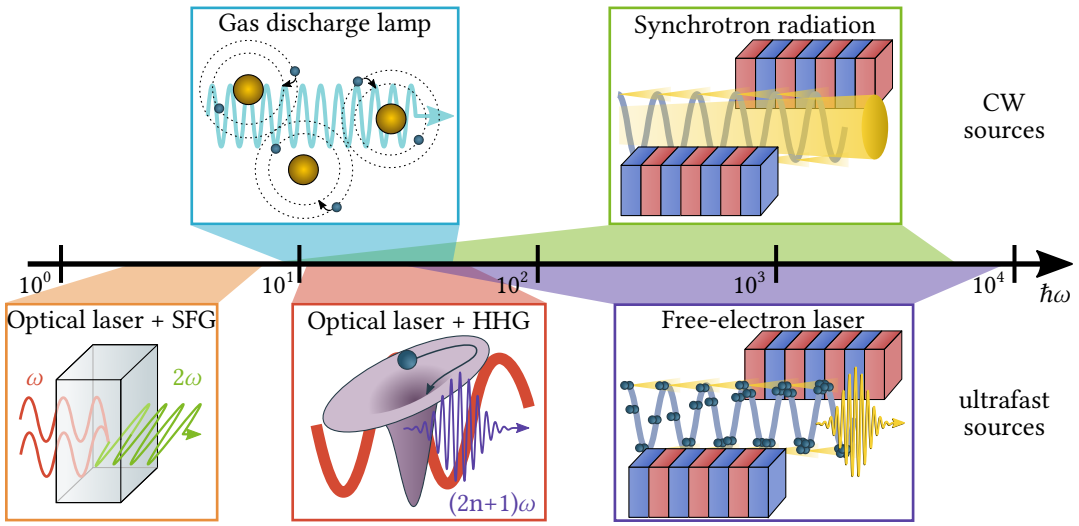


Figure 1.1: Overview of continuous wave (CW) and ultrafast light sources for ARPES. Adapted with permission from Ref. [1], © American Physical Society.

Different light sources suitable for ARPES are summarized in Figure 1.1. Static experiments employ continuous wave (CW) or quasi-CW sources such as gas-discharge lamps or synchrotron radiation. Time-resolved experiments require pulsed sources, ranging from frequency-converted tabletop lasers (ultraviolet (UV) regime) to facility-based free-electron lasers (extreme ultraviolet (XUV) to soft X-rays regime) [1]. Synchrotrons and free-electron lasers provide broad tunability and high flux, but their facility-based nature limits accessibility. In addition, high instantaneous photon density can lead to space-charge effects that degrade effective energy and momentum resolution. Tabletop sources offer high accessibility and can be optimized for high repetition rates to reduce electrons per pulse and mitigate space charge, but frequency conversion in nonlinear crystals typically limits photon energies to the UV range, which restricts the accessible photoelectron kinetic energy and therefore the reachable momentum range within the BZ [8]. High harmonic generation (HHG) in noble gases extends tabletop sources into the XUV regime, enabling access to larger regions of momentum space [20]. Continued progress in HHG-based beamlines relies on high-average-power ultrafast lasers and on efficient HHG operation

at repetition rates that mitigate space charge while maintaining high temporal and energy resolution [11, 21].

Advances in photon energy and multichannel acquisition have enabled trARPES studies across a wide range of quantum materials. Among these, van der Waals (vdW) crystals are particularly attractive: their crystal structure consists of atomically thin layers that are weakly coupled by vdW forces, allowing mechanical exfoliation down to the monolayer limit [22, 23]. Their intrinsically surface-dominated nature matches the high surface sensitivity of ARPES, which arises from the finite inelastic mean free path of photoelectrons. Moreover, weak interlayer coupling enables the modular assembly of artificial heterostructures [24]. In such 2D platforms, external control parameters including electrostatic gating, strain, twist-induced moiré potentials, optical excitation, and proximity coupling provide practical routes to tune electronic and, where present, magnetic properties (Fig. 1.2) [25–28].

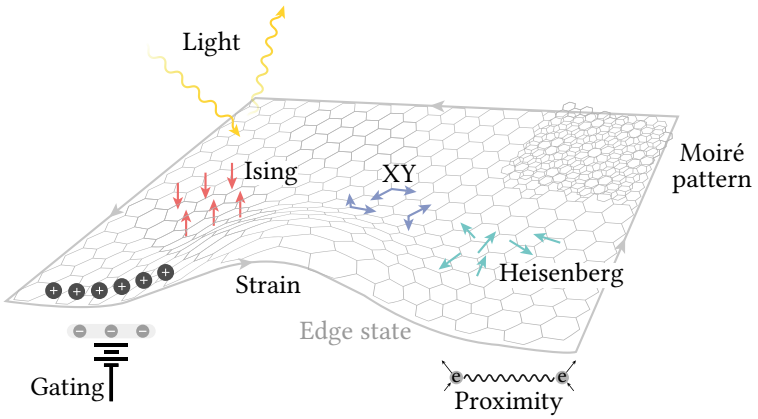


Figure 1.2: Schematic overview of control knobs and emergent phenomena in two-dimensional vdW materials and heterostructures. Electrostatic gating, strain, moiré superlattices (twist), optical excitation, and interlayer proximity coupling provide routes to tune electronic and magnetic behavior. The Ising/XY/Heisenberg labels indicate different magnetic anisotropy regimes. Reproduced from Ref. [25], with permission from Springer Nature.

In semiconducting vdW materials, reduced dielectric screening enhances Coulomb interactions, often leading to exciton binding energies in the range of hundreds of meV [29]. A prototypical material family is the class of transition metal dichalcogenides (TMDs), many of which are semiconductors and exhibit an indirect-to-direct band-gap transition when thinning from multilayers to a monolayer [30]. Their optical response is frequently dominated by excitonic resonances, and the presence of inequivalent valleys in the band structure enables valley-selective excitation and relaxation pathways. Strong spin–orbit coupling and broken inversion symmetry in monolayers can couple spin and valley degrees of freedom [31]. In multilayer and heterobilayer TMD systems, interlayer hybridization and charge transfer can give rise to additional excitonic species [32, 33], including moiré excitons in lattice- or twist-mismatched bilayers where an emergent periodic potential modifies electronic and excitonic states [34, 35]. In time-resolved momentum microscopy (trMM)/trARPES,

exciton-related physics is typically accessed indirectly through the nonequilibrium carrier populations and interaction-induced renormalizations of the single-particle spectral function, with momentum resolution providing insights on the underlying scattering and transfer processes [36].

Long-range magnetic order was demonstrated in atomically thin vdW crystals in 2017 [37, 38], sparking intense interest in two-dimensional magnetism and spintronic perspectives [39, 40]. Early material platforms often suffered from low transition temperatures and limited stability in ambient conditions. A promising semiconducting antiferromagnet in this context is CrSBr, whose bulk form is comparatively resilient against oxidation [41, 42]. Beyond its magnetic properties, CrSBr exhibits strong anisotropy and pronounced quasiparticle renormalization, consistent with quasi-one-dimensional transport along its crystallographic axes [43]. This anisotropy manifests in direction-dependent effective masses and strongly polarized optical resonances [44], distinguishing CrSBr from other semiconducting vdW antiferromagnets such as transition-metal thiophosphates (MPS3) [45].

These examples highlight both the scientific opportunities and the experimental challenges of studying ultrafast dynamics in two-dimensional vdW quantum materials. Valley-dependent carrier relaxation, exciton formation, anisotropic band structure, and defect-related spectral signatures all require momentum-resolved access to transient electronic states over a large region of the BZ. Realizing such measurements in practice further demands XUV probe pulses with sufficient photon energy, high repetition rates to mitigate space-charge effects, and optimized temporal and spectral resolution. Addressing this combination of requirements is a central objective of the present thesis.

The main scope of this thesis is the realization of a modern fs-XUV beamline with tunable trade-offs between temporal and energy resolution, its integration into a trMM platform, and its application to ultrafast carrier relaxation and interaction effects in 2D vdW quantum materials. The thesis is structured as follows:

Chapter 2 introduces the concepts and methods required for the remainder of the thesis. Fundamental aspects of ultrafast and nonlinear optics relevant for trMM and beamline design are discussed in Sec. 2.1. The principles of ARPES and MMs are then summarized in Sec. 2.2, with emphasis on transient signatures and observables (Sec. 2.3). Finally, the instrumentation used for the experiments is introduced in Sec. 2.4.

Chapter 3 details commissioning of an HHG-based beamline for fs-XUV probe pulse generation (Sec. 3.1) and its coupling to a MM with a HDA for trMM measurements (Sec. 3.3). Since temporal and energy resolution are linked by Fourier constraints, two operating modes are implemented to prioritize one resolution over the other. A photon energy $> 20\,\mathrm{eV}$ combined with a high repetition rate enables efficient multichannel acquisition over large regions of the BZ for many quantum materials. Pump-frequency modulation for tunable excitation is discussed in Sec. 3.2, including modifications to accommodate an optical parametric amplifier (OPA) in the pump line (Sec. 3.4).

Chapter 4 introduces the investigated materials. The Au(111) surface state and highly oriented pyrolytic graphite (HOPG) are presented as benchmark systems to characterize beamline performance (Sec. 4.1 and 4.3). The materials CrSBr and WS_2 are then introduced in more detail to motivate their ARPES and trARPES signatures (Sec. 4.5 and 4.4). Sample preparation is summarized with emphasis on fabrication of a WS_2 monolayer (Sec. 4.2).

Chapter 5 presents trMM studies on WS_2 and CrSBr. Bulk WS_2 is excited above the band gap and valley-resolved relaxation in the conduction band is analyzed as a function of electron energy (Sec. 5.1). The response is compared to a WS_2 monolayer on Au(111), where the transient signature indicates additional decay channels. A WS_2/WSe_2 bilayer is then excited resonantly with the WSe_2 exciton (Sec. 5.2). While signatures consistent with exciton formation in WSe_2 are observed, no clear evidence for subsequent interlayer exciton formation is found under the investigated conditions. Finally, defect-related phenomena in CrSBr are investigated (Sec. 5.3), including intrinsic *n*-type doping. Core-level spectroscopy combined with theoretical modeling identifies Cr interstitials as a likely doping source in addition to Br vacancies. Under below-band gap excitation, the trMM response is dominated by field effects that can mask intrinsic material dynamics.

The main results are summarized in **Chapter 6**, followed by a brief outlook.

2 Concepts and Methods

This chapter establishes the concepts and methods underpinning the experimental work presented in the subsequent chapters. Section 2.1 reviews ultrafast Gaussian beam optics and nonlinear frequency conversion, culminating in high harmonic generation (HHG) as a tabletop route to femtosecond extreme ultraviolet (XUV) pulses for photoemission. Section 2.2 introduces the photoemission process and summarizes the employed spectroscopic techniques, ranging from conventional X-ray photoelectron spectroscopy (XPS) to momentum microscopy and time-resolved photoemission, with particular emphasis on space-charge limitations. Because time- and angle-resolved photoemission spectroscopy (trARPES) can exhibit both genuine transient signatures and systematic artifacts, selected examples are discussed in Section 2.3, including excitonic fingerprints, laser-assisted photoemission, surface photovoltage, and pump-induced space charge. Finally, Section 2.4 provides an overview of the experimental instrumentation, while the pulsed photon beamline coupled to the KREIOS momentum microscope is described in detail later (Ch. 3).

2.1 Nonlinear Optics for Ultrafast Photoemission

Tabletop sources delivering efficient HHG with photon energies above 20 eV have become increasingly practical with the advent of high-power, high-repetition-rate femtosecond laser systems [11]. Describing such sources requires both spatial and temporal pulse control, which are governed by Gaussian-beam optics and dispersion, respectively. Accordingly, this section first introduces the basics of ultrafast optics (Sec. 2.1.1), then reviews nonlinear frequency conversion (Sec. 2.1.2), and finally focuses on HHG in gas targets at high intensities (Sec. 2.1.3).

2.1.1 Ultrafast Gaussian Optics

The photoemission experiments presented in this thesis utilize ultrashort light pulses on femtosecond and picosecond timescales. Such pulses are commonly described within the slowly varying envelope approximation, in which a rapidly oscillating electric field is modulated by an envelope function that varies only slowly in time. For propagation along z, the electric field can be written as

$$\mathbf{E}(z,t) = \mathrm{Re}\left\{\mathbf{E}_0 \mathscr{E}(z,t)\, u_{m,n}(\mathbf{r}) \exp\left[ikz - i\omega t\right]\right\}, \tag{2.1}$$

where $\mathbf{r} = (x, y, z)^\mathsf{T}$ is the position vector, $\mathbf{E}_0$ is the field amplitude vector, $\mathscr{E}$ is the envelope function, k is the wave number along the propagation direction, ω is the angular frequency, and $u_{m,n}$ is the transverse mode, which is discussed in more detail below [46, 47]. Propagation through a medium generally leads to temporal spreading due to dispersion, which is captured by the frequency dependence of k [46]:

$$k(\omega) = \underbrace{k(\omega)|_{\omega_0}}_{\equiv \omega/v_{\mathrm{ph}}} + \underbrace{\left.\frac{\mathrm{d}k}{\mathrm{d}\omega}\right|_{\omega_0}}_{\equiv v_{\mathrm{gr}}^{-1}} (\omega - \omega_0) + \frac{1}{2} \underbrace{\left.\frac{\mathrm{d}^2 k}{\mathrm{d}\omega^2}\right|_{\omega_0}}_{\equiv \mathrm{GVD}} (\omega - \omega_0)^2 + \mathcal{O}\left((\omega - \omega_0)^3\right) \tag{2.2}$$

Here, ω_0 denotes the central pulse frequency. The first and second terms define the phase and group velocities, v_{ph} and v_{gr}, respectively. The third term is the group velocity dispersion (GVD), which renders the group delay frequency dependent: different spectral components propagate with different group velocities, leading to temporal broadening for finite-bandwidth pulses. A related quantity is the group delay dispersion (GDD), i.e. the GVD accumulated over a path length L. After experiencing GVD, an optical pulse develops a frequency sweep across its temporal profile, referred to as *chirp* [47, 48]. For positive GVD, as found in most materials, higher frequencies exhibit a lower group velocity, which imparts positive chirp. Chirped pulses broaden in time and therefore exhibit reduced peak intensity. The characteristic length L_{disp}, after which the peak intensity has decreased by a factor $\sqrt{2}$, scales with the squared initial pulse duration, $L_{\mathrm{disp}} \propto \tau^2 / |\mathrm{GVD}|$ [48], highlighting that GVD becomes increasingly important for short pulse durations.

Time and frequency descriptions of a light pulse are connected via the Fourier transform. For a given pulse shape, this connection implies a lower bound on the product of spectral bandwidth $\Delta\nu$ and pulse duration $\Delta\tau$, defined here as intensity full width at half maximum (FWHM) values,

$$\Delta\nu \, \Delta\tau \geq K \tag{2.3}$$

with constant K [46, 48]. The exact value of K depends on the pulse shape and is $2\ln(2)/\pi \approx 0.441$ for Gaussian pulses, for example. This lower bound is commonly referred to as the *transform limit* and is reached only for pulses with flat spectral phase.

Ultrashort optical pulse durations are difficult to characterize using electronic measurement procedures [49]. In this thesis, pulse durations are therefore characterized via second-harmonic intensity autocorrelation measurements. In this approach, a laser beam is split in an interferometer-like geometry with adjustable delay between the two pulse replicas. At the output, both beams overlap and generate the second harmonic (SH) (Sec. 2.1.2) with an intensity proportional to the convolution of their intensities. Pulse durations can thus be obtained by recording the SH intensity as a function of delay and applying a pulse-shape-dependent deconvolution factor. However, this form of autocorrelation does not provide access to the spectral phase and therefore cannot retrieve chirp information. A more elaborate method is frequency-resolved optical gating (FROG), in which the SH signal is recorded with spectral

resolution. This yields a two-dimensional frequency–delay spectrogram and enables retrieval of the complex electric field via algorithmic reconstruction [50].

Real laser beams have finite spatial extent in the transverse direction and are therefore not well described by plane waves. Instead, the spatial mode $u_{m,n}$ perpendicular to the propagation direction is commonly expressed as an expansion in Hermite–Gauss modes with indices (m, n) for the x and y directions, respectively, also referred to as transverse electromagnetic mode (TEM). Most important for this thesis is the $\mathrm{TEM}_{0,0}$ mode with Gaussian beam profile

$$u_{0,0}(\mathbf{r}) = \frac{w_0}{w(z)} \exp\left[-\frac{x^2+y^2}{w^2(z)} - ik\frac{x^2+y^2}{2R(z)} + i\varphi(z)\right] \tag{2.4}$$

with beam radius $w(z)$ (defined at the $1/\mathrm{e}^2$ intensity level), waist radius w_0 at $z = 0$, wavefront radius of curvature $R(z) = (z^2 + z_\mathrm{R}^2)/z$, and Gouy phase $\varphi = \arctan(z/z_\mathrm{R})$ [47, 51]. The Rayleigh length $z_\mathrm{R} = \pi w_0^2 n/M^2\lambda$ specifies the position where $w(z) = \sqrt{2}w_0$ and includes the central vacuum wavelength λ and refractive index n. A parameter $M^2 \geq 1$ quantifies the deviation of a real beam from the ideal $\mathrm{TEM}_{0,0}$ mode ($M^2 = 1$ for an ideal mode). In practice, M^2 is determined by fitting the measured $w(z)$ with

$$w^2(z - z_0) = w_0^2\left[1 + \left(\frac{z - z_0}{z_\mathrm{R}}\right)^2\right] \tag{2.5}$$

and computing M^2 using the definition of z_R above [52]. Accordingly, the minimum achievable spot diameter at the focus of a lens is limited by diffraction and can be expressed as

$$2w_0 = M^2 \frac{4}{\pi}\lambda\frac{f}{d} \tag{2.6}$$

for a lens with focal length f and beam diameter d at the lens [51].

2.1.2 Nonlinear Optics

The response of a medium to a sufficiently weak electric field E is well approximated by the linear polarization $P = \varepsilon_0\chi^{(1)}E$, with vacuum permittivity ε_0 and linear susceptibility $\chi^{(1)}$. However, the general response includes nonlinear components of the form [47]

$$P = \varepsilon_0\left[\chi^{(1)}E + \chi^{(2)}E^2 + \chi^{(3)}E^3 + \mathcal{O}(E^4)\right], \tag{2.7}$$

which is written here in one-dimensional scalar form for illustrative purposes[1]. In general, the susceptibilities are tensors of rank n, as indicated by the above expression [48]. An order-of-magnitude estimate for their scaling is

$$\chi^{(i+1)} \sim \frac{\chi^{(i)}}{E_\mathrm{at}}, \quad E_\mathrm{at} = \mathrm{e}/\left(4\pi\varepsilon_0 a_0^2\right) = 5.14 \times 10^{11}\,\frac{\mathrm{V}}{\mathrm{m}} \tag{2.8}$$

[1] Scalar susceptibilities denote effective values derived from the actual tensor.

with elementary charge e and Bohr radius a_0 of the hydrogen atom [53]. This estimate illustrates why nonlinear responses become apparent only at high field strengths.

Nonlinear processes relevant for this thesis are of second and third order. Importantly, second-order effects vanish in media with an inversion center ($\chi^{(2)} = 0$) [53]. For non-centrosymmetric media, second-order processes can be illustrated by considering an input field with two frequency components,

$$E(t) = E_1 \mathrm{e}^{-i\omega_1 t} + E_2 \mathrm{e}^{-i\omega_2 t} + \text{c.c.}, \tag{2.9}$$

which yields [53]

$$\begin{aligned} P^{(2)}(t) = \varepsilon_0 \chi^{(2)} [&E_1^2 \mathrm{e}^{-2i\omega_1 t} + E_2^2 \mathrm{e}^{-2i\omega_2 t} \\ &+ 2E_1 E_2 \mathrm{e}^{-i(\omega_1+\omega_2)t} + 2E_1 E_2^* \mathrm{e}^{-i(\omega_1-\omega_2)t} + \text{c.c.}] + C. \end{aligned}$$

Here, C denotes a DC term that does not depend on t and describes optical rectification. This relation demonstrates frequency mixing with several components. The first two terms describe the conversion of two photons with frequency ω_n to $2\omega_\mathrm{n}$, commonly referred to as second harmonic generation (SHG). The third term corresponds to generation of a component at $\omega_1 + \omega_2$, referred to as sum-frequency generation (SFG). Finally, the last term at frequency $\omega_1 - \omega_2$ is termed difference-frequency generation.

Difference-frequency generation describes a frequency-mixing process in which two input waves at ω_1 and ω_2 generate a third frequency at $\omega_3 = |\omega_1 - \omega_2|$. An alternative viewpoint is *optical parametric amplification*, in which a very intense pump beam at $\omega_\mathrm{p} = \omega_1$ amplifies a weak seed beam at ω_2 into a stronger signal beam at $\omega_\mathrm{s} = \omega_2$ [54]. The additionally created beam at $\omega_\mathrm{i} = \omega_\mathrm{p} - \omega_\mathrm{s}$ is referred to as the idler beam. Both processes rely on the same $\chi^{(2)}$ nonlinear interaction. Seed generation typically involves white-light continuum generation, i.e. strong spectral broadening by nonlinear processes such as self-phase modulation (see below) [47]. Optical parametric amplifiers (OPAs) employ either collinear input of the interacting beams, which provides high conversion efficiency and simplified alignment, or non-collinear input, which supports higher bandwidth (from phase-matching considerations) and is advantageous for ultrashort pulses [55]. In addition, high-power optical parametric chirped-pulse amplifications (OPCPAs) may temporally stretch the seed pulse prior to amplification and apply compression after the amplification stage, thereby reducing peak power during amplification [55, 56].

In general, the nonlinear effects described above can be understood by deriving a wave equation from Maxwell's equations in a non-magnetic and dispersive medium without free charges. For each Fourier component ω_n, one obtains

$$\nabla^2 \mathbf{E}_\mathrm{n} - \frac{\boldsymbol{\varepsilon}(\omega_\mathrm{n})}{c^2} \cdot \frac{\partial^2 \mathbf{E}_\mathrm{n}}{\partial t^2} = \frac{1}{\varepsilon_0 c^2} \frac{\partial^2 \mathbf{P}_\mathrm{n}^\mathrm{NL}}{\partial t^2} \tag{2.10}$$

for the nonlinear component of the polarization P^{NL} ($P = P^{\mathrm{LIN}} + P^{\mathrm{NL}}$), with speed of light c and linear dielectric tensor $\boldsymbol{\varepsilon}(\omega_{\mathrm{n}})$ [48, 53]. Here, the polarization and electric field are expressed in terms of their Fourier components as

$$\mathbf{P}(t) = \sum_{\mathrm{n}} \mathbf{P}_{\mathrm{n}}(\mathbf{r})\mathrm{e}^{-i\omega_{\mathrm{n}}t} + \mathrm{c.c.} \quad \text{and} \quad \mathbf{E}(t) = \sum_{\mathrm{n}} \mathbf{E}_{\mathrm{n}}(\mathbf{r})\mathrm{e}^{-i\omega_{\mathrm{n}}t} + \mathrm{c.c.} \tag{2.11}$$

Equation (2.10) can thus be interpreted as a wave equation driven by the nonlinear polarization on the right-hand side, demonstrating that the nonlinear polarization acts as a source term for waves at new frequency components.

A practical limitation of nonlinear processes is the *phase-matching* condition, which follows from momentum conservation and generally reads

$$\Delta\mathbf{k} = \sum_{\mathrm{i}} \mathbf{k}_i^{\mathrm{out}} - \sum_{\mathrm{j}} \mathbf{k}_j^{\mathrm{in}}. \tag{2.12}$$

Energy transfer between frequency components is drastically reduced for $\Delta\mathbf{k} \neq \mathbf{0}$ [48, 53]. However, dispersion causes $k(\omega)$ to differ among interacting waves. There are several mitigation strategies, and within this thesis, birefringent uniaxial β barium borate (BBO) crystals are used.

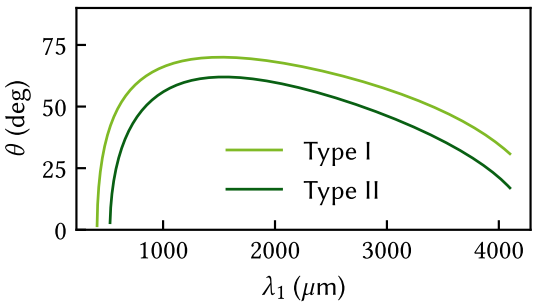


Figure 2.1: Phase-matching angle θ between k_1 and the crystal optical axis for SHG in a BBO crystal. Computed with refractive indices specified in Ref. [57].

These crystals exhibit an angle-dependent effective refractive index for the extraordinary axis. Phase matching is achieved by tuning the propagation angle θ relative to the optical axis such that the required effective index is met [47]. Fig. 2.1 displays the phase-matching angle as a function of input frequency for SHG. Depending on the ordinary/extraordinary polarization geometry of the interacting waves relative to the crystal axes, phase matching is categorized as type I, with identical polarizations for ω_1 and ω_2, or type II, with orthogonal polarizations. BBO crystals support second-order nonlinear processes from the infrared (IR) to the ultraviolet (UV) owing to their large transparency window and high $\chi^{(2)}$ in this spectral range.

Under perfect phase matching ($\Delta\mathbf{k} = \mathbf{0}$), the maximum second-harmonic intensity I_3 scales with the square of the propagation length L through the nonlinear medium, $I_3 \propto L^2$. For finite mismatch, however, this scaling only holds for $L \lesssim \pi/|\Delta k|$, because the generated wave can walk out of phase during propagation, resulting in oscillatory conversion [53]. For short pulses, the output efficiency and pulse duration depend strongly on the pulse parameters [47]. Comparatively long pulses with narrow bandwidth generate a SH temporal profile that is shorter than that of the driving fundamental due to the nonlinear intensity scaling $I_{2\omega}(t) \propto I_{\omega}^2(t)$. Ultrashort pulses, in contrast, have high bandwidth, and the spectral wings might not satisfy the phase-matching condition. In addition, group-velocity mismatch can cause non-negligible temporal walk-off, and birefringent crystals also feature spatial walk-off.

Consequently, the BBO crystal thickness for ultrashort pulses must be chosen as a compromise between conversion efficiency and preservation of pulse duration.

Within this thesis, third-order nonlinear processes are relevant primarily through the degenerate Kerr response, which is an intensity-dependent refractive index given by

$$n = n_0 + a\frac{1}{n_0^2 \varepsilon_0 c}\chi^{(3)} I = n_0 + n_2 I \tag{2.13}$$

with a prefactor a that depends on tensor and polarization conventions, driving-field intensity I, and linear refractive index n_0 [48]. This intensity-dependent modification of the refractive index has two important implications (for additional consequences, see, e.g., Ref. [53]). First, a Gaussian beam profile yields an increase of n that is largest on the optical axis (for $n_2 > 0$) and decreases toward the periphery. This profile acts as a lens, effectively focusing the beam inside the medium [53]. Such *self-focusing* can readily increase the beam intensity beyond the material's damage threshold, rendering the focusing process potentially catastrophic.

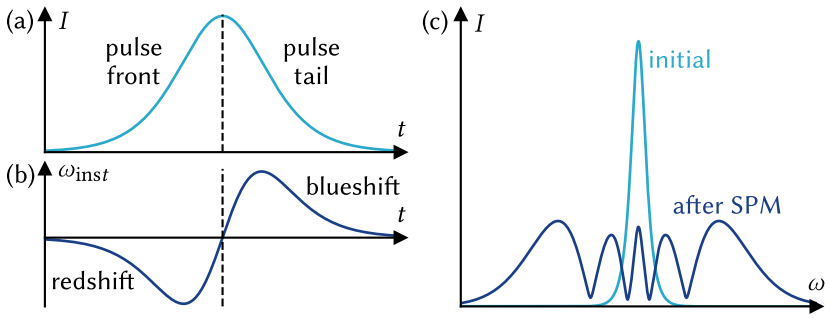


Figure 2.2: Calculated self-phase modulation (SPM) for $n_2 > 0$. (a) Intensity profile of a sech^2 pulse. (b) Self-phase modulation (SPM)-induced instantaneous frequency shift. (c) Resulting spectral broadening (schematic).

A second implication of an intensity-modulated refractive index is self-phase modulation (SPM), which arises from a modulation of the instantaneous frequency ω_{inst}, given by

$$\omega_{\text{inst}}(t) = -\frac{\mathrm{d}\phi(t)}{\mathrm{d}t} = \frac{\mathrm{d}}{\mathrm{d}t}(\omega_0 t - kz) = \frac{\mathrm{d}}{\mathrm{d}t}\left(\omega_0 t - \frac{\omega_0}{c} n_0 z - \frac{\omega_0}{c} n_2 I(t)\, z\right) \tag{2.14}$$

$$= \omega_0 - \frac{\omega_0}{c} z n_2 \frac{\mathrm{d}}{\mathrm{d}t} I(t) \tag{2.15}$$

with the temporal intensity profile defined in Equation (2.1) [47, 53]. The resulting modulation is displayed in Figure 2.2 and causes a spectral redshift on the leading edge of the pulse and a blueshift on the trailing edge (for $n_2 > 0$), thereby increasing the pulse bandwidth.

2.1.3 High Harmonic Generation

This section mainly builds on the review by Protopapas *et al.* [58] and on Refs. [48, 53], which are not cited repeatedly in the following. The nonlinear response of a medium upon optical illumination is introduced in the previous section, but this description no longer holds for very high optical intensities that enable electron ionization. At high intensities, N photons can excite an electron into a continuum (free-electron) state, which is referred to as *multiphoton ionization* (see Fig. 2.3a). If the electron absorbs more photons than required to overcome the ionization potential I_p, the process is called *above-threshold ionization*. Multiphoton ionization can be described within the perturbative regime, and its transition rate R scales with light intensity I according to $R \propto \sigma_\mathrm{N} I^N$ with generalized cross-section σ_N, even though saturation and depletion effects can break down this power law. For above-threshold ionization, this power-law relation breaks down with increasing field strength. Above-threshold ionization produces an ionized-electron spectrum with peaks separated by $\hbar\omega$.

For even higher optical intensities, the light's electric field distorts the atomic potential enough to enable tunneling of bound electrons into continuum states, which is commonly referred to as *tunneling ionization* (Fig. 2.3b). A key approximation for this description is that tunneling occurs rapidly within a fraction of the optical cycle, which allows a quasi-stationary treatment of the light's electric field. Moreover, the ionization probability is largest near electric-field maxima, with the drift momentum tied to the vector potential at the ionization time. The dominant ionization mechanism is approximately indicated by the conceptual Keldysh parameter γ, given by $\gamma = \omega\sqrt{2\mathrm{m_e} I_\mathrm{p}}/(\mathrm{e}E)$ with light frequency ω, electric field E, electron charge e, and electron mass $\mathrm{m_e}$. Tunneling dynamics dominate for $\gamma < 1$ (large E or small I_p), whereas multiphoton dynamics dominate for $\gamma > 1$ (smaller E or larger I_p).

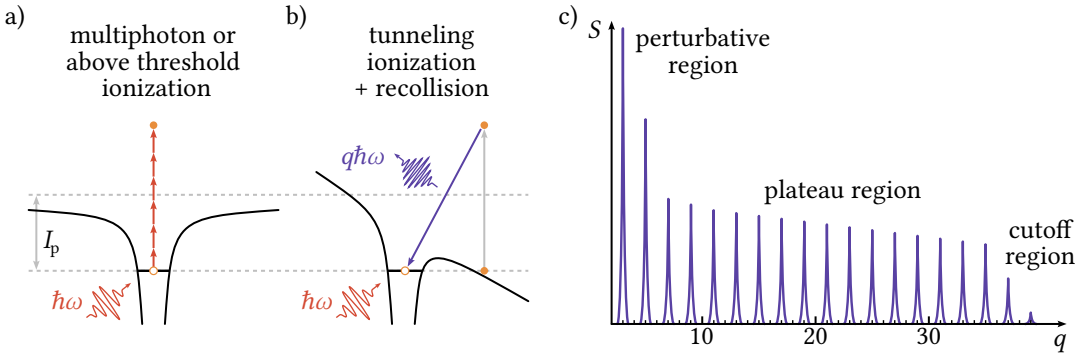


Figure 2.3: Schematic representation of electron ionization mechanisms and high harmonic generation. (a) Multiphoton ionization. (b) Tunneling ionization with recollision model, resulting in harmonic emission. (c) Schematic high-harmonic spectrum S as a function of harmonic order q at energy $q\hbar\omega$.

Within the oscillating electric field of the light, ionized electrons can undergo a quiver motion and recollide with their parent ion (see Fig. 2.3). This process is formulated for a single atom in the so-called *recollision* or *three-step model*, and its main features

can be understood from semiclassical theory [59, 60]. The three steps are (i) electron ionization described above, (ii) propagation within the light's electric field, and (iii) recombination at the ion. Upon recombination, the electron emits coherent dipole radiation with a maximum cutoff energy

$$\hbar\omega_{\mathrm{cutoff}} = I_{\mathrm{p}} + 3.17 \cdot U_{\mathrm{p}}, \tag{2.16}$$

with the classical maximum recollision kinetic energy $3.17 \cdot U_{\mathrm{p}}$ (first found experimentally by Krause *et al.* [61]). Here, $U_{\mathrm{p}} = \mathrm{e}^2 E^2/(4\mathrm{m_e}\omega^2)$ is the ponderomotive potential, which can be understood as the electron energy associated with quiver motion in an oscillating electric field E^2. For classification, the ponderomotive potential is $U_{\mathrm{p}}\ (\mathrm{eV}) = 9.33 \times 10^{-14} I\ (\mathrm{W/cm^2})\lambda^2\ (\mu\mathrm{m})$.

After tunneling ionization, the electron motion is often described classically with only the light field as the driving force, neglecting the ion Coulomb potential in the so-called *strong field approximation*. As ionization predominantly occurs at an electric-field maximum, the electron is first accelerated away from the parent ion. Upon reversal of the field direction, the electron is then accelerated back towards the ion and therefore possesses additional kinetic energy upon recollision. Importantly, light polarization with nonzero ellipticity results in electron trajectories that are more likely to miss the ion and thus strongly reduces radiation emission for elliptically polarized light and essentially suppresses it for circular polarization in the single-color case.

A typical radiation spectrum is shown in Figure 2.3c and features distinct harmonic peaks at multiples of the driving photon energy $q\hbar\omega$ with integer order q, motivating the term *high harmonic generation*. The spectrum can be roughly separated into the perturbative regime with characteristic power-law scaling I^q, a non-perturbative plateau region in which conversion efficiency declines much more slowly, and a cutoff region at $\hbar\omega_{\mathrm{cutoff}}$. For centrosymmetric media, the spectrum exhibits only odd harmonics due to parity considerations (antisymmetric dipole and driving electric field $E(t + T/2) = -E(t)$ with $T = 2\pi/\omega$). Since harmonic emission occurs every half cycle, a harmonic spacing of $2\hbar\omega$ is also plausible from Fourier considerations. In media lacking an inversion center, or for multicolor light fields, even-harmonic emission is possible. Similar to the wave equation (2.10), it can be shown that, under the assumption of a continuous plane wave E and a homogeneous medium without pump depletion, the harmonic pulse duration is $\tau_{\mathrm{q}} = \tau_1/\sqrt{q}$ and the divergence angle is $\theta_{\mathrm{q}} = \theta_1/\sqrt{q}$. However, these relations serve only as an instructive baseline, since harmonic distributions in the plateau region can be considerably wider and structured due to propagation in the ionizing medium and phase-matching conditions, for example.

Within this thesis, HHG was employed in a noble-gas jet, which leads to plasma formation under the intense driving field and therefore requires consideration of additional effects such as gas density n_{gas}, active-medium length, and the focal

[2] Assuming $E(t) = E_0 \cos(\omega t)$, the equation of motion is $\mathrm{m_e}\partial_{\mathrm{t}}^2 x = -\mathrm{e}E(t)$ with $\partial_{\mathrm{t}} x = \partial_{\mathrm{t}} x_{\mathrm{drift}} - \mathrm{e}E_0 \sin(\omega t)/(\mathrm{m_e}\omega)$, giving $U_{\mathrm{p}} = \mathrm{m_e}\left\langle(\partial_{\mathrm{t}} x)^2\right\rangle/2 = \mathrm{e}^2 E_0^2/(4\mathrm{m_e}\omega^2)$ when $\partial_{\mathrm{t}} x_{\mathrm{drift}} = 0$

geometry of the laser [59]. The phase-matching condition for harmonic order q is given by $\Delta k_q = k_q - qk_0$ and has several contributions in general (see Ref. [62]). Within this thesis, phase matching for a given harmonic order and a fixed focusing geometry involves tuning the gas density via the backing pressure and the relative position of the light focus and gas jet along the propagation direction. For a focused Gaussian beam in a collinear geometry, phase matching can typically be achieved after the optical focus [62]. Since the light intensity governs plasma formation and thus plasma dispersion, phase matching also sets an upper limit on the employed intensities, reflecting the maximum dispersion compensation achievable by pressure tuning [62]. For nonzero phase mismatch, constructive interference occurs only over a limited coherence length $L_{coh} = \pi/|\Delta k_q|$ (similar to Sec. 2.1.2).

The semiclassical model presented in this section offers an illustrative explanation of HHG and its main features, but it suffers from several oversimplifications and neglected effects. For example, quantum effects such as ground-state depletion, interference, and wave-packet spreading during propagation are not considered. A fully quantum-mechanical description is provided by Lewenstein *et al.* [63], who showed that the relation (2.16) for the cutoff energy is only an approximation, for example. In addition to HHG in gases, liquid and solid-state materials are also investigated [64]. Especially in solid-state materials, the strong-field approximation, which is fundamental to the three-step model, no longer holds. Finally, the experiments presented in this thesis mainly use HHG as a tool for coherent frequency conversion, but HHG can also be used to generate attosecond light pulses through appropriate pulse-gating techniques and dispersion correction [64].

2.2 Photoemission Electron Spectroscopy

This section introduces photoelectron spectroscopy (PES) as a versatile experimental tool for probing the electronic structure of solid surfaces. The electronic structure can be broadly divided into tightly bound core levels, which are investigated using X-ray photoelectron spectroscopy (XPS) (Sec. 2.2.2), and valence-electron states, which are investigated using angle-resolved photoemission spectroscopy (ARPES) and momentum microscopy (Sec. 2.2.3). Section 2.2.1 introduces a theoretical description of the photoemission process, which is extended in Section 2.2.4 to transient regimes with time- and angle-resolved photoemission spectroscopy (trARPES). Finally, the space-charge effect is discussed (Sec. 2.2.5), as it can induce spectral broadening and spectral shifts.

2.2.1 Three-Step Model

This section introduces the photoemission process and explains the meaning of the experimentally acquired intensity in a typical photoemission experiment. These fundamental aspects are covered in a broad range of literature, for example in Refs. [1, 65–67], which provide further reading beyond the brief description given in this thesis. The following discussion adopts the notation introduced by Sobota *et al.* [1] and Damascelli *et al.* [66], which are not cited repeatedly in the following.

Photoemission is one possible optical process that describes electron emission from a solid upon photon absorption, provided that the photon energy $\hbar\omega$ exceeds the material's work function Θ. Emitted electrons are analyzed with respect to their kinetic energy E_{kin} and momentum $\hbar\mathbf{K}$ in vacuum. Energy and momentum conservation yield

$$E_{\mathrm{kin}} = \hbar\omega - \Theta - E_{\mathrm{B}} \tag{2.17}$$

$$\hbar\mathbf{K}_{\parallel} = \sqrt{2\mathrm{m_e}E_{\mathrm{kin}}}\sin(\vartheta)\,, \tag{2.18}$$

with the electron binding energy E_{B} prior to emission, the electron mass $\mathrm{m_e}$, and the angle ϑ between the surface normal and the photoemitted electron trajectory. Since the surface is translationally invariant, the electron's parallel crystal momentum is conserved upon photoemission (modulo $\mathbf{G}_{\parallel}$), which enables angle-resolved mapping of the material's electronic structure.

A microscopic description of the photoemission process is provided by the quantum-mechanical *one-step model*. However, a more phenomenological description is often given by the *three-step model*, which captures the most important aspects while remaining more intuitive. The three steps are depicted in Fig. 2.4 and comprise

1. Photoexcitation of the electron within the solid, $P(\mathbf{k}, E, \hbar\omega)$.
2. Propagation of the electron to the surface, $T(E_{\mathrm{kin}}, \hbar\omega)$.
3. Emission of the electron into the vacuum, $D(E_{\mathrm{kin}})$.

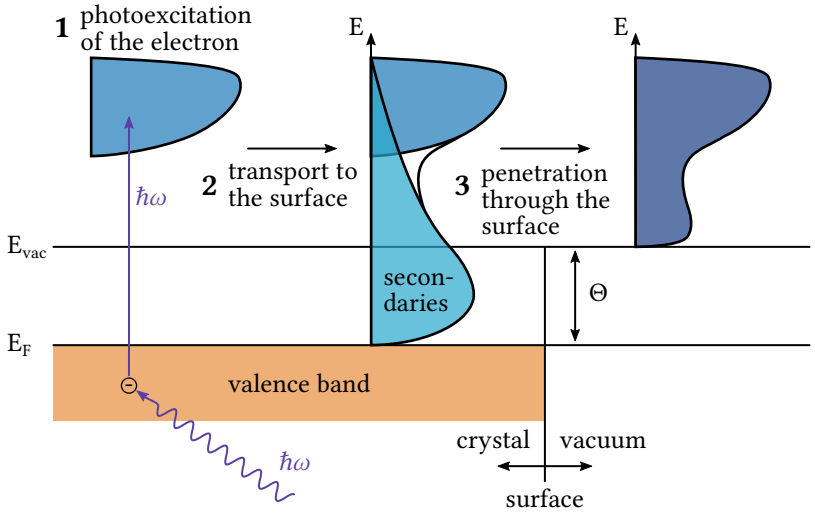


Figure 2.4: Schematic of the three-step model describing the photoemission process. The electron is excited above the vacuum energy in step 1, propagates to the surface in step 2, and leaves the surface barrier in step 3. Reproduced from Ref. [65], with permission from Springer Nature.

The total photoemission intensity $\mathcal{I}$ is given by the product of these three terms, which are discussed in more detail below.

Step 1: Photoexcitation

The first step can be described by a transition probability $P_{f,i}$ from initial state i to final state f using Fermi's golden rule, which in general reads

$$P_{f,i} = \frac{2\pi}{\hbar} \left| \langle \Psi_f^N | H_{per} | \Psi_i^N \rangle \right|^2 \cdot \delta \left(E_f^N - E_i^N - \hbar\omega \right), \tag{2.19}$$

with N-electron initial (final) state Ψ_i^N (Ψ_f^N), their energies E_i^N (E_f^N), and the perturbative Hamiltonian H_{per}. Here, H_{per} describes the electron–photon interaction and is typically approximated by neglecting two-photon processes ($\sim \mathbf{A}^2$), assuming the dipole approximation ($[\mathbf{A}, \mathbf{p}] \sim 0$), and applying Weyl gauge ($\Phi = 0$):

$$H_{per} = \frac{1}{2m_e} \left(\mathbf{p} + \frac{e}{c}\mathbf{A} \right)^2 - e\Phi - \frac{\mathbf{p}^2}{2m_e} \tag{2.20}$$

$$\approx \frac{e}{2m_e c} (\mathbf{A} \cdot \mathbf{p} + \mathbf{p} \cdot \mathbf{A}) \approx \frac{e}{m_e c} \mathbf{A} \cdot \mathbf{p}. \tag{2.21}$$

Here, $\mathbf{A}$ is the vector potential, $\mathbf{p}$ is the electron momentum, and Φ is an electric potential. The photoemission process is further described within the *sudden approximation*, which assumes that the electron is removed instantaneously and does not interact with the remaining $N-1$ electrons during emission. This approximation allows one to factorize $|\Psi_{i,f}^N\rangle$ in Equation 2.19 into the photoelectron wavefunction $|\varphi_{i,f}^{\mathbf{k}}\rangle$ with wave vector $\mathbf{k}$ inside the solid and final-state energy ε_f, and the remaining $|\Psi_{i,f}^{N-1}\rangle$: $|\Psi_{i,f}^N\rangle = |\Psi_{i,f}^{N-1}\rangle\, |\varphi_{i,f}^{\mathbf{k}}\rangle$. Neglecting photon momentum, the crystal momentum

is approximately conserved up to a reciprocal lattice vector, $\mathbf{k}_\mathrm{f} \approx \mathbf{k}_\mathrm{i}$ (mod $\mathbf{G}$). In this regime, the transition probability reads

$$P_\mathrm{f,i} = \left|M_\mathrm{f,i}^{\mathbf{k}}\right|^2 \sum_m \left|\langle \Psi_\mathrm{m}^{N-1} | \Psi_\mathrm{i}^{N-1} \rangle\right|^2 \cdot \delta\left(\varepsilon_\mathrm{f} + E_\mathrm{m}^{N-1} - E_\mathrm{i}^{N} - \hbar\omega\right). \tag{2.22}$$

Here, we introduced the one-electron dipole matrix element

$$M_\mathrm{f,i}^{\mathbf{k}} \equiv \langle \varphi_\mathrm{f}^{\mathbf{k}} | H_\mathrm{per} | \varphi_\mathrm{i}^{\mathbf{k}} \rangle \overset{(2.21)}{\approx} \frac{\mathrm{e}}{\mathrm{m_e c}} \langle \varphi_\mathrm{f}^{\mathbf{k}} | \mathbf{A} \cdot \mathbf{p} | \varphi_\mathrm{i}^{\mathbf{k}} \rangle, \tag{2.23}$$

which demonstrates that photoemission spectra can vary strongly with emission angle and also depend on the photon energy $\hbar\omega$. According to Moser [68], the photoemission matrix element (PME) of a Bloch band is associated with the Fourier transform of its Wannier orbital, multiplied by a polarization-dependent prefactor.

Since the $N-1$ electron system generally undergoes many-body interactions, sudden removal of the photoelectron leaves the $N-1$ wavefunction in a set of excited states m with eigenfunctions $|\Psi_\mathrm{m}^{N-1}\rangle$ and energies E_m^{N-1}. Without the matrix element $M_\mathrm{f,i}^{\mathbf{k}}$, Equation (2.22) is commonly written in terms of the single-electron removal spectral function

$$A^-(\mathbf{k}, E) = \sum_m \left|\langle \Psi_\mathrm{m}^{N-1} | c_{\mathbf{k}} | \Psi_\mathrm{i}^{N-1} \rangle\right|^2 \cdot \delta\left(E - E_\mathrm{m}^{N-1} + E_\mathrm{i}^{N}\right), \tag{2.24}$$

which describes the transition probability of the $N-1$ electron system at energy E after photoelectron removal with wave vector $\mathbf{k}$. Here, E is measured relative to the chemical potential μ. The full spectral function A is related to the single-electron removal function through the Fermi–Dirac distribution $f(E)$: $A^-(\mathbf{k}, E) = A(\mathbf{k}, E) f(E)$. Since the full spectral function is related to the retarded Green's function, interactions are often formulated via the complex *self-energy* $\Sigma(\mathbf{k}, E) = \Sigma'(\mathbf{k}, E) + i\Sigma''(\mathbf{k}, E)$, which gives

$$A(\mathbf{k}, E) = \frac{1}{\pi} \frac{\Sigma''(\mathbf{k}, E)}{\left[E - \varepsilon_{\mathbf{k}} - \Sigma'(\mathbf{k}, E)\right]^2 + \left[\Sigma''(\mathbf{k}, E)\right]^2}. \tag{2.25}$$

Here, Σ' shifts the single-electron band energy $\varepsilon_{\mathbf{k}}$, while Σ'' induces spectral broadening. Importantly, non-interacting systems with $\Sigma = 0$ exhibit $A = \delta(E - \varepsilon_{\mathbf{k}})$, which corresponds to a sharp peak that follows the electronic band dispersion. In contrast, strongly correlated materials can exhibit many-body effects such as satellite peaks in addition to spectral broadening.

Step 2: Propagation

After excitation, photoelectrons propagate to the surface in the second step, potentially undergoing elastic and inelastic scattering. Thus, $T(E_\mathrm{kin}, \hbar\omega)$ scales with the probability of reaching the surface without inelastic scattering, which is approximately $\alpha(\hbar\omega)\lambda_\mathrm{mp}(E_\mathrm{kin})$ with photon absorption coefficient α and electron inelastic mean free path λ_mp [67]. The former scales with photon energy, whereas the latter is typically dominated by electron–electron and electron–phonon coupling [65]. The inelastic mean free path exhibits a roughly universal energy dependence across solids,

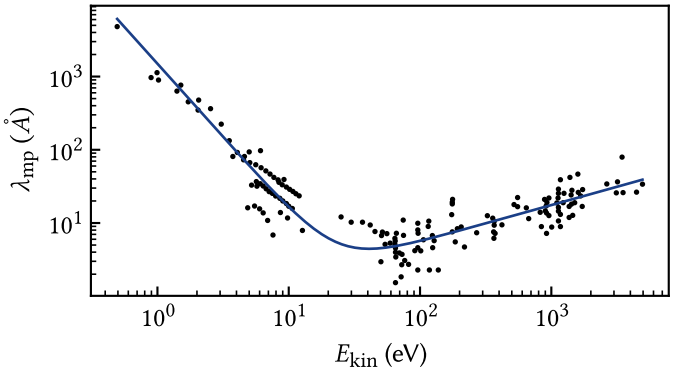


Figure 2.5: Electron inelastic mean free path of elemental solids. The solid line with empirical relation $\lambda_{mp} = AE_{kin}^{-2} + B\sqrt{E_{kin}}$ illustrates the general trend. Fit parameters A and B are not universal and depend on material class and dataset. Adapted from Ref. [69]. © 1979 Heyden & Son Ltd. Reproduced with permission of John Wiley & Sons Limited through PLSclear.

as shown in Figure 2.5. With a minimum of about 4 Å at 10 eV to 80 eV, this step highlights the surface sensitivity of PES. In addition, inelastic scattering introduces a background signal toward lower kinetic energies in the photoemission spectrum, which is typically referred to as *secondaries* (see Fig. 2.4).

Step 3: Emission

In the final step of photoemission, the electron crosses the surface barrier and transitions into a vacuum final state ($\langle\varphi_f^{\mathbf{k}}| \rightarrow \langle\varphi_f^{\mathbf{K}}|$). Common approximations model the boundary as a sharp transition, thereby neglecting the finite width of a real surface [65], and treat the vacuum state as a free wave. The transmission probability is then given by [67]

$$D(E_{kin}) = \frac{1}{2}\left(1 - \sqrt{\frac{V_0}{E_{kin} + V_0}}\right) \tag{2.26}$$

and depends on the photoelectron kinetic energy as well as the empirical inner-potential parameter V_0. During transmission into vacuum, the electron momentum perpendicular to the surface changes to account for the potential discontinuity according to

$$\hbar\mathbf{k}_{\perp solid} = \sqrt{2m_e\left[E_{kin}\cos^2(\vartheta) + V_0\right]}. \tag{2.27}$$

Since the photoelectron kinetic energy depends on $\hbar\omega$ (see Eq. 2.17), photon-energy-dependent measurements allow retrieval of $\mathbf{k}_\perp$.

The combination of all three steps motivates the total photocurrent

$$\mathcal{I} \sim \underbrace{I_0(\mathbf{k},\hbar\omega,\mathbf{A})A(\mathbf{k},E)f(E)}_{P(\mathbf{k},E,\hbar\omega)=\sum_{i,f}P_{f,i}} \cdot \underbrace{\alpha(\hbar\omega)\lambda_{mp}(E_{kin})}_{T(E_{kin},\hbar\omega)} \cdot \underbrace{\frac{1}{2}\left(1 - \sqrt{\frac{V_0}{E_{kin}+V_0}}\right)}_{D(E_{kin})}, \tag{2.28}$$

showing that the photoemission signal is proportional to the spectral function and modulated by the PME, among other factors. In the first part of Equation (2.28), I_0 accounts for intensity modulations by the photoemission matrix element, and the Fermi–Dirac function f ensures that only occupied states are probed. Since the measured E_{kin} depends on photon energy, experimentally acquired spectra are commonly converted to E_{B} (relative to E_{F} or E_{VBM}), whereas Equation 2.28 is formulated in terms of E with respect to μ. In addition to the spectral function, PES can also determine the work function by comparing the photon energy and total spectrum width (compare Fig. 2.4).

2.2.2 X-ray Photoemission Spectroscopy

As mentioned in the introduction to this section, electronic band structures can be roughly divided into tightly bound core levels and outer valence-electron levels. The former feature binding energies up to several keV [65], requiring X-ray photon sources for sufficient excitation energy in XPS measurements. Since core-level binding energies and photoionization cross sections are element- and shell-specific, XPS is, under many conditions, a non-destructive tool for determining the atomic composition of a material. Owing to the higher photoelectron kinetic energy, XPS is more bulk-sensitive than PES with UV photons (see Fig. 2.5).

In addition to compound identification, XPS spectra are strongly affected by many-body interactions. Upon photoexcitation of a core electron, a core hole is created, and this hole presents an attractive Coulomb potential for the valence levels. As a result, core-level binding energies depend on the chemical environment through both initial-state effects and final-state screening. In many systems, higher oxidation states correlate with higher binding energy, although screening can modify or even partially counteract the shift [67, ch. 2.6]. Many-body excitations accompanying core photoemission can produce intrinsic satellites and loss features, such as shake-up peaks and plasmon losses [70, ch. 12], while inelastic scattering on the way to the surface contributes an extrinsic background of secondary electrons [65]. One prominent example is an asymmetric line shape often observed in metallic compounds, featuring a tail toward higher binding energies (equivalent to lower kinetic energies). This behavior arises because the sudden creation of a core hole in a metal triggers low-energy electron–hole pair excitations near E_{F}, which screen the attractive Coulomb potential [65, 71]. Core holes may also decay via Auger processes, producing additional electron lines that are characteristic of the element and appear at approximately fixed kinetic energy, independent of the photon energy used.

For core levels with orbital angular momentum $l \neq 0$, the core spin $s = \pm 1/2$ couples to l and gives rise to a characteristic doublet. The relative peak intensities depend on the degeneracy of each total angular momentum $j = l + s$. For example, the p level ($l = 1$) splits into $j = 3/2$ with $m_{\mathrm{j}} = \{\pm 1/2, \pm 3/2\}$ (4 states) and $j = 1/2$ with $m_{\mathrm{j}} = \{\pm 1/2\}$ (2 states), yielding a ratio of 2:1. Accordingly, d orbitals have a ratio of $d_{5/2}$:$d_{3/2}$ = 3:2, and f orbitals have a ratio of $f_{7/2}$:$f_{5/2}$ = 4:3 [72]. Since the coupling

strength depends on the nuclear atomic number Z, the energetic separation between the doublet components increases for heavier elements.

For solids with partially filled valence orbitals, coupling between the core hole and unpaired valence electrons via spin and orbital angular momentum gives rise to a series of final states in the XPS spectrum. This so-called *multiplet splitting* depends on a variety of factors, including the number and configuration of unpaired valence electrons, their angular-momentum coupling to the core hole, and local crystal fields. Experimentally, multiplet splitting arises predominantly in first-row transition-metal compounds and in $4f$ elements [73], and it has often been mistaken for the presence of multiple oxidation states [73, 74]. While theoretical models can predict the atomic multiplet structure [75–77], a quantitative description requires accounting for charge transfer and hybridization between valence states and ligands, which is typically not included in these models [78].

Experimental XPS peaks comprise natural linewidth broadening of the core levels as well as instrument-related broadening arising from the photon linewidth and detector-resolution limits. This peak shape is captured by a Voigt function, defined as the convolution of a Lorentzian (natural linewidth) and a Gaussian (instrument broadening). In practice, a linear combination of Lorentzian and Gaussian is often applied, with a mixing parameter determining the relative weights (pseudo-Voigt) [79]. Asymmetric line shapes in metallic compounds can be captured by replacing the Lorentzian with a function that includes an asymmetry parameter α, such as a Doniach–Šunjić or Mahan profile, for example [65]. This thesis adopts a pseudo-Voigt function reported by Schmid *et al.* [80] that includes peak asymmetry by replacing the constant FWHM with an energy-dependent term. Another important aspect is the correct identification of the background signal from inelastic scattering. The background must match the data and is typically described using one of three choices: (i) linear background, (ii) Shirley background, or (iii) Tougaard background [79, 81, 82]. This thesis adopts the Shirley background, an empirical background proportional to the integrated signal above the background [81, 83]. It is determined iteratively during the fitting process and describes inelastic scattering well over a small energy range.

2.2.3 Momentum Microscopy

In contrast to tightly bound core levels, valence-electron states are generally much more delocalized. An experiment therefore has to map the photoemission intensity $\mathcal{I}(\mathbf{k}_\parallel, E_{\text{kin}})$ as a function of electron momentum ($\mathbf{k}_\parallel = \mathbf{K}_\parallel \mod \mathbf{G}_\parallel$ in the following) in addition to electron kinetic energy. In practice, angle-resolved photoemission spectroscopy (ARPES) experiments employing a single acquisition channel need to map the photoemission intensity as a function of emission angle by rotating the sample, which is subsequently converted into momentum. However, this technique suffers from long acquisition times and possible modifications of the photoemission matrix element upon sample rotation. Consequently, ARPES motivates multichannel

acquisition techniques, in which multiple observables ($\mathbf{k}_{\parallel}, E_{\text{kin}}$) can be acquired simultaneously. While energy-filtering techniques are described in more detail in Section 2.4, the following discussion focuses on parallel acquisition in $\mathbf{k}_{\parallel}$. A key component is the development of multichannel detectors, which often employ a multichannel plate to amplify the signal while preserving the spatial position of electrons in the final image plane at the detector [1]. The amplified electron distribution is then imaged onto a phosphor screen and recorded using a camera.

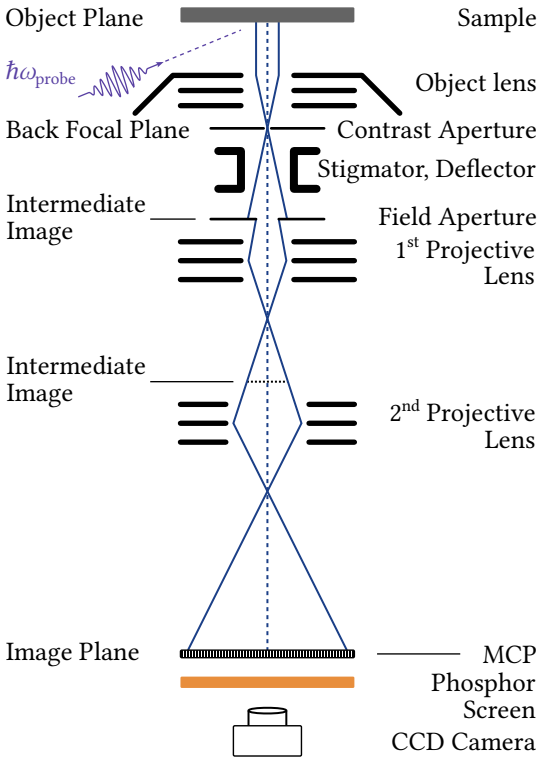


Figure 2.6: Schematic of a prototypical PEEM column. Reprinted from Ref. [84], with permission from Elsevier.

Using multichannel detectors, efforts toward simultaneous acquisition of a range of $\mathbf{k}_{\parallel}$ have led to the development of so-called momentum microscopes (MMs). They are based on a photoemission electron microscopy (PEEM)-like lens column in which the objective lens is operated as an immersion (cathode) lens by applying a high extraction and acceleration voltage to the sample [12]. This cathode lens and its immersion field collect electrons over nearly ±90° emission angles [17, 85]. PEEM is a PES technique that images the emitted photoelectron distribution as a function of sample position in real space. Spatial resolution is achieved by a lens column comprising electron optics and apertures upstream of the energy-filtering detector, as shown in Figure 2.6. An objective lens collects electrons and forms an image, which is corrected with deflectors and stigmators before being imaged onto the detector by projection lenses. This imaging creates a back focal plane, where a so-called contrast aperture (CA) selects a range of emission angles. A second, so-called field aperture (FA), placed at an intermediate image plane selects a region of interest (ROI) on the sample and thereby defines the field of view.

The lens system enables two modes of operation, classical PEEM and ARPES. Both benefit from the apertures in the lens column. In PEEM mode, momentum selection via the CA enables dark-field imaging [19]. In ARPES mode, which is achieved by projecting the back focal plane onto the detector, setting a FA enables spatial resolution. This constitutes an additional advantage over conventional ARPES, which requires light-spot sizes on the order of $\mathcal{O}(10\,\mu\text{m})$ for spatially resolved measurements (also referred to as μ-ARPES).

In ARPES mode, electrons entering the cathode lens at a post-acceleration angle α have a distance r from the optical axis of

$$r \propto \sin(\alpha) = \left|\mathbf{k}_{\parallel}\right| \frac{\hbar}{\sqrt{2\mathrm{m_e}\left(\mathrm{e}U_\mathrm{A} + E_\mathrm{kin}\right)}}, \tag{2.29}$$

with acceleration voltage U_A [67, 86]. Acceleration voltages are typically several keV up to 30 keV [67, ch. 11]. For $\mathrm{e}U_\mathrm{A} \gg E_\mathrm{kin}$, one has $(\mathrm{e}U_\mathrm{A} + E_\mathrm{kin}) \sim \mathrm{e}U_\mathrm{A}$, and the electron position on the detector is directly proportional to $k_{\parallel}$. This proportionality arises because the immersion field ideally accelerates electrons only along the surface normal and thus preserves $\mathbf{k}_{\parallel}$. Momentum conservation, formulated in Equation (2.18), yields a maximum photoelectron momentum of

$$k_{\parallel}^{\max} = \frac{1}{\hbar}\sqrt{2\mathrm{m_e}E_\mathrm{kin}} \quad (\text{for } \vartheta = 90^\circ), \tag{2.30}$$

which depends on the kinetic energy. This so-called *photoemission horizon* follows the dispersion of a free-electron wave in vacuum and gives the three-dimensional $(\mathbf{k}_{\parallel}, E_\mathrm{kin})$ data volume a parabolic shape.

2.2.4 Time-Resolved Photoemission

Conventional ARPES probes the occupied region of the electronic band structure, as indicated by the Fermi function in Eq. 2.28. The photoemission process leaves the $N-1$ electron system in an excited state, contributing many-body effects to the one-electron spectral function (see Eq. (2.25)). An extension to the time-resolved regime is therefore often understood as providing access to transiently occupied states above the Fermi energy, rather than simply "access to excited states." Time- and angle-resolved photoemission spectroscopy (trARPES) enables the study of electronic-structure dynamics and photoinduced phenomena. This is not limited to population dynamics, but also includes collective excitations such as phonons or charge-density waves [87], as well as the emergence of new phases without an equilibrium counterpart, such as Floquet–Bloch states (see Sec. 2.3.2) [11, 36, 88].

Practically, trARPES is employed in a two-color pump–probe configuration, where an intense pump pulse with photon energy $\hbar\omega_\mathrm{pump}$ excites the solid and a high-energy probe pulse images the nonequilibrium state via photoemission (see Fig. 2.7). The pump energy is often chosen below the work function Θ to avoid pump-initiated photoemission and thus reduce background. By controlling the temporal delay between pump and probe, the resulting stroboscopic snapshots can be stitched together to obtain the full four-dimensional $(\mathbf{k}_{\parallel}, E, t)$ data stack. The combined resolution in energy, momentum, and time constitutes a major advantage over all-optical spectroscopy for effects outside the light cone [36, 89]. In addition, transient dynamics that overlap in energy can be readily resolved and assigned to specific points of the Brillouin zone (BZ).

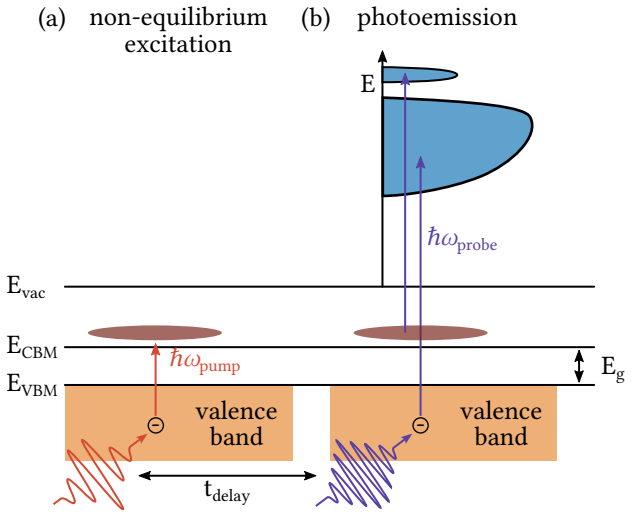


Figure 2.7: Schematic illustration of conduction-band excitation in a semiconductor, observed in trARPES. (a) Above-bandgap excitation with pump pulse $\hbar\omega_{pump}$ produces a hot-electron distribution in the conduction band. (b) The probe pulse follows the pump after time t_{delay} and induces photoemission with photon energy $\hbar\omega_{probe}$ from both the valence band and the transient conduction-band population.

Within the framework of the three-step model of photoemission, transient effects are often incorporated into the excitation (first) step [2, 90], yielding

$$P\left(\mathbf{k}_{\parallel}, E, \hbar\omega_{probe}, t\right) \approx I_0(\mathbf{k}_{\parallel}, \hbar\omega_{pump}, \hbar\omega_{probe}, \mathbf{A}, t) A(\mathbf{k}_{\parallel}, E, t) f(\mathbf{k}_{\parallel}, E, t) \tag{2.31}$$

with time t [2].

This description constitutes only an approximation, since pump-induced photoexcitation can also affect the second and third steps. Examples of such additional influences include vacuum-propagation effects, such as pump-induced space charge (Sec. 2.3.4), and modifications of the surface barrier, such as surface photovoltage (Sec. 2.3.3). Nevertheless, Eq. (2.31) already illustrates that trARPES spectra are generally not straightforward to interpret and that several parameters can influence the transient signal. The first factor, I_0, encodes time-dependent modifications of the photoemission matrix element, as demonstrated experimentally by Boschini *et al.* [91]. The second factor, A, includes modifications of the spectral weight at selected states in the BZ. The third factor, f, has an arbitrary form for a nonequilibrium distribution with potentially strong $\mathbf{k}_{\parallel}$ dependence, but it often relaxes toward a Fermi function $f(E,t)$ with elevated effective temperature. Freericks *et al.* [92] also extended the fully quantum-mechanical one-step model to the transient regime and developed a formalism to describe the signal observed in a pump–probe experiment. Although relaxation processes are generally difficult to disentangle, trARPES can determine relaxation rates when (i) a single scattering process dominates the response or (ii) competing scattering processes occur on different timescales [2, 92].

One prominent application of trARPES is the mapping of hot-electron relaxation in the conduction band of semiconductors and the determination of the electronic

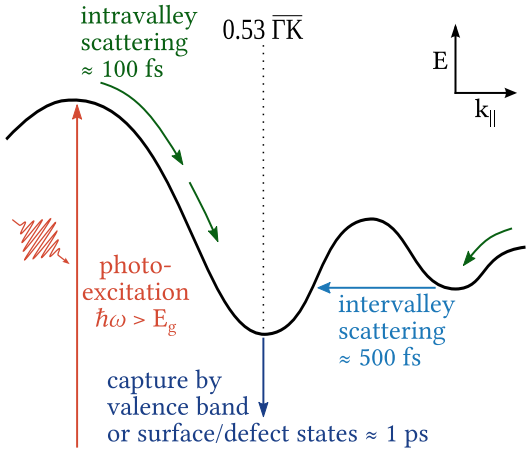


Figure 2.8: Hot-electron relaxation in bulk MoS_2 after above-bandgap excitation, captured with trARPES. Adapted with permission from Ref. [93]. © American Physical Society.

band gap of the material [93, 94]. Figure 2.8 illustrates possible relaxation dynamics observed in bulk $2H$-MoS_2, an indirect semiconductor with a 1.29 eV band gap. MoS_2 is a member of the transition metal dichalcogenide (TMD) family introduced in Sec. 4.4. Electrons are excited into the conduction band within the pump pulse duration and scatter via electron–electron scattering on the $\mathcal{O}(100\,\mathrm{fs})$ timescale to a local conduction-band minimum, where they either recombine with holes in the valence band or undergo trapping in surface or defect states on the $\mathcal{O}(1\,\mathrm{ps})$ timescale. Since the conduction band exhibits multiple local minima, electrons may also undergo intervalley scattering on the $\mathcal{O}(500\,\mathrm{fs})$ timescale. These timescales represent the experimental trARPES findings reported by Hein *et al.* [93]. Time-resolved photoemission enables identification of different scattering processes both through their characteristic timescales and through their location in energy and momentum.

Time-resolved photoemission requires pulsed light sources, whose bandwidth is typically much broader than that of continuous wave (CW) and quasi-CW sources due to the Fourier limit (see Sec. 2.1.1). Accounting for this contribution, the overall energy resolution ΔE_{tot} is generally given by

$$\Delta E_{\mathrm{tot}} = \sqrt{\sum_i (\Delta E_i)^2} = \sqrt{\left(\Delta E_{\mathrm{light}}\right)^2 + \left(\Delta E_{\mathrm{detector}}\right)^2}, \tag{2.32}$$

with the bandwidth of the light source $\Delta E_{\mathrm{light}}$ and the resolution of the analyzer $\Delta E_{\mathrm{detector}}$ [1, 67]. While this relation assumes independent Gaussian broadening and is most relevant for light sources that prioritize temporal resolution, it is generally applicable and can include additional sources of broadening (ΔE_i) neglected here, such as thermal broadening or space charge (discussed in Sec. 2.2.5).

2.2.5 Space Charge

In general, experimental photoemission setups aim to combine high energy and angular resolution with high fluence for rapid data acquisition. In terms of photon fluence, the so-called *space charge* effect constitutes a fundamental limitation in this pursuit [17, 95]. When an optical pulse emits more than one photoelectron, these electrons interact via Coulomb forces during their propagation to the detector, which can significantly modify their properties for sufficiently large electron numbers per pulse. Space charge therefore primarily affects pulsed light sources because of the high number of photons per optical pulse. As shown in Figure 2.4, photoelectrons undergo inelastic scattering on their transport to the surface, which, after surface ejection, gives rise to a large background of secondary electrons that can outnumber primary electrons by orders of magnitude [96], depending on the experimental parameters. These secondary electrons can make a major contribution to space charge in standard ARPES.

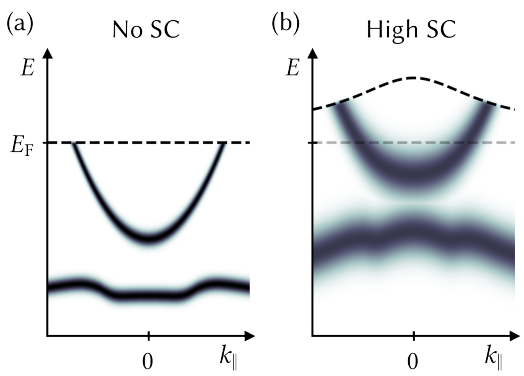


Figure 2.9: Schematic illustration of space-charge (SC) effects on an arbitrary band structure. Deterministic SC produces Lorentzian-shaped energy warping, and stochastic SC induces energy broadening.

Space charge is often modeled by distinguishing between primary and secondary electrons due to their distinct properties. For femtosecond optical pulses and sufficiently high initial kinetic energies, primary electrons exhibit negligible longitudinal spread along the propagation direction compared to their transverse spread, motivating their description as an expanding disc of electrons. In contrast, secondary electrons typically have very low kinetic energies, lower momenta, and comparatively little transverse expansion [17]. These characteristics influence the resulting Coulomb interactions, which can be separated into a deterministic contribution, corresponding to the mean force of the secondary-electron cloud on the primary electrons, and a stochastic contribution, which can be viewed as random scattering events. The former results in an energy shift of the photoelectron spectrum, whereas the latter induces energetic and angular broadening (see Fig. 2.9).

Both the space-charge-related energy shift and the broadening depend non-trivially on a wide range of experimental parameters [95]. The most important factors include pulse duration τ, spot diameter d, mean photoelectron kinetic energy $E_{\mathrm{kin}}^{\mathrm{mean}}$, and the number of photoexcited electrons per pulse N_{e}. While ARPES experiments using synchrotron-based light sources with $\mathcal{O}(10\,\mathrm{ps})$ pulse durations typically display linear dependencies of broadening and shift on N_{e}/d [97], laser-based experiments with femtosecond resolution have found a $\sqrt{N_{\mathrm{e}}}$ dependence of the space-charge energy

shift under typical conditions [98]. These relations apply only within a limited parameter window, since decreasing spot diameters in nano-ARPES experiments, for example, lead to different characteristics [99].

Both deterministic and stochastic space-charge contributions have been modeled in previous reports (see, e.g., [17, 95]), and electron densities of $N_e/d \approx 3000\,\mathrm{mm}^{-1}$ were reported to yield energy broadening below 5 meV in conventional hemispherical analyzers [95]. In MM, the photoelectron distribution is accelerated by the cathode lens and focused within the lens column, increasing Coulomb interaction and yielding dramatically lower space-charge limits [85]. Deterministic space charge was found to induce an energy shift following a two-dimensional Lorentzian profile in $\mathbf{k}_\parallel$ that is highest at zero momentum [17], enabling correction in post-processing via fits to iso-energy surfaces and energy renormalization. Within this thesis, space charge was mitigated in MM experiments by adjusting the photon fluence while tracking a small ($\mathbf{k}_\parallel$, E) volume close to the Fermi energy.

2.3 Selected Transient Signatures and Artifacts

A central excitation probed by trARPES in semiconductors is the promotion of electrons from the valence band into the conduction band, i.e., the creation of a transient electron–hole population. Beyond this single-particle picture, many-body interactions can substantially reshape the electronic response and leave clear fingerprints in the measured photoemission intensity. A prominent example is exciton formation and decay, discussed in Section 2.3.1.

Table 2.1: Overview of all discussed signatures in trARPES experiments.

Sec.	Effect	Physical origin	Photoemission hallmark
2.3.1	Excitonic signature	Bound electron-hole correlation	Additional discrete feature(s), binding-energy shifted
2.3.2	LAPE / Volkov sidebands	Final-state dressing of the photoelectron	Replica peaks spaced by $\hbar\omega_{\text{pump}}$
2.3.2	Floquet sidebands	Initial state dressing (periodic drive)	Replica bands, possible avoided crossings
2.3.4	Dynamic space charge	Coulomb interaction of emitted electrons	Transient energy shift and broadening
2.3.3	Surface photovoltage	Transient surface potential / band bending	Predominantly rigid spectral shift

In pump–probe photoemission, the detected signal is governed not only by dynamics inside the solid, but also by interactions of the outgoing photoelectrons with transient electromagnetic fields and electrostatic potentials near the surface and in the vacuum. These couplings can serve either as a deliberate handle to manipulate the surface electronic structure or as unwanted artifacts that mask intrinsic processes. A prominent example of the former is Floquet engineering, where a time-periodic Hamiltonian, e.g. imposed by a tailored oscillatory field, modifies the band structure and can generate Floquet–Bloch replica bands (see Sec. 2.3.2). Another is surface photovoltage, i.e., transient changes in the near-surface electrostatic potential (band bending) that rigidly shift spectral features and are particularly relevant for semiconductor heterostructures and photovoltaic materials (see Sec. 2.3.3).

In the present work (Ch. 5), most experimentally observed pump-induced spectral distortions are parasitic in nature and predominantly affect the photoelectron after emission. A key example is laser-assisted photoemission (LAPE) (Sec. 2.3.2), where the near-surface pump field dresses the continuum final state and generates Volkov-type sidebands. In addition, multiphoton emission driven by a strong pump pulse can produce a dense electron cloud that gives rise to dynamic space-charge effects, manifesting as transient energy shifts and spectral broadening (Sec. 2.3.4). All signatures discussed in this section are summarized in Table 2.1.

2.3.1 Exciton Fingerprint

Excitons are fundamental excitations in semiconductors that are commonly created by light–matter interaction [100]. They consist of an electron and a hole (an unoccupied state) bound by Coulomb interaction and form a Rydberg-like series of discrete states that converge to the electron–hole continuum [101]. Excitons can carry energy and momentum, but no net charge. Their coherent optical excitation is well described by the semiconductor Bloch equations, which are explained in detail in Refs. [101–103]. Assuming a two-level system with ground state $|0\rangle$ and excited state $|1\rangle$ as a model system, the electric field $\mathbf{E}$ of an optical pulse drives the system into a coherent superposition

$$|\psi(t)\rangle = c_0(t)\,|0\rangle + c_1(t)\,|1\rangle$$

with time-dependent complex coefficients $c_i(t)$. Within the dipole approximation, the interaction Hamiltonian is $H_{\text{int}} = -\hat{d}\cdot\mathbf{E}\,(t)$. The macroscopic polarization P of the material is given by the expectation value of the electric dipole moment operator $\hat{d}$, summed over all N dipole-allowed interband transitions,

$$P(t) = N\,\langle\psi|\hat{d}|\psi\rangle = N d_{01}\left(c_0^* c_1 + c_1^* c_0\right),$$

where $d_{01} = \langle 0|\hat{d}|1\rangle$ is the transition dipole matrix element. The quantity $\rho_{01} = c_0^* c_1$ is the off-diagonal element of the density matrix and represents interband coherence. It evolves with time as $\propto \exp\left(-i\omega_0 t - t/T_2\right)$ with the exciton resonance frequency ω_0 and coherence time T_2. This term describes an oscillating electric dipole density in the material and can be understood as bright excitons acting as dipoles with a well-defined phase relation inherited from the optical driving field [101].

Within the effective-mass approximation and for small center-of-mass momenta, the exciton energy in state λ can be approximated by a parabolic center-of-mass dispersion,

$$E_{\lambda,\mathbf{Q}} = E_{\text{g}} - E_\lambda^{\text{B}} + \frac{\hbar^2\mathbf{Q}^2}{2M} \tag{2.33}$$

with quasiparticle band-gap energy E_{g}, exciton binding energy E_λ^{B}, combined electron and hole mass $M = \text{m}_\text{e}^* + \text{m}_\text{h}$, and center-of-mass momentum $\mathbf{Q}$ [104]. Optically, only coherent excitons without center-of-mass momentum can be excited ($\mathbf{Q} = \mathbf{0}$) when phonon-assisted excitation is neglected. After the driving optical pulse, the coherent polarization in TMDs dephases within $\sim 100\,\text{fs}$ into an incoherent exciton population [105, 106]. This dephasing is driven by exciton–phonon scattering, which enables the formation of excitons with finite center-of-mass momentum $\mathbf{Q} \neq \mathbf{0}$ [107].

As the exciton arises from many-body interactions and cannot be described within a single-particle band-structure picture, its fingerprint in trARPES spectra is not trivial. Upon photoemission, the electron is detached from the bound state and detected as a single particle, while the hole remains in the valence band. Several theoretical studies found that the exciton appears at the exciton binding energy below the conduction band [104, 107–109], with a kinetic energy of

$$E_\text{e} = \hbar\omega - \Phi + E_{\text{g}} - E_\lambda^{\text{B}} + \frac{\hbar^2\mathbf{Q}^2}{2M} - E_{\text{hole}} \tag{2.34}$$

where Φ is the work function and E_{hole} is the hole energy in the valence band [104]. Experimentally, exciton energies at different momenta within the BZ can therefore be compared by referencing them to the corresponding hole energy in the valence band. Figure 2.10 displays exciton formation upon optical excitation with a pump pulse according to Equation (2.33), and the exciton final state upon photoemission according to Equation (2.34). The predicted exciton fingerprint has been confirmed experimentally in various semiconductor systems, such as Si(100) [110], Cu_2O [111], bulk WSe_2 [109], monolayer WSe_2 [33, 112, 113], and heterobilayer WSe_2/MoS_2 [33].

Under suitable experimental conditions, e.g. in the low-excitation regime and with a weak probe pulse, the in-plane momentum of the exciton's electron is conserved, and the probed population directly images the modulus squared of the excitonic envelope function in reciprocal space [104, 107, 112]. Hence, the electron distribution relative to the hole, i.e. the real-space exciton wave function, and the exciton Bohr radius can be obtained via Fourier transformation. This concept has already been demonstrated experimentally in Refs. [109, 112].

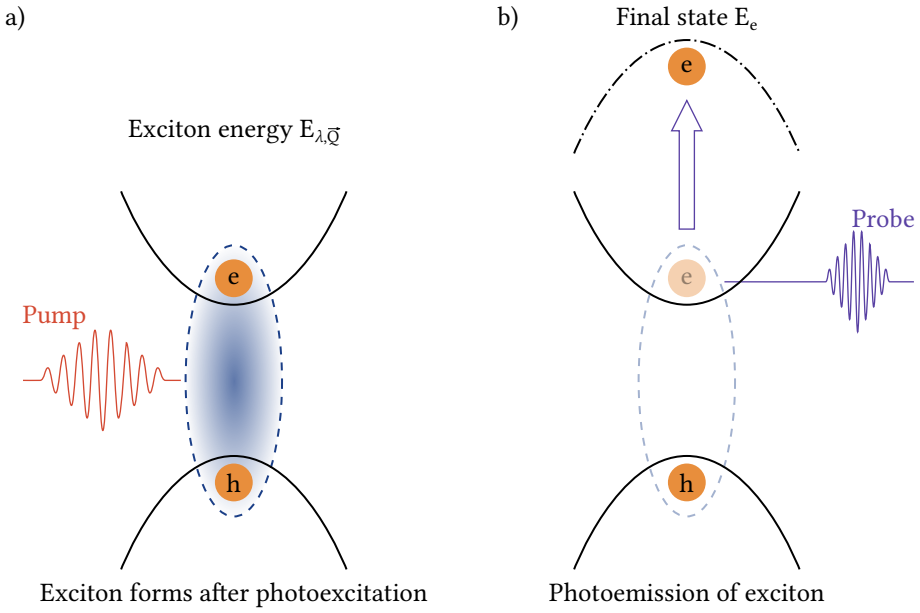


Figure 2.10: Exciton fingerprint in photoemission, adapted from Ref. [112] (Man *et al.*), licensed under CC BY-NC 4.0. (a) Exciton formation upon optical excitation. (b) Valence-band-like dispersion signature of the photoemitted electron.

As the exciton can be described as a linear combination of electron–hole pairs [104], the photoemitted electron can have a range of momenta. According to Equation (2.34), the resulting ARPES feature resembles the valence-band dispersion of the hole rather than that of the conduction band where the electron resided. However, Rustagi *et al.* predicted a slightly different fingerprint for an exciton distribution with a broad distribution of center-of-mass momenta $\mathbf{Q}$ in both direct- and indirect-gap semiconductors, which again follows a trace similar to the conduction band while retaining some remnant of valence-band-like dispersion [104]. Christiansen *et al.*

further predicted that the exciton signal exhibits only weak shadows of the valence band for coherent excitons and no trace of valence-band-like dispersion for incoherent excitons [107].

In agreement with the above discussion, trARPES is not limited to discriminating bright and dark excitons at different positions of the BZ. A theoretical study by Meneghini *et al.* predicted a double-peak signature for hybrid excitons in bilayer TMDs, where the electron and/or hole is hybridized between layers [114]. This prediction has since been confirmed experimentally [32]. Finally, interlayer excitons with the electron and hole located in separate layers of a TMD heterobilayer were found to exhibit distinct momentum fingerprints arising from the twist angle [34].

2.3.2 Laser-Assisted Photoemission

In the presence of an intense IR or visible pump pulse, the outgoing photoelectron can exchange energy with the pump field after photoemission by absorbing pump photons or undergoing stimulated emission of pump photons. As a consequence, the detected kinetic-energy spectrum exhibits replicas of the original photoemission feature, shifted by integer multiples of the pump photon energy $\hbar\omega_{\mathrm{pump}}$ (see Fig. 2.11). These replicas are commonly referred to as sidebands [115]. In the standard description, the continuum final state is treated as a laser-dressed free-electron state (a Volkov solution), i.e. a free particle whose phase is modulated by the oscillatory pump field [116, 117]. In this sense, LAPE is a final-state (continuum) dressing effect rather than a modification of the initial electronic band structure.

In the regime of high photoelectron kinetic energy ($E_{\mathrm{kin}} \gg \hbar\omega_{\mathrm{pump}}$) and weak laser field ($U_{\mathrm{p}} \ll \hbar\omega_{\mathrm{pump}}$), the sideband intensities follow a Bessel law. The ratio of the first sideband to the photopeak without pump is given by (see Refs. [21, 116])

$$\frac{I_1}{I_0} = J_1^2\left(\frac{\mathrm{e}}{\hbar \mathrm{m}_{\mathrm{e}}} \cdot \frac{\mathbf{p}\cdot\mathbf{E}_{\mathrm{pump}}}{\omega_{\mathrm{pump}}^2}\right) \underset{\mathbf{p}\,\|\,\mathbf{E}_{\mathrm{pump}}}{\sim} \frac{\mathrm{e}^2}{2\mathrm{m}_{\mathrm{e}}\hbar^2}\frac{E_{\mathrm{pump}}^2 E_{\mathrm{Kin}}}{\omega_{\mathrm{pump}}^4}. \tag{2.35}$$

Here, J_1 is the Bessel function of order 1, $\mathbf{p}$ is the photoelectron momentum, $E_{\mathrm{Kin}} = \mathbf{p}^2/(2\mathrm{m}_{\mathrm{e}})$, and $\mathbf{E}_{\mathrm{pump}}$ and ω_{pump} are the pump electric-field amplitude and angular frequency, respectively. Higher sideband orders are governed by higher-order Bessel functions J_{n}.

The scalar product $\mathbf{p}\cdot\mathbf{E}_{\mathrm{pump}}$ in Equation (2.35) implies a strong dependence on geometry and polarization. The sideband intensity is maximized when the pump field has a large component along the photoelectron emission direction, which in near-normal-emission geometries translates to pump configurations with a substantial field component normal to the surface. Since the first sideband intensity I_1 scales with E_{pump}^2, i.e. linearly with pump intensity, the delay-dependent sideband yield provides a convenient measure of temporal pump–probe overlap via the pump intensity envelope imprinted on the photoemission signal. A recent time-resolved XPS study by Wenthaus *et al.* reported that the observable sideband yield can be

additionally modulated by material-dependent dielectric screening, consistent with a modification of the effective near-surface pump field experienced by the outgoing photoelectrons [118].

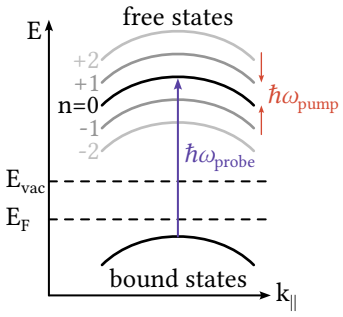


Figure 2.11: Schematic illustration of LAPE sidebands: absorption and stimulated emission of pump photons lead to replicas of the photoemission feature spaced by $\hbar\omega_{pump}$.

In addition to such Volkov-type final-state dressing, a sufficiently strong potential that is periodic in time can generate photon-dressed electronic states within the solid according to the Floquet theorem [2]. Such Floquet or Floquet–Bloch states can also produce replicas separated by $\hbar\omega_{pump}$ and may coexist with Volkov sidebands in trARPES. While both mechanisms share similar energy-spacing signatures, Floquet–Bloch dressing can lead to hybridization accompanied by characteristic gap openings in the electronic band structure [2]. Moreover, Volkov contributions can be strongly reduced by choosing pump geometries that minimize the pump-field component along the photoelectron emission direction [119]. Experimental studies on topological insulators reported momentum-dependent fingerprints that are only reproduced when including both Floquet–Bloch and Volkov contributions in the modeling [119, 120].

2.3.3 Surface Photovoltage Effect

The surface photovoltage (SPV) effect is the photoinduced change of the near-surface electrostatic potential in a semiconductor, i.e. a transient modification of the surface band bending [121]. In a pedagogical nonequilibrium picture, one may imagine that the surface and bulk would exhibit different Fermi-level positions if considered separately. Upon electrostatic equilibration in the connected material, however, the Fermi level is uniform throughout the sample and the mismatch is accommodated by an electrostatic potential drop across a near-surface space-charge region, i.e. band bending. SPV plays a major role, for example, in photovoltaic devices [122] and Schottky junctions [123]. Several mechanisms can create or modify the built-in surface potential, such as semiconductor–metal contact (work-function mismatch and charge transfer) or adsorbate- and defect-induced surface doping [124]. In addition, surface reconstructions and dangling bonds can introduce a high density of surface states, which can fix the Fermi level (Fermi-level pinning), meaning that the near-surface band alignment is determined by surface states rather than by the bulk doping level [121].

As an example, consider an *n*-doped semiconductor whose bulk Fermi level lies close to the conduction band minimum (CBM), while surface states pin the surface Fermi level closer to mid-gap. Charge transfer between bulk and surface states establishes equilibrium and forms a space-charge region whose width depends on doping and

screening and can range from tens of nanometers to micrometers [125, 126]. The resulting electric field shifts the local band edges as a function of the distance to the surface z, producing band bending. As shown in Figure 2.12, this corresponds to upward band bending of the electronic structure toward the surface.

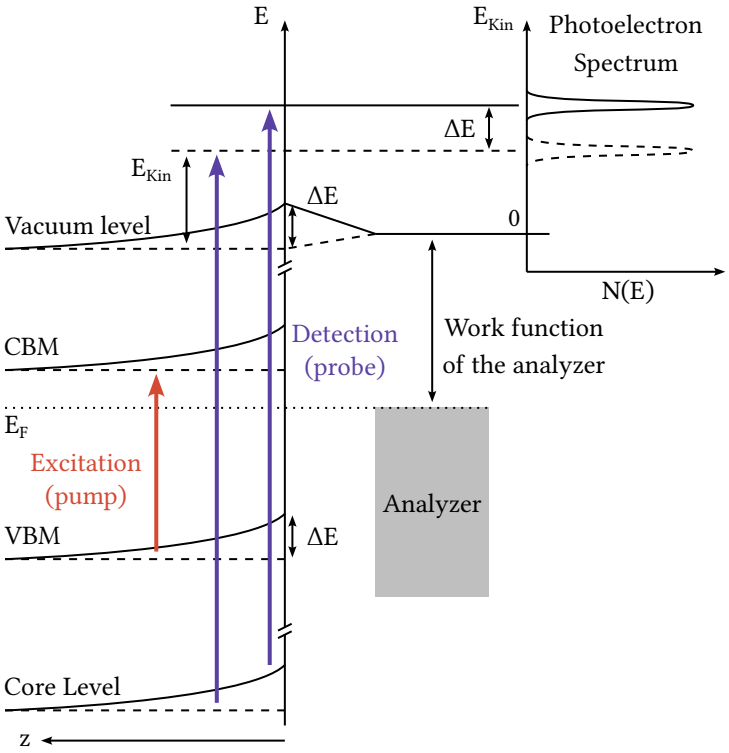


Figure 2.12: Schematic surface photovoltage effect on the energy-band alignment. Dashed lines mark energy levels with flat bands and solid lines mark upward band bending at the surface. Upon optical excitation, photocarriers partially screen the space-charge field and induce dynamic band flattening, which causes an apparent energy shift in the photoemission spectrum because the analyzer defines a fixed energy reference via Fermi-level alignment. Reprinted from Ref. [127], with permission from Elsevier.

At first glance, one might incorrectly expect that band bending does not shift photoemission spectra because the electrostatic potential shifts all electronic levels, including the vacuum level. In a real photoemission experiment, however, the measured binding-energy scale is referenced to the analyzer Fermi level, which is aligned with the sample Fermi level, while the analyzer work function is fixed [121]. Consequently, an electrostatic potential in the emission region changes the kinetic energy at the analyzer and leads to a measurable spectral shift. For upward band bending (as in Fig. 2.12), the near-surface electronic states are shifted closer to E_F, which is synonymous with a reduced binding energy $E_B = E_F - E_i$ compared to the bulk. If the photoemission signal contains contributions from a depth range that spans a significant potential gradient, the spectrum can additionally broaden due to depth averaging across the space-charge region [128]. Increasing photon energy increases

the effective probing depth and can therefore modify both the apparent shift and the broadening when probing across the band-bending profile [128].

Surface photovoltage refers to the light-induced modification of an existing band-bending profile [121]. For an *n*-doped semiconductor with upward band bending, optically excited electron–hole pairs are separated by the space-charge field, which reduces the net space charge and screens the built-in field. In a trARPES experiment, this dynamic manifests as a transient shift of the entire spectrum. For upward band bending, the reduction of bending shifts spectral features to higher binding energy (lower kinetic energy) relative to the equilibrium spectrum. For *p*-doped semiconductors with downward band bending, the sign is reversed, making trARPES sensitive to the nature of the doping [125, 126].

In a naive picture, the observed kinetic-energy shift would directly equal the internal voltage change. In practice, photoelectrons continue to experience the time-dependent electric field in front of the sample even after emission. This measurement response is characterized by an escape time τ^*, defined as the time required for the photoelectrons to traverse 99 % of the field region, approximately given by

$$\tau^* \approx \left(13.4\,\frac{\mathrm{ns}\sqrt{\mathrm{eV}}}{\mathrm{mm}}\right)\frac{R_0}{\sqrt{E_{\mathrm{Kin}}}}, \tag{2.36}$$

where R_0 denotes the pump radius and E_{Kin} depends on the XUV photon energy for a fixed initial state [127] (a good approximation for $E_{\mathrm{Kin}} > 5\,\mathrm{eV}$). Importantly, τ^* is primarily set by pump geometry and probe photon energy, whereas the SPV amplitude depends on excitation fluence, typically increasing until saturation [125]. For typical spot sizes and kinetic energies, τ^* is on the order of hundreds of picoseconds to a few nanoseconds, which can produce characteristic energy shifts and distortions even at negative pump–probe delays [129]. Photoelectrons emitted at negative delays propagate away from the surface before the pump-induced field is established and therefore acquire a delay-dependent momentum impulse when the field turns on [130, 131].

2.3.4 Pump-Induced Space Charge

In static ARPES, space-charge effects arise from Coulomb interactions within the photoelectron cloud, leading to rigid energy shifts and spectral broadening. The effect is most pronounced at high photoelectron densities and low kinetic energies (see Sec. 2.2.5). In time-resolved experiments, an additional space-charge contribution can be introduced when the pump pulse also emits electrons [89]. Although the pump photon energy is typically below the work function, multiphoton photoemission can occur at sufficiently high pump fluence. In such cases, the lowest-order process that exceeds the work function usually dominates [88], producing a pump-induced electron distribution with characteristic kinetic energies on the order of a few electronvolts. As discussed below, this additional electron cloud leads to a

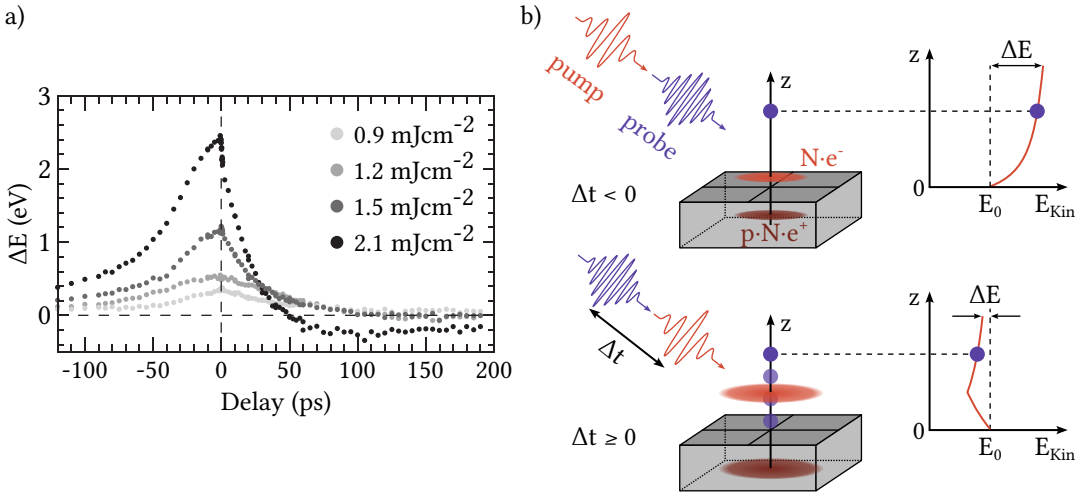


Figure 2.13: Pump-induced space charge. (a) Extracted energy shift of σ-band emission from highly oriented pyrolytic graphite (HOPG) as a function of delay. Pump fluence strongly modifies both the timescale and the sign of the shift. (b) Schematic interaction geometry between pump- and probe-emitted photoelectrons before and after temporal overlap. The plots to the right show the energy shift of the probe-emitted electrons as a function of distance from the sample surface z. Adapted from Ref. [88], with the permission of AIP Publishing.

characteristic transient, strongly asymmetric signal that depends sensitively on the pump properties.

An example of pump-induced spectral shifts at different pump fluences is shown in Figure 2.13a. Here, ΔE denotes the kinetic-energy shift of the probe photoelectrons, $\Delta E > 0$ therefore corresponds to a shift to lower binding energy in the spectrum. Oloff *et al.* [88] reported transient energy shifts of the highly oriented pyrolytic graphite (HOPG) σ-band of several electronvolts, with a pronounced asymmetry between negative and positive delays. The maximum shift occurs near temporal overlap, and relaxation typically proceeds on the order of $\mathcal{O}(100\,\mathrm{ps})$ for fluences around $1\,\mathrm{mJ/cm^2}$ [88, 89, 132]. Increasing pump fluence not only changes the relaxation timescale, but can also reverse the sign of the spectral shift (see Fig. 2.13a). Experimentally, the shift magnitude scales approximately as a power law in pump fluence, with an exponent close to the relevant multiphoton order, as demonstrated, for example, in Ref. [88].

The interaction between the pump-induced electron cloud and the XUV-probe photoelectrons is schematically illustrated in Figure 2.13b, separating negative and positive delays (see also Refs. [88, 132]). Because the emitted electron clouds typically extend much further laterally than along the surface normal [132], they are often approximated as thin discs, enabling a one-dimensional treatment. For negative delays, i.e. when the probe arrives before the pump, the pump electron cloud is created after probe photoemission. Its Coulomb field repels and thereby accelerates the already emitted probe electrons, producing a shift toward higher kinetic energy

($\Delta E > 0$). In this regime, the shift timescale is mainly set by the probe-electron velocity and the pump spot size, whereas the pump fluence primarily controls the shift magnitude [88].

For positive delays, the dynamics are more complex because the probe photoelectrons typically have substantially higher kinetic energies than the multiphoton-emitted pump electrons. The faster probe electrons can therefore overtake the pump electron cloud during propagation to the detector. Immediately after emission, the probe electrons experience a retarding field from the pump cloud, leading to a shift to lower kinetic energy ($\Delta E < 0$). After passing the pump cloud, the field direction reverses and partially compensates the initial deceleration. In practice, this compensation is often incomplete because overtaking occurs after the pump cloud has expanded and its field has weakened, which can leave a residual negative shift at long positive delays. Compared to the negative-delay case, the initial relaxation can become faster at higher pump pulse energies, while increasing the pump spot size again slows the relaxation [88]. Within the mean-field picture of Ref. [88], this behavior is consistent with a higher electron density driving faster lateral expansion of the pump cloud and thus more rapid dilution of its Coulomb field.

Many reported model calculations address this effectively one-dimensional problem using mean-field approaches and often focus on the rigid energy shift [88, 132]. However, pump-induced space charge can also cause stochastic spectral broadening in addition to the average shift. More advanced simulations, combined with careful comparison to experiment, can help disentangle these contributions and enable quantitative extraction of the underlying dynamics [133].

2.4 Experimental Instrumentation

Two central components of a PES experiment are the photon source and the energy analyzer. Both are introduced here for the three experimental setups used in this thesis, with one exception: the pulsed photon source of the KREIOS beamline (Sec. 2.4.2), whose design and characterization are part of this work (details in Ch. 3). In addition to outlining the instrumentation, this section highlights the different energy-analyzer geometries, which were omitted in Section 2.2. In general, two analyzer concepts were used: dispersive hemispherical deflection analyzers (HDAs) for both XPS and (tr)ARPES, and a time of flight (TOF) analyzer for (tr)ARPES only.

2.4.1 XPS Setup

The near-ambient-pressure XPS setup employs a classical HDA that disperses electrons by kinetic energy along one (energy-dispersive) axis of the detector, while the non-dispersive (transverse) axis can encode one-dimensional angular information over a limited acceptance angle. In general, a HDA consists of two concentric hemispherical electrodes with radii R_1 and R_2 ($R_2 > R_1$) held at different electrostatic potentials. This configuration creates a radial electric field that deflects electrons onto Kepler-type orbits with a central trajectory at $R = (R_1 + R_2)/2$ [1, 67]. The electric field disperses the electron distribution and enables energy filtering using entrance and exit slits with widths S_{en} and S_{ex} (see Fig. 2.14). Under ideal geometric considerations, electrons with pass energy E_{pass} traverse the analyzer on the central trajectory with an energy spread δE given by

$$E_{\mathrm{pass}} = \mathrm{e}\Delta V \frac{R_1 R_2}{R_2^2 - R_1^2} \tag{2.37}$$

$$\delta E = E_{\mathrm{pass}} \frac{S_{\mathrm{en}} + S_{\mathrm{ex}}}{4R}, \tag{2.38}$$

where $\Delta V = |V_2 - V_1|$ is the potential difference between the hemispheres [16, 67]. Notably, for a fixed detector geometry and fixed S_{ex}, the energy resolution depends on E_{pass} and S_{en}. The PHOIBOS 150 hemispherical analyzer (Specs GmbH) used in this setup has a maximum acceptance angle of ±22°, a mean hemisphere radius of 150 mm, and eight entrance slits of variable size. In this thesis, only the 3 mm×25 mm slit was used, with the first number corresponding to the energy-dispersive axis.

The XPS setup can operate at near-ambient pressures up to 1 mbar at the sample, enabled by a modified HDA design. Lens stages placed upstream of the HDA, together with an entrance nozzle, differential pumping, and an aperture, allow maintaining $\mathcal{O}(1 \times 10^{-8}\,\mathrm{mbar})$ at the hemisphere under these conditions (details in Ref. [134]). However, this capability was not used for the measurements in this thesis[3], and a base pressure of 1×10^{-10} mbar was maintained.

[3] Entrance nozzle and Al-coated silicon nitride window were removed

Core-level electrons were photoemitted using emission from an X-ray source (XR-MF, Specs GmbH), which is monochromatized (μ-Focus 600 X-Ray tube, Specs GmbH) and focused to provide Al $K_{\alpha 1}$ radiation at 1486.6 eV [70, ch. 12]. The Al anode was operated at a potential of 15 kV and a current of 9.2 mA, corresponding to a power of 138 W. The incidence angle was 55° relative to the surface normal, and the spot size on the sample was approximately 500 µm. All measurements were acquired at room temperature and 0° electron emission angle (normal emission). Binding energies were referenced to the Fermi level of Au(111). Survey scans were acquired at 50 eV pass energy with a total energy resolution of approximately 700 meV. All other scans were acquired at 20 eV pass energy, yielding (335 ± 135) meV total energy resolution (see Fermi edge fit in Sec. 4.2).

2.4.2 KREIOS Momentum Microscope

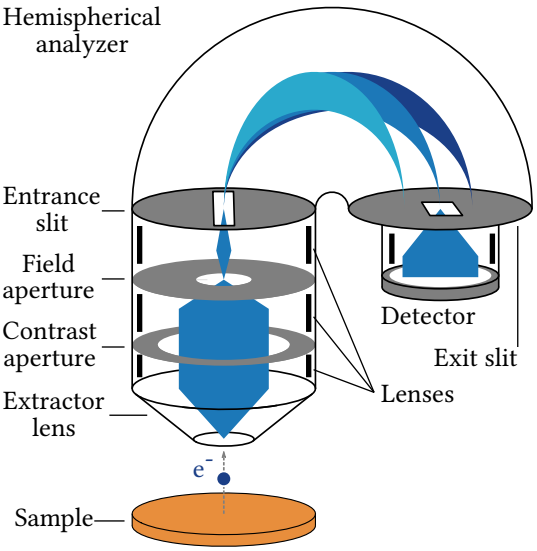


Figure 2.14: Schematic illustration of the KREIOS 150 MM. Published in Ref. [135].

The KREIOS 150 MM (Specs GmbH), shown in Figure 2.14, combines a hemispherical deflection analyzer (HDA) for energy selection with an MM lens column. In classical ARPES, a HDA typically acquires a 2D image representing a narrow kinetic-energy interval on one axis and the emission angle θ on the other axis [65]. In momentum microscopy, the analyzer instead transmits two-dimensional distributions in (x, y) or (k_x, k_y) at an approximately constant selected kinetic energy [67, ch. 11]. This is possible because the imaging HDA transfers the relevant angular information from entrance to exit (neglecting the sign), enabling two-dimensional imaging by encoding the respective coordinate in the entrance angle at the entrance-slit plane [16, 86]. The encoding is implemented by an electron-optical lens before the HDA, which projects the reciprocal-space image (corresponding to a Fourier transform) onto the entrance-slit plane, and a second lens after the HDA, which applies the inverse Fourier transform in the exit-slit plane [16]. In momentum mode, the resulting iso-energetic contour at the selected kinetic energy is referred to as a *momentum map* in this thesis. Notably, this geometry enables simultaneous acquisition of all accessible $\mathbf{k}_{\parallel}$ (see Eq. 2.30) and requires scanning only E_{kin} to obtain a complete three-dimensional data stack. The lens column further allows setting a magnification M, which restricts the maximum observable $\mathbf{k}_{\parallel}$ at high kinetic energies. In practice, the pass energy is kept constant, and energy selection is performed using a

pre-retardation stage in front of the analyzer. This approach yields an approximately constant analyzer contribution δE across the full spectrum [65, ch. 1].

Tusche *et al.* [16] showed that, up to second order, the dominant aberration contribution for imaging HDAs is *nonisochromaticity*, caused by non-vanishing aberrations along the energy-dispersive axis. Nonisochromaticity manifests as a weak quadratic variation of the pass energy across the field of view, rendering the image slightly non-monochromatic along one axis. This result was obtained assuming a simple $1/R$ potential with symmetric entrance and exit at fixed radii. According to the manufacturer, the KREIOS MM compensates this effect through an adapted lens and hemisphere design.

The KREIOS 150 MM specifications were described in detail by Matsui *et al.* [136] and Chuang *et al.* [137], including the field of view as a function of magnification for both operation modes, as well as the available apertures and entrance slits. The mean hemisphere radius of the KREIOS is 150 mm. The exit slit has size 0.2 mm × 3 mm, with the first number corresponding to the radial axis. The working distance between extractor lens and sample is approximately 4 mm and can be slightly tuned using appropriate lens settings.

Within this thesis, the extractor (cathode) lens voltage was set to 10 kV and E_{pass} was set to 50 eV, with magnification $M = 2$ for momentum mode (about $\pm 2.0\,\text{Å}^{-1}$ field of view) and $M = (1; 2)$ for PEEM mode ($\sim 200\,\mu\text{m}$ and $\sim 100\,\mu\text{m}$ field of view), unless stated otherwise. Only the smallest entrance slits 3 to 5 were used, with sizes 1.0 mm × 1.8 mm, 0.2 mm × 0.8 mm, and 0.5 mm × 1.0 mm, respectively, again with the first number corresponding to the radial axis. These settings do not represent the minimum achievable energy resolution due to the high pass energy. From Equation (2.38), the slit-limited lower bound is approximately 13 meV ($R = 150\,\text{mm}$, $S_{\text{en}} = S_{\text{ex}} = 0.2\,\text{mm}$). This estimate neglects additional broadening mechanisms, including lens and retardation aberrations, photon bandwidth, space charge, power-supply stability, and related effects. Existing literature [136, 137] reported an energy resolution of about 23 meV at $E_{\text{pass}} = 20\,\text{eV}$ and 15 kV extractor voltage, as well as 50 nm spatial resolution and $0.012\,\text{Å}^{-1}$ momentum resolution. Minimum-resolution settings substantially reduce the count rate, requiring a trade-off between energy resolution and acquisition time.

The KREIOS resolution in momentum mode was characterized on the Au(111) surface using 6 eV photons described in Ref. [138][4]. Figure 2.15 shows the Au(111) surface state at $M = 4$, $E_{\text{pass}} = 50\,\text{eV}$, $T = 6.5\,\text{K}$, and $S_{\text{en}} = 0.2\,\text{mm} \times 0.8\,\text{mm}$. Figure 2.15a shows the momentum map at 10 meV below E_{F}, exhibiting two concentric rings for the Rashba-split surface state (compare Sec. 4.1). A cut along the solid line is shown in Figure 2.15b and demonstrates the parabolic dispersion of the spin-split band, consistent with the report by Tusche *et al.* [86]. The line profile along the solid line in Figure 2.15a was fitted with four pseudo-Voigt functions (see Fig. 2.15c), whose shared Gaussian width corresponds to $0.005\,\text{Å}^{-1}$ and defines the experimental momentum resolution. The retrieved separation of inner and outer ring of $0.025\,\text{Å}^{-1}$ agrees well

[4] Measurements conducted by Ass.-Prof. Dr. Giovanni Zamborlini and published in Ref. [135]

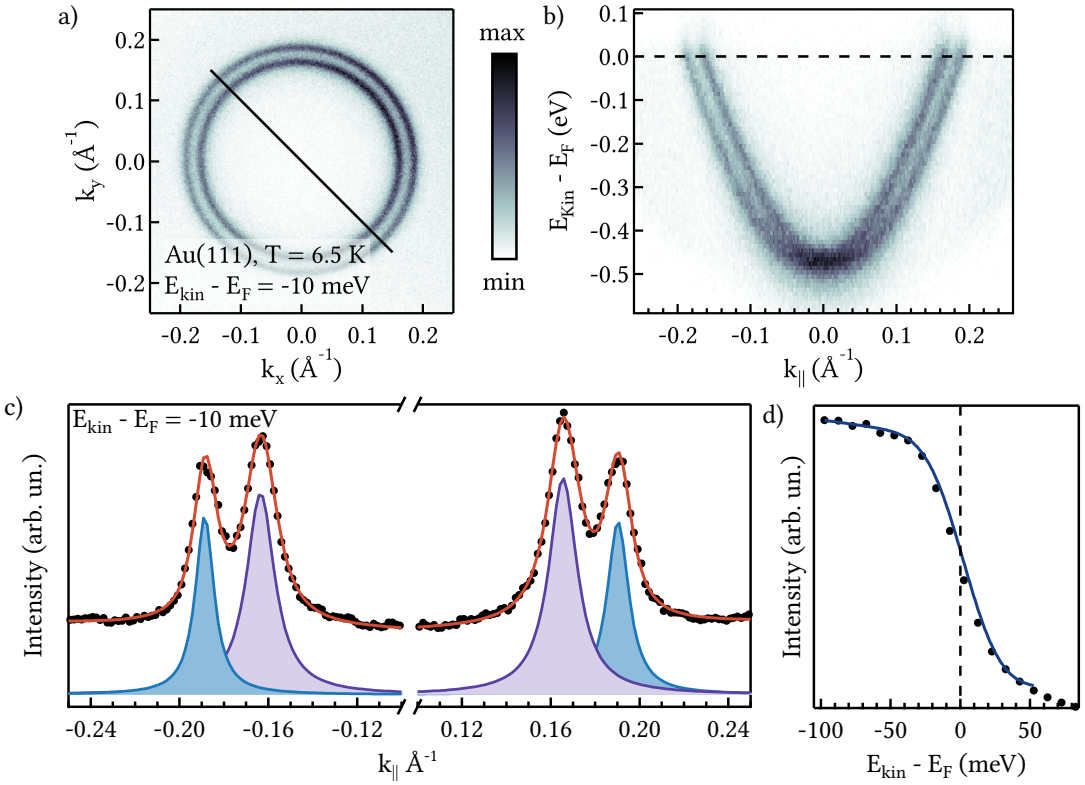


Figure 2.15: KREIOS momentum mode characterization on the Au(111) surface state. (a) Momentum map close to Fermi, showing two rings from Rashba spin-orbit splitting. The solid line marks the cut in (b), showing the surface state's parabolic dispersion, and the line profile in (c). The line profile was fitted with four pseudo-Voigt functions. (d) Angle-integrated Fermi edge, yielding 49 meV Gaussian width from a fit according to Equation (3.2). Published in Ref. [135].

with the report by Tusche *et al.* [86]. Finally, the total experimental energy resolution was determined by fitting an angle-integrated Fermi edge using a convolution of a Gaussian with a (fixed-temperature) Fermi function multiplied by a linear background (see Eq. (3.2)), yielding 49 meV from the Gaussian FWHM. The two other slits used in this thesis yield a total energy resolution of 92 meV ($S_{\mathrm{en}} = 0.5\,\mathrm{mm} \times 1.0\,\mathrm{mm}$) and 184 meV ($S_{\mathrm{en}} = 1.0\,\mathrm{mm} \times 1.8\,\mathrm{mm}$), determined at $T = 80\,\mathrm{K}$.

In addition to the KREIOS 150 MM, the analysis chamber comprises a sample stage with six-axis motorization for three translations and three rotations (HESTIA, Specs GmbH). An integrated cryostat allows cooling with liquid nitrogen and helium down to about 6 K. Attached to the KREIOS vacuum chamber with a base pressure of 1×10^{-10} mbar is a preparation chamber with standard ultra-high vacuum (UHV) preparation and sample characterization equipment, as well as a load lock for sample transfer into vacuum.

2.4.3 METIS Beamline

The METIS beamline combines a high-repetition-rate XUV photon beamline with a MM featuring a time of flight (TOF) analyzer (METIS 1000, Specs GmbH). In contrast to the HDA of the KREIOS MM, TOF analyzers do not disperse electrons by electrostatic deflection. Instead, they resolve the kinetic energy via the flight time through a cylindrical drift tube. A delay-line detector records the electrons' time of arrival as well as their spatial position on the detector, enabling simultaneous acquisition of the full (k_x, k_y, E_{kin}) data stack over the accessible energy window. Similar to the pre-retardation stage in the KREIOS, the TOF analyzer employs a drift energy E_d, which sets the electron flight time and indirectly affects the achievable energy resolution. The total flight time in a drift tube of length l is given by $\tau = l\sqrt{m_e/2E_d}$ and typically amounts to $\mathcal{O}(200\,\text{ns})$ [67, ch. 11]. The relative energy resolution,

$$\frac{\delta E}{E} \approx \sqrt{\left(\frac{2\delta\tau}{\tau}\right)^2 + \left(\frac{2\delta l}{l}\right)^2} \tag{2.39}$$

with the kinetic energy E mapped from TOF, is approximated by two contributions. The first is the total time resolution $\delta\tau$, which includes contributions from the light-source pulse duration and the analyzer time-to-digital converter (TDC). The second is the uncertainty in flight path δl, arising from the finite photoemission area on the sample, field inhomogeneities, and angular spread or off-axis trajectories [67, ch. 3].

The primary advantage of TOF analyzers is the parallel acquisition of all kinetic energies and the lack of an entrance slit, enabling rapid data acquisition. However, this architecture requires pulsed light sources with short pulse durations. In addition, the secondary-electron background increases the total intensity on the detector and can risk detector saturation at high flux unless additional measures are taken to suppress low-energy electrons. The electron flight time also limits the maximum repetition rate to $\mathcal{O}(1\,\text{MHz})$ [1], as energy separation forbids overlap of TOF spectra from consecutive pulses: high-energy photoelectrons from a subsequent pulse would overtake low-energy electrons from the previous pulse. The repetition-rate limit can be increased by raising E_d or reducing the energy window. However, for a detector with fixed temporal resolution, higher E_d degrades the energy resolution. Finally, the kinetic-energy spread across the spectrum induces chromatic aberration in the electron optics, such that magnification and other distortions vary with energy and only a limited energy window exhibits weak distortions. Extensive post-processing can correct resulting artifacts within certain limitations [35].

The METIS 1000 MM is attached to an analysis chamber featuring a sample stage (HESTIA, Specs GmbH) with an integrated helium cryostat comparable to the KREIOS setup, and a base pressure of 2×10^{-10} mbar. An additional preparation chamber includes standard Ar^+-ion sputtering and annealing stages, as well as a load lock for sample insertion. Two light sources are coupled to the MM. The first is a CW UV diode (Thorlabs GmbH) with 4.68 eV photon energy, used to illuminate a large area for PEEM inspection in energy-integrated mode. The second is a pulsed light source

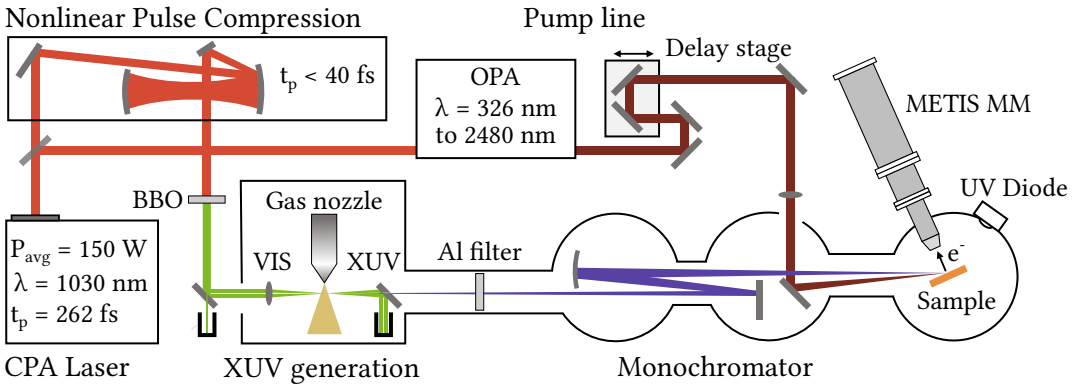


Figure 2.16: Schematic layout of the METIS beamline. The layout shares many similarities with the beamline presented in Chapter 3, but key differences are the higher average-power laser system, gas-filled multi-pass cell (MPC), beam separation of XUV and SHG light, and the TOF detector for the MM.

for time-resolved momentum microscopy (trMM) that shares many similarities with the XUV beamline described in Chapter 3.

The pulsed light source (see Fig. 2.16, specifications from Ref. [139]) is driven by a commercial chirped-pulse amplification laser system (Active Fiber Systems GmbH) with an average power of up to 300 W (operated at 150 W), an adjustable repetition rate up to 1 MHz (operated at 300 kHz), a photon energy of 1.2 eV, and a pulse duration of 262 fs. The output is split into a pump beamline comprising an OPA with one non-collinear amplification stage and a motor-controlled delay line, and a probe beamline featuring pulse compression in a gas-filled multi-pass cell (MPC) and HHG in an Ar gas jet driven by the frequency-doubled beam. XUV-pulse monochromatization and beam steering are comparable to the setup described in Chapter 3: probe monochromatization uses an Al filter to suppress <20 eV photons, and band-pass mirrors transmit the 11th harmonic at 26.4 eV, followed by focusing to a spot size of 40 µm × 200 µm on the sample.

The main difference in the probe monochromatization is the filter geometry for the driving visible light after HHG. Here, the beam is transformed into a hollow annular beam before HHG, which allows filtering after HHG by steering the driving beam into a beam dump using a donut-shaped mirror. Because the generated XUV beam has a significantly smaller divergence angle, higher harmonics transmit through the mirror hole. Pump and probe beams impinge on the sample approximately collinearly at a grazing incidence angle of 80° relative to the surface normal, with an estimated XUV photon flux of 5×10^8 photons/s. The ARPES field of view is ± 1.8 Å^{-1} under standard operating conditions ($M = 2$, extractor voltage 10 kV). The system energy resolution of 270 meV is determined from the Fermi edge of an Au(111) surface and includes analyzer and space-charge contributions as well as the XUV bandwidth, which is dominant in this case.

3 Commissioning of a trMM Beamline

Time-resolved momentum microscopy (trMM) is a powerful tool to characterize non-equilibrium electron dynamics on an ultrafast timescale. However, the MM's ability to map the entire first BZ without additional sample rotation or tilt implies a minimum probe photon energy (Eq. 2.30), which is roughly 20 eV for many materials [12]. Laboratory-scale pulsed photon sources based on frequency conversion in nonlinear optical crystals are typically limited to photon energies below 10 eV [8, 138, 140]. An alternative is HHG, which requires high pulse energies for efficient frequency conversion.

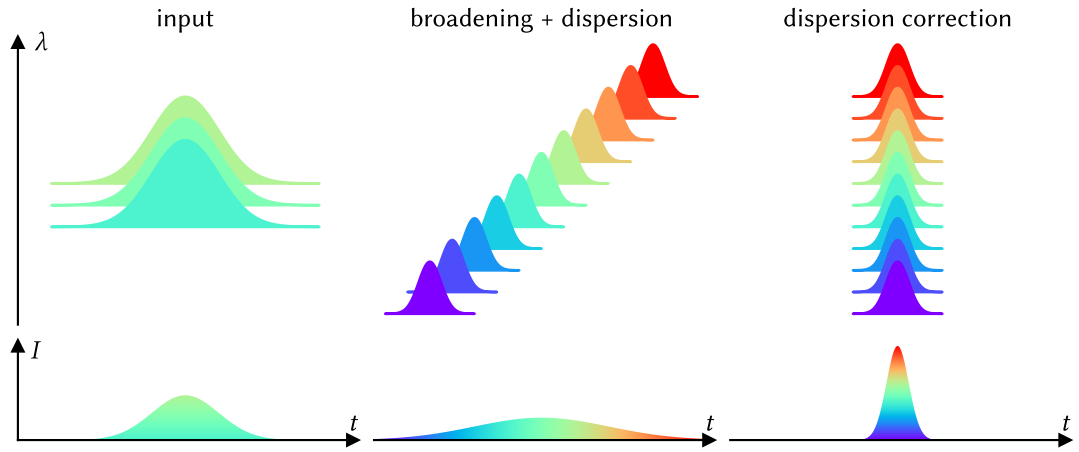


Figure 3.1: Nonlinear compression schematic. The narrowband input pulse is spectrally broadened via SPM and undergoes additional dispersion that stretches the pulse in time (second column). Dispersion correction temporally aligns all frequency components, yielding a broadband output pulse with shorter pulse duration and higher peak intensity (third column).

Early experiments achieved sufficient pulse energies for HHG at repetition rates on the order of 10 kHz [141–144]. However, the number of emitted electrons per pulse is limited by space charge (see Sec. 2.2.5), which motivates higher repetition rates for rapid data acquisition, preferably in the multi-100 kHz to 1 MHz range. Passive enhancement cavities have demonstrated photoemission above 10 MHz repetition rate below the space-charge limit [21, 145, 146]. In this regime, however, providing sufficient pump-photon flux in a trARPES experiment can pose an excessive thermal load on the material and may cause optically induced damage [11]. In addition, the significantly reduced temporal separation between pulses might prevent relaxation to equilibrium in the sample, which is a fundamental assumption for interpreting pump–probe experiments. An alternative route to passive enhancement cavities

is the combination of high-average-power, high-repetition-rate lasers such as Yb lasers [147] with nonlinear post-compression, which offers greater flexibility at multi-100 kHz repetition rates.

The working principle of a nonlinear compression stage is schematically shown in Figure 3.1 and comprises two stages [46, 47]. First, a nonlinear optical effect such as SPM spectrally broadens the narrowband input pulse. Propagation in the nonlinear medium also induces GVD, which stretches the pulse in time. Typical nonlinear media are solids [148] or gases [149]. Second, a dispersion-correcting geometry aligns spectral components in time, yielding shorter broadband pulses. Dispersion correction can be realized in different forms employing gratings, prisms, or specifically coated mirrors, for example [54].

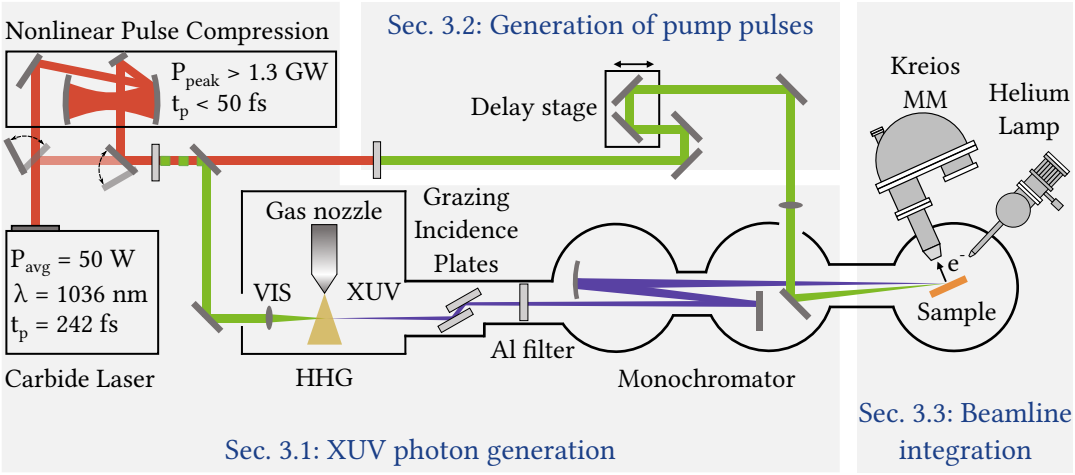


Figure 3.2: Schematic layout of the beamline, which is explained in detail in the following chapters. A commercial laser with optional post-compression is used to generate XUV photons, which emit electrons from a studied sample that are collected by a MM. A second beam path is frequency-doubled and utilized as pump for time-resolved experiments. Published in Ref. [135].

In this chapter, we report the design and implementation of a state-of-the-art trMM setup with the following key requirements for the photon source, enabling maximum versatility:

- Photon energy exceeding 20 eV to map the band structure across the entire first BZ for many materials.
- High repetition rate in the multi-100 kHz regime for fast acquisition below the space charge limit.
- Temporal resolution of a few tens of fs, ideally with minimal accompanying degradation in energy resolution.

With these system requirements in mind, we built a trMM setup delivering 21.6 eV photons at 600 kHz. Coupling the light source to the KREIOS 150 MM, we introduce two modes of operation that prioritize either temporal or energy resolution. The

beamline is shown in Fig. 3.2, and the following sections detail its individual components. Section 3.1 describes coherent XUV-photon generation using an optional temporal post-compression scheme based on a custom-built MPC. In a time-resolved experiment, these pulses serve as the probe beam. Next, a separate layout for frequency conversion of the optical laser pulses is presented (Sec. 3.2) and applied to generate pump photons. Both optical paths are coupled to a commercial photoemission end station, and the overall performance is presented (Sec. 3.3). Finally, integration of an OPA in the pump path required beamline modifications described in Section 3.4. The results presented in this chapter (except for OPA integration) are published in Ref. [135]:

K. J. Schiller, L. Sternemann, M. Stupar, A. Omar, M. Hoffmann, J. E. Nitschke, V. Mischke, D. M. Janas, S. Ponzoni, G. Zamborlini, C. J. Saraceno, and M. Cinchetti, "Time-resolved momentum microscopy with fs-XUV photons at high repetition rates with flexible energy and time resolution", *Scientific Reports* **15**, 3611 (2025)

3.1 Generation of Coherent XUV Photons

The XUV photons generated in the probe line drive the photoemission process. Here, the time–bandwidth product sets a lower limit on the achievable energy and temporal resolution (see Sec. 2.1.1). In addition, reaching this theoretical limit is experimentally challenging, further motivating a compromise between the two resolutions. Therefore, our beamline integrates two modes of operation: one for improved energy resolution and one for enhanced temporal resolution. The latter is achieved by post-compressing the optical pulses before HHG.

The probe line of the trMM setup uses the near-infrared output of a commercial high-power laser system to generate coherent XUV photons. In our setup, we use the Carbide Laser (Light Conversion) with 50 W average power, 1036 nm central wavelength, 242 fs pulse duration, and adjustable repetition rate from 100 kHz to 1000 kHz. As spectral broadening in the MPC scales with pulse energy, the repetition rate is fixed to 600 kHz, corresponding to a pulse energy of 83 µJ.

Optical pulse compression is implemented using a hybrid bulk–air MPC setup, which is displayed in Figure 3.3a. The pulse compression was designed and built by a team from the group of Prof. Clara Saraceno[1]. It consists of two highly reflective concave mirrors (Heriott-type layout) with an effective focal length (EFL) of 150 mm, which reflect the optical beam for a total of 16 round trips. Mode-matching optics before the MPC facilitate a uniform beam caustic between the two mirrors, where an anti-reflection-coated fused silica plate of 6.35 mm thickness is positioned. Upon transmission, the optical pulses undergo self-phase modulation, which causes spectral broadening. Figure 3.3b displays the spectrum of the laser output before and after

[1] Alan Omar, Martin Hoffmann, and Clara Jody Saraceno, Photonics and Ultrafast Laser Science, Ruhr University Bochum, Germany

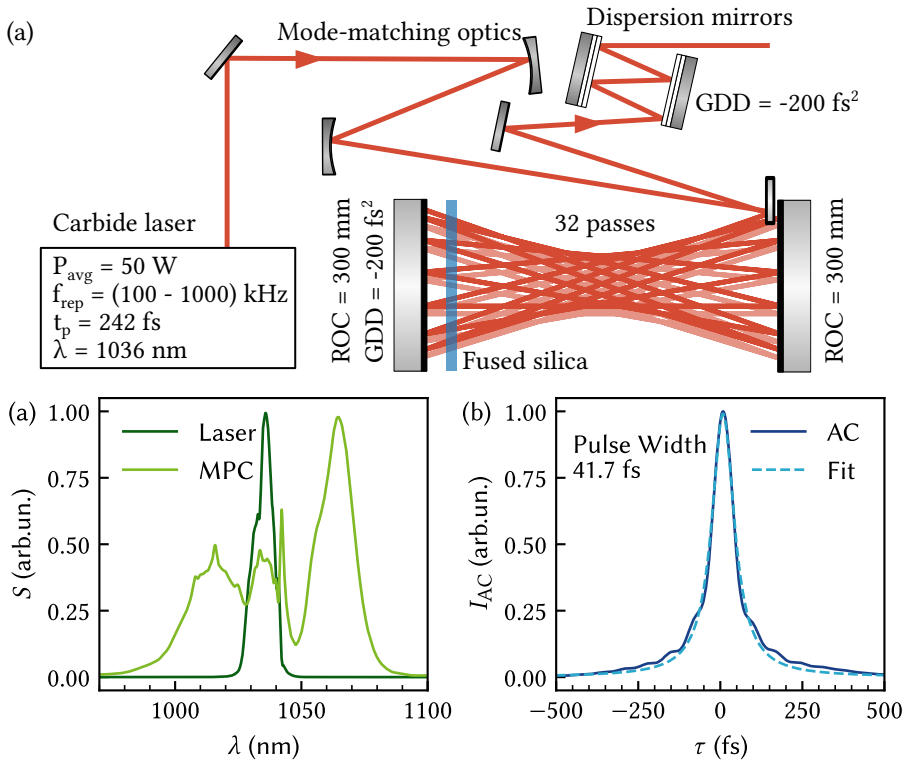


Figure 3.3: Experimental nonlinear pulse compression. (a) Optical layout of the MPC and subsequent dispersion correction. (b) Output spectrum of the laser and MPC, quantifying the bandwidth broadening inside the fused silica. (c) Intensity autocorrelation after dispersion compensation with Lorentzian fit. Published in Ref. [135].

the MPC. Their widths are determined at −20 dB, where the dB scale is calculated via $\mathrm{dB} = 10 * \log_{10}(S)$ from the spectral intensity S. After the MPC, the spectrum is broadened from an initial 22.2 nm to 68.5 nm. The advantage of such Heriott-type MPCs is the gradual SPM accumulation per round trip with minimal spatial beam quality degradation and high transmission. Furthermore, the design and choice of nonlinear medium are highly customizable to accommodate a wide range of pulse energies [150–152].

In addition to spectral broadening, transmission through the fused silica plate accumulates positive chirp. This is partially compensated by a coating of one MPC mirror adding $-200\,\mathrm{fs}^2$ GDD, but transform-limited pulses require additional compensation. We use a mirror pair with negative GDD coating of $-200\,\mathrm{fs}^2$, which allows chirp adjustment by the number of reflections on the mirrors. Optimal compensation is achieved with 12 reflections on the mirror pair, equivalent to $-2400\,\mathrm{fs}^2$, giving a total GDD of $-5600\,\mathrm{fs}^2$ when including the MPC mirror. We measured the pulse duration by second-harmonic intensity autocorrelation, which is displayed in Figure 3.3c. Assuming a Lorentzian pulse shape, fitting yields 41.7 fs FWHM pulse width. Notably, this value should be regarded as a coarse classification, because additional effects such as chirp details, pulse asymmetry, or spatio-temporal couplings are not resolved and can also lead to the formation of ambiguous pedestals, for example [49].

HHG requires strong-field intensities on the order of $1 \times 10^{13}\,\mathrm{W/cm^2}$ in the generation medium [153], corresponding to a few-hundred µJ- to mJ-class ultrashort pulses in typical focusing geometries. Next to high-average-power laser output, this requirement necessitates a well-defined mode for tight focusing (compare Eq. (2.6)). We measured the M^2 parameter before and after the MPC to assess possible mode degradation. Figure 3.4 displays the beam waist along two perpendicular axes u and v along a focus. Both axes are fitted with relation (2.5) and yield (1.11×1.21) for the laser output and (1.17×1.23) after the MPC. While this minimal increase demonstrates good mode preservation during pulse compression, the M^2 parameter alone does not unambiguously characterize the mode. The final test is the efficiency in HHG.

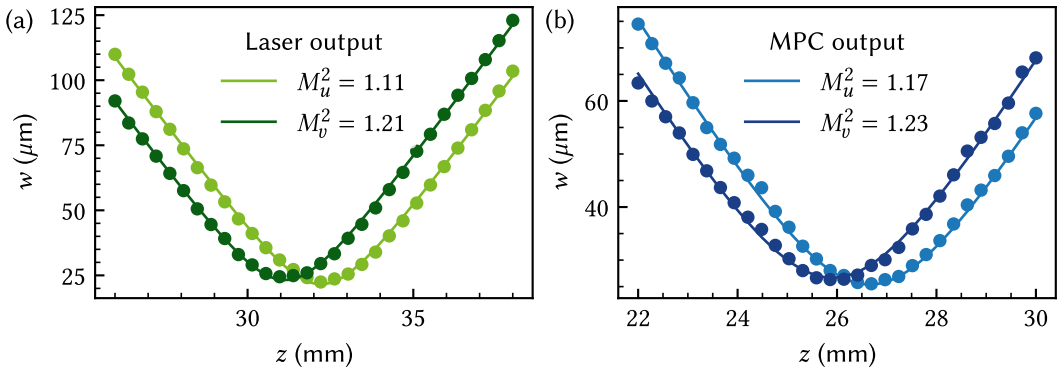


Figure 3.4: M^2 measurement for (a) Carbide laser and (b) MPC output. The acquired beam waist w is fitted according to Eq. 2.5 (solid line) along two perpendicular axes u and v. Published in Ref. [135].

The achieved peak power after compression can be estimated from the pulse duration and the pulse energy. We determine the transmission of MPC and dispersion correction to 86 %, which gives a pulse energy of 71.7 µJ. The peak power is calculated by

$$P_{\mathrm{peak}} = \frac{E_{\mathrm{pulse}}}{\tau_{\mathrm{FWHM}}} \cdot A_{\mathrm{shape}}$$

with a form factor of the pulse shape A_{shape}. A Gaussian pulse with factor $\sqrt{4 \ln 2/\pi}$ gives 1.61 GW peak power, and a Lorentzian pulse with factor $2/\pi$ gives 1.09 GW. The performance of the pulse compression was also simulated by the group of Clara Saraceno, who solved the nonlinear Schrödinger equation in three dimensions (x, y, t) and included linear and nonlinear optical effects in the model (compare Ref. [135]). Here, a peak power of >1.3 GW was calculated, which lies between the Gaussian and Lorentzian approximations [135].

After the optional compression stage, the second harmonic at 518 nm (or 2.4 eV) is generated in a 0.5 mm thick BBO crystal. For uncompressed pulses, the conversion efficiency is 59.0 %, yielding 42.3 µJ pulse energy, while compressed pulses have 27.9 % efficiency, giving 20 µJ pulse energy. A dichroic mirror filters the second harmonic for HHG, while the non-converted 1036 nm pulses are recycled as pump pulses (see

next section). As time-resolved measurements require several days of continuous acquisition, we installed active beam stabilization (Aligna, TEM Messtechnik) before the split into pump and probe arms. The stabilization stage includes two detectors for pointing and angular instabilities, which feed back to two motorized mirrors. Servo motors adjust for long-term drift, and piezo motors react to short-term fluctuations with a refresh rate of several kHz. The resulting beam drift is drastically reduced and yields only 30 % reduction of the initial count rate after 4 h.

For HHG, the *p*-polarized 518 nm pulses are tightly focused into a noble-gas jet with a 200 mm lens. The gas jet is created by a nozzle with 200 µm diameter and adjustable backing pressure up to 13.5 bar. For the experiments in this thesis, we used a backing pressure of about 1 bar and Argon gas, which is then captured by a second exhaust nozzle at a distance of about 0.5 cm. Argon has a moderate ionization potential I_p of 15.76 eV and a large single-atom HHG yield in the 20 eV to 50 eV range, as lower I_p facilitates a higher yield at a given intensity [154]. This results in a good compromise between efficiency and energy cutoff. Practically, Argon is relatively cheap, chemically inert, and readily available at high purity. To avoid absorption of generated XUV light, the gas jet and subsequent light filtering are placed inside vacuum chambers. For the fixed experimental geometry, phase matching is tuned via the gas backing pressure and the optical focus position with respect to the gas jet (see Sec. 2.1.3). Therefore, the focus lens outside the vacuum is positioned with a micrometer stage, and the gas nozzle is motorized along all three axes.

To monochromatize the generated XUV light, the beam is first filtered from the driving 2.4 eV photons by grazing-incidence plates. The anti-reflection coating of these mirrors requires *p* polarization of the 2.4 eV photons, fixing the otherwise polarization-independent XUV generation to *p* polarization. Next, the beam transmits through a 0.2 µm thin Aluminum film, which blocks both residual Argon gas and low-energy harmonics. Al is chosen for its transparency window between 20 eV and 73 eV, which is limited on the low-energy side by the bulk plasmon (plasma) frequency of Al at about 15 eV [155], and on the high-energy side by the onset of core-level photoabsorption at the $\mathrm{Al}_{2\mathrm{p}}$ binding energy around 74 eV [72]. Finally, a single harmonic is filtered via reflection on two band-pass-coated multilayer mirrors. Within this thesis, two pairs of band-pass mirrors for the 9th and 11th harmonic have been used with reflected energies at 21.6 eV and 26.4 eV, respectively. The second band-pass mirror has a spherical shape with a radius of curvature (ROC) of 2 m, focusing the XUV photons onto the studied sample at an incidence angle of 22°.

During operation, the pressure is about 1×10^{-2} mbar inside the HHG chamber and 1×10^{-10} mbar inside the analysis chamber. This reduction happens stepwise across the connected vacuum chambers following harmonic generation and is referred to as differential pumping. The separation of the driving 2.4 eV photons and XUV occurs in a chamber between the HHG chamber and the Al filter, which is connected to the former only via a small tube and features additional pumping, reducing the pressure to about 1×10^{-5} mbar. After the Al filter, the pressure in the monochromator is better than 1×10^{-9} mbar.

For photoemission experiments, driving HHG with the second harmonic has two main advantages compared to the fundamental wavelength. First, neighboring harmonics have twice the energetic separation, namely 4.8 eV instead of 2.4 eV. This relaxes the coating design of the monochromator mirrors and improves the filtering efficiency of neighboring harmonics. Especially for trARPES signals, which can be two orders of magnitude lower [20, 143, 156] than the equilibrium spectrum, reduced noise from duplicated spectra of neighboring harmonics lowers the required integration time for a given signal-to-noise ratio (SNR). Second, comparable XUV photon energies require a lower harmonic order. For example, 21.6 eV is the 9th harmonic of 2.4 eV pulses, whereas 22.8 eV is the 19th harmonic of 1.2 eV. This increases HHG efficiency, as a shorter driving wavelength requires lower ponderomotive energy for a desired harmonic, reducing the required intensity and relaxing phase-matching and ionization-induced dephasing constraints [63, 153] (see Sec. 2.1.3).

3.2 Frequency Conversion of Optical Pump Pulses

TrMM experiments require a pump pulse for excitation. Ideally, this pump pulse is tunable in photon energy and polarization and matches the probe pulse duration for the desired temporal resolution. Here, we utilize the non-converted IR pulse from the probe-beam frequency-doubling stage in a 0.5 mm thick BBO crystal as the pump. This layout allows both matching of the pump duration to the probe in the case of prior pulse compression and high average power for further frequency conversion. With a maximum conversion efficiency of 59 % for the probe frequency doubling, the minimum pump average power is 17.6 W (pulse energy of 29.3 µJ).

As a first step, the pump polarization is set to p with a $\lambda/2$ waveplate and thin-film plate polarizer. Rotation of the waveplate away from the optimal position increases the filtered fraction at the polarizer, thus enabling power adjustment of the beam. The pump then reflects from a motorized, computer-controlled delay stage, which allows precise temporal control of the pump pulse with respect to the probe during an experiment. When required, additional waveplates allow polarization change to s or circular polarization. Finally, the pump beam couples into the monochromator vacuum chamber via an anti-reflection-coated window. Inside the chamber, a broadband-coated, computer-controlled mirror guides the pump onto the sample. This mirror is positioned close to the probe beam (compare Fig. 3.2), making both beams impinge almost collinearly at 68° with respect to the surface normal of the sample. Before incoupling, the pump is focused with a 2 m EFL lens, yielding a spot size in the focal position of about 300 µm FWHM.

Nonlinear frequency conversion in BBO crystals allows generation of the second and third harmonic of the IR pump beam. For excitation above the WS_2 band gap in Section 5.1, the pump beam is frequency doubled in a 0.5 mm thick BBO crystal. As all mirrors in the pump beam path use a broadband coating that includes both 1036 nm and 518 nm, only transmissive optics such as waveplates and the focusing lens need replacement. According to Gaussian optics and Equation (2.6), the frequency-doubled

pump should have half the minimum spot size. However, we did not achieve a reduced spot size experimentally. This could have several causes, such as a smaller beam diameter at the lens d or a degraded beam shape with a higher M^2.

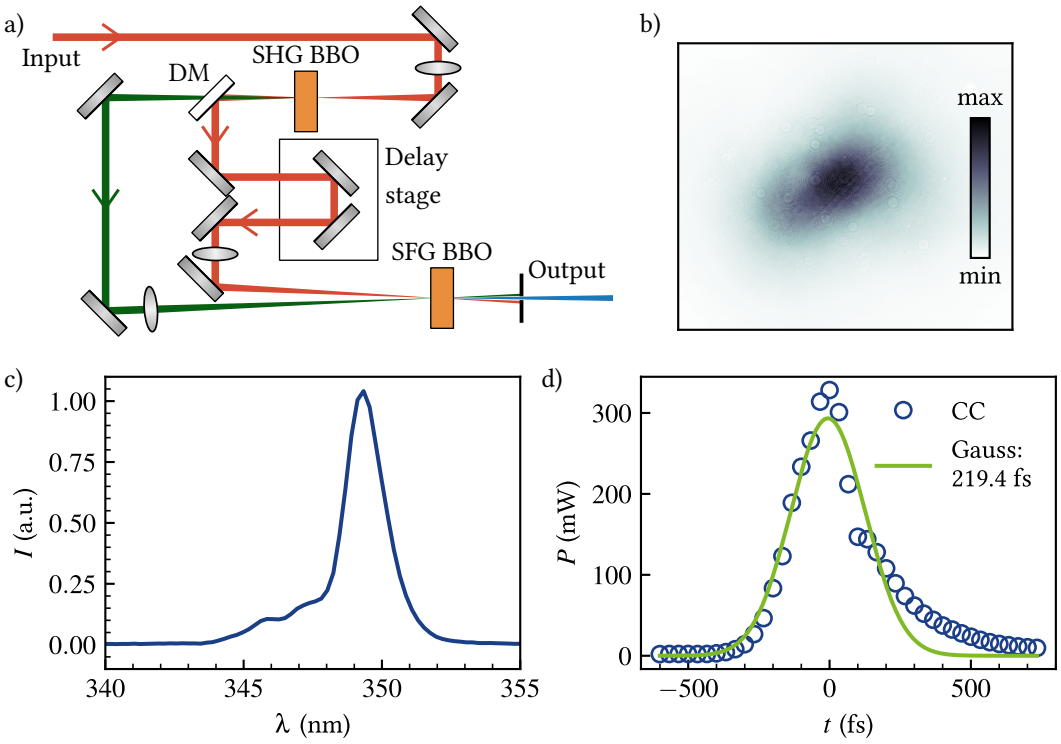


Figure 3.5: A compact setup for third harmonic generation of 1036 nm photons. (a) Schematic layout for the portable setup, where DM stands for dichroic mirror. The generated output is characterized in the following plots: (b) Beam profile, (c) spectrum, and (d) cross correlation signal of IR and SH. The last is fitted with a Gaussian distribution and gives a pulse duration of 219 fs FWHM.

In addition to the laser fundamental and its second harmonic, we built a compact and portable setup to generate the third harmonic at 3.6 eV (or 343 nm). Although not used for the experiments within this thesis, a higher pump photon energy is useful for molecular excitations due to large gaps between the highest occupied and lowest unoccupied orbital [157, 158], for example.

Figure 3.5a displays the schematic layout of the third-harmonic generation setup. The incoming IR beam is focused with a 500 mm lens into a BBO crystal to generate the second harmonic ($\theta = 23.4°$, $d = 0.2$ mm), which is then separated from the non-converted part by a dichroic mirror. Both split paths are focused with $f = 150$ mm lenses and directed into a second BBO crystal for SFG ($\theta = 62.8°$, $d = 1.5$ mm). In addition, two mirrors on the IR beam path are mounted on a manual delay stage with a fine-adjustment micrometer screw to align temporal overlap inside the SFG BBO. The SFG is non-collinear to enable background-free third-harmonic signal by spatial separation of the IR and second-harmonic beams.

Using the post-compressed laser pulses with sub-50 fs pulse duration, we achieved a conversion efficiency of 14.7 % to the third harmonic. The beam profile is displayed in Figure 3.5b and shows a uniform, but slightly elongated mode. The output spectral width measures 10.3 nm at −15 dB and is shown in Figure 3.5c. While our commercial autocorrelator does not support these wavelengths, the pulse duration of the third harmonic can be estimated from the cross-correlation signal of the IR and SH pulses. Figure 3.5d shows the third-harmonic intensity as a function of delay between the two pulses. A Gaussian fit gives a FWHM of about 219.4 fs. This pulse duration is much larger than that of the input pulses, which is likely caused by the BBO crystal thickness inducing dispersion. While the presented setup optimizes conversion efficiency at the cost of pulse duration, switching to different BBO crystals modifies the output characteristics. These simple adaptations are particularly useful when changing the input beam characteristics, either by using the uncompressed pulses of this beamline or by using this portable setup in the METIS beamline presented in Section 2.4.3, for example.

3.3 Beamline Integration

We coupled the beamline described above to a KREIOS 150 MM (Specs GmbH, see Ch. 2.4.2) as depicted in Figure 3.2. In addition, we integrated a gas-discharge lamp (UVS 300, Specs GmbH) with an attached grating monochromator (TMM 304, Specs GmbH). In this section, the discharge lamp and XUV flux control are introduced, and the overall energy and temporal resolution of the beamline are determined.

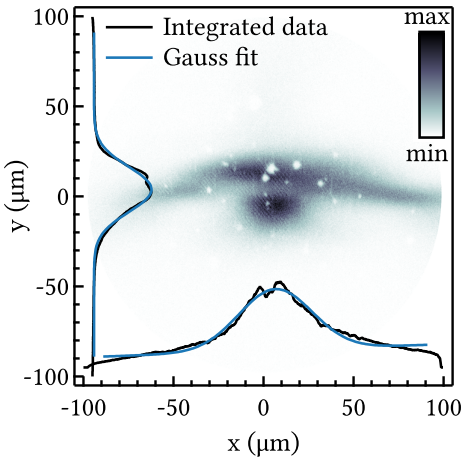


Figure 3.6: PEEM image of XUV probe spot on HOPG. Integrated side profiles are fitted with Gaussian distributions yielding 19.5 µm × 31.7 µm. Published in Ref. [135].

The CW emission of the discharge lamp enables photoemission below the space-charge limit with a high photon flux of $<2 \times 10^{16}$ s^{-1} before monochromatization [11, 159]. Together with the grating monochromator, which transmits only He I or He II emission lines at 21.22 eV and 40.81 eV [1], focusing the light to about 180 µm × 320 µm at the sample surface, and polarizing the light to p, this source enables rapid acquisition of equilibrium photoemission spectra. In particular, when focusing on a small energy window, the high flux allows acquisition rates that can compete with a TOF detector. Even though TOF-MMs allow parallel acquisition over multiple kinetic energies, they require pulsed light sources to define the photoelectron kinetic energy, preventing the use of a gas-discharge lamp.

Space charge becomes an issue with the XUV pulses of the beamline. To ensure undistorted spectra, we first optimize the HHG process by adjusting the Ar backing pressure and gas nozzle position in all three dimensions. We then acquire static spectra at different photon fluxes by artificially reducing the count rate through retracting the nozzle and lowering the backing pressure. As space charge modifies the spectrum particularly around the Fermi level (see Sec. 2.2.1), we compare these spectra and set the HHG parameters to the highest count rate below the space-charge limit. While we do not have the capability to determine the XUV photon flux directly, we can reach the space-charge limit with all tested sample systems (HOPG, Au (111), WS_2, and CrSBr). The space-charge limit also depends on the spot size on the sample. Figure 3.6 displays the XUV beam on HOPG measured in PEEM mode, which is assumed to scale with the optical mode of the beam. The side profiles integrate the data along one dimension and are fitted with a Gaussian distribution plus linear background. We thus determine the spot FWHM to 19.5 µm × 31.7 µm. Freckles in the image are attributed to surface impurities.

As explained in Section 2.2.1, the total energy resolution depends on both the bandwidth of the light source and the analyzer (see Eq. (2.32)). Here, we compare the UVS 300 He Iα line to the pulsed beamline using a 0.2 mm × 0.8 mm entrance slit and 50 eV pass energy. Figures 3.7a and b display the angle-integrated Fermi edge of an Au (111) bulk at 80 K, and Figures 3.7c and d display the spin-split valence band of WS_2 (compare Sec. 4.4). We fit the Au(111) spectra with a convolution of a fixed Fermi edge f multiplied by a linear function l and a Gaussian distribution G accounting for the total energy resolution,

$$I_{\text{fit}}(E) = \int \mathrm{d}E'\, l(E') \cdot f(E') \cdot G(E - E') \tag{3.1}$$

$$= \int \mathrm{d}E'\, (a + bE') \cdot \frac{1}{\exp\left(\frac{E'-E_{\text{F}}}{\mathrm{k_B}T}\right) + 1} \cdot \frac{1}{\sqrt{2\pi}\sigma} \exp\left(-\frac{(E-E')^2}{2\sigma^2}\right). \tag{3.2}$$

The additional linear function approximates a non-constant density of states close to the Fermi energy. For the He Iα line in Figure 3.7a, we extract a Gaussian FWHM of (49 ± 7) meV, which we attribute mainly to the analyzer settings. In contrast, the energy resolution of the compressed XUV pulses in Figure 3.7b fits to an instrument response function (IRF) of (233 ± 20) meV. Here, the low energy resolution is attributed to the large bandwidth of the XUV pulses. Unfortunately, we do not have a comparable Fermi-edge measurement for the uncompressed XUV pulses. Therefore, we compare the uncompressed pulses to He Iα measurements on the energy distribution curve (EDC) of bulk WS_2 at the $\overline{\text{K}}$ point within a radius of 0.07 Å^{-1} in Figures 3.7c and d. Here, we fit the spectra with two Gaussian distributions and a linear background. For the He Iα in Figure 3.7c, we fit a bandwidth of (108 ± 5) meV for the upper band and (114 ± 5) meV for the lower band, respectively. In comparison, we fit (107 ± 2) meV and (113 ± 4) meV for the uncompressed pulses in Figure 3.7d. As the bandwidth is higher than the instrument resolution from Figure 3.7a, it has to be the intrinsic linewidth of bulk WS_2. Also, the uncompressed pulses must have a

bandwidth smaller than 107 meV, demonstrating a large difference to the compressed pulses as expected.

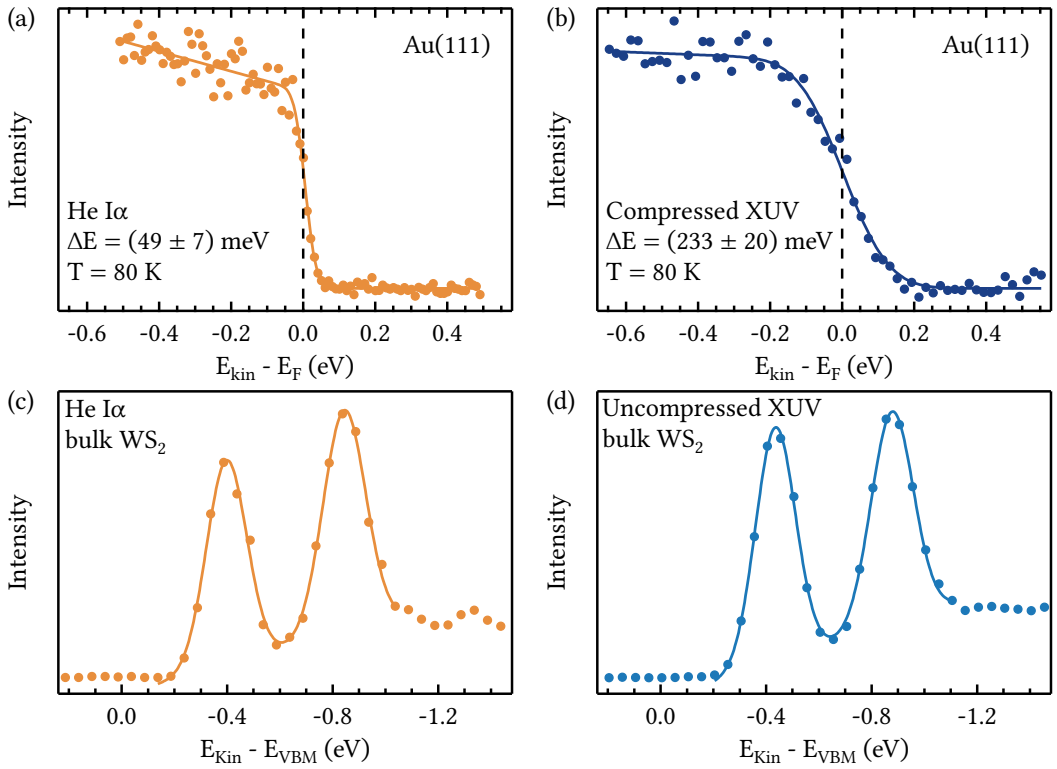


Figure 3.7: Comparison of total energy resolution for He Iα, compressed XUV, and uncompressed XUV photons. (a, b) Angle-integrated Fermi edge of Au(111) for He Iα and compressed pulses, respectively. Fits according to Eq. (3.2) show significant resolution broadening for the compressed light pulses, as expected. (c, d) Angle-integrated EDC at the bulk WS_2 $\overline{\text{K}}$-point acquired with He Iα and uncompressed pulses, respectively. Within the experimental settings, Gaussian fits with linear background yielded the same band widths. Published in Ref [135].

After determining the energy resolution, we measured the temporal resolution of the beamline. We use a p-polarized pump at 2.4 eV for both compressed and uncompressed pulses, and we track the non-equilibrium dynamics on HOPG at room temperature. Figures 3.8a and b display the transient electron population at 265 meV above the Fermi level. We fit the data points with a convolution of a Gaussian distribution with standard deviation σ and a double-exponential decay multiplied with the Heaviside function Θ,

$$I_{\text{fit}}^{\text{double}} = I_0 + I_{\text{fit}}(t, A, \tau_1, \sigma, t_0) + I_{\text{fit}}(t, B, \tau_2, \sigma, t_0) \tag{3.3}$$

with

$$I_{\text{fit}}(t, A, \tau, \sigma, t_0) = A \int_{-\infty}^{\infty} \mathrm{d}t' \, \frac{1}{\sqrt{2\pi}\sigma} \exp\left(-\frac{(t-t')^2}{2\sigma^2}\right) \exp\left(-\frac{t'-t_0}{\tau}\right) \Theta(t'-t_0) \tag{3.4}$$

$$= \frac{A}{2} \exp\left(\frac{\sigma^2}{2\tau^2} - \frac{t-t_0}{\tau}\right) \operatorname{erfc}\left(\frac{t_0 + \sigma^2/\tau - t}{\sqrt{2}\sigma}\right). \tag{3.5}$$

Here, erfc denotes the complementary Gaussian error function and t_0 denotes a rigid shift in time. The FWHM of the Gaussian distribution resembles the cross correlation of pump and probe, assuming instantaneous response by the material. We determine a FWHM of (181 ± 5) fs and (66 ± 6) fs for the uncompressed and compressed pulses, respectively. While the post-compression reduces the pulse duration quite significantly, the extracted temporal resolution might be sufficiently fast to be affected by electron cascading processes from higher energy levels described in Section 4.3. Therefore, we cross-checked the fitted resolution on bulk WS_2 at the $\overline{K}$ point. The transient electron distribution at 1.5 eV above the valence band maximum (VBM) is displayed in Figure 3.8c, and fitting yields a temporal resolution of (48.8 ± 1.7) fs. Details on ultrafast electron excitation and relaxation mechanisms are given in Section 5.1.

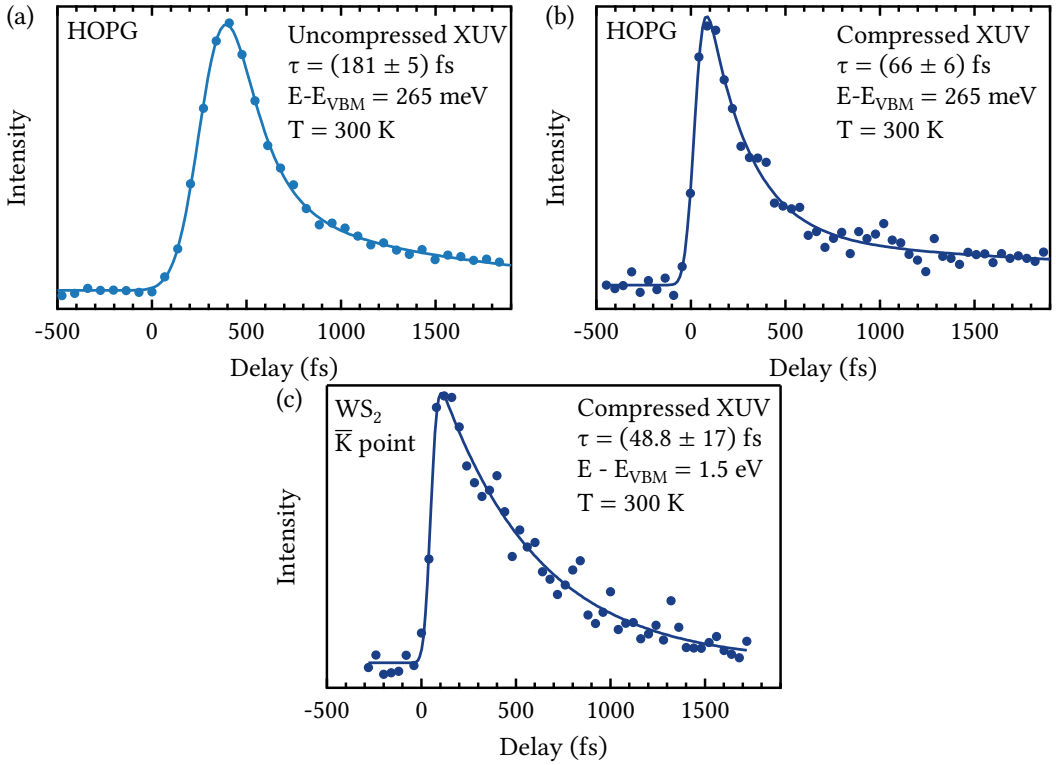


Figure 3.8: Temporal resolution for compressed and uncompressed XUV pulses. (a, b) Transient response of HOPG for both pulses with fits according to Eq. (3.3), yielding enhanced temporal resolution for the compressed pulses, as expected. (c) Transient response of the bulk WS_2 $\overline{K}$-point, with a fit yielding the ultimate temporal resolution in the compressed configuration. Published in Ref. [135].

Any pulsed light source has an intrinsic Fourier limit of 1825 meV fs for temporal and energy resolution (see Sec. 2.1.1). In our setup, we measured a temporal resolution[2] of 48.8 fs and an energy resolution of 233 meV, resulting in a time–bandwidth product

[2]The temporal resolution written here is the pump–probe cross correlation and not the probe pulse alone. The resulting time–bandwidth product is therefore only an approximate overall assessment of the system's performance.

of 11 370 meV fs. Several factors might cause the large time–bandwidth product in the presented system. One possibility is that the XUV monochromator's multilayer mirror has a band-pass coating that is too broad, or that slight misalignment causes geometric dispersion. Unlike grating monochromators, where the transmitted bandwidth is adjustable by changing the slit size or grating density, multilayer mirrors have fixed properties and can only be swapped for mirrors with different coatings. Another contributing factor could be beam misalignment or spatial irregularities in the beam profile, which can stretch the pulse duration. It is also likely that the pump pulses are longer than the XUV probe pulses, which would reduce the overall time resolution. Adding an extra compression stage to the pump could help bring its duration closer to that of the XUV pulses.

While comparable trARPES beamlines are tuned either for optimized temporal or energy resolution without switchability, systems employing HHG and a grating monochromator have come closer to the Fourier limit. For example, Puppin *et al.* achieved 40 fs pulses at 110 meV resolution, corresponding to a product of 4400 meV fs, by carefully tuning an OPCPA system [20]. Also, Cucini *et al.* tuned their system to 22 meV and 105 fs, yielding a low 2310 meV fs time–bandwidth product [160].

3.4 Beamline Modification for OPA Integration

The pump pulses described in Section 3.2 offer three distinct frequencies for trMM experiments. However, narrow excitation resonances require finer tuning of the pump frequency, such as the WS_2 exciton resonances (see Sec. 4.4), for example. The pump-line design allows integration of an OPA, but the short pulse duration of the compressed pulses below 50 fs poses a challenge in terms of conversion efficiency and damage threshold. We integrated an ORPHEUS-ONE-HP (Light Conversion), which does not support compressed pulses with sub- 50 fs duration at the comparatively low average power of 17.6 W that our setup can provide at 600 kHz (equivalent to 29.3 µJ pulse energy). Therefore, we redesigned the beamline to split the laser output into pump and probe paths before the post-compression, and we reduced the repetition rate to 300 kHz. In the following, I will first describe the layout of the OPA and then detail the setup modifications and resulting performance.

The schematic layout of the ORPHEUS-ONE-HP is displayed in Figure 3.9a. The input pulse at 1036 nm is split into two arms. One arm with low average power (on the order of 100 mW) generates white light, and one arm with high average power generates the second harmonic to pump the parametric amplification. In a first collinear stage, the signal output is generated that covers 660 nm to 860 nm (or 1.44 eV to 1.88 eV) and is named SIG1 in the following. The idler output of the first stage is then amplified in a non-collinear stage and becomes the signal of this second stage, covering 1350 nm to 2100 nm (or 0.59 eV to 0.91 eV), named SIG2. The third output is the second-stage idler covering 2100 nm to 4300 nm (or 0.29 eV to 0.59 eV) with the name IDL. None of the outputs include post-compression and yield

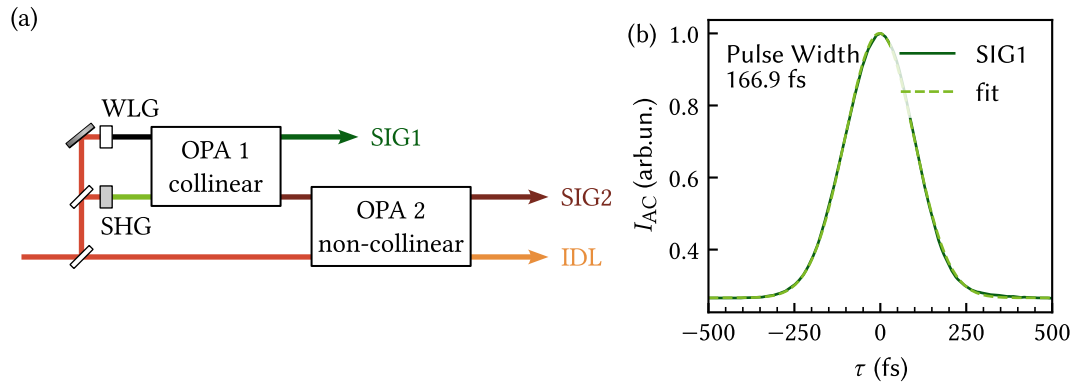


Figure 3.9: ORPHEUS-ONE-HP OPA. (a) Schematic OPA layout comprising two amplification stages. (b) Intensity autocorrelation of SIG1 output with Gaussian fit.

comparable pulse durations, such as the SIG1 output in Figure 3.9b, which is fitted with a Gaussian to 166.9 fs pulse duration.

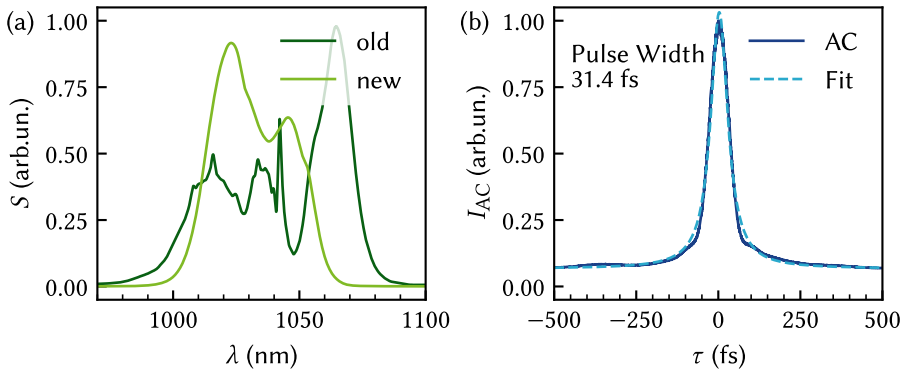


Figure 3.10: Output characterization of the adapted MPC. (a) Spectrum comparison of old and new MPC design. (b) Intensity autocorrelation after dispersion compensation with Lorentzian fit.

Splitting the pump and probe paths directly at the laser output poses a challenge for the post-compression scheme in terms of optical path length. The MPC mirrors are separated by 54 cm, resulting in 14 m optical path length for the MPC alone, which must be compensated in the pump line. Therefore, the research team from the group of Prof. Clara Saraceno redesigned the post-compression to maintain sub-50 fs pulses while reducing the optical path as much as possible. The new design includes two different MPC mirrors with a ROC of 5 m and 2 m, respectively. The optical pulses take 23 round trips inside the MPC with a mirror distance of only 13 cm, which reduces the optical path to 6 m. With a 1 mm thick fused silica plate close to the mirror with 5 m ROC, the spectrum broadens to 74 nm width at −20 dB, as displayed in Figure 3.10a. The pulses then reflect 18 times off mirrors with −200 fs^2 GDD coating for a total of −3600 fs^2. Figure 3.10b shows the SH autocorrelation signal, giving a pulse duration of 31 fs with a Lorentzian fit function. Compared to the previous MPC design, the spectral width is smaller while the pulse duration is

shorter. This seemingly contradictory result is likely affected by the simple pulse deconvolution of the intensity autocorrelation signal, which exhibits non-uniform contributions in the pedestal region for both cases. Thus, the simple Lorentzian fit does not capture the entire pulse shape correctly and should be treated as a rough estimate. The total compressor transmission is 92 %. As before, the compressed pulses are frequency doubled in a 0.5 mm thick BBO crystal and focused with a 200 mm lens into an Argon gas jet for HHG.

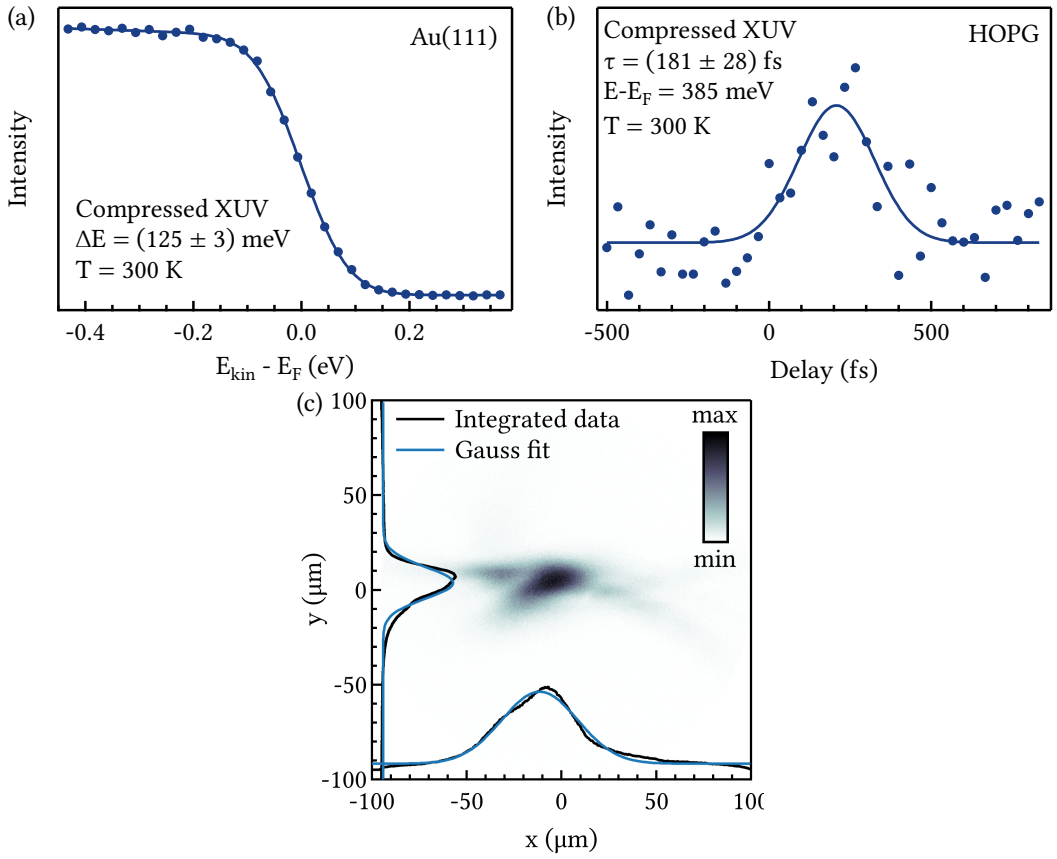


Figure 3.11: Beamline performance after OPA integration. (a) Fermi edge of Au(111) fitted with Eq. (3.2). (b) Transient response on HOPG with SIG1 as pump, fitted with a Gaussian function. (c) XUV spot size in PEEM with Gaussian fits for integrated distributions.

Figure 3.11 displays the performance of the modified beamline. The energy resolution of the compressed XUV pulses was determined from the Fermi edge of Au (111) at room temperature. A fit according to Equation 3.2 is displayed in Figure 3.11a and yields an energy resolution of (125 ± 3) meV. The spot size on the sample is (31.1 ± 0.2) μm × (13.0 ± 0.1) μm, determined by Gaussian fits of the intensity distribution in PEEM on Au (111) along the x and y axes, respectively (see Fig. 3.11c). With the SIG1 output of the OPA, the cross correlation was measured on room-temperature HOPG at 385 meV above Fermi, as shown in Figure 3.11b. At this energy, the signal is Gaussian and is thus fitted to an FWHM of (181 ± 28) fs. The improvement in energy resolution relative to the previous 233 meV results from less spectral broadening in the MPC and thus comes at the cost of longer pulse durations.

However, the current setup does not include post-compression of the OPA output pulses and is therefore the limiting factor for temporal resolution.

4 Materials and Preparation

This thesis focuses on selected transient phenomena in two-dimensional (2D) materials, whose thickness is reduced to the atomic scale so that reduced dimensionality and quantum confinement strongly modify their electronic and optical properties [161]. More specifically, the 2D materials discussed in this chapter are restricted to van der Waals (vdW) systems, which exhibit a layered crystal structure in bulk form. Within each layer, the atoms are bound covalently or ionically, whereas neighboring layers interact only via weak vdW forces. This structure allows removal of individual layers down to the few-layer limit using tools as simple as adhesive-tape exfoliation, famously employed by Novoselov *et al.* in 2004 to isolate monolayer graphene from bulk graphite [22].

Since its first isolation from bulk graphite, monolayer graphene has been studied intensively. It features exceptionally high carrier mobility, and its low-energy quasiparticles behave as massless Dirac fermions with linear dispersion near the K and K′ points [162]. While bulk HOPG is presented in more detail in Section 4.3, its main role in this thesis is to serve as a metallic reference sample for determining the temporal overlap and cross-correlation of the pump and probe pulses. Here, we exploit its strong photoemission signal and well-characterized hot-electron dynamics [163, 164]. An important family of 2D vdW materials are transition metal dichalcogenides (TMDs), many of which exhibit semiconducting behavior and show pronounced optical and electronic differences between monolayer and bulk crystals. They are introduced in detail in Section 4.4 and studied in bulk and monolayer form in Section 5.1. Both samples were prepared in substantially different ways, which are described in detail in Section 4.2: bulk crystals were cleaved in situ to obtain fresh surfaces, while monolayer WS_2 was grown in situ on an Au(111) surface. Section 4.1 briefly summarizes the main features of the Au(111) surface state, as its Fermi edge is also used in Section 3.3 to characterize the energy resolution of the experimental beamline.

Owing to the weak vdW forces between layers, functional structures can be assembled in a Lego-like manner, because the weak interlayer interaction largely relaxes the conventional lattice-matching constraints that apply in epitaxial growth [23, 24]. This opportunity for material engineering is exploited in fields ranging from fundamental research to applications [161], including electronics and optoelectronics [165]. One focus is band-structure engineering in TMD bi- and multilayers through material choice, stacking order, and twist angle [12, 36, 166]. Another is the incorporation of magnetic materials into vdW structures since the discovery of long-range magnetism in vdW monolayer crystals (see Sec. 4.5 for details). Section 4.5 introduces the

semiconductor and antiferromagnet CrSBr, which combines a comparatively high magnetic ordering temperature among vdW magnets with highly anisotropic (quasi-1D) electron transport and excitonic resonances that couple strongly to the magnetic order, for example [39, 167].

4.1 Gold (111) Surface State

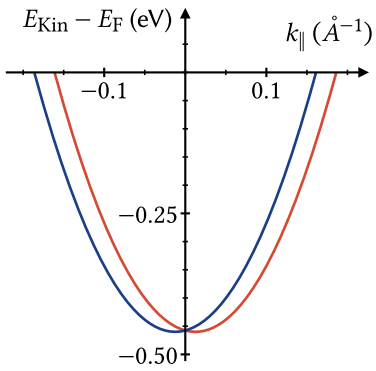


Figure 4.1: Schematic of the surface state in Au(111) with plot parameters taken from Ref. [86].

Gold crystallizes in an *fcc* structure, and its (111) surface is used in this thesis to determine the angular and energy resolution of the KREIOS detector (Sec. 2.4.2) and the trMM beamline (Sec. 3.3). A clean Au(111) surface hosts a Shockley-type surface state near the Fermi level. It resides in the projected bulk band gap (L-gap) around the $\overline{\Gamma}$ point, where no bulk states are available, and exhibits a nearly free-electron-like dispersion [168]. The broken inversion symmetry at the surface, together with the strong spin–orbit coupling in gold, gives rise to a Rashba-type spin splitting described by

$$\mathscr{H}_{\mathrm{Rashba}} = \frac{\hbar^2 k_{\parallel}^2}{2\mathrm{m}^*} + \alpha_R \left(\mathbf{e}_z \times \mathbf{k}_{\parallel}\right) \cdot \boldsymbol{\sigma},$$

where m^* is the effective mass of the surface state, $\mathbf{k}_{\parallel}$ is the in-plane momentum, α_R is the Rashba parameter, and $\boldsymbol{\sigma}$ denotes the Pauli matrices [169, ch. 12]. This yields two spin-split parabolic branches with opposite spin helicities and a band minimum at $\overline{\Gamma}$ about 450 meV to 500 meV below the Fermi level (see Fig. 4.1) [86, 168, 170].

The Au(111) surface-state Fermi crossing provides a sharp, well-defined feature in energy and momentum, governed by the intrinsic electronic structure of the sample rather than by photon-energy- or detector-specific artifacts. It therefore serves as an excellent reference for calibrating the instrumental energy and momentum resolution [86].

4.2 Sample Preparation

Sample structures based on two-dimensional vdW crystals can be prepared either in a top-down or a bottom-up manner. In a top-down approach, bulk crystals are exfoliated to expose fresh surfaces and to obtain thin flakes. This method is discussed first and was used here to prepare clean surfaces on bulk WS_2 and CrSBr crystals, as well as few-layer CrSBr and a WS_2/WSe_2 heterobilayer. In contrast, a bottom-up approach directly grows the desired sample structure on a substrate, enabling in situ,

reproducible, large-area sample fabrication with high surface quality. The second part of this section describes the in situ growth of monolayer WS_2 on Au(111).

The layered structure of vdW crystals allows mechanical exfoliation with adhesive tape, thereby simplifying the preparation of fresh surfaces for photoemission experiments on bulk crystals. Commercial WS_2 and CrSBr crystals presented in Sections 5.1 and 5.3, respectively, were attached to metallic sample plates using conductive, UHV-compatible glue. Adhesive tape was then applied ex situ, and exfoliation was performed in UHV in the preparation chamber or in a load lock before measurement, so that no additional sputter–anneal cleaning was required. However, this preparation routine can still lead to charging in poorly conducting semiconductor substrates during photoemission experiments, especially at cryogenic temperatures [171, 172].

Few-layer samples could, in principle, be obtained by repeated exfoliation directly on a glued bulk crystal, but flakes with the desired thickness are typically micrometer-sized and randomly distributed [22, 173]. This random distribution renders deterministic fabrication of heterostructures impractical. Instead, the bulk crystal is first exfoliated onto adhesive tape, and the remaining thin layers are stamped repeatedly onto an intermediate substrate before the resulting flake distribution is examined by optical microscopy. A selected flake is then transferred onto the target substrate using a viscoelastic stamp that behaves like an elastic solid when peeled off quickly and like a viscous material when peeled off slowly [174]. This approach allows fabrication of designed structures in a LEGO-like manner with relatively low surface contamination, suitable for ARPES experiments after mild annealing. For surfaces sensitive to ambient conditions, the transfer can also be performed under inert-gas conditions [175]. The WS_2/WSe_2 heterobilayer investigated in Section 5.2 was prepared using this method.

Exfoliation typically yields only a small number of monolayer flakes with limited lateral size, but exfoliation onto a gold surface can mitigate both issues. Because the Au surface can bind more strongly to the outermost vdW layer than adjacent layers bind to each other, monolayer flakes with lateral sizes of several hundred µm can be obtained [173]. However, the gold surface must be flat, with a root-mean-square roughness <1 nm, and minimally contaminated [177]. Such surfaces can be prepared in UHV [178], but so-called template-stripping allows suitable Au substrates to be prepared rapidly and in bulk [179]. The process, sketched in Figure 4.2, starts with gold evaporation onto a flat and clean surface such as a Si wafer with native SiO_2. Immediately before exfoliation, the wafer is separated from the glued sandwich structure, and the fresh Au surface inherits the flatness of the substrate material [179]. The vdW crystal is then pressed against the gold, transferred into vacuum, and exfoliated in situ. In addition, the gold-evaporated sandwich structures can be prepared in bulk and protect the Au surface from atmospheric exposure [180]. We adapted this preparation technique for the trARPES experiment on CrSBr samples in Section 5.3, using flakes with thicknesses of several tens of nm, which has been reported to substantially reduce charging in ARPES experiments at cryogenic temperatures [139, 176].

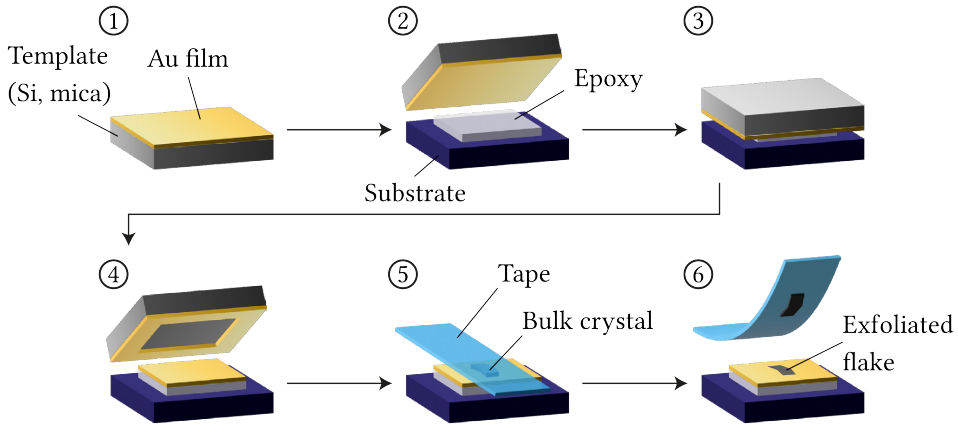


Figure 4.2: Schematic Au-assisted exfoliation on template-stripped gold. (1) Gold is evaporated on a smooth substrate. (2) The gold film is glued onto a sample plate to form (3) a sandwich structure that protects the Au surface from exposure to air. (4) Immediately before use, the substrate is peeled off to expose a fresh Au surface, onto which (5) a bulk vdW crystal is pressed. (6) In vacuum, the crystal is exfoliated, leaving a thin flake with a fresh surface suitable for low-temperature ARPES. Reproduced from Ref. [176] under the license CC BY-NC-ND 4.0, font style modified.

Apart from exfoliating bulk crystals, large-area monolayers can also be grown in UHV. A WS_2 monolayer film on Au(111) was grown in the XPS setup described in Section 2.4.1 by Dr. Michele Capra[1], who optimized the growth procedure and summarized the process in Ref. [181]. The growth consists of four steps: (i) the Au(111) substrate is cleaned by cycles of Ar^+ sputtering and annealing at approximately 670 °C for 30 min. (ii) the substrate is exposed to dimethyl disulfide (DMDS) gas using a nozzle in proximity to the sample surface at a temperature of ~ 650 °C. (iii) while maintaining the DMDS atmosphere (3.5×10^{-7} mbar in the chamber) and sample temperature, tungsten is evaporated from an e-beam evaporator, and (iv) the sample is post-annealed in DMDS atmosphere (2.5×10^{-7} mbar in the chamber) at ~ 670 °C and subsequently in vacuum at ~ 500 °C to remove excess DMDS from the surface.

The XPS spectra were analyzed with the XPST package for Igor Pro [80] and are shown in Figure 4.3. The survey spectrum in Figure 4.3a shows only the expected core-level contributions from Au, W, and S atoms. Core-level positions were checked against the NIST XPS database [182]. The absence of detectable C 1*s* signal in Figure 4.3f indicates a low level of adventitious carbon on both the clean and the WS_2-covered surfaces. All spectra are calibrated to the Fermi level of the gold substrate, obtained from a fit of the Fermi edge in Figure 4.3b using a convolution of a Gaussian function and the fixed Fermi distribution (see Eq. (3.2)). The Gaussian FWHM yields an instrumental energy resolution of (335 ± 135) meV under the conditions of this experiment.

[1]Dr. Michele Capra, Department of Physics, TU Dortmund University, Otto-Hahn Str. 4, Dortmund, Germany

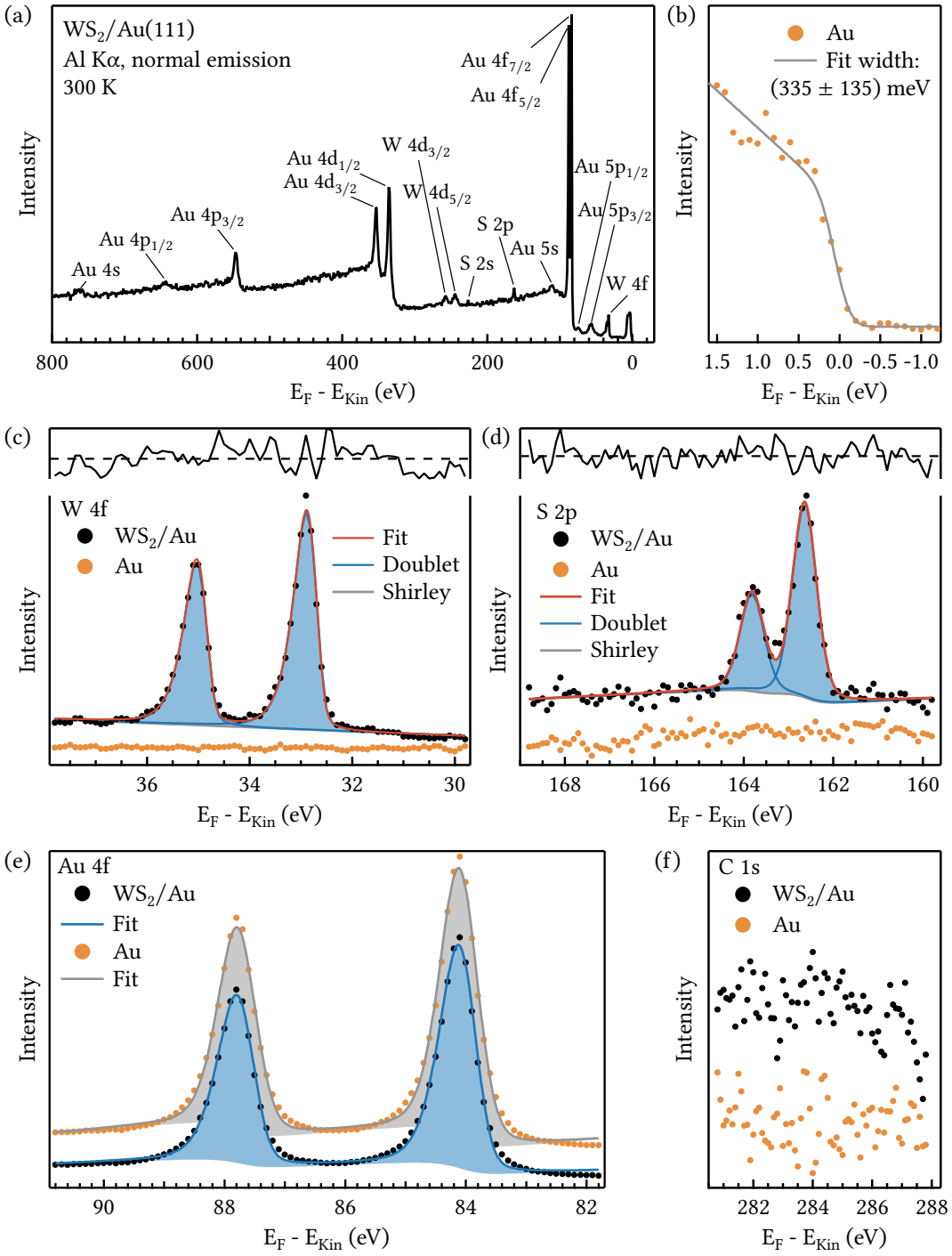


Figure 4.3: XPS characterization of WS_2 growth on Au(111). Black (orange) markers denote XPS data points after WS_2 growth (clean Au). (a) Survey spectrum showing only expected contributions from Au, W, and S core levels. (b) Fermi edge of clean Au(111). (c, d) W $4f$ and S $2p$ core levels with fitted spin–orbit doublet, respectively. The solid black line indicates the fit residual. (e) Au $4f$ level before and after growth, fitted with the same doublet line shape. (f) C $1s$ region, confirming the absence of detectable carbon contamination.

The W $4f$ and S $2p$ core levels in Figures 4.3c and d were fitted with spin–orbit doublet line shapes using a pseudo-Voigt profile as implemented in XPST [80] and a standard Shirley background (clean Au(111) spectra offset along the intensity axis for clarity). The S $2p$ doublet is well described by a symmetric line shape, whereas the W $4f$ peaks require a modest asymmetry parameter of 0.28, visible as a tail on the high-binding-energy side. Such an asymmetry is not expected for purely semiconducting WS_2 and may indicate additional weak components, for example metallic states [183, 184]. In contrast, W atoms in sulfur-deficient WS_{2-x} environments would be expected at lower binding energies relative to stoichiometric WS_2 [185]. Within the SNR ratio of our data, no distinct extra doublets attributable to higher or lower oxidation states are resolved, indicating predominantly stoichiometric WS_2 in the probed area.

Finally, the WS_2 coverage is estimated from the attenuation of the Au $4f$ signal. Figure 4.3e shows the Au $4f$ spectra for the clean substrate and after growth, both fitted with the same pseudo-Voigt + Shirley model. Assuming that the photoelectron signal from uncovered regions and regions covered by a single WS_2 layer adds linearly, the Au $4f$ intensity after growth can be written as

$$I_{WS_2} = I_{Au} \cdot \left[(1 - C) + C \exp\left(-\frac{d}{\lambda \cos\theta}\right)\right],$$

where C is the fractional monolayer coverage ($0 \leq C \leq 1$), d is the layer thickness, λ is the effective attenuation length, and θ is the electron takeoff angle [81]. For normal emission and $r = I_{WS_2}/I_{Au}$, this yields

$$C = \frac{1 - r}{1 - \exp(-d/\lambda)}. \tag{4.1}$$

From the integrated peak areas in Figure 4.3e we obtain $r = 0.805$. Using $d = 0.7\,\text{nm}$ and $\lambda = 2.38\,\text{nm}$, we obtain a coverage of $C = 76.6\,\%$ for the WS_2 monolayer film[2]. This value is comparable to the ~70 % coverage reported by Dendzik *et al.* for a similar growth procedure [185].

4.3 Highly Oriented Pyrolytic Graphite

Graphene is a two-dimensional honeycomb lattice of carbon atoms, with each carbon atom in approximately sp^2 hybridization forming strong in-plane σ bonds [162]. The remaining p_z orbital is oriented perpendicular to the plane and overlaps with neighboring p_z orbitals to form half-filled π bands in neutral graphene. These bands

[2]Here, λ is approximated by the inelastic mean free path from the Tanuma–Powell–Penn (TPP-2M) predictive formula via the NIST Standard Reference Database 71 [186], using an electron kinetic energy of 1400 eV, a WS_2 density of 7.5 g/cm^3, a band-gap energy of 2.0 eV, and 18 valence electrons per formula unit (6 from W and 2×6 from S). d is the monolayer thickness, assumed here as half of the unit-cell lattice parameter.

govern the electronic structure near the Fermi energy [187], which is well described in a tight-binding model by two bands

$$E_{\pi^*}(\mathbf{k}) = -E_{\pi}(\mathbf{k}) = \gamma_0 \sqrt{1 + 4\cos^2\left(\frac{k_y a_0}{2}\right) + 4\cos\left(\frac{k_x\sqrt{3}a_0}{2}\right)\cos\left(\frac{k_y a_0}{2}\right)},$$

with lattice constant a_0 and nearest-neighbor hopping parameter γ_0 [187]. These two bands are displayed in Figure 4.4a and cross at the K and K′ points in the Brillouin zone. Due to the vanishing density of states at the crossing (Dirac) point, graphene exhibits the properties of a zero-band-gap semiconductor (semimetal), because the Fermi energy lies exactly at this point for an undoped crystal [162, 187]. Bulk crystals of vdW-coupled graphene layers are called graphite, and highly oriented pyrolytic graphite (HOPG) is a synthetic polycrystal of graphite crystallites whose c axes (stacking direction) are aligned within <1° [188].

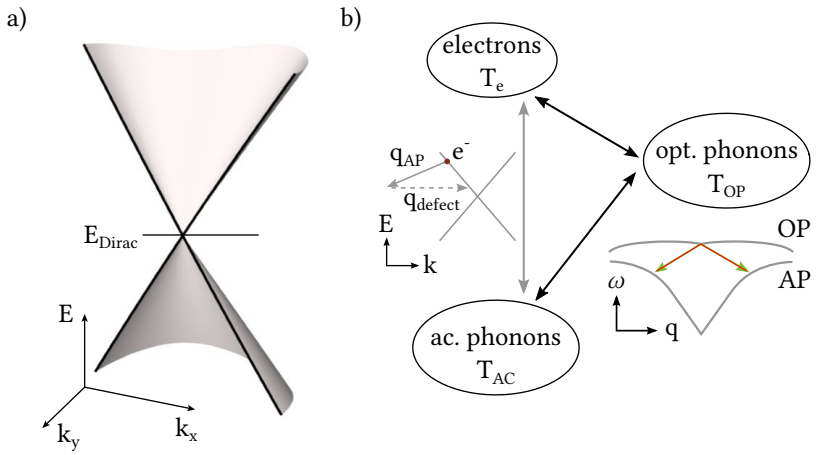


Figure 4.4: (a) HOPG Dirac cone at K/K′. (b) Three-temperature model for hot-electron decay. (a) Adapted from Ref. [120] (Merboldt *et al.*), licensed under CC BY 4.0. (b) Adapted with permission from Ref. [14]. © American Physical Society.

Upon optical excitation of undoped HOPG with pulses of energy $\hbar\omega$ in the visible and near-infrared range, electrons are excited from π to π^* states across the Dirac point (or across the Fermi level in the semimetallic band structure), which initially creates a highly non-thermal population of electrons and holes, roughly centered around energies $\pm\hbar\omega/2$ from the Fermi level in the Dirac-cone approximation [164]. The subsequent decay dynamics are nearly symmetric for electrons and holes (for weak doping and near the Dirac point) [189], and electron relaxation is typically described within a three-temperature model (see Fig. 4.4b) [14]. First, electrons undergo ultrafast intraband relaxation on the order of 10 fs to 30 fs [164, 190] and form a thermal distribution with temperature T_e. The electrons then relax via optical phonon scattering with energy $\hbar\omega_{OP} \approx 200$ meV on the order of 150 fs to 250 fs [14, 163]. This relaxation increases the temperature of the optical-phonon bath T_{OP}, which subsequently heats the acoustic-phonon bath T_{AC} within several picoseconds through anharmonic coupling. Exact relaxation times depend strongly on excitation

fluence via the electron temperature and optical-phonon population. While this model described trARPES data on HOPG well [14], a comparable experiment on graphene found relaxation via supercollision to play a major role [163]. Supercollision links the electron and acoustic-phonon baths via three-particle scattering at an impurity and allows large-q acoustic-phonon emission that would normally be suppressed. This deviation has been attributed to stronger disorder and substrate effects in monolayer graphene [14], which enhance disorder-assisted (supercollision) cooling and often lead to significant doping of the Dirac bands [163, 164].

4.4 Transition-Metal Dichalcogenides

Transition metal dichalcogenides (TMDs) are layered compounds with formula MX_2, and many members can be exfoliated into 2D crystals. Each TMD comprises a plane of transition-metal atoms M, which is covalently bonded to two planes of chalcogen atoms (X) [191] (see Figure 4.5a). In this thesis, we focus on group-VI TMDs based on tungsten (W) and the chalcogens sulfur (S) and selenium (Se). Weak vdW interactions between neighboring layers permit several stacking configurations with varying alignment, rotation, and translation [192]. As an example, Figure 4.5a shows *2H* hexagonal stacking. Here, adjacent layers are rotated by 180° with respect to each other, which results in *AB* stacking with a primitive unit cell containing two MX_2 formula units [191]. A monolayer lacks inversion symmetry (point group D_3h), whereas bulk 2H stacking restores inversion symmetry (D_6h) [193].

Semiconducting TMDs are widely studied for their electronic structure in the monolayer limit, as they combine a direct band gap in the K/K′ valleys with strong spin–orbit coupling [165], tightly bound excitons [29, 193], and a well-defined valley degree of freedom [194, 195]. In the following, we explain these properties using WS_2 as a representative example. Figure 4.5b shows the hexagonal BZ of WS_2 with the high-symmetry points relevant for this thesis. In the bulk, WS_2 is an indirect semiconductor with a band gap of 2.1 eV [29, 196], where the VBM is located at Γ and the CBM in the valley along Γ–K (here denoted Q; compare Fig. 4.5c). When reducing the layer number to a single monolayer, the band gap becomes direct, with both VBM and CBM located at the K/K′ valleys [197] (compare Fig. 4.5d). This indirect-to-direct crossover originates from the orbital character of the relevant bands and their distinct interlayer hybridization. The topmost valence band and lowest conduction band are formed by a combination of metal d and chalcogen p orbitals. At the K point, the valence band has predominantly in-plane orbital character arising from the metal $d_{x^2-y^2}$ and d_{xy} orbitals and the chalcogen p_x and p_y orbitals [197], which confines the electronic states within each layer and strongly suppresses interlayer hybridization. In contrast, the states at Γ are mainly composed of metal $d_{3z^2-r^2}$ and chalcogen p_z orbitals [197], whose out-of-plane character leads to substantial wave-function overlap between adjacent layers. This results in pronounced thickness-dependent splittings in few-layer and bulk crystals and strong hybridization in heterobilayer structures [198].

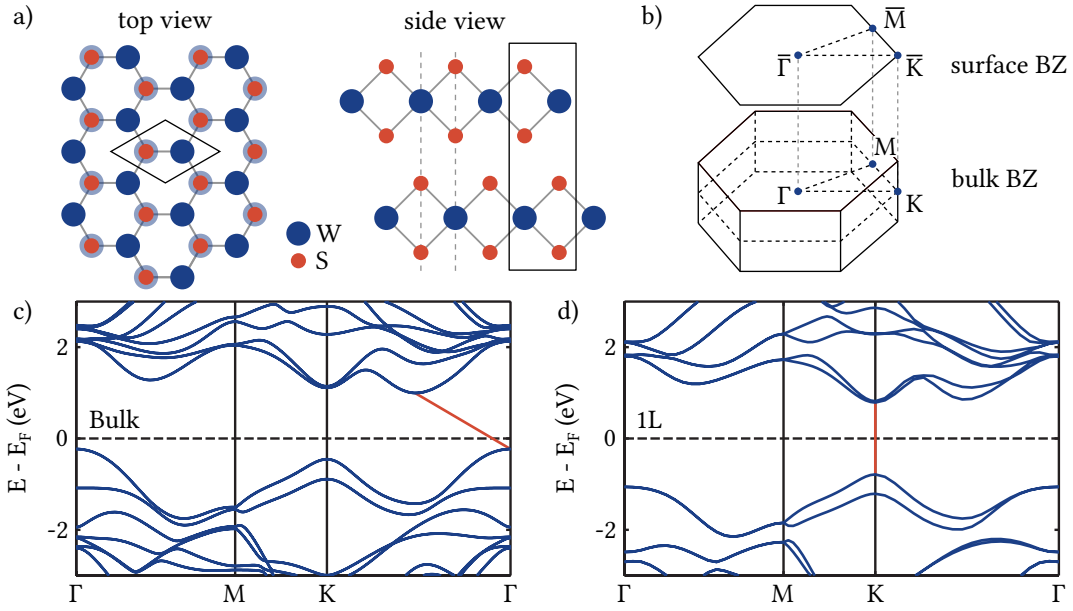


Figure 4.5: WS_2 crystal and electronic structure. (a) Schematic hexagonal lattice of a bilayer with *2H* stacking geometry in top and side view. Solid black lines mark the unit cell and gray dotted lines visualize the vertical layer alignment. (b) Bulk and hexagonal Brillouin zone of a hexagonal crystal with high-symmetry points relevant for this thesis marked in blue. (c) and (d) display *ab initio* band-structure calculations for bulk and monolayer crystals, respectively. Both VBM and CBM positions change in the monolayer limit to the K point, and the band gap, indicated by a red line, increases. (c) and (d) adapted from Ref. [30], with the permission from AIP publishing.

The same orbital character, combined with the heavy transition-metal ion W, gives rise to a large spin–orbit splitting of the upper valence band at K, on the order of 430 meV [199–201]. Due to the broken inversion symmetry in a monolayer, time-reversal symmetry enforces opposite spin orientations at the nonequivalent K and K′ valleys [193]. An electron that changes valley must either undergo a spin flip or an energetically unfavorable transition, which locks spin orientation and valley index [31]. However, the spin texture is not measured directly within this work.

Monolayer TMD semiconductors host strongly bound excitons with large oscillator strengths that dominate the optical response (excitons were introduced in Sec. 2.3.1). They are typically described as Wannier–Mott-like excitons, in which the exciton wave function extends over several unit cells [109, 202, 203], in contrast to localized Frenkel excitons [204]. For monolayer WS_2, reported binding energies of the lowest (1*s*) exciton are in the range of 350 meV to 400 meV [29, 205, 206]. Owing to the spin–orbit splitting of the valence band, two prominent excitonic series occur at the *A* and *B* transitions. Experimental studies have shown deviations from a simple Rydberg scaling $E_B \propto (n - 1/2)^{-2}$, particularly for higher-n states, as well as a pronounced reduction of the binding energy with increasing layer number or dielectric screening from substrates and encapsulation [29].

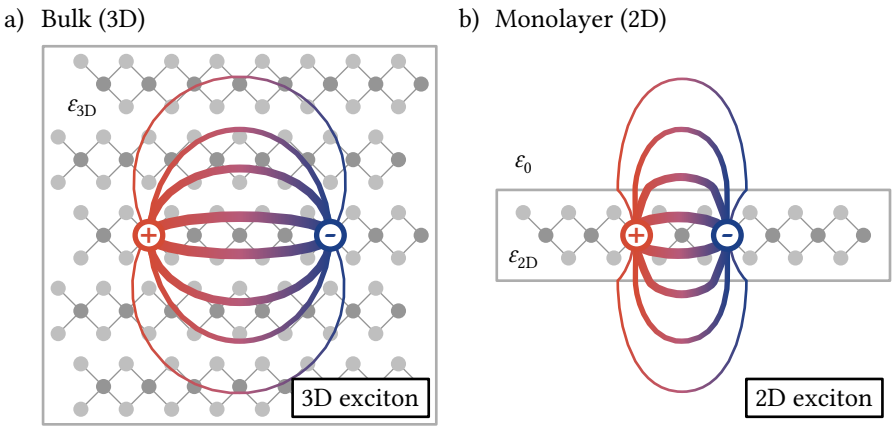


Figure 4.6: Effect of dielectric screening. The schematic electric field lines generated by the Coulomb interaction of the exciton's electron and hole are displayed in real space for a (a) bulk and (b) monolayer TMD. Reduced screening in the monolayer increases both the band gap and the exciton binding energy. Adapted with permission from Ref. [29]. © American Physical Society.

The change of the exciton binding energy with layer number and environment arises from modified screening of the Coulomb interaction. As illustrated in Figure 4.6, the electric field lines between electron and hole extend well outside the monolayer into the surrounding medium, where the dielectric constant can differ strongly from ε_{2D} [29, 199]. Here, ε_{2D} is a simplified effective parameter, not a true bulk dielectric constant. The deviations from pure Rydberg behavior and the sensitivity of higher excitonic states to the environment are well captured by the Rytova–Keldysh potential [207]. Screening also reduces the electronic band gap, explaining the intrinsically smaller band gaps of bulk crystals and the strong band-gap renormalization induced by substrates.

Experimental reflectance measurements on monolayer WS_2 on SiO_2, combined with modeling of the excitonic Rydberg series, yielded an extracted quasiparticle band gap of about 2.4 eV and a 1*s* exciton binding energy of ~350 meV [29, 205]. Moreover, Waldecker *et al.* combined ARPES and reflectivity measurements on monolayer WS_2 and found a rigid shift of the valence band and, together with optical spectroscopy, inferred a nearly symmetric shift of the conduction band. This corresponds to a band-gap renormalization of about 600 meV with increasing dielectric screening, whereas the exciton 1*s* resonance shifted by only ~50 meV [199]. This subtle shift reflects the small spatial extent of the 1*s* exciton and a partial compensation of the reduced binding energy by the simultaneous band-gap renormalization.

The creation of a coherent optical polarization and the ultrafast relaxation into an incoherent exciton population are discussed in Section 2.3.1. Because dielectric screening strongly affects both conduction and valence bands, exciton relaxation pathways depend on layer number, stacking order, and substrate material [100, 208]. The conduction band features multiple local minima (valleys, see Fig. 4.5),

and intervalley scattering via exciton–phonon coupling can produce momentum-indirect excitons [107]. In multilayers, hybrid excitons form when either the electron or the hole is delocalized across layers [114]. Finally, heterobilayers with type-II band alignment such as WS_2/WSe_2 have the VBM and CBM in different layers. This configuration enables the formation of interlayer excitons with an out-of-plane electric dipole moment [208]. By rotating the layers with respect to each other, a moiré pattern of the two lattices translates into an additional periodic potential that can trap interlayer excitons (ILXs) and provides a highly tunable excitonic landscape [209].

4.5 Chromium Sulfur Bromide

The Mermin–Wagner theorem forbids spontaneous long-range magnetic order at finite temperature in one- and two-dimensional systems with *continuous* spin-rotation symmetry and short-ranged interactions in the thermodynamic limit [210]. This restriction applies, for example, to the isotropic Heisenberg model. Long-range order can nevertheless be stabilized down to the monolayer at finite temperatures by introducing magnetic anisotropy, e.g. through spin–orbit interaction or lattice distortions [25]. In addition, a finite sample size cuts off long-wavelength spin fluctuations: Jenkins *et al.* showed that, for experimentally relevant lateral dimensions, exchange interactions can produce an apparent ordering crossover at finite temperature even in the absence of anisotropy [211]. Pushing this crossover below 1 K would require astronomically large lateral dimensions.

Since 2017, when intrinsic long-range ferromagnetism was demonstrated down to the monolayer limit in $Cr_2Ge_2Te_6$ [37] and CrI_3 [38], magnetic vdW materials have become a widely used platform for studying magnetism in the 2D limit [25, 212, 213] and for tuning magnetic states through external stimuli such as strain, gating, or light [25, 212, 213]. A practical limitation of many early vdW magnets is their low ordering temperature and/or poor environmental stability [214]. For instance, CrI_3 has a Curie temperature of about 61 K and degrades rapidly under ambient exposure, motivating encapsulation strategies in device geometries [215]. In this context, CrSBr has attracted renewed interest as an air-stable layered magnetic semiconductor with comparatively high magnetic ordering temperatures and pronounced in-plane anisotropy.

Bulk CrSBr crystallizes in an orthorhombic layered structure. Each layer consists of a buckled, covalently bonded Cr–S network sandwiched between two Br-terminated surfaces (see Fig. 4.7a). Within the layer, Cr sites are connected along the crystallographic a direction by both Cr–S–Cr and Cr–Br–Cr bridges with near-90° bond angles, whereas along b the dominant linkage is a Cr–S–Cr bridge with a larger bond angle of about 160° [216, 217]. Bromine atoms are bonded only to Cr and form chains along the a direction. The lattice parameters at room temperature are $a = 3.506$ Å, $b = 4.767$ Å, and $c = 7.965$ Å [218]. The pronounced in-plane anisotropy between a and b is already visible on the macroscopic level: exfoliated flakes typically cleave

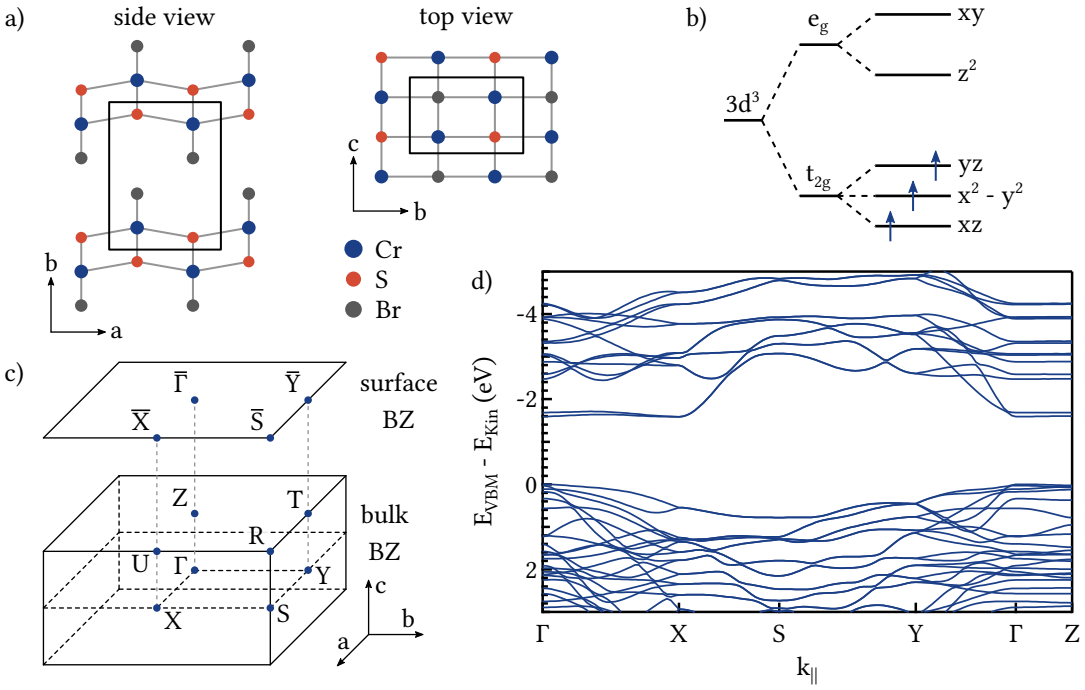


Figure 4.7: Bulk CrSBr crystal and electronic structure. (a) Schematic orthorhombic lattice of a bilayer shown in top and side view. The unit cell is marked by solid black lines. (b) Crystal field splitting of the Cr 3*d* manifold in CrSBr, yielding a high-spin configuration. The material-specific orbital ordering follows Ref. [77]. (c) Bulk and surface BZ of a simple orthorhombic crystal, with high-symmetry points relevant for this thesis marked in blue. (d) Bulk band structure calculated using density functional theory (DFT) with the meta-GGA SCAN functional, highlighting the anisotropic conduction-band dispersion along Γ–X and Γ–Y.

into elongated rectangles whose long edge is parallel to the crystallographic *a* axis. In bulk, the layers stack in an AA-type configuration without in-plane rotation or shift, providing a well-defined cleavage plane.

The Cr ions are in a Cr^{+3} configuration and are coordinated by six ligands (four S and two Br) forming a distorted octahedron [44]. In an octahedral crystal field, the *d* manifold splits into t_{2g} and e_g levels. For a high-spin d^3 configuration, this corresponds to a half-filled t_{2g} shell and empty e_g states (see Fig. 4.7b). The reduced local symmetry further lifts the degeneracy within both manifolds, which becomes relevant when discussing orbital character in the electronic structure below and for selection rules in photoemission.

CrSBr is a semiconductor with a direct band gap at Γ exceeding 1.5 eV. The precise value remains under debate, as discussed in more detail in Section 5.3.1. Figure 4.7d shows a calculated band structure in the *ab* plane (details in Sec. 5.3.1), while the corresponding high-symmetry points are indicated schematically in Figure 4.7c. A key feature is the extreme in-plane anisotropy of the conduction band. It is nearly flat along the Γ–X direction (corresponding to the *a* direction) but dispersive along

Γ–Y (the b direction). This results in a large electron effective-mass anisotropy of $m_e^X/m_e^Y \sim 50$, while the valence band is less anisotropic but still pronounced, with $m_h^X/m_h^Y \sim 6$ [44]. In transport, this corresponds to a quasi-one-dimensional electronic response within a structurally two-dimensional crystal [43].

This anisotropy can be traced to the orbital composition and bonding geometry. The lower conduction band has dominant Cr 3d character (with primarily d_{z^2}-like weight) hybridized with S 3p states, while the Br contribution is comparatively small. The resulting wave function supports strong dispersion along b and weak interchain coupling along a [44]. In contrast, states near the VBM carry substantial weight from Cr 3d and Br 4p orbitals [39].

Magnetically, CrSBr is an A-type antiferromagnet: Spins have ferromagnetic (FM) alignment within each layer, while adjacent layers have antiferromagnetic (AFM) coupling along the stacking direction. Below the Néel temperature $T_N \approx 132\,\mathrm{K}$, long-range interlayer order sets in with an easy axis along b [219]. Above T_N, experiments report pronounced short-range in-plane correlations that persist to substantially higher temperatures, and additional crossover anomalies have been discussed up to about 185 K [220]. Interlayer coupling is 2 to 3 orders of magnitude weaker than intralayer exchange, consistent with its super–superexchange path mediated by Br atoms [39]. The combination of strong in-plane anisotropy and layered magnetic order is reflected in a triaxial magnetic anisotropy with easy, intermediate, and hard axes along b, a, and c, respectively [41, 221].

Optical spectroscopy reveals a prominent near-infrared excitonic resonance in the range of roughly 1.25 eV to 1.36 eV, whose spectral position and linewidth depend on layer number and temperature [41, 44, 222]. The strong linear polarization of this resonance along the b axis is commonly attributed to the quasi-1D character of the electronic structure. While the exciton wave function has not been observed directly yet, it is predicted to be elongated along b and compressed along a [44].

Switching the interlayer spin alignment from AFM to FM (e.g. by an external magnetic field) modifies interlayer hybridization and leads to an abrupt shift of the exciton energy observed in photoluminescence (PL) [41, 223]. In pump–probe experiments, excitonic resonances in CrSBr have furthermore been shown to couple to magnon excitations, enabling access to the magnetic configuration even without direct magnetic sensitivity of the probe [224–226]. These interactions can be tuned, for example, by strain and magnetic field [227, 228], providing multiple control knobs for the coupled charge–spin dynamics in this material.

In summary, CrSBr combines (i) a sizable semiconducting gap, (ii) layered antiferromagnetism with a relatively high critical temperature among vdW magnets, (iii) comparatively robust ambient stability [225], (iv) strong in-plane anisotropy leading to a quasi-1D electronic response, and (v) magneto-correlated excitonic resonances.

5 Ultrafast Dynamics in 2D vdW Semiconductors

This chapter presents static and time-resolved MM studies on WS_2 and CrSBr. First, hot-electron relaxation following above-bandgap excitation is used to showcase the commissioned beamline (Ch. 3) on bulk WS_2 (Sec. 5.1), and the relaxation dynamics are then compared to those of a WS_2 monolayer on an Au(111) substrate. Second, exciton formation after resonant excitation in a WS_2/WSe_2 bilayer is traced (Sec. 5.2), highlighting the ability to track many-body phenomena in energy, momentum, and time. Finally, point-defect formation in bulk CrSBr is investigated, and its transient response is explored. Here, the dynamics are dominated by field effects (Sec. 5.3). All data presented in this chapter were analyzed using IGOR Pro 8 [229].

5.1 Conduction Band Electron Relaxation in WS_2

WS_2 is a well-studied member of the TMD family that features semiconducting properties, with an indirect-to-direct band gap transition at the monolayer limit and optically dominant excitonic resonances (see Sec. 4.4). In this chapter, we focus on the ultrafast relaxation of hot electrons upon optical above-bandgap excitation in bulk WS_2 with 2*H* stacking. Previous studies on comparable systems have demonstrated intra- and intervalley scattering in bulk TMDs of both hot carriers [93, 143, 194] and excitons [107, 230] with characteristic timescales in the femtosecond to picosecond regime. These relaxation mechanisms make bulk WS_2 an ideal model system to showcase the capabilities of the trMM beamline presented in Chapter 3.

We first map the equilibrium band structure over the full BZ (Sec. 5.1.1), before tracking hot-electron relaxation dynamics after above-bandgap excitation (Sec. 5.1.2). Here, we analyze the electron dynamics in a valley-dependent manner and use a rate-equation model to describe the relaxation pathways. Finally, we compare the band structure and relaxation dynamics of the bulk system to those of a monolayer on a metal substrate (Sec. 5.1.3). The following results take advantage of the two measurement modes by acquiring the static spectra with enhanced energy resolution and the time-resolved spectra with enhanced temporal resolution. The findings on bulk WS_2 were also published in Ref. [135]:

> K. J. Schiller, L. Sternemann, M. Stupar, A. Omar, M. Hoffmann, J. E. Nitschke, V. Mischke, D. M. Janas, S. Ponzoni, G. Zamborlini, C. J. Saraceno, and M. Cinchetti, "Time-resolved momentum microscopy with fs-XUV photons at high repetition rates with flexible energy and time resolution", *Scientific Reports* **15**, 3611 (2025)

5.1.1 Static Characterization

Bulk WS_2 samples are prepared by gluing a macroscopic crystal onto a sample plate and cleaving it in situ with scotch-tape. Static spectra were then acquired with the uncompressed XUV pulses for enhanced energy resolution, using 50 eV pass energy and a 0.5 mm × 1.0 mm entrance slit at 300 K. The resulting 3D data stack is shown in Figure 5.1.

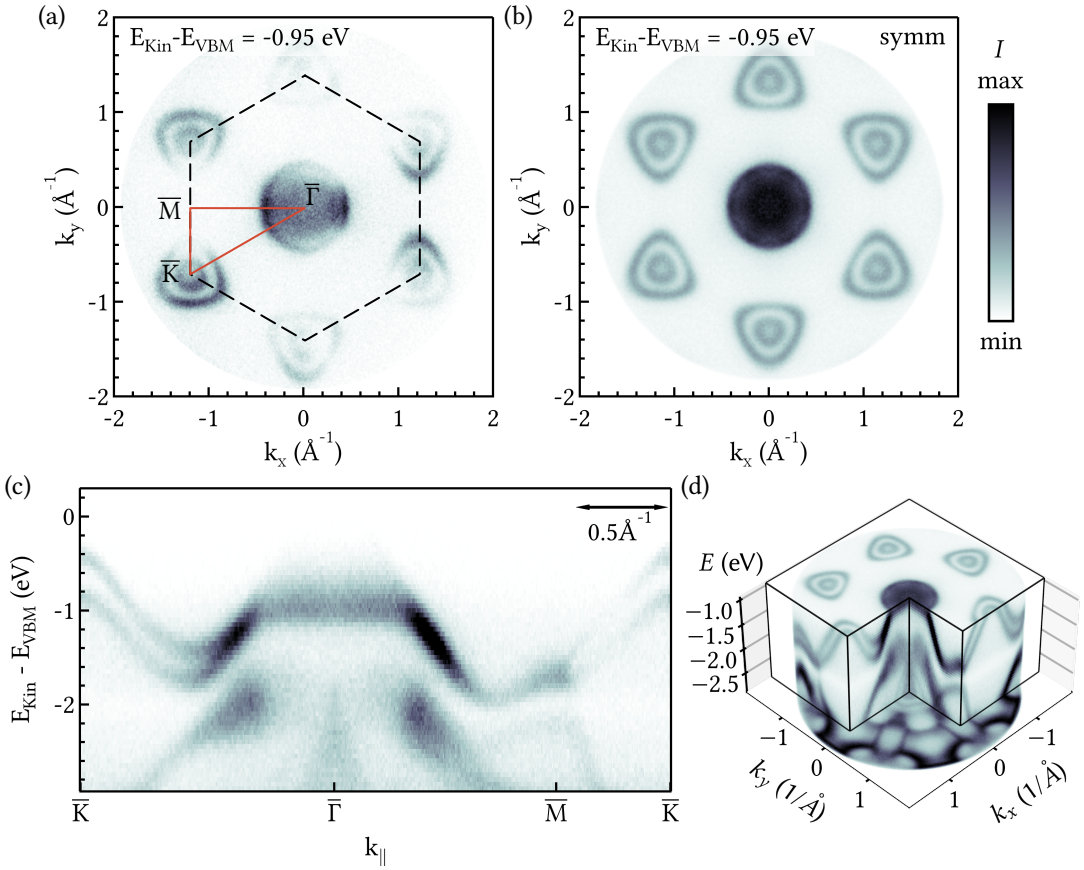


Figure 5.1: Bulk WS_2 band structure characterization. (a) Momentum map with dashed surface BZ and path along high-symmetry points (red solid line), which is used for the band structure cut in (c). (b) Symmetrized momentum map for illustrative purposes, clearly showing triangular warping at the $\overline{\text{K}}$ points. (d) Three-dimensional plot that illustrates an acquired data cube. Published in Ref. [135].

Figure 5.1a shows the momentum map along the in-plane momenta (k_x, k_y) at −0.95 eV binding energy relative to the VBM. Overlaid with a dashed line is the hexagonal Brillouin zone of WS_2, which allows assignment of the observed intensity to the $\overline{\Gamma}$ point and to the $\overline{\text{K}}$ points. While the $\overline{\Gamma}$ point displays rather uniform intensity with a circular shape, each $\overline{\text{K}}$ point comprises two triangular shapes, with one enclosing the other. These two shapes result from the spin splitting of the valence band at the $\overline{\text{K}}$ point. Their shape is distorted from a circular contour due to the orbital structure of the valence bands and the underlying threefold crystal lattice symmetry, which

give rise to non-isotropic terms in the system's Hamiltonian [231, 232]. This effect is commonly referred to as trigonal warping and affects, for example, the density of states.

Notably, the KREIOS MM can acquire this momentum map without rotating or moving the sample. The data in Figure 5.1a was integrated for 72 s and contains about 6.6×10^5 counts, yielding an effective rate of $9200\,s^{-1}$ at this energy. Due to the incidence direction of the XUV photons, the momentum map displays an intensity gradient from left to right. This effect can be removed by averaging the image with rotated and inverted copies in accordance with the underlying crystal symmetry. For $2H$-WS_2, this includes rotations of 120° and 240°, and three mirror planes which are rotated by 60° with respect to each other. The resulting symmetrized momentum image is displayed in Figure 5.1b. For a full 3D stack (E_{kin}, k_x, k_y) shown in Figure 5.1d, iso-energetic momentum maps are acquired for a range of kinetic energies. Importantly, this symmetrization may introduce artifacts and should be considered illustrative only. A vertical cut through the non-symmetrized data cube that connects the high-symmetry points $\overline{\Gamma}$, $\overline{M}$, and $\overline{K}$ (red solid line in Fig. 5.1a) is presented in Figure 5.1c.

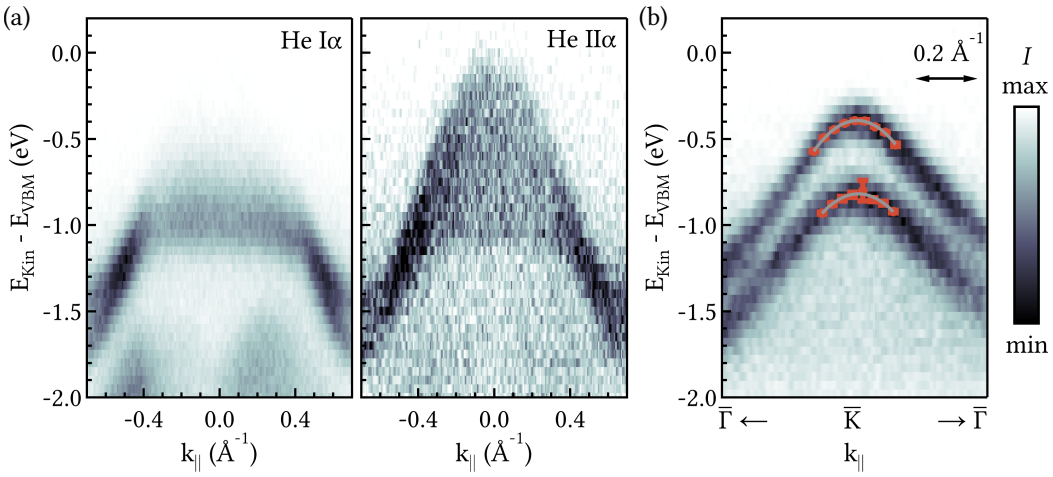


Figure 5.2: (a) Influence of the PME on the photoemission intensity close to the VBM at the $\overline{\Gamma}$ point. (b) Dispersion of the $\overline{K}$ point. Markers denote the momentum-dependent band position extracted from Gaussian fitting. Consecutive fitting with a parabolic function yields the effective masses for the spin-split valence band. Partly published in Ref. [135].

The acquired band structure of bulk WS_2 in Figure 5.1c is displayed as a function of binding energy referenced to the VBM. However, the spectrum does not show intensity at $\overline{\Gamma}$ close to the VBM. The energetic position of the VBM at either $\overline{\Gamma}$ or $\overline{K}$ is a key difference between monolayer and multilayer samples (see Sec. 4.4). We believe this lack of intensity to be an effect of the PME. Given the significance of this feature, we verify the PME hypothesis by acquiring the spectrum with XUV photons from He IIα emission at 40.81 eV. Figure 5.2a compares the band structure at $\overline{\Gamma}$ at the different photon energies (21.2 eV vs. 40.8 eV). The spectrum acquired with He IIα clearly demonstrates the expected intensity dispersion.

Around the $\overline{\mathrm{K}}$ point, the acquired band structure readily resolves the spin splitting of the valence band. The dispersion of the spin-split bands can be traced individually by determining the energy position as a function of in-plane momentum. Figure 5.2b displays a zoom-in on the $\overline{\mathrm{K}}$ point, with black dots marking the center position of fitted Gaussian distributions. A parabolic fit, shown as a solid line, then extracts the effective masses of (-0.39 ± 0.01) m_e and (-0.43 ± 0.05) m_e for the upper and lower valence band, respectively. These values agree well with a previous study by Tanabe *et al.* [200], who reported (-0.35 ± 0.02) m_e and (-0.43 ± 0.07) m_e. In addition, a line profile at the $\overline{\mathrm{K}}$ point was fitted with two Gaussian distributions, yielding a spin splitting of (442 ± 2) meV, which also aligns closely with (425 ± 18) meV found by Latzke *et al.* [232].

5.1.2 Transient Behavior of Bulk WS_2

After static characterization, we employ pump–probe spectroscopy to trace the ultrafast electron relaxation in bulk WS_2. Here, we switch to the compressed XUV pulses with enhanced temporal resolution. As pump, we utilize 2.4 eV pulses with *p*-polarization and a fluence of $472\,\mu J/cm^2$ for above-bandgap excitation. The analyzer pass energy is again 50 eV, but we use a larger entrance slit of 1.0 mm × 1.8 mm.

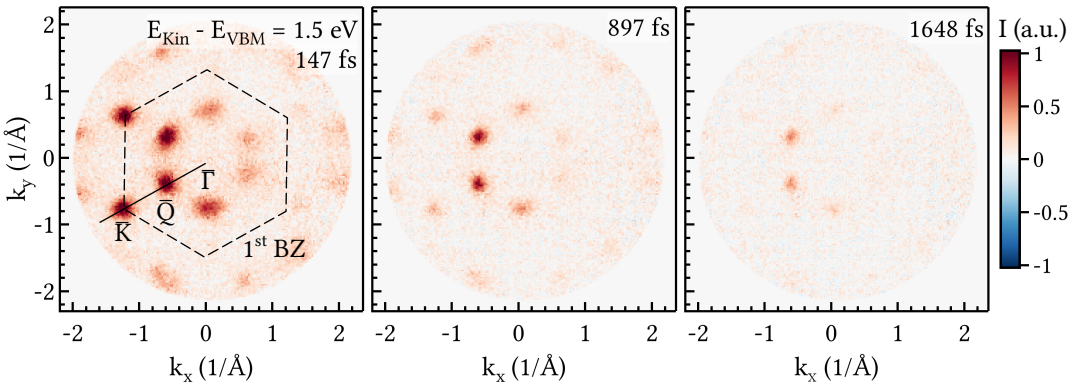


Figure 5.3: Bulk WS_2 momentum map above the VBM for three delays. The dashed line marks the first surface BZ and the solid line marks the position of the band-structure cut shown in Fig. 5.4a. Published in Ref. [135].

Figure 5.3 shows a momentum map above the VBM for three selected time steps, all three taken after temporal pump–probe overlap t_0. Due to the low signal strength of transient phenomena in general, we recorded one additional map at negative delays and subtracted this equilibrium intensity from the displayed data. Within our experimental geometry, this step especially removes duplicate signal of occupied states that are photoexcited by neighboring, higher-energy XUV harmonics, as the multilayer monochromator has a finite suppression factor. After subtraction, the map at 1.5 eV and 147 fs holds about 3.8×10^5 counts with 500 s acquisition time, giving an effective detection rate of $760\,s^{-1}$. All three maps display a pronounced intensity

gradient from left to right, which we attribute to the incidence direction of the XUV beams combined with stronger forward emission.

Shortly after photoexcitation, distinct electron distributions can be observed in a hexagonal pattern. When comparing the observed intensity to the dashed BZ, we can classify the observed occupation as belonging to either the $\overline{\mathrm{K}}$ or $\overline{\mathrm{Q}}$ valleys. With increasing delay, the intensity in both valley types decays as electrons relax to the respective valley minimum and recombine with holes in the valence band. However, the time scales appear to differ: the $\overline{\mathrm{K}}$-valley intensity has already vanished at the latest time step of 1648 fs (Fig. 5.3c), in contrast to the $\overline{\mathrm{Q}}$ valleys.

It is insightful to map the transient carrier distribution in an energy-resolved manner and to compare its momentum position to the equilibrium band structure. A band-structure cut along the $\overline{\Gamma}$–$\overline{\mathrm{K}}$ direction (solid line in Fig. 5.3) is shown in Figure 5.4a, with the corresponding static spectrum from the previous section shown below. The observed band gap is approximately 1.2 eV, which is below previously reported values of 1.35 eV from photocurrent measurements [233] and (1.4 ± 0.1) eV from transport measurements [234]. We attribute this deviation to the high density of photoexcited free carriers at the comparatively high pump fluence. The additional carriers screen the Coulomb interaction and likely renormalize the band structure, which transiently shrinks the observed band gap (see Sec. 4.4).

For a more quantitative assessment of carrier relaxation, we describe the hot-electron relaxation with a two-valley rate-equation model whose pathways are indicated in Figure 5.4a with dashed lines. We assume optical excitation at the $\overline{\mathrm{K}}$ point, from where electrons either recombine to the valence band or scatter into the $\overline{\mathrm{Q}}$ valley. In turn, electrons at the $\overline{\mathrm{Q}}$ valley can recombine indirectly with holes at the $\overline{\mathrm{K}}$ point or at $\overline{\Gamma}$ after hole scattering. The rate equations read

$$\frac{\mathrm{d}N_K(t)}{\mathrm{d}t} = -\left(\frac{1}{\tau_{\mathrm{K}\to\mathrm{Q}}} + \frac{1}{\tau_{\mathrm{K}}}\right)\cdot N_K \tag{5.1}$$

$$\frac{\mathrm{d}N_Q(t)}{\mathrm{d}t} = -\frac{1}{\tau_{\mathrm{Q}}}\cdot N_Q(t) + \frac{1}{\tau_{\mathrm{K}\to\mathrm{Q}}}\cdot N_K \tag{5.2}$$

with the population N_K (N_Q) at $\overline{\mathrm{K}}$ ($\overline{\mathrm{Q}}$), the initial population $N_{K,0}$ at $\overline{\mathrm{K}}$, and the three relaxation rates τ_{K}, τ_{Q}, and $\tau_{\mathrm{K}\to\mathrm{Q}}$. Taking the total temporal resolution into account, we convoluted a Gaussian distribution with the respective relaxation function times a Heaviside function Θ. The resulting valley-dependent fit functions read

$$I_K(t) = \int \frac{N_{K,0}}{\sqrt{2\pi\sigma^2}} \times \exp\left(-\frac{(t'-\mu)^2}{2\sigma^2}\right) \times \exp\left(-(t-t')\left(\frac{1}{\tau_{\mathrm{K}}} + \frac{1}{\tau_{\mathrm{K}\to\mathrm{Q}}}\right)\right) \times \Theta(t-t')\,\mathrm{d}t' \tag{5.3}$$

$$I_Q(t) = \int \frac{N_{Q,0}}{\sqrt{2\pi\sigma^2}} \times \exp\left(-\frac{(t'-\mu)^2}{2\sigma^2}\right) \times \left(\exp\left(-\frac{t-t'}{\tau_{\mathrm{K}\to\mathrm{Q}}}\right) - \exp\left(-\frac{t-t'}{\tau_{\mathrm{Q}}}\right)\right) \times \Theta(t-t')\,\mathrm{d}t' \tag{5.4}$$

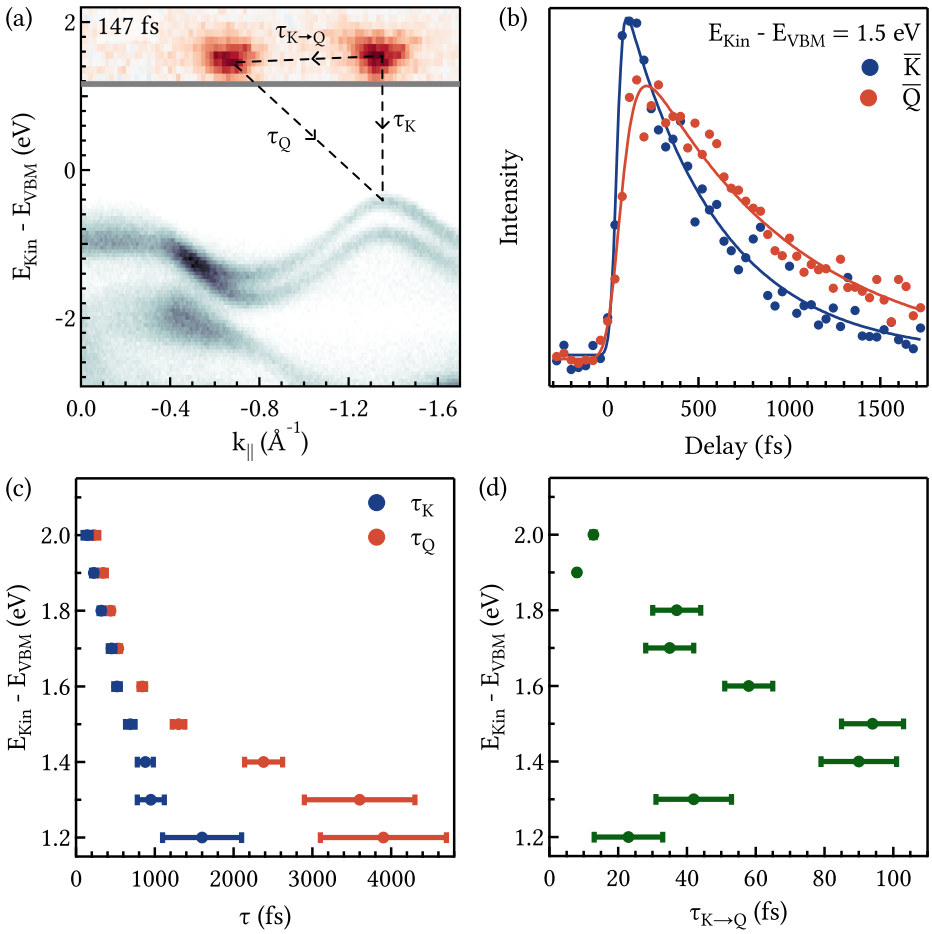


Figure 5.4: Hot electron relaxation in bulk WS_2. (a) Band structure along $\overline{\Gamma}$–$\overline{K}$ with the static spectrum at the bottom and the transient spectrum at 147 fs at the top. The dashed lines illustrate the relaxation pathways of the rate-equation model. (b) Exemplary transient intensities at $\overline{Q}$ and $\overline{K}$ for 1.5 eV with the model fit plotted as a solid line. (c, d) Energy-dependent scattering rates for $\overline{K}$, $\overline{Q}$, and intervalley scattering. Published in Ref. [135].

with the Gaussian standard deviation σ marking the temporal resolution of the experiment. To fit the experimental data, we integrate the photoemission intensity at the high-symmetry points within a circular ROI of 0.5 Å^{-1} diameter each. As an example, the integrated valley-selective data at 1.5 eV is displayed in Figure 5.4b. By fitting the above model curves (solid lines in Fig. 5.4b), we obtain $\tau_K = (690 \pm 60)$ fs, $\tau_Q = (1300 \pm 80)$ fs, and $\tau_{K\to Q} = (94 \pm 9)$ fs. Notably, the $\overline{K}$-valley curve is also used in Sec. 3.3 to infer the total temporal resolution from the Gaussian distribution FWHM, which yields (48.8 ± 1.7) fs.

By fitting the model curves (5.3) and (5.4) for every measured kinetic energy, we extract the energy-dependent relaxation times shown in Figures 5.4c and d. Both intravalley relaxation times τ_K and τ_Q increase monotonically towards the valley minimum (compare Fig. 5.4c) at roughly 1.2 eV. This behavior is in line with the picture of fast scattering to the bottom of the respective valley via electron–electron

and electron–phonon scattering before recombining with the hole population (see Sec. 2.2.4). In addition, the relaxation time at $\overline{\mathrm{Q}}$ is consistently greater than at $\overline{\mathrm{K}}$, which agrees well with our model of indirect recombination. In contrast, the intervalley scattering time $\tau_{\mathrm{K}\to\mathrm{Q}}$ in Figure 5.4d has a maximum at around 1.5 eV. We assume a model breakdown for high energies and for energies close to the CBM. At high kinetic energies, rapid intravalley relaxation is expected to dominate. As the CBM resides at $\overline{\mathrm{Q}}$ in bulk WS_2, the fitted $\tau_{\mathrm{K}\to\mathrm{Q}}$ at 1.2 eV might not describe intervalley scattering at all, because the $\overline{\mathrm{K}}$ valley minimum lies above. These assumptions are substantiated by retrieved $\tau_{\mathrm{K}\to\mathrm{Q}}$ values below the temporal resolution.

Even though the rate-equation model reflects the main dynamic trends observed, it neglects certain effects and relaxation pathways, for example

- Carrier diffusion outside the probed area induces a natural intensity decline with time.
- Possible transient band-position and band-gap renormalization with decreasing carrier density is neglected.
- Hole relaxation from $\overline{\mathrm{K}}$ to $\overline{\Gamma}$ is neglected.
- Back-scattering $\tau_{\mathrm{Q}\to\mathrm{K}}$ is neglected.
- Capture of carriers by defects or surface states is neglected.

Importantly, these different mechanisms are difficult to disentangle in trARPES if their characteristic timescale coincides with another process [93, 235].

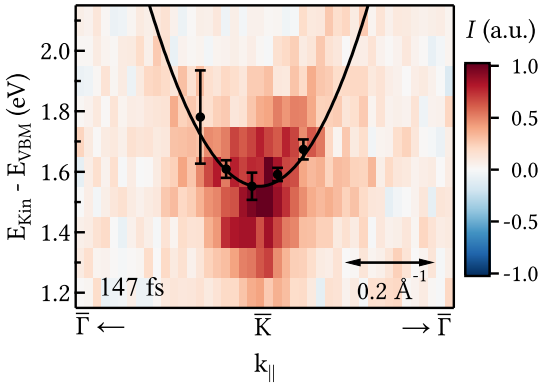


Figure 5.5: Dispersion of the transiently occupied conduction band at $\overline{\mathrm{K}}$. Markers show the momentum-dependent band position retrieved from Gaussian fitting, but the SNR does not allow unambiguous extraction of the effective mass. The solid line uses 0.36 m_e from Ref. [236].

While the 2.4 eV photon energy of the pump is in principle resonant with the WS_2 B-exciton [237], we do not observe additional transient signatures beyond conduction band hot electrons. The absence of excitons is likely caused by the high pump fluence,

which excites approximately 8.6×10^{13} cm^{-2} free carriers per pulse[1]. This value falls in the range of the Mott transition threshold at around 1×10^{13} cm^{-2} to 1×10^{14} cm^{-2} [238, 239]. The Mott transition occurs when the density of photo-generated electron-hole pairs is large enough to screen the interaction between carriers [240]. This screening leads to a transition from an insulating excitonic regime to a metallic-like conducting state and to the dissociation of excitons into a free electron-hole plasma [238].

Similar to the dispersion of the valence band in the previous section, we can estimate the effective mass in the unoccupied energy levels at $\overline{\mathrm{K}}$. Figure 5.5 displays a band-structure cut at the $\overline{\mathrm{K}}$ point along with black dots that mark the fitted Gaussian center of the line profile. Due to the low SNR in combination with degraded energy resolution from the compressed pulses, the dispersion cannot be traced unambiguously. Thus, the solid line in Figure 5.5 does not represent a fit, but rather a calculated parabola that uses an effective mass of 0.36 m_e reported by Oliva *et al.* [236]. The calculated parabola matches the acquired spectrum well, confirming the observed intensities as conduction band electrons.

5.1.3 Comparison to WS_2 Monolayer on Gold

As a comparison to the bulk WS_2 in the previous section, we have also tracked hot-carrier relaxation on monolayer WS_2 on a metallic substrate. Here, the band structure significantly changes, with the most prominent difference being that the band gap is now direct and located at the $\overline{\mathrm{K}}$ point (see Sec. 4.4). The sample was grown in situ on an Au(111) surface, which is described in detail in Section 4.2. Before measurement, the sample was cleaned by annealing at approximately 350 °C for 90 min. All photoemission experiments were conducted at 80 K with the setup described in Sec. 3.4.

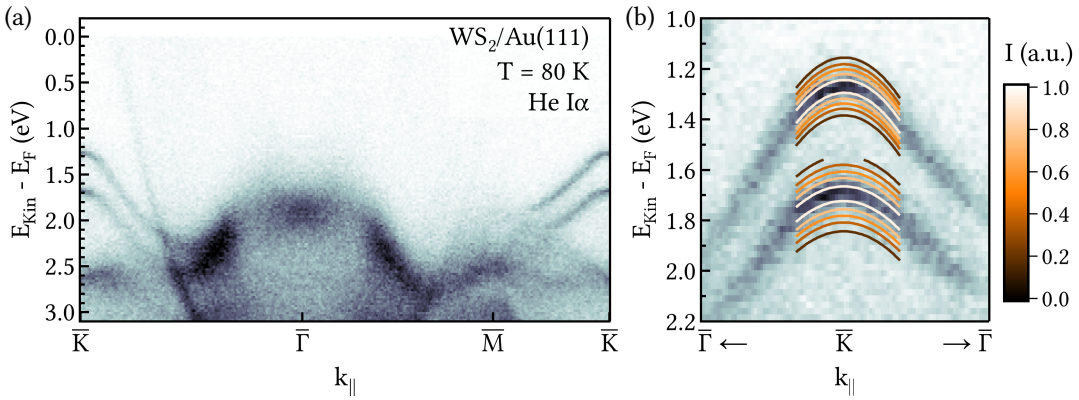


Figure 5.6: (a) Band structure of monolayer WS_2 on Au(111). In contrast to the bulk WS_2 spectra, the VBM now lies at $\overline{\mathrm{K}}$ and the *sp*-band of the substrate is prominent. (b) Zoom-in at the WS_2 $\overline{\mathrm{K}}$ point with two fits using Eq. 5.5, which are overlaid as contour lines.

[1]Assuming one emitted electron per absorbed photon, the free carrier density is approximately $n = AN_{\mathrm{ph}} = AF/(\hbar\omega)$ with absorbance $A \approx 7\,\%$ and fluence $F = 471.6\,\mu\mathrm{J/cm^2}$.

The static ARPES spectrum of WS_2/Au(111) was acquired with He Iα radiation and clearly exhibits the VBM shift from $\overline{\Gamma}$ in bulk to $\overline{K}$ (see Fig. 5.6). Owing to the small thickness of the monolayer, spectral features of the Au(111) substrate are also visible and are most prominent in the *sp* bands. The dispersion of the spin-split valence band of WS_2 at $\overline{K}$ is fitted with a two-dimensional function of the form

$$I(k,E) = A \cdot \exp\left(-\frac{\left(E - \left(a \cdot (k-k_0)^2 + E_0\right)\right)^2}{2\sigma^2}\right), \tag{5.5}$$

which describes a Gaussian distribution along the energy axis whose center position shifts parabolically with k. The fit is overlaid to the experimental data in Figure 5.6b as contour lines and yields $(0.40 \pm 0.01)\,m_e$ and $(0.58 \pm 0.02)\,m_e$ for the upper and lower valence band, respectively, which matches a previous report by Dendzik *et al.* of $(0.40 \pm 0.02)\,m_e$ and $(0.57 \pm 0.09)\,m_e$ [185]. The spin splitting is (417 ± 3) meV, also matching the previously reported (419 ± 11) meV. In addition to the XPS results of Section 4.2, the high-resolution ARPES spectra confirm successful growth of a high-quality WS_2 monolayer.

As time-resolved measurements were performed after the OPA integration into the setup (see Sec. 3.4), the total energy resolution using compressed XUV pulses was 125 meV. However, the OPA was bypassed for the measurements in this section, and the IR pump pulses were frequency-doubled in a 0.5 mm thick BBO crystal for direct comparison to the bulk experiments. The pump pulse duration (determined by SH autocorrelation) measures 177 fs FWHM, the pump polarization is *p*, and the pump fluence is 545 $\mu J/cm^2$. All spectra were taken at 80 K sample temperature with 50 eV pass energy and 0.5 mm × 1.0 mm entrance slit.

Figure 5.7 displays the electron occupation at temporal overlap. Similar to bulk WS_2, the electrons are excited into the $\overline{K}$ valleys. However, the momentum map in Figure 5.7a does not display an occupation of the $\overline{Q}$ valleys. A cut along the dashed line yields the band structure of Figure 5.7c, which is again aligned with the static spectrum for comparison. The VBM lies 1.28 eV below Fermi and the CBM lies 0.6 eV above Fermi, giving a band gap of 1.88 eV. Here, the reduced band gap (compared to 2.2 eV on hexagonal boron nitride (h-BN) [199]) might result from screening and charge transfer by the metallic substrate, in addition to the optically excited carrier distribution. The dispersion of the transient signal at $\overline{K}$ is also fitted with the model function (5.5) and yields an effective mass of $(0.177 \pm 0.009)\,m_e$ (compare Fig. 5.7b), which is much smaller than reported values for bulk WS_2 of $(0.36)\,m_e$ [236]. This stark difference is surprising, because valence and conduction band at K have primarily in-plane character and are thus expected to experience only minor shifts. However, Graham *et al.* also found an unexpectedly small effective mass of $(0.15 \pm 0.02)\,m_e$ [241] on a WS_2/WSe_2 bilayer, which they attributed to moiré-induced band-structure renormalization. It is therefore possible that substrate interaction or proximity effects also cause renormalization that in turn affects the CBM effective mass.

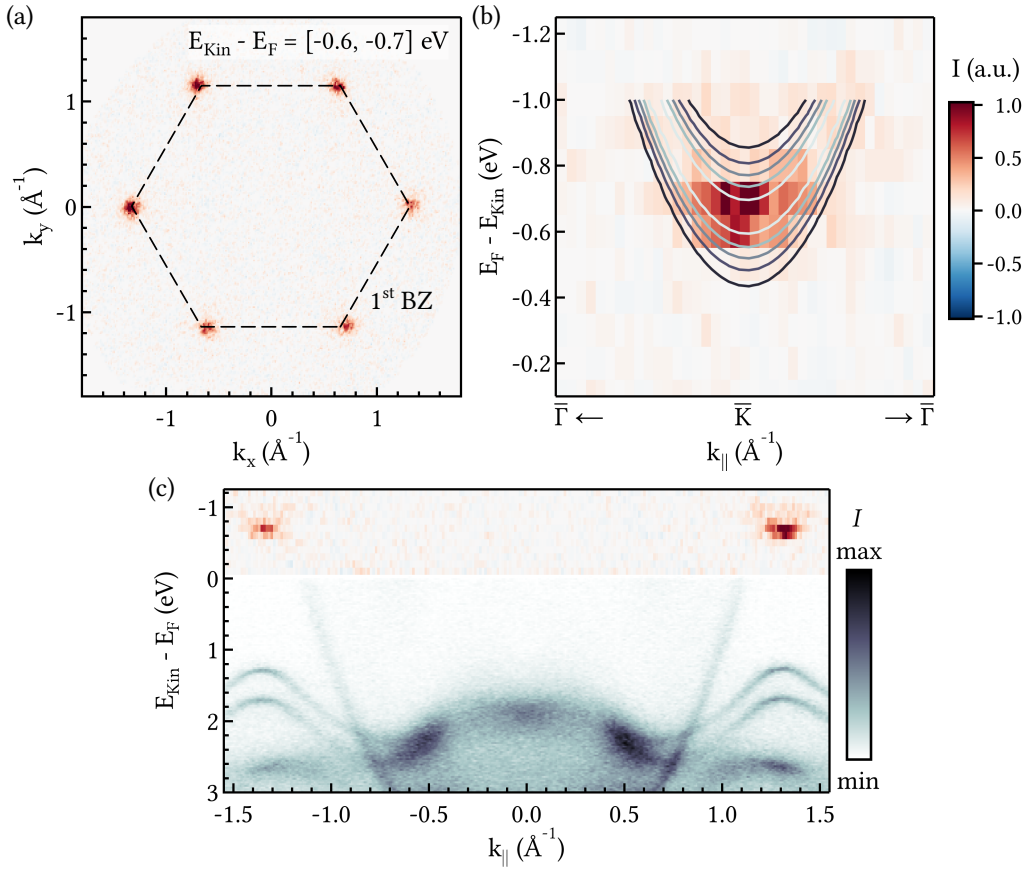


Figure 5.7: Transient WS_2/Au(111) signal at temporal overlap. (a) Integrated momentum map from −0.6 eV to −0.7 eV, only exhibiting intensity at the $\overline{\text{K}}$ points. A dashed line marks the first surface BZ. (b) Dispersion of the signal at $\overline{\text{K}}$, which is fitted according to Eq. (5.5). (c) Band structure cut along $\overline{\text{K}}$–$\overline{\Gamma}$–$\overline{\text{K}}$, with the static band structure as reference.

The transient behavior of hot electrons is displayed in Figure 5.8 and shows a qualitatively different behavior than the electron relaxation in bulk WS_2. Intuitively, interaction with the substrate is expected to heavily modify the transient response of WS_2, as previous reports on metallic substrates [235, 242] and Graphene [243] demonstrate extensive interaction. The angle-integrated signal in Figure 5.8a was integrated over the whole BZ since there is no contribution from the $\overline{\text{Q}}$ points. However, the dynamics at the $\overline{\text{K}}$ points do not suggest increasing relaxation times towards the local valley minimum, but rather decay within the temporal resolution of the experiment. Figure 5.8b displays the binding energies −0.6 eV to −1.0 eV, which are all fitted with a single Gaussian that yields a FWHM consistent with the pump–probe cross-correlation of approximately 135 fs. The temporal resolution is mainly limited by the pump pulse, as the additional post-compression only affects the probe pulses.

Unexpectedly, the energies between the CBM and the Fermi level also display a transient signature, which is shown in Figure 5.8d. Fitted with a convolution of a Gaussian and exponential decay plus a linear background (see Eq. (3.5)), they visually

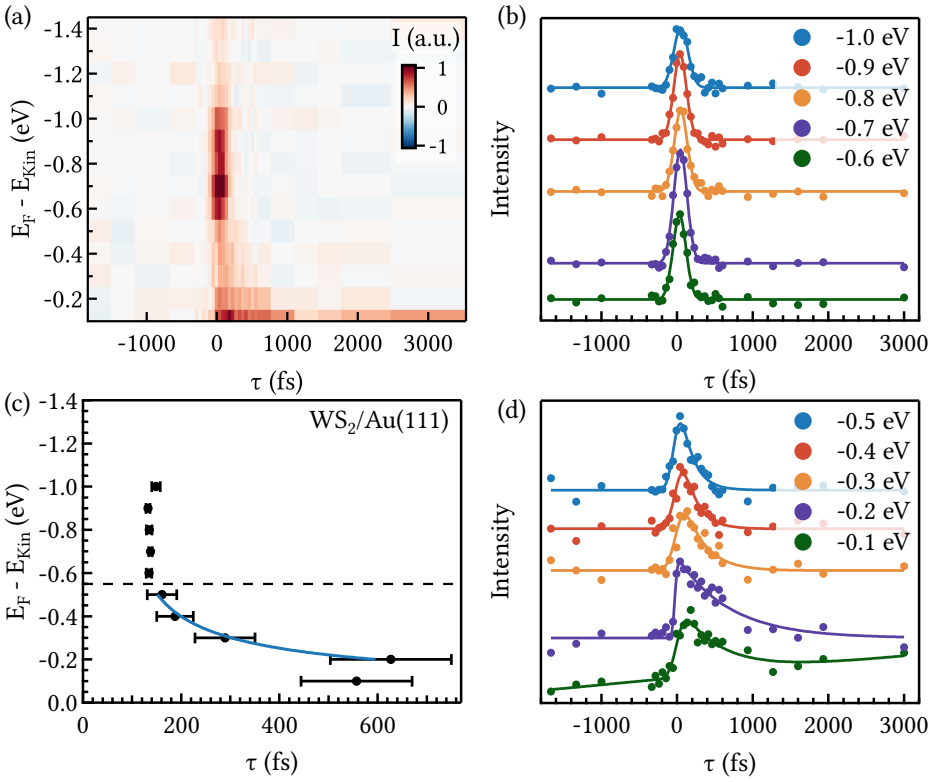


Figure 5.8: Hot electron relaxation in WS_2/Au(111). (a) Angle-integrated delay map. The single traces above −0.6 eV are plotted in (b) with single Gaussian fits and the traces below −0.6 eV are plotted in (d) with fits according to (3.5). (c) Gaussian widths for the high energy window and exponential decay rates for the low energy window. The latter is fitted with a Fermi-liquid fit function.

reveal longer relaxation times closer to Fermi. The linear background becomes paramount at −0.1 eV, where the signal is likely influenced by slight pump-induced space charge. The resulting decay times are displayed in Figure 5.8c and indeed show a nonlinear increase towards Fermi, except for the lowest analyzed energy, which is strongly influenced by space charge.

The lack of $\overline{\text{Q}}$-valley electron occupation might be rooted in the different conduction band alignment compared to the bulk crystal. In the monolayer, the $\overline{\text{K}}$ valley is the CBM [30, 197], making scattering into other valleys energetically unfavorable. In addition, the hot-electron relaxation time is even faster than the experimental resolution, further hindering valley scattering and explaining the observed momentum map. The rapid relaxation likely stems from substrate interaction, which could at the same time explain the transient signal between CBM and Fermi energy. Indeed, previous findings on Au(111) [242] and Ag(111) [235] observed similar behavior with MoS_2 and proposed an Auger-type electron–electron decay channel involving the TMD and metal substrate. Figure 5.9 schematically displays this interaction channel. Electrons in the conduction band can recombine with unoccupied states in the Au bulk continuum states while exciting an electron–hole pair in the metal for energy

conservation. A similar mechanism also enables ultrafast hole relaxation from the TMD VBM to the metallic substrate. Other prominent relaxation mechanisms were excluded by Grubišić Čabo *et al.* as their characteristic timescales are longer than the observed relaxation times.

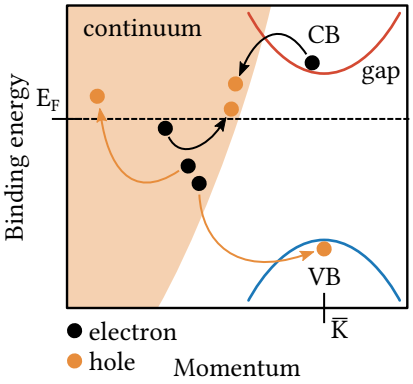


Figure 5.9: Schematic Auger-like scattering channel for TMDs on metallic substrates. Reprinted with permission from Ref. [242]. © 2015 American Chemical Society.

With the additional Auger decay channel and non-uniform WS_2 coverage (compare Sec. 4.2), hot electrons form in the Au(111) substrate. As validation, we fitted the extracted decay times with a Fermi-liquid fit function of the form

$$\tau(E) = \frac{A}{(E - E_F)^2} + \tau_0 \tag{5.6}$$

that features the typical inverse quadratic energy dependence of the inelastic electron–electron scattering lifetime [244]. The fit is displayed in Figure 5.8c and matches the decay times well. Only the lowest energy point is excluded, but the strong influence of pump-induced space charge might have distorted the extracted exponential decay rate. The parameter A combines several prefactors determining energy-dependent scattering strength, and the parameter $\tau_0 = (67 \pm 40)$ fs describes the intrinsic minimum (asymptotic) lifetime for electrons near or at E_F and reflects rapid interfacial charge transfer to substrate states on Au(111) [36].

Overall, the presented trMM experiments on bulk WS_2 and monolayer WS_2/Au(111) demonstrate the potential of the commissioned setup to resolve ultrafast processes in energy, momentum, and time. In particular, the switchable operation between an energy- and temporal-resolution-optimized configuration provides an additional degree of freedom to enhance setup performance, for example for static characterization followed by transient mapping.

5.2 Exciton Formation in Bilayer WS_2/WSe_2

Excitons dominate the optical response of TMD materials [193, 245, 246]. Their properties depend on the momentum and spin configuration of the bound electron–hole pair, for example, on whether the electron and hole reside in the same valley (momentum-direct) or in different valleys (momentum-indirect). In heterostructures formed from different TMD monolayers, a type-II band alignment can furthermore enable additional exciton species, including interlayer and hybrid excitons [247–249].

In this section, we first compare the electronic band structure of monolayer WS_2 with that of the overlap region in a WS_2/WSe_2 heterobilayer. We then perform trMM measurements on the heterobilayer, using the microscope's spatial selectivity to restrict photoemission acquisition to a defined ROI. By resonantly exciting WSe_2 excitons and monitoring the transient photoemission response at selected points in the BZ, we track the ultrafast build-up and decay of the corresponding nonequilibrium spectral signatures. The observed dynamics are consistent with the formation of hybrid excitons, whereas no signatures are observed that we attribute to ILX formation.

The studied sample was prepared by Tatyana Ivanova, Dr. Mauro Brotons-Gisbert, and Prof. Brian Gerardot[2]. Monolayer WS_2 and WSe_2 flakes were mechanically exfoliated and stacked by all-dry transfer in air onto a *p*-doped Si wafer with native SiO_2, yielding a $WS_2/WSe_2/SiO_2$ structure. Prior to the photoemission experiments, the sample was annealed in UHV at 400 °C for 140 min to reduce surface adsorbates. All measurements were performed at the METIS beamline described in Chapter 2.4.3, at a sample temperature of 80 K, magnification 2, and a nominal pass energy of 30 eV. The probe was *p*-polarized, with a photon energy of 26.4 eV and a repetition rate of 300 kHz. The conversion from photoelectron flight time to kinetic energy was calibrated using EDCs acquired at different drift voltages in the TOF tube. Because the software parameter denoted "TOF voltage" also slightly affected additional lens potentials, which was unknown at the time of the experiment, the absolute energy calibration may carry a small systematic uncertainty.

5.2.1 Equilibrium Spectrum

A microscope image of the heterobilayer flake is shown in Figure 5.10a. Red and black outlines indicate the WS_2 and WSe_2 monolayer regions, respectively. In the optical image, the monolayer areas exhibit only weak contrast on the Si substrate, whereas adjacent thicker flakes appear with different gray levels. A marker etched into the substrate (bottom left in Fig. 5.10a) facilitates locating the flake in the MM, whose field of view is limited.

[2]Tatyana Ivanova, Dr. Mauro Brotons-Gisbert, Prof. Brian Gerardot, Institute of Photonics and Quantum Sciences, SUPA, Heriot-Watt University, Edinburgh EH14 4AS, United Kingdom

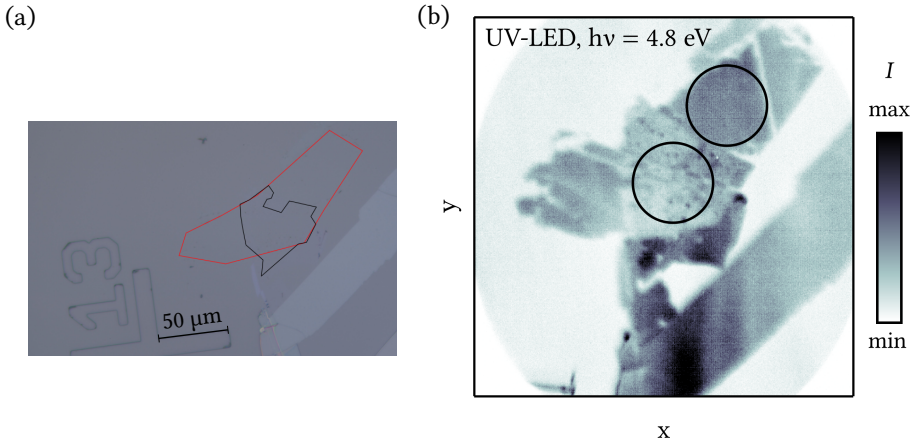


Figure 5.10: Identification of the WS_2/WSe_2 flake. (a) Optical microscope image with red and black outlines marking the WS_2 and WSe_2 monolayer regions, respectively. (b) Energy-integrated PEEM image of the same region, resolving bubbles and fissures in the transferred layers. The circles indicate the field-aperture positions used for ARPES on the heterobilayer overlap region and on monolayer WS_2.

Using a UV LED at 4.8 eV, we first locate the flake and record the energy-integrated PEEM image shown in Figure 5.10b. The pronounced contrast between the SiO_2 surface and the TMD layers is consistent with differences in the photoemission work-function threshold [34, 237] and additionally reveals small fissures and bubbles in the transferred stack.

Experimental Observations

After switching to the focused XUV probe, the MM enables acquisition of ARPES spectra from user-defined ROIs. Here, the field aperture was positioned either on the heterobilayer overlap region or on a monolayer WS_2 region, yielding the spectra shown in Figures 5.11a and b. The corresponding ROIs are indicated in the PEEM image.

The monolayer WS_2 spectrum in Figure 5.11a differs from the bulk band structure in Figure 5.1, most notably by the location of the VBM, which is now at the $\overline{\mathrm{K}}$ point rather than at $\overline{\Gamma}$. The relative spectral weight of the upper valence band around $\overline{\Gamma}$ is pronounced in the present geometry. This should primarily be attributed to PMEs and the experimental configuration (photon energy, incidence angle, and polarization), rather than to a change in intrinsic band renormalization. The expected spin splitting of the top valence band at $\overline{\mathrm{K}}$ (on the order of a few hundred meV) is not clearly resolved here. This indicates substantial broadening, for example from limited energy resolution, photon bandwidth, and/or sample-related disorder or contamination.

To compare the monolayer and heterobilayer spectra more directly, Figure 5.12 shows the corresponding EDCs at $\overline{\mathrm{K}}$ and $\overline{\Gamma}$. At $\overline{\mathrm{K}}$ (Fig. 5.12a), the two EDCs are

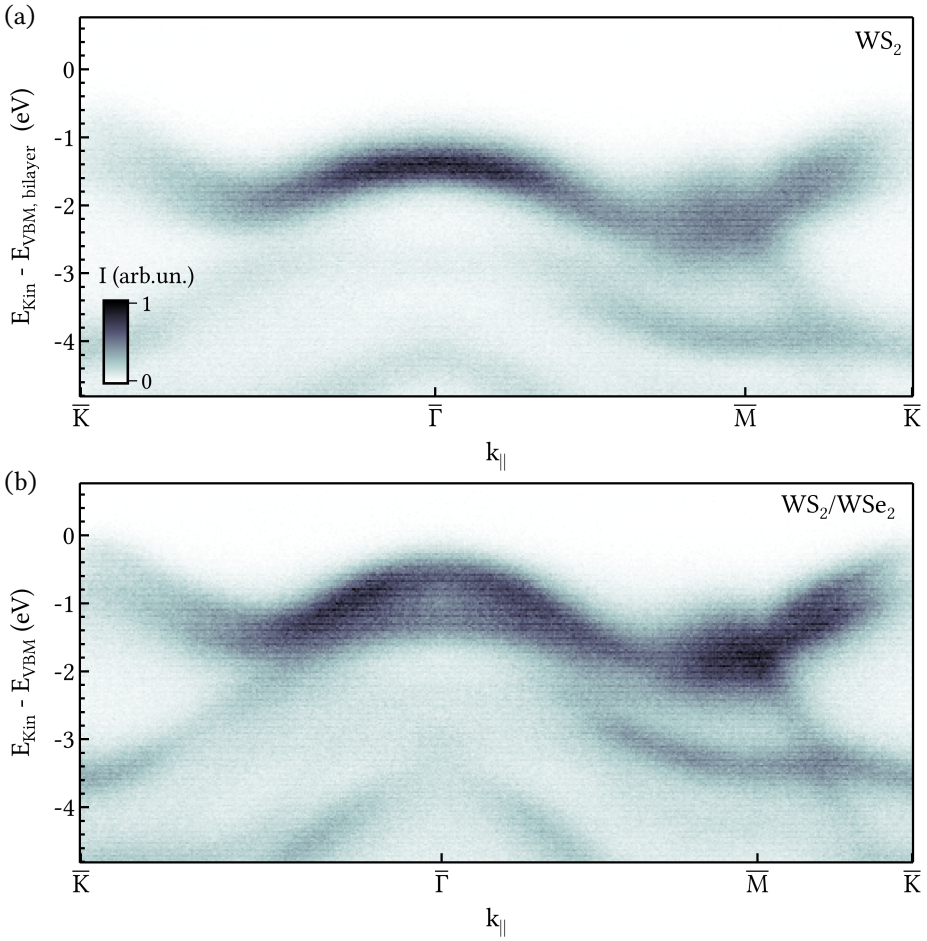


Figure 5.11: ARPES spectra of (a) the WS_2 monolayer region and (b) the WS_2/WSe_2 heterobilayer overlap region.

offset in energy, and Gaussian fits to the dominant features yield a separation of approximately 0.5 eV. This value should be regarded as an order-of-magnitude estimate because systematic uncertainties of the absolute energy scale likely exceed the statistical fit errors. At $\overline{\Gamma}$ (Fig. 5.12b), the comparison is particularly relevant for assessing interlayer coupling. The monolayer WS_2 EDC is described by a peak at (1.403 ± 0.003) eV, whereas the heterobilayer requires two peaks at (0.63 ± 0.01) eV and (1.24 ± 0.01) eV.

All EDCs in Figure 5.12 exhibit a "picket-fence" modulation superimposed on the spectral intensity. A plausible origin are resampling artifacts in the TOF digitization chain: the detector time-to-digital converter (TDC) records arrival times on a fixed hardware time grid, which is then rebinned to the user-defined binning [251]. If the grids are not commensurate, periodic variations in counts per output bin can occur. While mitigation strategies, such as jittering time stamps prior to rebinning, have been proposed [251], the commercial METIS 1000 software does not provide user access to such low-level processing.

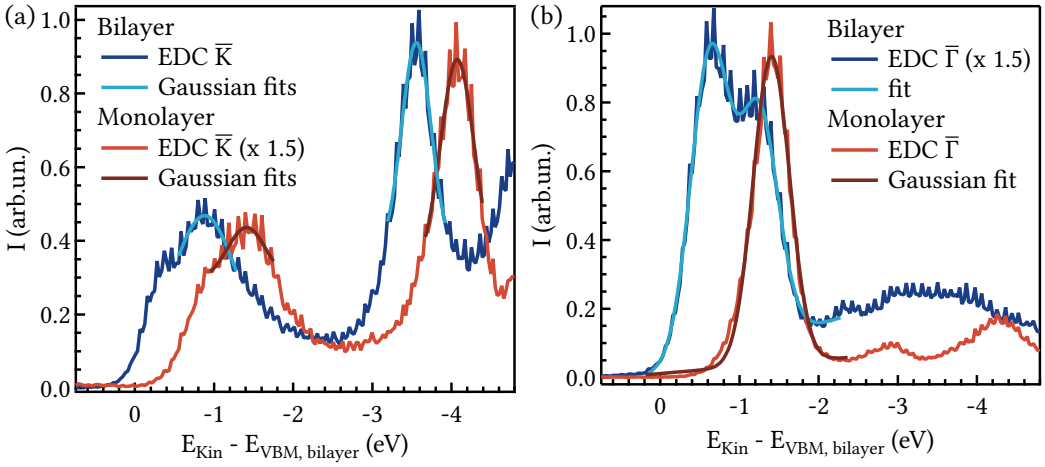


Figure 5.12: EDC comparison of monolayer WS_2 and the WS_2/WSe_2 heterobilayer at (a) $\overline{K}$ and (b) $\overline{\Gamma}$. Peak fits in (a) yield an estimated valence-band offset of order 0.5 eV, consistent with a type-II band alignment. At $\overline{\Gamma}$ in (b), the higher-binding-energy feature in the heterobilayer is shifted by approximately 160 meV with respect to the corresponding monolayer WS_2 feature. Such a fingerprint is consistent with screening-induced energy renormalization but is not, by itself, a unique signature of strong hybridization [250].

Interpretation

The heterobilayer spectrum in Figure 5.11b differs clearly from that of monolayer WS_2. In the following, we assess (i) the valence-band alignment, (ii) whether the data contain signatures consistent with interlayer coupling, and (iii) whether the relative crystallographic orientation can be constrained.

At $\overline{K}$, the dominant valence-band feature in the heterobilayer appears at lower binding energy than in monolayer WS_2. This is consistent with the bilayer signal at $\overline{K}$ being dominated by WSe_2, which naturally explains the observed 0.5 eV offset in terms of the expected valence-band alignment. In that picture, the WS_2 VBM lies at larger binding energy than the WSe_2 VBM, with a reported offset on the order of 0.5 eV [252], in agreement with our estimate (see Fig. 5.13). Stansbury *et al.* likewise reported a type-II alignment for WS_2/WSe_2 from comparison with monolayer reference calculations [250]. The absence of a clearly resolved second set of bands attributable to WS_2 in our bilayer spectrum can be explained by the high surface sensitivity of ARPES, which strongly suppresses the photoemission intensity from the covered layer. In addition, even the monolayer WS_2 spectrum exhibits only weak spectral weight at $\overline{K}$ in the present geometry.

Hybridization effects are expected to be most pronounced at $\overline{\Gamma}$ in strongly coupled, near-aligned heterobilayers because the relevant states have stronger out-of-plane orbital character, whereas the $\overline{K}$ valence states are predominantly in-plane and therefore typically less sensitive to layer number (see Sec. 4.4). This behavior is consistent with prior studies on $MoSe_2/WSe_2$ by Wilson *et al.* and on WS_2/WSe_2 by

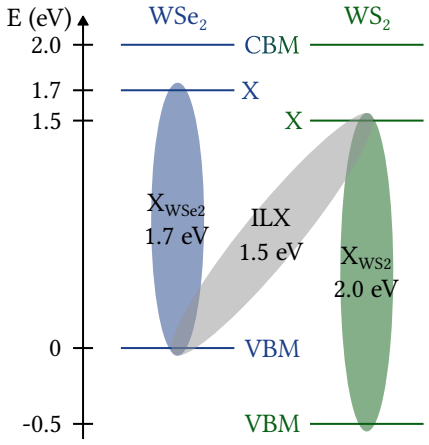


Figure 5.13: Expected energy level alignment of a WS_2/WSe_2 heterobilayer. Level positions taken from Refs. [199, 252, 253].

Stansbury *et al.* [250, 254]. In misaligned samples, both works found spectra that largely resembled a superposition of monolayer contributions, while Stansbury *et al.* additionally reported modest rigid shifts attributed to dielectric screening [250, 254]. By contrast, near-aligned samples ($< 1°$) exhibited more pronounced changes near $\overline{\Gamma}$, including additional spectral features in $MoSe_2/WSe_2$ and band flattening together with a larger binding-energy offset in WS_2/WSe_2 [250, 254].

In our data, the heterobilayer spectrum at $\overline{\Gamma}$ exhibits two distinct valence-band features, indicating contributions from both layers and/or modified dispersion in the overlap region. During the analysis, no clearly separated second hexagonal Brillouin-zone pattern was resolved in momentum space. This is compatible with a near-aligned configuration, for example around $0°$ or $60°$, but it could also result from suppression of the weaker layer contribution by matrix elements, attenuation, or disorder broadening. The twist angle therefore cannot be determined uniquely from the present data alone. Optical identification is likewise limited by the low contrast of the individual monolayers on the substrate (Fig. 5.10a). Comparing the EDCs at $\overline{\Gamma}$, we assign the higher-binding-energy feature to the WS_2-derived state and obtain a shift of (160 ± 20) meV in the bilayer. However, such a shift is not by itself evidence for strong hybridization, because comparable shifts can also arise from modified dielectric screening by the adjacent layer [199, 235].

Overall, our equilibrium data do not show the clear hallmarks reported for strongly coupled, near-zero-twist bilayers, such as pronounced band flattening or additional hybridization-induced features beyond a largely superposition-like picture. In addition, spatially resolved PL measurements performed by the Gerardot group did not reveal a pronounced modification of the bilayer emission relative to the monolayer regions. While this does not rule out interlayer coupling, it suggests that interlayer charge transfer and/or radiative ILX emission is weak under the measured conditions [255]. In our sample, interlayer coupling may have been reduced by residual contamination and bubbles introduced during fabrication.

5.2.2 Transient Behavior of WS_2 / WSe_2

In the previous section, we characterized the static electronic structure of the bilayer. The equilibrium spectra do not provide unambiguous evidence for strong interlayer hybridization, and the twist angle cannot be uniquely constrained from the available momentum-space contrast. Time-resolved measurements can nonetheless provide additional sensitivity, because the valley-resolved transient response differs markedly between monolayers and heterobilayers and can be strongly affected by interlayer charge transfer and excitonic scattering pathways [34, 109, 113, 237].

Experimental Conditions and Overview

We probe the transient response of the WS_2/WSe_2 bilayer using an OPA pump tuned close to the WSe_2 A-exciton resonance at 1.7 eV. The pump photon energy of (1.70 ± 0.05) eV lies well below the lowest WS_2 A-exciton transition energies reported for comparable dielectric environments [29, 230, 237], so that the excitation is expected to be predominantly WSe_2-derived (compare Fig. 5.13). The measured pump spectrum (see Fig. 5.14a) has a bandwidth of 119 meV (FWHM). The pump is *p*-polarized and the applied average power is 100 mW, corresponding to a pulse fluence of $93\,\mu J/cm^2$ at the sample (using the measured pump spot size). Interlayer excitons are generally less optically accessible than intralayer excitons because of the reduced electron–hole wavefunction overlap. In a twisted heterostructure, direct radiative transitions are further suppressed by momentum mismatch, often requiring phonon- or moiré-assisted processes [208].

Figure 5.14 summarizes the transient photoemission intensity near temporal overlap. The angle-integrated data in Figure 5.14b reveal a broad distribution shortly after excitation, which is still present after about 4 ps. The momentum map (see Fig. 5.14c) exhibits a hexagonal symmetry with maxima consistent with excitation near the $\overline{K}$ points and the conduction-band satellite valley along $\overline{\Gamma}$–$\overline{K}$ (here labeled $\overline{Q}$). The displayed intensity is a difference spectrum before and after optical excitation to enhance transient contrast. A cut through a $\overline{K}$ valley along $\overline{K}-\overline{K}$ is shown in Figure 5.14d.

The intensity distribution in Figure 5.14d is fitted with a Gaussian in energy, and the resulting center positions are displayed as a solid line. Within the experimental energy resolution (270 meV), the extracted peak position shows only weak dispersion and does not exhibit a clearly resolvable free-carrier parabola (compare Fig. 5.5). This behavior is compatible with an excitonic signal, but the present resolution does not permit a definitive curvature-based discrimination between bound-state signatures and a strongly broadened continuum response.

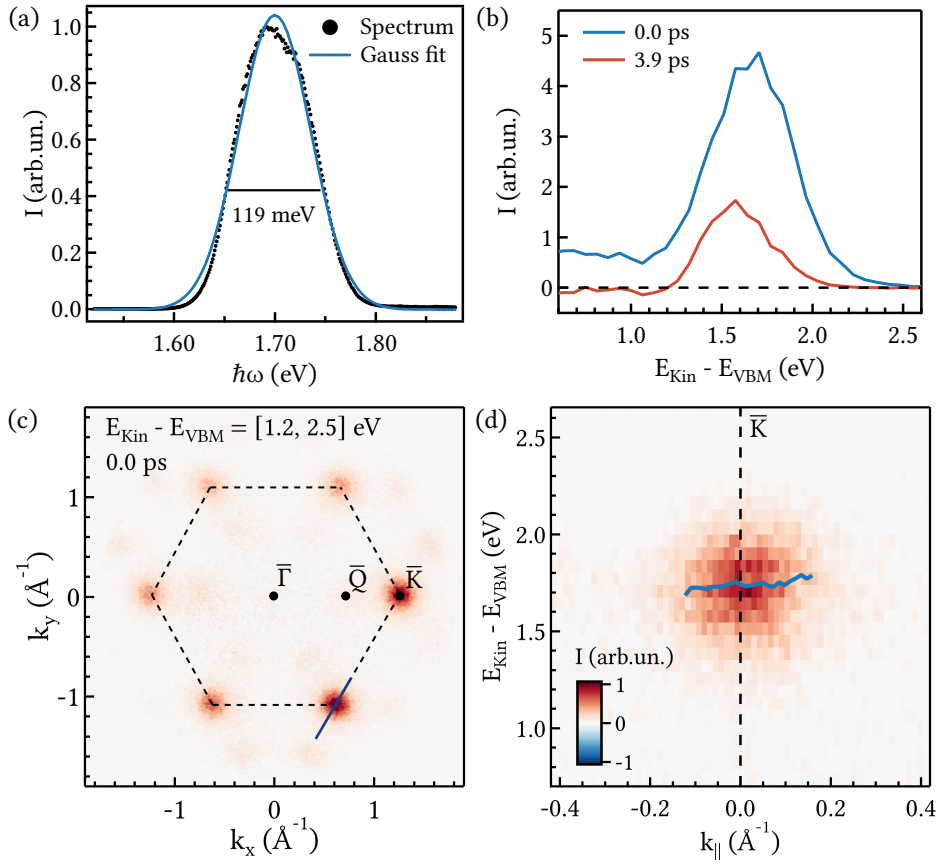


Figure 5.14: ARPES signal on WS_2/WSe_2 at temporal overlap. (a) Pump spectrum with a Gaussian fit, yielding a bandwidth of 119 meV (FWHM) centered at 1.70 eV. (b) Angle-integrated signal at temporal overlap and at 3.5 ps. (c) Momentum map at temporal overlap with high-symmetry points and the dotted BZ. (d) Band-structure cut along the solid line in (c), revealing the dispersion at $\overline{\mathrm{K}}$. Gaussian center positions as a function of momentum are shown as a solid line.

Time-resolved Dynamics and Artifact Separation

The transient evolution of the excited population is shown in Figure 5.15. Figures 5.15a and b show the integrated signal of all six $\overline{\mathrm{K}}$ and $\overline{\mathrm{Q}}$ points of the first BZ, respectively. At $\overline{\mathrm{K}}$, we observe a strong, prompt feature in the range 1.45 eV to 1.70 eV (limited by the experimental time resolution of $\sim$ 100 fs), as well as a long-lived tail that does not fully decay within the measurement window (−0.5 ps to 4 ps). A weaker feature around temporal overlap is also visible at 2.0 eV to 2.5 eV. At $\overline{\mathrm{Q}}$, a long-lived population is likewise observed at 1.45 eV to 1.70 eV, together with a short-lived low-energy feature at 0.1 eV to 1.0 eV near temporal overlap. In the following, we first separate artifacts from intrinsic features and then interpret the remaining long-lived $\overline{\mathrm{K}}$ and $\overline{\mathrm{Q}}$ signals.

The main transient features in Figure 5.15 appear in the energy window 1.45 eV to 1.70 eV at both valleys. We attribute the additional, short-lived signals around

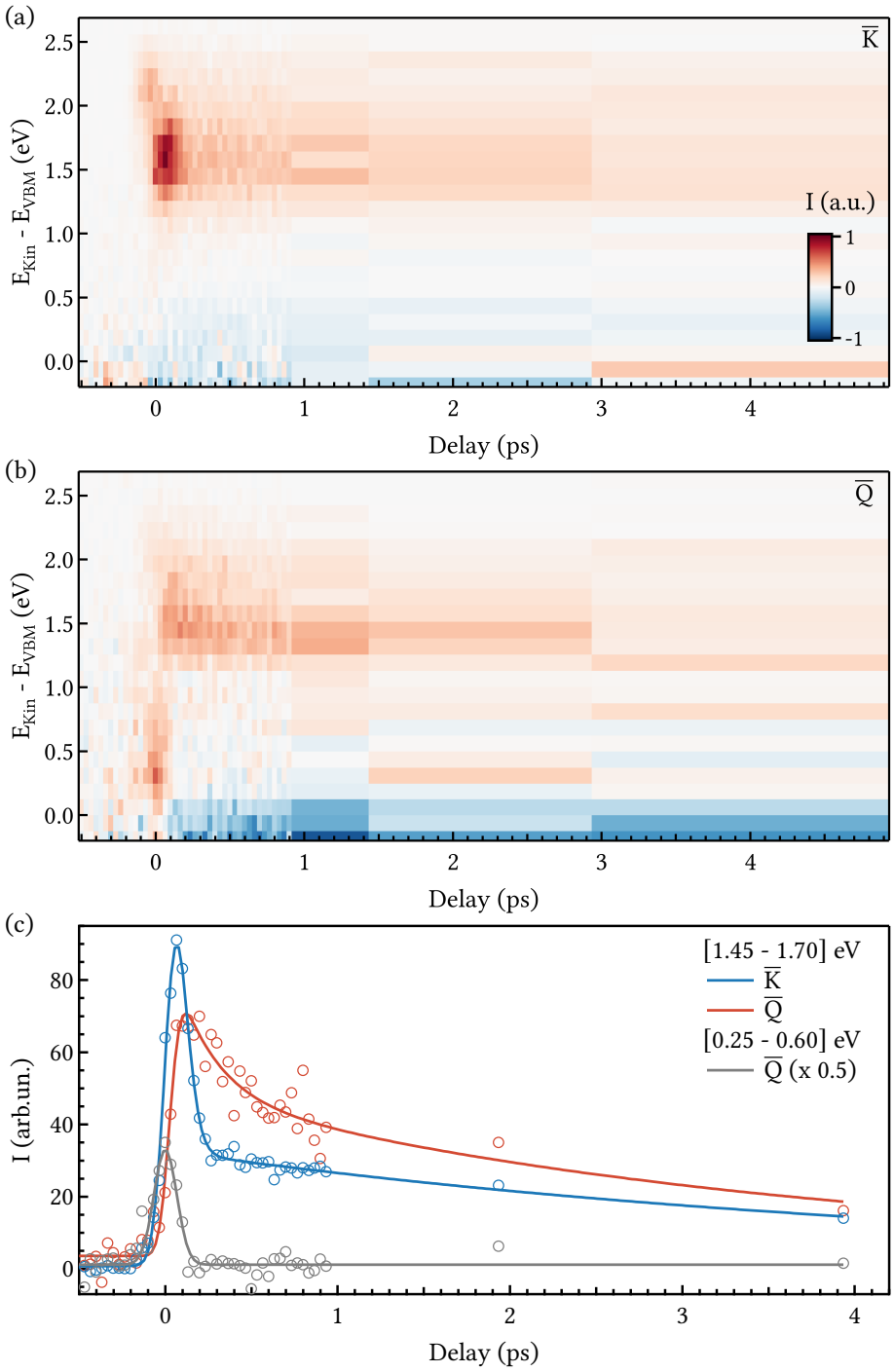


Figure 5.15: Transient ARPES signal. (a) and (b) show the transient response at $\overline{\mathrm{K}}$ and $\overline{\mathrm{Q}}$, respectively. Both exhibit a long-lived signal in the range 1.45 eV to 1.70 eV, together with short-lived features near temporal overlap. (c) Integrated intensity at the two high-symmetry points, fitted with Eq. (5.7). The 0.25 eV to 0.60 eV LAPE signal at $\overline{\mathrm{Q}}$ is fitted with a Gaussian plus linear background.

temporal overlap to experimental artifacts. At $\overline{\mathrm{Q}}$, the low-energy artifact is consistent with LAPE, since both pump and probe are *p*-polarized and have an electric-field component parallel to the photoelectron flight direction (see Sec. 2.3.2). The signal integrated over 0.25 eV to 0.60 eV (Fig. 5.15c) is well described by a Gaussian distribution, yielding (103 ± 7) fs (FWHM). This width is largely set by the pump–probe cross correlation and therefore provides the overall experimental time resolution. At $\overline{\mathrm{K}}$, an ultrafast feature appears near 2.0 eV to 2.4 eV. It is shifted by (-158 ± 25) fs relative to the main feature and by (-82 ± 16) fs relative to the LAPE signal, strongly suggesting a parasitic origin. Moreover, the momentum maps do not show a distinct pattern at the corresponding delay and energy, as would be expected, for example, for dispersive conduction-band electrons. One possible microscopic origin is excitation from mid-gap defect states [256], such as sulfur vacancies [257].

The angle-integrated intensity in the excitonic energy window 1.45 eV to 1.70 eV is shown in Figure 5.15c. Both traces are fitted with a bi-exponential decay multiplied by a Heaviside step function and convolved with a Gaussian time-resolution function. The fit model reads

$$I(t) = \int_{t_0}^{\infty} \left(A_1 \mathrm{e}^{-(\tau - t_0)/\tau_1} + A_2 \mathrm{e}^{-(\tau - t_0)/\tau_2} \right) \frac{1}{\sqrt{2\pi}\sigma} \exp\left(-\frac{(t-\tau)^2}{2\sigma^2} \right) \mathrm{d}\tau \qquad (5.7)$$

with decay constants τ_1 and τ_2, amplitudes A_1 and A_2, temporal overlap t_0, and Gaussian standard deviation σ. For $\overline{\mathrm{K}}$, we obtain (36 ± 12) fs and (4.7 ± 0.8) ps. For $\overline{\mathrm{Q}}$, the corresponding decay constants are (230 ± 129) fs and (3.54 ± 1.39) ps.

Interpretation of the K and Q dynamics

From the static spectrum in Section 5.2.1, it is not entirely clear whether the two layers are strongly coupled. If the layers are effectively decoupled, the transient signal could, in principle, arise from conduction-band occupation in either layer or from intralayer exciton formation. If the layers are coupled, the type-II band alignment can additionally enable interlayer charge transfer. Beyond pure intralayer excitons, hybrid excitons can form in which either the exciton-bound electron or hole is delocalized over both layers [33]. Despite being hosted by a multilayer structure, hybrid excitons can retain a purely in-plane dipole moment [247]. In the fully charge-separated limit, electron and hole reside in different layers, yielding an out-of-plane dipole moment characteristic of interlayer excitons (ILXs). Schmitt *et al.* [34] directly tracked the formation of such ILXs with a MM in MoS_2/WSe_2, where a stacking angle of 9.8° produces a mini-BZ and a distinct momentum-space footprint for the ILX.

A dominant population of unbound conduction-band carriers created by above-gap absorption is not expected here for two reasons. First, the pump photon energy lies below the electronic band gaps of both WSe_2 and WS_2. Although the gap is reduced by dielectric screening compared with a freestanding monolayer, reported values of 1.95 eV for WSe_2 on bilayer graphene [253] and ~2.2 eV for WS_2 on h-BN [199] should be comparable to our bilayer flake geometry. Second, the observed signal

at $\overline{\mathrm{K}}$ (Fig. 5.14d) is offset in energy from the VBM by roughly 1.7 eV, as expected for an excitonic sideband. The apparent dispersion is flat within the experimental energy resolution of 270 meV, which precludes definitive assignment of the band curvature. This flatness is consistent with (a) an exciton satellite that follows the valence-band dispersion with negative effective mass (see Sec. 2.3.1) as well as with (b) a continuum conduction-band response broadened beyond recognition. Based on the pump and the $\overline{\mathrm{K}}$ feature energy, we nevertheless favor an excitonic interpretation. Direct optical excitation of WS_2 excitons is unlikely because the lowest $\overline{\mathrm{K}}$ exciton in WS_2 has reported transition energies of 1.93 eV on h-BN [237] and 2.04 eV on *p*-doped Si [230].

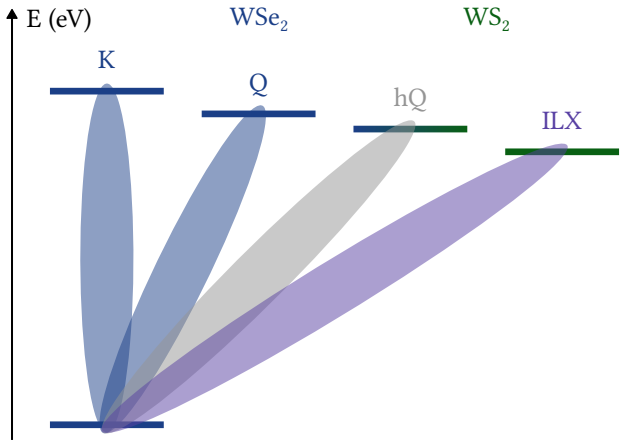


Figure 5.16: Possible exciton species in heterobilayer WS_2/WSe_2 after excitation of the K exciton in WSe_2. In WSe_2, the heterobilayer lowers the Q valley relative to K, thus shifting the CBM to $\overline{\mathrm{Q}}$. In addition, energetically favorable hybrid excitons with hybridized electron or hole wave function could form with a plethora of conduction- and valence-band valley combinations (here, electron hybridization at Q is shown). Finally, electron transfer allows formation of ILX.

We interpret the data as direct, resonant formation of bright WSe_2 K excitons at $\overline{\mathrm{K}}$. Subsequently, electrons scatter into the $\overline{\mathrm{Q}}$ conduction-band valley while remaining bound to holes at $\overline{\mathrm{K}}$, resulting in momentum-indirect excitons (compare Fig. 5.16). In the following, we refer to these as Q excitons. This cascaded formation has been reported previously [33, 113, 230] and is supported here by a delayed onset of the Q-valley signal by (76 ± 41) fs, estimated from the peak positions in Figure 5.15c. The delay is consistent with intervalley scattering times of a few tens of femtoseconds [33, 230]. The fast decay component of the K-valley trace reflects ultrafast scattering towards Q as well as the dephasing of a coherent optical polarization into an incoherent K-exciton population [33, 230]. The coherent polarization (see Sec. 2.3.1) forms under optical excitation as a quantum superposition of the ground and excitonic state. It has a well-defined phase and vanishing center-of-mass momentum $\mathbf{Q} = \mathbf{0}$ [103, ch. 18]. Within $\sim$ 100 fs, this polarization dephases via Coulomb and phonon scattering into an incoherent exciton population with $\mathbf{Q} \neq \mathbf{0}$ [105, 106].

The interpretation of the slow K-exciton decay component depends on the degree of interlayer coupling. If the layers are coupled, the picosecond component can arise from twist-angle-dependent interlayer charge transfer and from intervalley scattering between K and Q [258, 259]. These channels compete with (and can outpace) radiative recombination, which also contributes to the decay of the trARPES signal [33, 260, 261]. The observed picosecond decay is qualitatively consistent with trARPES studies on monolayer WSe_2, which report K-exciton lifetimes of $\sim$ 1 ps to 2 ps reflecting intervalley thermalization and recombination [33, 113]. Given the sensitivity of these dynamics to twist angle and temperature [262] and our limited measurement window of 4 ps, we do not attempt a quantitative comparison of the extracted decay constants to literature values.

Excitons at $\overline{\mathrm{Q}}$ in the heterobilayer can likewise be described by a bi-exponential decay. The signal could originate either from purely intralayer Q excitons or from hybrid hQ excitons, where the electron wave function at Q is delocalized over both layers [33]. To constrain the exciton species in our experiment, it is instructive to compare with the recent trARPES study by Bange *et al.* on monolayer WSe_2 and a WSe_2/MoS_2 heterobilayer, which quantitatively analyzes thermalization, phonon-mediated scattering, and recombination of bright, dark, hybrid, and interlayer excitons [33]. For both $\overline{\mathrm{K}}$ and $\overline{\mathrm{Q}}$, they report markedly different dynamics in the mono- and heterobilayer. In the monolayer, the bright K exciton shows, in addition to slow recombination, a clearly resolved fast depletion with a time constant of (70 ± 10) fs, attributed to exciton–phonon scattering into momentum-dark $\overline{\mathrm{Q}}$ excitons. The corresponding monolayer signal at $\overline{\mathrm{Q}}$ is well described by a single-exponential decay associated with Q-exciton relaxation. In the heterobilayer, by contrast, the bright K-exciton population is rapidly depleted to about 10 % of its initial value within the first 200 fs, reflecting efficient transfer into lower-lying dark and interlayer states. This behavior is explained by a modified conduction-band landscape: hybridization with the MoS_2 layer stabilizes the momentum-dark hybrid hQ excitons relative to the bright K excitons, rendering back-scattering from $\overline{\mathrm{Q}}$ to $\overline{\mathrm{K}}$ energetically unfavorable [33]. Consistently, the hQ excitons in the heterobilayer exhibit a bi-exponential decay, with a short decay time of (110 ± 40) fs attributed to exciton–phonon scattering into the ILX manifold and a slower component reflecting their intrinsic relaxation. In addition, the hQ excitons are found to be red-shifted by (0.13 ± 0.20) eV relative to the corresponding intralayer dark exciton, consistent with microscopic theory predicting an energy lowering and characteristic ARPES signatures of hybrid excitons in strongly tunnel-coupled van der Waals systems [33, 114].

Because our data do not include a monolayer WSe_2 reference region, we cannot determine the $\overline{\mathrm{Q}}$-exciton species from an energetic comparison (also given a potentially small absolute energy-calibration offset). Nevertheless, the transient behavior of our WS_2/WSe_2 sample resembles the hybrid-exciton scenario reported by Bange *et al.* [33]. The K-exciton population decreases rapidly to about 35 % within the first 200 fs, rather than showing only a weak early-time depletion. Moreover, the $\overline{\mathrm{Q}}$-valley dynamics are not well captured by a single-exponential decay, which has been reported to describe monolayer Q-exciton recombination [113, 143, 230]. For a WS_2/WSe_2 bilayer, the

conduction-band minimum is also reported to lie at Q [262]. With WSe_2 as the top layer, Sebait *et al.* observed a downshift of the WSe_2 Q valley (relative to the monolayer) of about 60 meV using scanning tunneling spectroscopy [263], which is of the same order as the difference between K and Q excitons of (200 ± 100) meV reported for WSe_2/MoS_2 by Bange *et al.* [33]. Taken together, the bi-exponential kinetics are consistent with the formation of hybrid excitons, which requires non-negligible tunneling/hybridization. We emphasize, however, that bi-exponential traces are not unique fingerprints: alternative multichannel relaxation pathways could, in principle, produce similar dynamics. A schematic comparison of the different exciton-species energies is presented in Figure 5.16. No relaxation or quantitative energy-level alignment scheme is provided, as these relaxation processes strongly depend on multiple factors, including the interlayer twist angle (see below).

Table 5.1: Bi-exponential decay times of K excitons in the WS_2/WSe_2 bilayer as a function of binding energy. Within the uncertainties, no systematic trend of the fast or slow component with binding energy is observed.

	K exciton	
$E_{Kin} - E_{VBM}$	τ_1	τ_2
1.83 eV	(43.1 ± 53.8) fs	(4.80 ± 2.41) ps
1.71 eV	(39.4 ± 16.1) fs	(5.12 ± 1.74) ps
1.58 eV	(38.7 ± 16.3) fs	(3.50 ± 0.91) ps
1.45 eV	(73.0 ± 20.8) fs	(6.89 ± 3.46) ps
1.32 eV	(71.2 ± 22.5) fs	(12.47 ± 10.40) ps

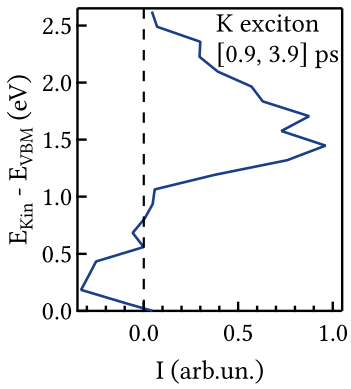


Figure 5.17: Angle-integrated ARPES signal of the K exciton for 0.9 ps to 3.9 ps.

When integrating the trARPES intensity of the K exciton over all in-plane momenta, the resulting EDC is often reported to have an approximately Gaussian line shape [33, 230, 237]. For delays > 0.9 ps, however, the EDC displayed in Figure 5.17 is clearly asymmetric. We attribute this to two effects. First, theory predicts that excitonic photoemission line shapes can be intrinsically asymmetric, because the photocurrent is proportional to the exciton wave function in energy space [264] (see Sec. 2.3.1). Second, the pump bandwidth of 119 meV (FWHM) significantly exceeds the intrinsic exciton linewidth (~40 meV at room temperature [265]), leading to simultaneous excitation of resonant 1s excitons and higher Rydberg states. While exciton formation and cascade relaxation occur on sub-100 fs timescales [105], the initially broad excitation creates a hot exciton population with excess kinetic energy. The subsequent thermalization proceeds on picosecond timescales [106, 266], so that the momentum distribution may not yet be fully equilibrated to a thermal (Boltzmann-like) distribution in Figure 5.17. In contrast to the conduction-band relaxation discussed

in Chapter 5.1.2, the K exciton does not show a systematic change with binding energy (compare Table 5.1 and temporal resolution of ≈ 100 fs from LAPE), further supporting an excitonic origin of the observed signal.

Absence of an Observable ILX Signature

In contrast to many TMD heterostructures with type-II band alignment, we do not observe an additional feature that would indicate interlayer exciton formation. In related TMD heterostructures, ILXs have been observed to form on sub-ps timescales [259, 267], often fed by intralayer or hybrid excitons [33, 249, 268] (compare Fig. 5.16). Similar pathways have been suggested by optical studies in WS_2/WSe_2 [268], where the ILX is reported at an optical transition energy of 1.3 eV to 1.5 eV for a range of twist angles and sample conditions [262, 269, 270]. With the ARPES spectra referenced to the WSe_2 VBM, ILX signatures would therefore also be expected at 1.3 eV to 1.5 eV (compare Sec. 2.3.1). However, we neither observe a transient signal in that window nor a corresponding fingerprint in the momentum maps. Several factors may account for the absence of an observable ILX signal:

- Because the WS_2 CBM lies below the WSe_2 CBM, ILX formation requires electron charge transfer from WSe_2 to WS_2. In our sample configuration, WS_2 is buried below the vacuum-exposed WSe_2, so the ILX signal may be strongly suppressed by the surface sensitivity of ARPES. Consistently, the static spectra do not show discernible WS_2 valence-band intensity at $\overline{\mathrm{K}}$ (compare Fig. 5.11), whereas reports that image the ILX have been able to detect signatures of the buried layer [34, 35]. In contrast, the hybrid hQ exciton is not limited to emission from the buried layer because it has contributions from the vacuum-exposed WSe_2.
- In WS_2/WSe_2, the ILX ground state can be a momentum-indirect K–Q exciton with the electron at Q_{WS_2} and the hole at K_{WSe_2}, depending on the twist angle [262, 269]. For such momentum-indirect excitons, the trARPES signal is expected to be weaker and broader than for coherent K excitons [107, 113]: the electron can occupy any of the six equivalent Q valleys, partitioning the photoemission signal, while the thermal center-of-mass momentum distribution further broadens the spectral feature. Photoemission intensity scales with the squared modulus of the exciton wave function in reciprocal space, $|\phi(\mathbf{k})|^2$ [104]. While this dilution reduces visibility, it does not by itself explain a complete absence of the ILX feature, especially when integrating the signal over all $\overline{\mathrm{Q}}$ points of the first BZ.
- In trARPES, the exciton photocurrent depends on the overlap of the exciton wave function and the photoemission final state (i.e. the photoemission matrix element), which is sensitive to layer localization, orbital character, spatial extent, and the probe photon energy and polarization [32, 68, 114]. The XUV probe may therefore have a much smaller effective matrix element for the ILX

than for intralayer or hybrid excitons, which would strongly suppress its signal in our experiment.

- Under our specific excitation conditions (pump fluence) and sample conditions (doping, twist-angle disorder), the ILX population may be small, and its spectral weight may remain below our detection limit. For example, defect-mediated trapping can occur on picosecond timescales [271], comparable to typical ILX formation times. Such trapping, combined with disorder- or substrate-induced loss channels [272, 273], may quench the ILX population before it becomes observable.
- If the interface is contaminated or twisted such that interlayer coupling is strongly reduced, ILX formation may be suppressed. In that scenario, the observed hQ feature could arise from residual band-alignment effects without true interlayer hybridization, and K–K ILX pathways would be strongly quenched.

In summary, we interpret the transient dynamics at $\overline{\mathrm{K}}$ and $\overline{\mathrm{Q}}$ as the formation of bright K excitons upon resonant photoexcitation, followed by intervalley scattering into $\overline{\mathrm{Q}}$ and a transient response consistent with hybrid hQ exciton formation. No clear signature of an interlayer exciton is observed, which may reflect weak population, unfavorable matrix elements, and/or suppression due to the sample geometry and interface cleanliness.

5.3 Defect-Driven Phenomena in CrSBr

This section addresses how native defects and related electrostatic effects shape the electronic response of CrSBr in static and time-resolved photoemission. In the first part, we identify the microscopic origin of unintentional *n*-type doping in bulk CrSBr. In collaboration with T. Biktagirov and W. G. Schmidt[3], we investigated unintentional *n*-type doping in CrSBr caused by intrinsic defects. Combining ARPES with DFT-based defect calculations, we identify chromium interstitials, bromine-on-sulfur antisites, and bromine vacancies as the most likely intrinsic donor defects. The corresponding study is published in Ref. [274]:

> T. Biktagirov, W. G. Schmidt, K. J. Schiller, M. Capra, J. E. Nitschke, L. Sternemann, M. S. Arndt, G. Zamborlini, A. Isaeva, and M. Cinchetti, "Intrinsic defects as a source of n-type conductivity in CrSBr", *npj 2D Materials and Applications* **9**, 106 (2025)

In the second part, we demonstrate how such near-surface electrostatics can dominate trARPES observables under sub-bandgap excitation and obscure exciton-related signatures. Motivated by the excitonic response of CrSBr, we performed trARPES on thin bulk crystals below the Néel temperature. Rather than revealing a clear exciton fingerprint, the transient spectra are dominated by electrostatic field effects, which may be facilitated by doping-induced band bending and/or defect-related surface states. The measurements therefore serve as a practical example of parasitic, field-driven phenomena in trARPES on semiconductors. In particular, the data show a substantial transient response already at negative pump–probe delays, highlighting that the detected photoelectron energies and intensities can be modified by transient electric fields in the interaction region and are not solely determined at the instant of emission from the surface.

5.3.1 Doping Through Intrinsic Defects

In pristine semiconductors, intrinsic defects are typically the prime source of electrons and holes that contribute to electrical conductivity. Previous studies on CrSBr reported intrinsic defects in studied crystals, where bromine vacancies are observed to be most frequent [275, 276] and likely responsible for observed *n*-type doping in as-grown crystals [277]. Torres *et al.* [225] observed a pronounced stability difference between monolayer and multilayer ($\geq$ 2 layer) samples and suggested hydrolysis—with water displacing bromine—as a possible mechanism. However, scanning tunneling microscopy (STM) [275] and scanning transmission electron microscopy (STEM) [276] measurements found additional defect types at the surface, but the STM study did not provide a microscopic assignment, and the STEM measurements were not sensitive to sulfur-related defects.

[3] Dr. Timur Biktagirov, Prof. Dr. Wolf Gero Schmidt, Department of Physics, Paderborn University, Warburger Str. 100, Paderborn, Germany.

Apart from conductivity, Klein *et al.* [275] found optically active defects that probe the local magnetic environment. In addition, Telford *et al.* [277] proposed strong coupling between charge transport and magnetic defects. They also observed a magnetic anomaly in magnetotransport data at 40 K, well below the Néel temperature, which they suggest may arise from FM polarization of magnetic defects.

Our study of intrinsic defects in bulk CrSBr was motivated by the observation of spectral weight above the VBM in the ARPES band structure of pristine bulk crystals at room temperature, which is presented first. These observations are then complemented by microscopic density functional theory (DFT) modeling focusing on intrinsic point defects and their doping behavior. Finally, our interpretation is substantiated by additional XPS measurements.

ARPES Findings

Commercial bulk CrSBr crystals (HQ Graphene) were glued with silver epoxy (EPO-TEK H21D) onto copper sample plates to ensure electrical grounding and cleaved in situ in the load lock of the UHV system at a pressure < 3×10^{-7} mbar. Photoemission data were acquired with the KREIOS analyzer and He Iα radiation from the UV-discharge lamp. We used the 0.5 mm × 1.0 mm entrance slit and 50 eV pass energy, giving an IRF of 92 meV (see Sec. 2.4.2).

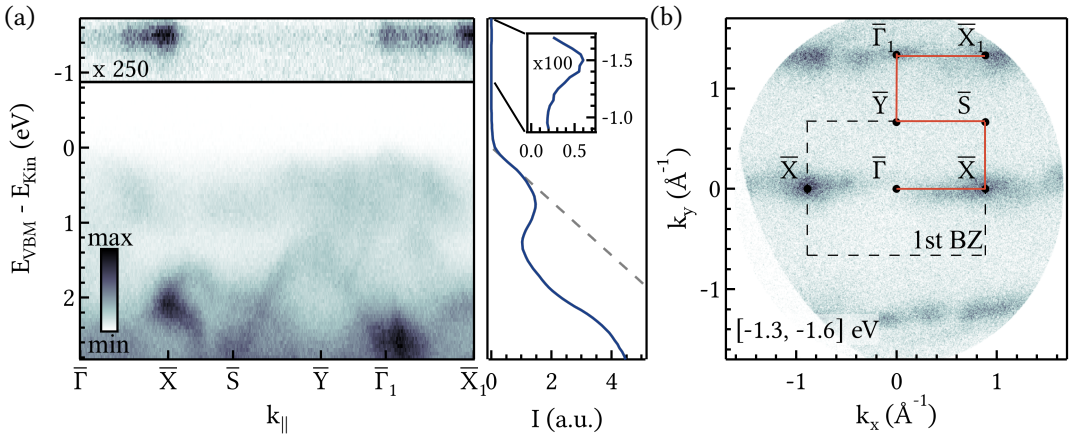


Figure 5.18: Experimental band structure of bulk CrSBr at room temperature. (a) ARPES band structure along high symmetry points of the surface BZ. Data above −0.85 eV have x25 acquisition time and x10 contrast increase. The EDC on the right highlights spectral intensity above the VBM, which in turn is determined by linear extrapolation (dotted gray line). (b) Momentum map of the integrated energy range −1.6 eV to −1.3 eV, exhibiting highly localized intensity patterns along $\bar{\Gamma}$–$\bar{X}$. Overlaid are high symmetry points, the 1st BZ boundary (dotted line), and the path of the band-structure cut (solid line). Published in Ref. [274].

The acquired band structure of bulk CrSBr is shown in Figure 5.18a along the high-symmetry points of the first and neighboring surface BZs. Next to the band-structure

plot, the angle-integrated EDC was fitted with a linear function to determine the VBM energy. Even though the bulk crystals were cleaved in situ, the EDC exhibits a small intensity peak above the valence band at binding energy (-1.48 ± 0.09) eV (determined by Gaussian fitting). This unexpected feature is comparatively weak, which is why the band-structure data above -0.85 eV were acquired with x25 acquisition time in addition to a contrast increase. Throughout this section, energies are reported relative to the VBM using

$$E_{\mathrm{B}} \equiv E_{\mathrm{VBM}} - E_{\mathrm{Kin}}, \tag{5.8}$$

so that $E_{\mathrm{B}} < 0$ corresponds to higher kinetic energies, i.e. to states "above the VBM" in Figure 5.18.

The additional spectral weight above the valence band exhibits non-uniform dispersion across the BZ. Figure 5.18b shows the momentum map of this feature obtained by integrating the photoemission signal from -1.6 eV to -1.3 eV. Comparing the spectral intensity to the BZ outline drawn on top, we find a highly anisotropic intensity distribution centered at $\overline{\mathrm{X}}$. However, neighboring BZs also display intensity at $\overline{\Gamma}$, resulting in a more stripe-like pattern. Missing intensity for the top valence band was also observed on WS_2 in Section 5.1 and on CrSBr by Bianchi *et al.* [172], who attributed this effect to PME variations.

We attribute the additional spectral weight to the conduction band of CrSBr. An alternative interpretation would be photoemission from defect-related mid-gap states at the surface, which would be consistent with the range of possible surface defects reported by Weile *et al.* [276], with bromine defects (V_{Br}) being the most abundant [275]. However, Weile *et al.* calculated a rather uniform and flat dispersion for these defect states, which is in stark contrast to the momentum map observed here. The conduction-band dispersion was mapped in ARPES before by Bianchi *et al.* [278] using substrate-induced charge transfer in exfoliated thin flakes and shows excellent qualitative agreement with our measurements in Figure 5.18. While the band gap is commonly assumed to be direct, Bianchi *et al.* reported an indirect band gap with the CBM located at $\overline{\mathrm{X}}$. The same observation was made by Smolenski *et al.* [279] following potassium dosing of bulk CrSBr. We therefore compared the intensity onset at different visible $\overline{\Gamma}$ and $\overline{\mathrm{X}}$ points and did not find consistent evidence for an indirect band gap in our data.

Accurate assessment of the band-gap magnitude in 2D vdW systems is inherently difficult due to sample-to-sample variations in screening and renormalization effects [167] (compare Sec. 4.4), which helps explain why the band gap of CrSBr remains a topic of debate. These variations are likely influenced by varying defect concentrations from material synthesis, contributing to variations in doping and experimental charging and therefore the experimentally determined band gap [167]. Scanning tunneling spectroscopy and micro-reflectance microscopy reported a gap of approximately 1.5 eV, whereas earlier ARPES studies suggested larger values. A lower boundary can be set by the separation between the VBM and the Fermi level position on metallic substrates, as the latter is pinned to the detector (compare Sec. 2.3.3). Here, reported VBM positions are 1.6 eV-1.8 eV [176], 1.5 eV [172], and 1.84 eV [279] below

the Fermi level. Doped crystals may also be subject to band bending at the surface (see Sec. 2.3.3), further contributing to variations in reported VBM positions and to the appearance of conduction-band signal in ARPES spectra.

In contrast to previous ARPES studies that observed the conduction band via charge transfer from alkali dosing or a metallic substrate, our crystals support an intrinsic origin of conduction band filling: we employed millimeter-thick crystals, ruling out substrate effects. This motivates a microscopic study of the defect landscape and doping pathways in CrSBr.

DFT Modeling of Native Point Defects

The theoretical modeling of native point defects in bulk CrSBr within the framework of DFT was performed by T. Biktagirov and W. G. Schmidt and is summarized here in abbreviated form (see Ref. [274] for details). First, the thermodynamic stability region of CrSBr is determined. Next, selected points within that region are used to calculate defect formation energies. Finally, the charge transition levels of intrinsic point defects are evaluated to identify shallow donor defects that likely contribute to *n*-type doping. We only included point defects expected to be the most important:

- Three vacancies (V_{Cr}, V_S, and V_{Br}): Vacant lattice sites that are occupied in perfect crystals.
- Three interstitials (Cr_i, S_i, and Br_i): Occupied sites in the crystal structure that are vacant in perfect crystals.
- Two antisites (S_{Br} and Br_S): Occupation of lattice sites with a different atomic species compared to perfect crystals.

Formation of defects is related to the atomic chemical potentials of Cr, S, and Br (μ_{Cr}, μ_S, and μ_{Br}), which determine the formation energy of CrSBr. The region of stable CrSBr formation is confined by competing phases, which are Cr_2S_3, Cr_3S_4, and $CrBr_2$ in this case. These boundaries are displayed in Figure 5.19a and allow the assignment of three set points marking the synthesis boundary. Point **A** denotes Cr-rich conditions, point **B** denotes S-rich conditions, and point **C** denotes S- and Br-rich conditions. At these points and at the midpoint **M**, defect formation energies were calculated in a $4 \times 3 \times 2$ supercell representing two CrSBr layers (see Fig. 5.19b). The neutral defect-formation energies were obtained from the total-energy difference between defective and pristine supercells, corrected for atoms added/removed via their chemical potentials. For charged defects, the full expression additionally contains a Fermi-level-dependent term (and finite-size/alignment corrections), which we include below when discussing charge transition levels.

Among all four synthesis points, chromium interstitials Cr_i have favorable formation energies, especially under Cr-rich conditions. In addition, bromine vacancies V_{Br} have the lowest formation energy in S-rich synthesis, and bromine-on-sulfur antisites Br_S are the most favorable defect type under S-rich and Br-rich conditions. These

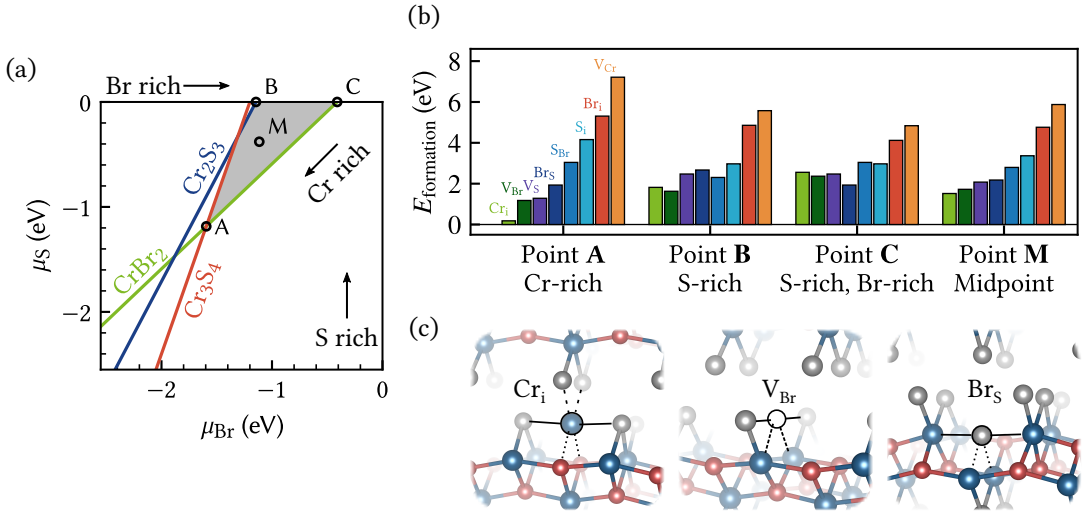


Figure 5.19: DFT-calculated formation of native point defects in CrSBr. (a) Thermodynamic stability region of bulk CrSBr (shaded region) as a function of the individual elements' chemical potentials. (b) Individual point-defect formation energies at different points of the stability region. (c) Atomic structure of the three most favorable point defects. Published in Ref. [274].

findings are consistent with previous experimental reports of high V_{Br} concentrations [225, 275]. A schematic representation of these three point defects is shown in Figure 5.19c.

Having identified the most probable defect species, we now investigate their contribution to *n*-type doping of bulk CrSBr. As the previously used PBE + U functional underestimates the band gap to 0.62 eV, further calculations adopted the meta-GGA SCAN functional. This choice is corroborated by comparison of experimentally retrieved and calculated band structure; the latter is shown in Fig. 4.7 of Sec. 4.5. The calculated band structure is overlaid on the experimental data in Figure 5.20a, showing good qualitative agreement. To mitigate intensity gradients from the incidence direction and angle of the XUV photons, the experimental band structure was symmetrized. This symmetrization involves averaging the $I(k_x, k_y, E)$ data stack with inverted and rotated copies. For CrSBr with D_{2h} symmetry, this includes a 180° rotation and mirror reflections across the k_x and k_y plane. An exemplary momentum map at 2.35 eV in Figure 5.20b and c demonstrates removal of a horizontal intensity gradient and a general SNR improvement without introducing major artifacts.

Within the adopted DFT functional, the defect formation energies of all investigated point defects were calculated as a function of Fermi energy. This includes calculation of the charge transition level, which is the Fermi energy at which two charged states of the same defect have the same formation energy. Favorable *n*-type dopants exhibit (a) stable positive charge states across major parts of the band gap and (b) low formation energies at Fermi levels close to the CBM. Calculations were performed at the midpoint (**M**) and under Cr-poor conditions (point **C**) and highlighted Cr_i as a

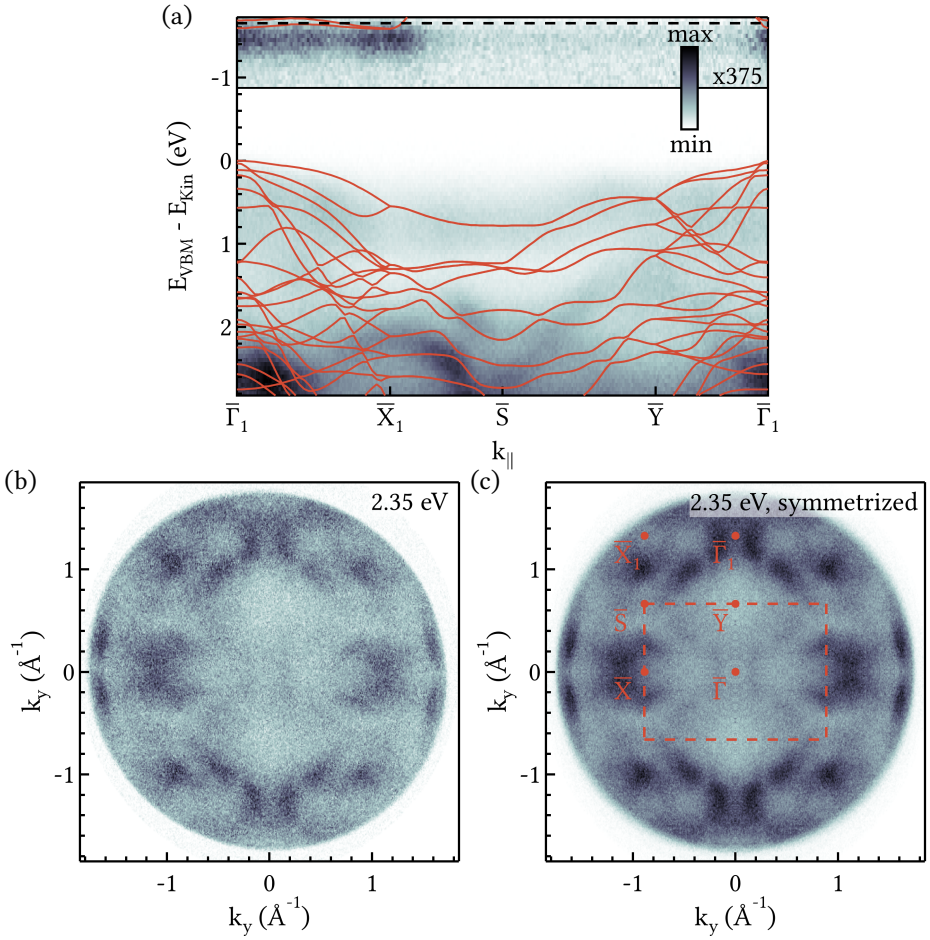


Figure 5.20: Comparison of calculated and experimental band structure of CrSBr. (a) ARPES band structure, symmetrized to negate intensity gradients from the probe incidence direction. Above −0.9 eV, acquisition time is increased x25 and contrast is increased x15. The dotted line indicates E_F. Overlaid is the calculated band structure from DFT within the meta-GGA SCAN functional. The calculation visually agrees with experimental data, including the conduction band dispersion. (b, c) Momentum map at 2.35 eV before and after symmetrization. Published in Ref. [274].

potent shallow donor next to Br_S. V_{Br} was identified as a deep donor, making Cr_i and Br_S the most likely candidates for unintentional *n*-type doping.

XPS Characterization

To corroborate the results from DFT modeling, we characterized bulk CrSBr using XPS in normal-emission mode, which decreases surface sensitivity compared to grazing incidence. The XPS spectra were acquired with the setup described in Section 2.4.1. Analogous to the ARPES measurements, bulk CrSBr was cleaved in the load lock at $< 5 \times 10^{-8}$ mbar, and measurements were performed at room temperature. The resulting spectra were analyzed using the XPST package for Igor Pro [80], which

uses a Gauss–Lorentzian sum function to approximate a Voigt profile. Inelastic scattering was corrected using a standard Shirley background.

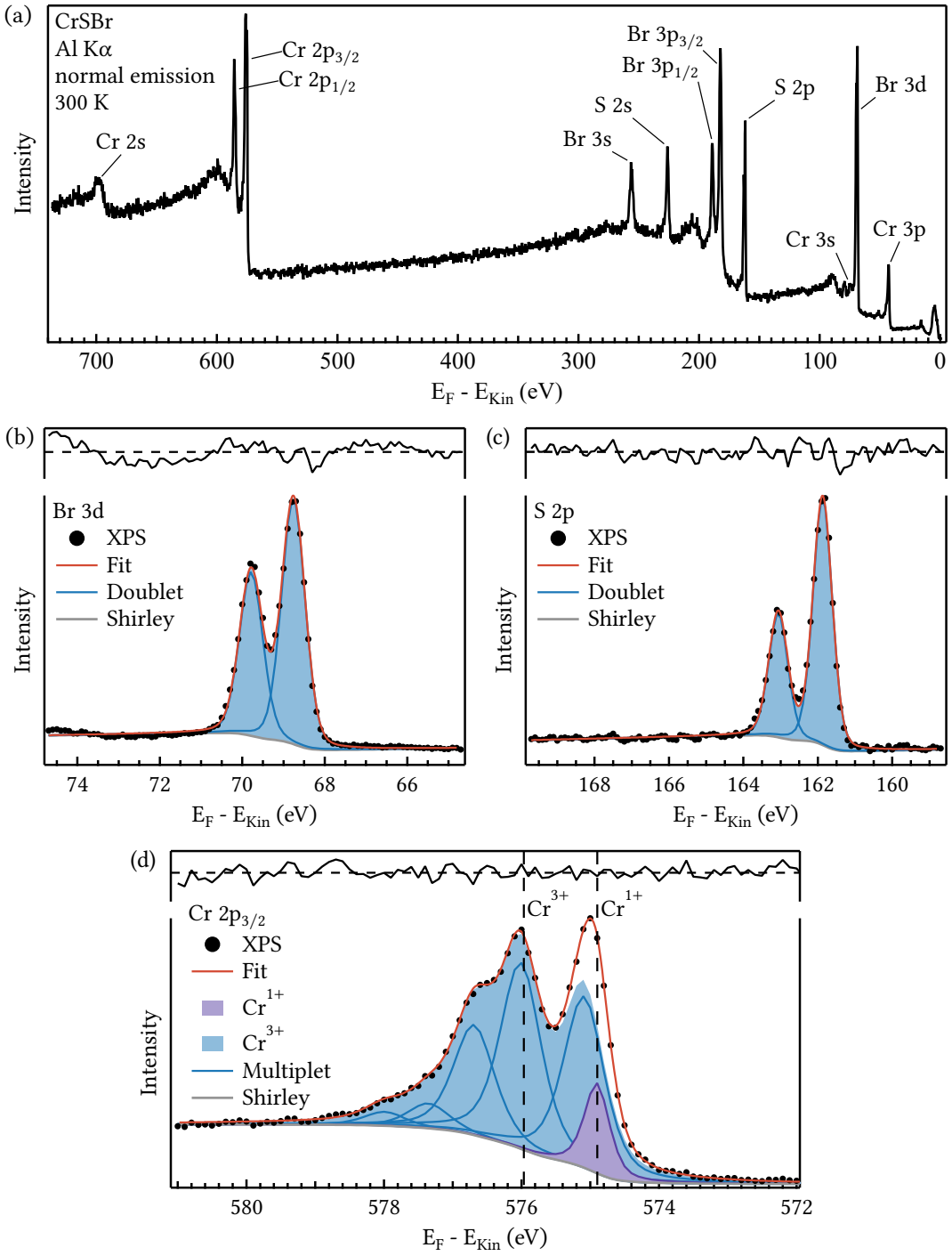


Figure 5.21: XPS characterization of bulk CrSBr. (a) Survey spectrum showing only expected contributions from Cr, S, and Br core levels. (b, c) Br 3*d* and S 2*p* core levels with fitted spin–orbit doublet, respectively. The solid black line indicates the fit residual. (d) Cr $2p_{3/2}$ core level, exhibiting multiplet splitting and an additional component for the Cr_i. Published in Ref. [274].

Figure 5.21 shows the acquired spectra and fitting. The survey spectrum (Fig. 5.21a) only exhibits expected features from Cr, S, and Br ions, without additional spectral weight from common contaminants such as carbon or oxygen. The Br and S resonances also do not exhibit additional features attributable to defect states (see Figs. 5.21b and c), which is confirmed by standard doublet fitting of the Br $3d$ and S $2p$ resonances that reflects the expected spin–orbit splitting (see Sec. 2.2.2). Detailed best-fit parameters are listed in Appendix A.

The Cr contribution is analyzed using the Cr $2p_{3/2}$ peak shown in Figure 5.21d. Here, the spectrum exhibits a multiplet structure that arises from exchange coupling of the open $3d$-shell electrons with the remaining $2p$ core electron after photoemission (compare Sec. 2.2.2). Previous studies on CrSBr either lacked energy resolution [280, 281] or neglected this effect [282], potentially leading to misassignment of the Cr binding energy [73, 78]. Other XPS studies including the multiplet structure reported a splitting into 5 observable peaks [73, 74], which we also employ for the regular Cr^{3+} component. To account for possible Cr_i interstitials, we further include an additional pseudo-Voigt component in the fit. Detailed best-fit parameters are summarized in Appendix A and yield a spectral weight of 90.1 % Cr^{3+} and 9.9 % Cr_i by comparing the fitted peak area. The binding energy of Cr^{3+} is determined by an area-weighted mean of the individual multiplet components, yielding (575.97 ± 0.04) eV. With the Cr_i peak centered at (574.90 ± 0.04) eV, both components are separated by (1.07 ± 0.08) eV.

T. Biktagirov and W. G. Schmidt computed the binding energy of the Cr $2p_{3/2}$ core level for both pristine and defect-containing supercells using DFT. Their calculation yields 577.1 eV binding energy for the Cr^{3+} in bulk CrSBr and 576.1 eV for the Cr_i in the +1 charge state, giving an energy separation of about 1 eV. Other relevant interstitial charge states ${Cr_i}^{2+}$ and ${Cr_i}^{3+}$ have calculated binding energies of 576.31 eV and 576.32 eV, respectively, giving an energy shift of about 0.8 eV to the bulk value. Other energetically favorable defects (${V_{Br}}^{0}$ and ${Br_S}^{0}$) yield an energy shift of the nearest-neighbor Cr resonance of 0.2 eV to 0.3 eV.

The calculated Cr $2p_{3/2}$ resonances differ slightly from experimental findings in absolute value. However, the experimentally found energy separation of approximately 1 eV matches the theoretical prediction of Cr^{1+} interstitials well, which suggests the existence of Cr interstitials in as-grown CrSBr crystals. Given the complex multiplet structure of the Cr $2p_{3/2}$ resonance, XPS cannot unambiguously determine the defect species by itself, and careful interpretation requires theoretical modeling or complementary experimental characterization.

5.3.2 Field Effects at Sub-Bandgap Excitation

This section presents trARPES measurements on bulk CrSBr, optimized for resonant excitation of the $1s$ exciton at ~ 1.36 eV [44]. In practice, the transient response was dominated by field-driven effects that mask any exciton-related feature, as discussed below. Owing to the selected energy and time window for acquisition, the physical origin of the field effect cannot be identified unambiguously.

Measurement Configuration

Resonant excitation of the A exciton requires fine-tuning of the pump photon energy. For this reason, we used the SIG2 output of the integrated OPA described in Section 3.4. Unfortunately, the OPA does not support the required 1.36 eV, which corresponds to 912 nm. We therefore focused the SIG2 0.68 eV output into an additional BBO crystal (1 mm thick, $\theta = 20.2°$) to generate the second harmonic. The resulting spectrum is shown in Figure 5.22a and has a spectral width of 80.3 meV at −15 dB. The pulse duration was determined from a second-harmonic autocorrelation (see Fig. 5.22b) by Gaussian fitting and deconvolution, yielding 154 fs FWHM. This is the dominant limitation of the temporal resolution, as the probe pulse duration is < 50 fs. Multiple nonlinear conversion stages in the OPA, followed by successive frequency doubling, amplify existing spatial inhomogeneities in the beam profile and can readily produce diffraction patterns in the far field. Consequently, the mode profile (shown in Fig. 5.22c) exhibits a distorted shape and diffraction artifacts next to the main intensity maximum. Two orthogonal projections yield a spot size of 957 µm × 437 µm.

Bulk CrSBr was exfoliated onto a template-stripped gold surface (process described in Section 4.2). The gold film (270 nm thick) was evaporated onto a Si wafer with native SiO_2. A commercial CrSBr crystal (HQ Graphene) was pressed onto the gold surface in a nitrogen glovebox, and the sample was cleaved in the load lock of the KREIOS beamline at 3×10^{-8} mbar. An optical image acquired after the photoemission experiments (see Fig. 5.22d) shows multiple regions of different thickness, visible via distinct color shading. Thin films exhibit interference effects, giving a color that is qualitatively indicative of the layer thickness [176, 283]. With increasing thickness, the appearance gradually approaches the metallic look of the bulk crystal, which is also visible in the top left corner of Figure 5.22d. The probed region in photoemission is shown in the PEEM image in Figure 5.22e, where the work-function contrast between gold and CrSBr enables unambiguous identification of the flake. For the subsequent ARPES measurements, a field aperture (black circle in the PEEM image) was used to isolate the flake signal. Atomic force microscopy across the flake edge indicates a thickness of approximately 30 nm.

Table 5.2: Pump power and fluence.

P (mW)	F (µJ/cm^2)
160	81.2
110	55.8
70	35.5
26	13.2

Exfoliation on template-stripped gold yielded a flake thickness that allows cooling with minimal sample charging. All experiments were performed at 80 K using liquid-nitrogen cooling. By comparing room-temperature and cryogenic static spectra, we observed a shift of approximately 100 meV, which is corrected by adapting the VBM reference position. Data acquisition below the Néel temperature of 132 K [220] yields a sharper exciton resonance [41] and an intrinsically sharper band structure [176] compared to room temperature. We used p-polarized XUV pulses at 300 kHz repetition rate, with a 0.5 mm × 1.0 mm entrance slit and a pass energy of 50 eV. The pump

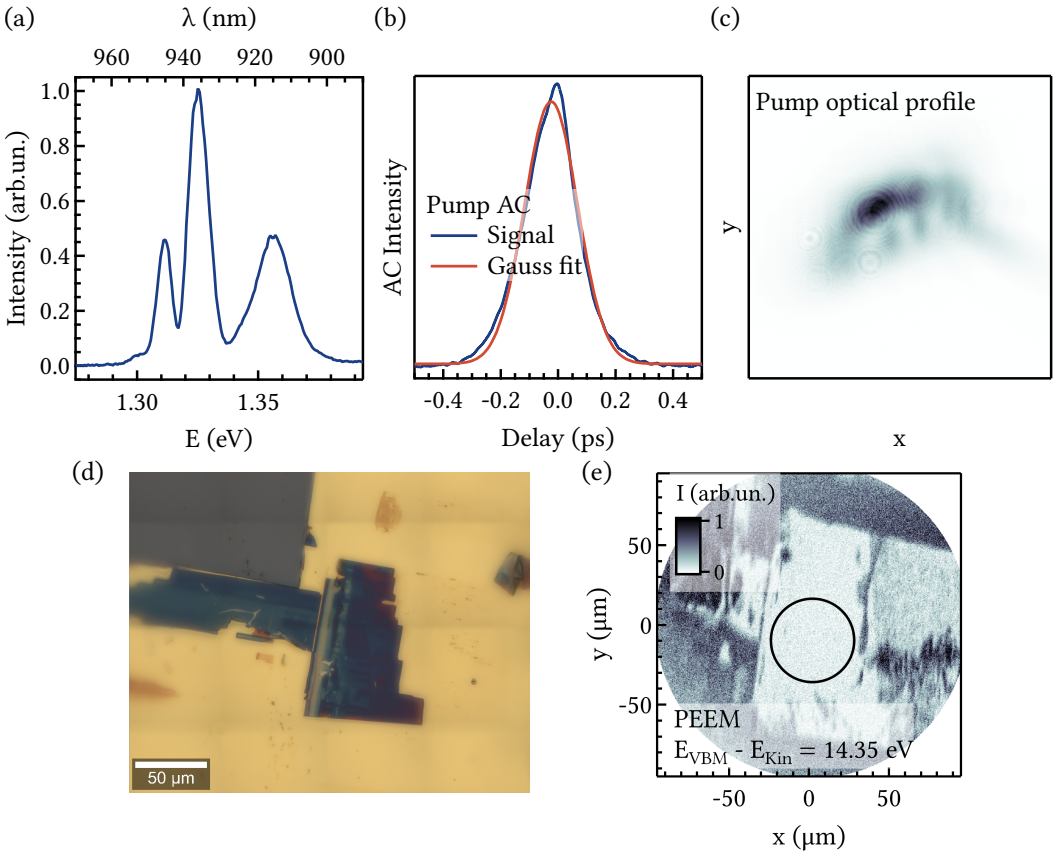


Figure 5.22: Characterization of the optical pump pulse and the exfoliated sample. (a) Spectrum of the pump pulse tuned to the CrSBr exciton resonance at 1.3 eV to 1.4 eV. (b) Pump autocorrelation with Gaussian fitting, yielding a pulse duration of 154 fs. (c) Optical beam profile. (d) Optical image of the exfoliated bulk CrSBr on gold. Different-sized flakes appear as different color shadings. (e) PEEM image of the studied flake area, with a circle marking the field aperture.

pulses were *p*-polarized and aligned parallel to the crystallographic *a*-axis of CrSBr. Four different average pump powers correspond to the fluences listed in Table 5.2, calculated assuming an elliptical beam profile. Related trARPES studies targeting excitonic resonances report comparable fluences up to 100 µJ/cm^2 [19, 230, 284].

Experimental Observations

A static spectrum was acquired using the monochromatic He Iα radiation of the helium lamp and exhibits a comparable spectral quality to the data in Section 5.3.1 (compare Fig. 5.23a). Three colored lines mark the energies at which the angle-integrated transient traces in Figure 5.23b are evaluated.

The temporal traces show an unexpected behavior. First, the transient intensity modulation is largest at the lowest extracted energy, $E_B = -0.5$ eV. Second, the signal extends to negative delay times over an unusually long interval: at the highest

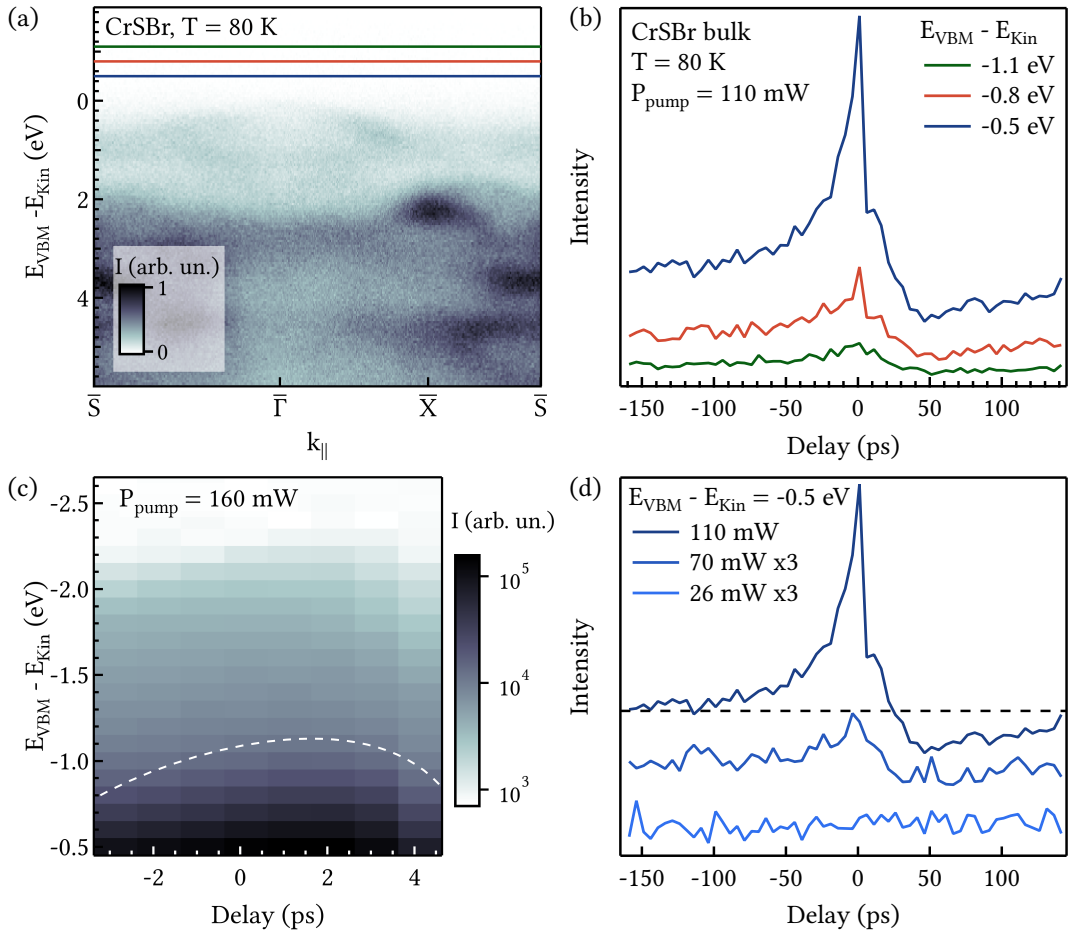


Figure 5.23: Transient ARPES signal on bulk CrSBr. (a) Static band structure with colored lines highlighting the energy positions of the traces in (b), which display a strong asymmetric signal over tens of ps. (c) Binding energy versus delay map around temporal overlap. The white dotted line is drawn by hand and serves as guide to the eye. (d) Transient intensity as a function of pump fluence, with the dotted line drawn by hand.

fluence, the traces deviate from their far-delay baseline already up to ~ 100 ps before temporal overlap, rather than showing a sharp onset only near t_0. Third, at the highest fluence, the signal displays a pronounced minimum around 50 ps, followed by a slow recovery towards larger positive delays.

An angle-integrated close-up around temporal overlap is shown in Figure 5.23c as a binding-energy–delay map (logarithmic color scale), covering states up to 2.4 eV above the VBM. In this window, only the exponential tail of the valence band is visible, without additional features that would show the sharp rise time and subsequent decay expected for a resonantly driven excitonic signature (compare, e.g., Sec. 5.2.2). Instead, the exponential tail appears to shift as a function of delay time (dashed line as guide to the eye). Importantly, this “moving tail” interpretation is qualitative: within the present dataset, a rigid energy shift cannot be cleanly separated from changes in broadening and/or lineshape intensity, because we neither track a sharp dispersive

band edge nor the work-function cutoff. The fixed-energy traces in Figure 5.23b are therefore treated as being *consistent with* a delay-dependent spectral displacement, but they do not constitute standalone proof of a rigid shift.

The dynamic response scales strongly with pump fluence, as shown in Figure 5.23d, and vanishes at an optical pump power of 26 mW. Unlike the data in the preceding chapters, the traces shown here are not presented as difference spectra relative to an equilibrium reference at negative delays.

Discussion

The experiment was tuned for resonant exciton excitation in CrSBr. However, the data do not show a transient feature with a characteristic excitonic fingerprint, and neither do the momentum maps reveal a clear emergence of new population features at or after temporal overlap. Dedicated measurements at $13.2\,\mu J/cm^2$ fluence did not exhibit an observable SPV effect or pump-induced space charge (not shown), but they also did not reveal a resolvable exciton resonance. Compared to other studies on two-dimensional systems [19, 230, 284], this fluence is low and may not yield a detectable response within our integration time. In addition, the static ARPES data in Section 5.3.1 indicate a faint occupation of the conduction band at the surface, which could also inhibit exciton formation by screening.

Because the KREIOS MM scans every kinetic energy sequentially, the transient acquisition was limited to $E_B = -0.5\,eV$. This restriction reduces the available observables: a quantitative energy-shift determination would ideally track a well-defined band position and/or the work-function cutoff. Since neither is accessible here, the discussion remains qualitative and focuses on mechanisms compatible with (a) the strong fluence dependence, (b) the apparent displacement/redistribution of the near-gap tail, and (c) the pronounced negative-delay response.

For optical pulse durations on the order of 100 fs, only a few processes can produce a substantial signal at negative delays. One possibility is the creation of long-lived states whose lifetime exceeds the temporal separation between two pump pulses. Such a scenario would more likely appear as a quasi-static offset [285] (or slowly varying background), rather than the distinct rise towards t_0 observed between -50 ps and 0 ps in Figure 5.23. A second, and generally more relevant, explanation is the dominance of field-driven effects [89]. Section 2.3 introduced two such mechanisms: surface photovoltage and pump-induced space charge. The former describes a change in the electrostatic surface potential upon photoexcitation, while the latter arises from Coulomb interaction between probe-emitted photoelectrons and an electron cloud created by pump-induced photoemission.

We first discuss the data under the assumption that a relevant SPV contribution is present. As outlined in Section 5.3.1, CrSBr is prone to *n*-type doping and defect-related surface states, making a transient modification of band bending plausible (see Sec. 2.3.3). In our data, a SPV-like, shift-type response is qualitatively consistent with the delay–energy map near temporal overlap (see Fig. 5.23c), where the

contour of the near-gap tail is displaced along the energy axis (dashed guide). The particularly strong modulation in the fixed-energy traces at $E_B = -0.5\,\mathrm{eV}$ (Fig. 5.23b) then follows naturally if the dominant effect is a spectral displacement, because this window samples the steep exponential tail. Even a modest transient displacement can therefore translate into a large apparent intensity change at a fixed E_B.

The temporal evolution can be interpreted as a superposition of (a) the strongest perturbation near temporal overlap and (b) a slower relaxation towards the equilibrium potential at later delays. In particular, the pronounced minimum around $\sim 50\,\mathrm{ps}$ followed by a gradual intensity increase (compare Fig. 5.23d) is compatible with partial relaxation back towards the equilibrium band bending. Non-monotonic dynamics can arise from trapping and (de-)charging of defect and surface states that transiently reshape the near-surface potential [121]. Bromine-related defects represent one plausible microscopic source of such states [225], but they are mentioned here only illustratively and are not identified in the present experiment.

An inversion of the effective SPV sign is plausible if charging of defect and surface states dominates the response. Surface states can contribute to SPV even under sub-bandgap excitation, as they can be depopulated into the conduction band or populated from the valence band [121]. However, the present dataset does not allow an unambiguous determination of the SPV sign, nor can a sign inversion be excluded based on the late-time relaxation alone.

Finally, the pronounced negative-delay response (extending to $\sim 100\,\mathrm{ps}$ at high fluence) is difficult to reconcile with a purely SPV-driven picture. A SPV persisting between pump pulses could generate an offset, but it does not naturally explain the strong rise towards t_0 on the negative-delay side. Thus, even if a SPV contribution is present, an additional mechanism is likely involved under the present conditions.

Apart from SPV, the spectrum may be affected by pump-induced space charge. As explained in Section 2.3.4, an electron cloud from pump-induced multiphoton photoemission can interact via Coulomb forces with the XUV photoemitted electrons. Multiphoton emission most likely occurs on the surrounding gold substrate and possibly from defect states. This mechanism naturally produces (a) a strong fluence dependence and (b) a pronounced negative-delay response, because probe-emitted photoelectrons can still interact with the pump-emitted cloud even when the pump arrives after the probe. The observed asymmetric temporal behavior is therefore compatible with a space-charge contribution. In our geometry, photoemission from the surrounding metallic area can further enhance the pump-induced electron cloud.

Similar to SPV, pump-induced space charge can yield an apparently rigid spectral displacement, and it often introduces spectral broadening. In the present dataset, however, no sharp feature is tracked whose width could be reliably compared between equilibrium and overlap. A broadening-based discrimination is therefore not possible here.

In trARPES, SPV and pump-induced space charge can, in principle, be distinguished using several diagnostics:

- **Fluence scaling:** Both effects increase with pump fluence, but SPV often shows sublinear, saturating behavior (close to logarithmic) [125, 129], whereas pump-induced space charge commonly exhibits a stronger-than-linear scaling over the relevant fluence range [88]. Quantifying the exponent requires systematic fluence sweeps with sufficient SNR.
- **Spectral broadening:** SPV predominantly induces a shift-like response while largely preserving intrinsic spectral widths [126], whereas space charge tends to introduce additional broadening because photoelectrons experience a distribution of Coulomb interactions [88].
- **Momentum dependence:** A SPV-induced shift affects the electronic structure largely uniformly across the BZ, whereas space-charge-induced shifts can depend on momentum and often decrease with increasing distance from the BZ center [17]. Tracking a dispersive band at different momenta can therefore be diagnostic.

These criteria cannot be applied decisively here, because the dataset does not provide reliable tracking of energy position and width for a sharp spectral feature.

Overall, this trARPES experiment on CrSBr illustrates how field effects can dominate the transient response and obscure expected exciton-related signatures. In particular, pump fluence and pump illumination geometry (e.g., excitation of metallic surroundings) must be carefully controlled to mitigate these artifacts before acquiring resonant exciton dynamics.

6 Summary and Outlook

In Chapter 3, we characterized a beamline generating fs-XUV pulses for pump–probe experiments and coupled it to a commercial MM. Using optional nonlinear post-compression, we established two modes of operation: one prioritizing energy resolution (better than (107 ± 2) meV) and one prioritizing temporal resolution ((49 ± 2) fs). Rapid and efficient data acquisition is facilitated by multi-100 kHz repetition rates and photon energies above 20 eV.

The two operating modes allow prioritizing either temporal or energy resolution. The theoretical transform limit of 1800 meV fs governs many design choices and trade-offs in experimental beamlines and is, in practice, difficult to achieve, as the survey in Figure 6.1 demonstrates. As an example, the compressed pulses of the setup presented here provide resolutions of 49 fs and 230 meV, corresponding to a system figure of merit of 11 300 meV fs. This deviation likely results from a combination of effects. First, the band-pass multilayer mirrors in the XUV monochromator have a fixed bandwidth and are optimized for overall harmonic transmission rather than minimal bandwidth (in part because the XUV spectrum cannot be monitored directly). In contrast, grating monochromators allow tuning via the exit-slit size and the grating groove density [144, 286]. Second, spatial inhomogeneities can effectively increase the pulse duration. Finally, pump and probe pulse durations likely do not perfectly match, such that one bandwidth dominates the cross-correlation in a time-resolved experiment.

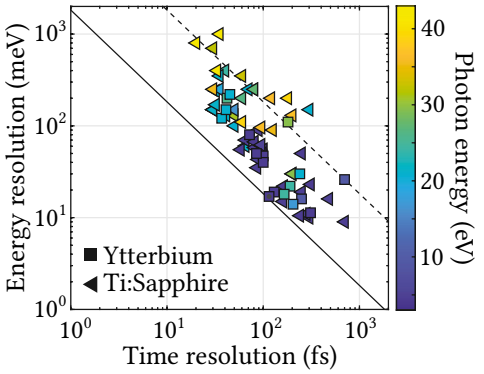


Figure 6.1: Survey of the time–bandwidth product in experimental probe sources. The solid line marks the transform limit, and the dotted line marks ten times the transform limit. Reprinted from Ref. [11], Copyright 2026, with permission from Elsevier.

Overall, trMM setups increasingly aim for rapid acquisition and improved energy resolution [11]. Because space-charge effects limit the achievable energy and momentum resolution, rapid acquisition often translates into higher repetition rates, and ultrafast high-average-power lasers push towards the MHz regime. In the setup presented in Chapter 3, the achieved repetition rates of 600 kHz (Sec. 3.3) and 300 kHz (Sec. 3.4) could be further increased with integration of a higher average-power laser

and slight modifications to the pulse compression and OPA. Another possible extension of trMM in general is the integration of a spin filter after the MM lens column, enabling spin-resolved mapping of the photoemission intensity [12].

Two-dimensional vdW materials provide an ideal platform to showcase the beamline's capabilities. In Chapter 5, we mapped the ultrafast relaxation of hot conduction-band carrier populations with energy and valley sensitivity, investigated exciton formation under resonant excitation, and observed field effects as artifacts that can mask excitonic response.

The material systems studied in Chapter 5 represent only a small subset of the vast landscape of two-dimensional solids. In general, ARPES spectra are highly sensitive to impurities, local strain, and surface contamination, and reproducible sample preparation for experiments in UHV remains challenging. Exfoliation of artificial heterostructure flakes enables fabrication of suitable samples, but such structures are prone to imperfections such as bubbles, trapped residues, and local strain [36]. Where possible, in-situ synthesis of established material systems may pave the way towards improved reproducibility and surface quality. As an example, the presented WS_2/Au(111) could serve as a substrate for subsequent molecular evaporation to design TMD–molecule interfaces [181].

While the comparatively straightforward assembly of vdW heterostructures is a major advantage of these materials, many studies to date still focus on exploration and characterization of monolayers, whereas trMM on heterostructures remains a young field. A prominent manifestation of interlayer coupling in TMD heterobilayers is the formation of hybridized exciton states and, under suitable band alignment, interlayer excitons (ILXs). The model system WS_2/WSe_2 investigated in Section 5.2 exhibited spectral signatures that are compatible with hybrid exciton formation after resonant excitation of intralayer excitons. Section 5.2.2 further discusses plausible relaxation pathways and experimental conditions that govern whether a distinct ILX contribution becomes observable.

As a member of the magnetic two-dimensional material family, CrSBr stands out through its high anisotropy and pronounced quasiparticle coupling. Optical studies have proposed a highly anisotropic exciton wave function, which is inherited by the quasi-one-dimensional conduction band. However, the trMM study presented in Section 5.3 exhibited dominant field effects that mask possible excitonic response. In combination with DFT, we assigned Cr interstitials as a source of intrinsic *n*-type doping, which is likely a major contributing factor to the field effects observed.

A Appendix

This appendix lists the XPS fit parameters obtained for bulk CrSBr and for monolayer WS_2/Au(111) in detail. All spectra were fitted with the XPST package [80] in IGOR Pro 8 [229], using a Shirley background and pseudo-Voigt functions with an additional asymmetry parameter (as implemented in XPST).

XPS Fitting results of WS_2/Au(111)

For Table A.1, Lorentz–Gaussian mixing parameter was fixed to 0.3. Spin–orbit split core levels were modeled by two components with fixed intensity ratios (compare Sec. 2.2.2). The asymmetry parameter was set to zero for S $2p$ and fitted for the remaining core levels. For W $4f$, the fitted asymmetry of 0.28 is consistent with additional metallic screening contributions (compare Sec. 4.2). For Au $4f$, the fitted asymmetry increases from 0.06 on clean Au to 0.14 after WS_2 growth.

Table A.1: Extracted fit parameters from pseudo-Voigt fits on the individual components of monolayer WS_2/Au(111). Compare Figure 4.3 for the acquired spectra and fit curves.

Peak	Position (eV)	Normalized Area (%)	FWHM (eV)	Description
W $4f_{7/2}$	32.89	57.1	0.62	Doublet
W $4f_{5/2}$	35.03	42.9	0.62	Doublet
S $2p_{3/2}$	162.64	66.7	0.63	Doublet
S $2p_{1/2}$	163.81	33.3	0.63	Doublet
Au $4f_{7/2}$	84.11	57.1	0.74	Clean Au(111)
Au $4f_{5/2}$	87.79	42.9	0.74	Clean Au(111)
Au $4f_{7/2}$	84.11	57.1	0.72	WS_2/Au(111)
Au $4f_{5/2}$	87.79	42.9	0.72	WS_2/Au(111)

XPS Fitting results of bulk CrSBr

For Table A.2, the Lorentz–Gaussian mixing parameter was fixed to 0.27 and symmetric peak shapes were used for all components.

Table A.2: Extracted fit parameters from pseudo-Voigt fits on the individual components of bulk CrSBr. Compare Figure 5.21 for the acquired spectra and fit curves.

Peak	Position (eV)	Normalized Area (%)	FWHM (eV)	Description
Br $3d_{5/2}$	68.76	60.0	0.67	Doublet
Br $3d_{3/2}$	69.78	40.0	0.67	Doublet
S $2p_{3/2}$	161.87	66.7	0.61	Doublet
S $2p_{1/2}$	163.06	33.3	0.61	Doublet
Cr $2p_{3/2}$ 1	575.09	30.4	0.71	Cr^{3+} Multiplet
Cr $2p_{3/2}$ 2	576.01	33.1	0.71	Cr^{3+} Multiplet
Cr $2p_{3/2}$ 3	576.69	19.6	0.71	Cr^{3+} Multiplet
Cr $2p_{3/2}$ 4	577.35	4.4	0.71	Cr^{3+} Multiplet
Cr $2p_{3/2}$ 5	577.99	2.5	0.71	Cr^{3+} Multiplet
Cr $2p_{3/2}$ 6	574.90	9.9	0.44	Cr^{1+}

Bibliography

[1] J. A. Sobota, Y. He, and Z.-X. Shen, "Angle-resolved photoemission studies of quantum materials", *Reviews of Modern Physics* **93**, 025006 (2021)
DOI: 10.1103/RevModPhys.93.025006.

[2] F. Boschini, M. Zonno, and A. Damascelli, "Time-resolved ARPES studies of quantum materials", *Reviews of Modern Physics* **96**, 015003 (2024)
DOI: 10.1103/RevModPhys.96.015003.

[3] Y. Deng et al., "Quantum anomalous Hall effect in intrinsic magnetic topological insulator $MnBi_2Te_4$", *Science* **367**, 895 (2020)
DOI: 10.1126/science.aax8156.

[4] R. Mori et al., "Spin-polarized spatially indirect excitons in a topological insulator", *Nature* **614**, 249 (2023)
DOI: 10.1038/s41586-022-05567-3.

[5] C. L. Smallwood et al., "Tracking Cooper Pairs in a Cuprate Superconductor by Ultrafast Angle-Resolved Photoemission", *Science* **336**, 1137 (2012)
DOI: 10.1126/science.1217423.

[6] A. Zong et al., "Evidence for topological defects in a photoinduced phase transition", *Nature Physics* **15**, 27 (2019)
DOI: 10.1038/s41567-018-0311-9.

[7] X. Shi et al., "Ultrafast electron calorimetry uncovers a new long-lived metastable state in 1T-$TaSe_2$ mediated by mode-selective electron-phonon coupling", *Science Advances* **5**, eaav4449 (2019)
DOI: 10.1126/sciadv.aav4449.

[8] C. Huang, S. Duan, and W. Zhang, "High-resolution time- and angle-resolved photoemission studies on quantum materials", *Quantum Frontiers* **1**, 15 (2022)
DOI: 10.1007/s44214-022-00013-x.

[9] H. Hertz, "Über einen Einfluss des ultravioletten Lichtes auf die electrische Entladung", *Annalen der Physik* **267**, 983 (1887)
DOI: 10.1002/andp.18872670827.

[10] A. Einstein, "Über einen die Erzeugung und Verwandlung des Lichtes betreffenden heuristischen Gesichtspunkt", *Annalen der Physik* **17**, 132 (1905)
DOI: 10.1002/andp.2005517S111.

[11] M. Na, A. K. Mills, and D. J. Jones, "Advancing time- and angle-resolved photoemission spectroscopy: The role of ultrafast laser development", *Physics Reports* **1036**, 1 (2023)
DOI: 10.1016/j.physrep.2023.09.005.

[12] O. Karni, I. Esin, and K. M. Dani, "Through the Lens of a Momentum Microscope: Viewing Light-Induced Quantum Phenomena in 2D Materials", *Advanced Materials* **35**, 2204120 (2023)
DOI: 10.1002/adma.202204120.

[13] P. S. Kirchmann et al., "Quasiparticle lifetimes in metallic quantum-well nanostructures", *Nature Physics* **6**, 782 (2010)
DOI: 10.1038/nphys1735.

[14] A. Stange et al., "Hot electron cooling in graphite: Supercollision versus hot phonon decay", *Physical Review B* **92**, 184303 (2015)
DOI: 10.1103/PhysRevB.92.184303.

[15] F. Liu, Q. Li, and X.-Y. Zhu, "Direct determination of momentum-resolved electron transfer in the photoexcited van der Waals heterobilayer WS_2/MoS_2", *Physical Review B* **101**, 201405 (2020)
DOI: 10.1103/PhysRevB.101.201405.

[16] C. Tusche et al., "Imaging properties of hemispherical electrostatic energy analyzers for high resolution momentum microscopy", *Ultramicroscopy* **206**, 112815 (2019)
DOI: 10.1016/j.ultramic.2019.112815.

[17] B. Schönhense et al., "Multidimensional photoemission spectroscopy—the space-charge limit", *New Journal of Physics* **20**, 033004 (2018)
DOI: 10.1088/1367-2630/aaa262.

[18] R. Ovsyannikov et al., "Principles and operation of a new type of electron spectrometer – ArTOF", *Journal of Electron Spectroscopy and Related Phenomena* **191**, 92 (2013)
DOI: 10.1016/j.elspec.2013.08.005.

[19] D. Schmitt et al., "Ultrafast nano-imaging of dark excitons", *Nature Photonics* **19**, 187 (2025)
DOI: 10.1038/s41566-024-01568-y.

[20] M. Puppin et al., "Time- and angle-resolved photoemission spectroscopy of solids in the extreme ultraviolet at 500 kHz repetition rate", *Review of Scientific Instruments* **90**, 023104 (2019)
DOI: 10.1063/1.5081938.

[21] C. Corder et al., "Ultrafast extreme ultraviolet photoemission without space charge", *Structural Dynamics* **5**, 054301 (2018)
DOI: 10.1063/1.5045578.

[22] K. S. Novoselov et al., "Electric Field Effect in Atomically Thin Carbon Films", *Science* **306**, 666 (2004)
DOI: 10.1126/science.1102896.

[23] K. S. Novoselov et al., "2D materials and van der Waals heterostructures", *Science* **353**, aac9439 (2016)
DOI: 10.1126/science.aac9439.

[24] A. K. Geim and I. V. Grigorieva, "Van der Waals heterostructures", *Nature* **499**, 419 (2013)
DOI: 10.1038/nature12385.

[25] K. S. Burch, D. Mandrus, and J.-G. Park, "Magnetism in two-dimensional van der Waals materials", *Nature* **563**, 47 (2018)
DOI: 10.1038/s41586-018-0631-z.

[26] J. Jo et al., "Nonvolatile Electric Control of Antiferromagnet CrSBr", *Nano Letters* **24**, 4471 (2024)
DOI: 10.1021/acs.nanolett.4c00348.

[27] H. Yu et al., "Moiré excitons: From programmable quantum emitter arrays to spin-orbit–coupled artificial lattices", *Science Advances* **3**, e1701696 (2017)
DOI: 10.1126/sciadv.1701696.

[28] W. S. Yun et al., "Thickness and strain effects on electronic structures of transition metal dichalcogenides: 2H-MX_2 semiconductors (M = Mo, W; X = S, Se, Te)", *Physical Review B* **85**, 033305 (2012)
DOI: 10.1103/PhysRevB.85.033305.

[29] A. Chernikov et al., "Exciton Binding Energy and Nonhydrogenic Rydberg Series in Monolayer WS_2", *Physical Review Letters* **113**, 076802 (2014)
DOI: 10.1103/PhysRevLett.113.076802.

[30] D. Wickramaratne, F. Zahid, and R. K. Lake, "Electronic and thermoelectric properties of few-layer transition metal dichalcogenides", *The Journal of Chemical Physics* **140**, 124710 (2014)
DOI: 10.1063/1.4869142.

[31] J. R. Schaibley et al., "Valleytronics in 2D materials", *Nature Reviews Materials* **1**, 1 (2016)
DOI: 10.1038/natrevmats.2016.55.

[32] J. P. Bange et al., "Probing electron-hole Coulomb correlations in the exciton landscape of a twisted semiconductor heterostructure", *Science Advances* **10**, eadi1323 (2024)
DOI: 10.1126/sciadv.adi1323.

[33] J. P. Bange et al., "Ultrafast dynamics of bright and dark excitons in monolayer WSe_2 and heterobilayer WSe_2/MoS_2", *2D Materials* **10**, 035039 (2023)
DOI: 10.1088/2053-1583/ace067.

[34] D. Schmitt et al., "Formation of moiré interlayer excitons in space and time", *Nature* **608**, 499 (2022)
DOI: 10.1038/s41586-022-04977-7.

[35] O. Karni et al., "Structure of the moiré exciton captured by imaging its electron and hole", *Nature* **603**, 247 (2022)
DOI: 10.1038/s41586-021-04360-y.

[36] F. Liu, "Time- and angle-resolved photoemission spectroscopy (TR-ARPES) of TMDC monolayers and bilayers", *Chemical Science* **14**, 736 (2023)
DOI: 10.1039/D2SC04124C.

[37] C. Gong et al., "Discovery of intrinsic ferromagnetism in two-dimensional van der Waals crystals", *Nature* **546**, 265 (2017)
DOI: 10.1038/nature22060.

[38] B. Huang et al., "Layer-dependent ferromagnetism in a van der Waals crystal down to the monolayer limit", *Nature* **546**, 270 (2017)
DOI: 10.1038/nature22391.

[39] M. E. Ziebel et al., "CrSBr: An Air-Stable, Two-Dimensional Magnetic Semiconductor", *Nano Letters* **24**, 4319 (2024)
DOI: 10.1021/acs.nanolett.4c00624.

[40] D. D. Awschalom and M. E. Flatté, "Challenges for semiconductor spintronics", *Nature Physics* **3**, 153 (2007)
DOI: 10.1038/nphys551.

[41] N. P. Wilson et al., "Interlayer electronic coupling on demand in a 2D magnetic semiconductor", *Nature Materials* **20**, 1657 (2021)
DOI: 10.1038/s41563-021-01070-8.

[42] K. Lee et al., "Magnetic Order and Symmetry in the 2D Semiconductor CrSBr", *Nano Letters* **21**, 3511 (2021)
DOI: 10.1021/acs.nanolett.1c00219.

[43] F. Wu et al., "Quasi 1D Electronic Transport in a 2D Magnetic Semiconductor", *Advanced Materials* **n/a**, 2109759 (2022)
DOI: 10.1002/adma.202109759.

[44] J. Klein et al., "The Bulk van der Waals Layered Magnet CrSBr is a Quasi-1D Material", *ACS Nano* **17**, 5316 (2023)
DOI: 10.1021/acsnano.2c07316.

[45] M. Birowska et al., "Large exciton binding energies in $MnPS_3$ as a case study of a van der Waals layered magnet", *Physical Review B* **103**, L121108 (2021)
DOI: 10.1103/PhysRevB.103.L121108.

[46] J.-C. Diels et al., *Ultrashort Laser Pulse Phenomena: Fundamentals, Techniques, and Applications on a Femtosecond Time Scale*, 2nd ed. (Elsevier Science & Technology, San Diego, United States, 2006),
DOI: 10.1016/B978-0-12-215493-5.X5000-9.

[47] A. M. Weiner, *Ultrafast optics*, Wiley Series in Pure and Applied Optics (Wiley, Hoboken, New Jersey, 2009),
DOI: 10.1002/9780470473467.

[48] G. New, *Introduction to Nonlinear Optics* (Cambridge University Press, Cambridge, 2011),
DOI: 10.1017/CBO9780511975851.

[49] G. Steinmeyer, "Wie misst man kurze Laserpulse? – Welche Verfahren gibt es?", *Laser Technik Journal* **2**, 34 (2005)
DOI: 10.1002/latj.200790063.

[50] R. Trebino et al., "Measuring ultrashort laser pulses in the time-frequency domain using frequency-resolved optical gating", *Review of Scientific Instruments* **68**, 3277 (1997)
DOI: 10.1063/1.1148286.

[51] H. J. Eichler and J. Eichler, *Laser*, 8th ed. (Springer, Berlin, Heidelberg, 2015),
DOI: 10.1007/978-3-642-41438-1.

[52] H. Sun, "Thin lens equation for a real laser beam with weak lens aperture truncation", *Optical Engineering* **37**, 2906 (1998)
DOI: 10.1117/1.601877.

[53] R. W. Boyd, *Nonlinear optics* (Elsevier, 2020),
DOI: 10.1016/C2015-0-05510-1.

[54] G. Cerullo, S. De Silvestri, and C. Manzoni, in *Encyclopedia of Modern Optics*, edited by B. D. Guenther and D. G. Steel, 2nd ed. (Elsevier, Oxford, 2018), pp. 290–301,
DOI: 10.1016/B978-0-12-803581-8.09632-6.

[55] C. Manzoni and G. Cerullo, "Design criteria for ultrafast optical parametric amplifiers", *Journal of Optics* **18**, 103501 (2016)
DOI: 10.1088/2040-8978/18/10/103501.

[56] F. Boschini et al., "An innovative Yb-based ultrafast deep ultraviolet source for time-resolved photoemission experiments", *Review of Scientific Instruments* **85**, 123903 (2014)
DOI: 10.1063/1.4903347.

[57] G. Tamošauskas et al., "Transmittance and phase matching of BBO crystal in the 3–5 μm range and its application for the characterization of mid-infrared laser pulses", *Optical Materials Express* **8**, 1410 (2018)
DOI: 10.1364/OME.8.001410.

[58] M. Protopapas, C. H. Keitel, and P. L. Knight, "Atomic physics with super-high intensity lasers", *Reports on Progress in Physics* **60**, 389 (1997)
DOI: 10.1088/0034-4885/60/4/001.

[59] J. L. Krause, K. J. Schafer, and K. C. Kulander, "Calculation of photoemission from atoms subject to intense laser fields", *Physical Review A* **45**, 4998 (1992)
DOI: 10.1103/PhysRevA.45.4998.

[60] P. B. Corkum, "Plasma perspective on strong field multiphoton ionization", *Physical Review Letters* **71**, 1994 (1993)
DOI: 10.1103/PhysRevLett.71.1994.

[61] J. L. Krause, K. J. Schafer, and K. C. Kulander, "High-order harmonic generation from atoms and ions in the high intensity regime", *Physical Review Letters* **68**, 3535 (1992)
DOI: 10.1103/PhysRevLett.68.3535.

[62] L. Hareli, G. Shoulga, and A. Bahabad, "Phase matching and quasi-phase matching of high-order harmonic generation—a tutorial", *Journal of Physics B: Atomic, Molecular and Optical Physics* **53**, 233001 (2020)
DOI: 10.1088/1361-6455/abb937.

[63] M. Lewenstein et al., "Theory of high-harmonic generation by low-frequency laser fields", *Physical Review A* **49**, 2117 (1994)
DOI: 10.1103/PhysRevA.49.2117.

[64] J. Li et al., "Attosecond science based on high harmonic generation from gases and solids", *Nature Communications* **11**, 2748 (2020)
DOI: 10.1038/s41467-020-16480-6.

[65] S. Hüfner, *Photoelectron Spectroscopy: Principles and Applications*, 3rd ed., Advanced Texts in Physics (Springer, Berlin, Heidelberg, Germany, 2003),
DOI: 10.1007/978-3-662-09280-4.

[66] A. Damascelli, Z. Hussain, and Z.-X. Shen, "Angle-resolved photoemission studies of the cuprate superconductors", *Reviews of Modern Physics* **75**, 473 (2003)
DOI: 10.1103/RevModPhys.75.473.

[67] S. Suga, A. Sekiyama, and C. Tusche, *Photoelectron Spectroscopy: Bulk and Surface Electronic Structures*, Vol. 72, Springer Series in Surface Sciences (Springer International Publishing, Cham, 2021),
DOI: 10.1007/978-3-030-64073-6.

[68] S. Moser, "An experimentalist's guide to the matrix element in angle resolved photoemission", *Journal of Electron Spectroscopy and Related Phenomena* **214**, 29 (2017)
DOI: 10.1016/j.elspec.2016.11.007.

[69] M. P. Seah and W. A. Dench, "Quantitative electron spectroscopy of surfaces: A standard data base for electron inelastic mean free paths in solids", *Surface and Interface Analysis* **1**, 2 (1979)
DOI: 10.1002/sia.740010103.

[70] S. K. Sharma, ed., *Handbook of Materials Characterization* (Springer International Publishing, Cham, 2018),
DOI: 10.1007/978-3-319-92955-2.

[71] D. J. Morgan, "XPS insights: Asymmetric peak shapes in XPS", *Surface and Interface Analysis* **55**, 567 (2023)
DOI: 10.1002/sia.7215.

[72] J. F. Moulder et al., *Handbook of X Ray Photoelectron Spectroscopy: A Reference Book of Standard Spectra for Identification and Interpretation of XPS Data* (Physical Electronics, Minnesota, United States, 1992).

[73] M. A. Isaacs, A. Graf, and D. J. Morgan, "XPS Insight Note: Multiplet Splitting in X-Ray Photoelectron Spectra", *Surface and Interface Analysis* **57**, 285 (2025)
DOI: 10.1002/sia.7383.

[74] M. C. Biesinger et al., "X-ray photoelectron spectroscopy studies of chromium compounds", *Surface and Interface Analysis* **36**, 1550 (2004)
DOI: 10.1002/sia.1983.

[75] R. P. Gupta and S. K. Sen, "Calculation of multiplet structure of core *p*-vacancy levels", *Physical Review B* **10**, 71 (1974)
DOI: 10.1103/PhysRevB.10.71.

[76] R. P. Gupta and S. K. Sen, "Calculation of multiplet structure of core *p* -vacancy levels. II", *Physical Review B* **12**, 15 (1975)
DOI: 10.1103/PhysRevB.12.15.

[77] V. Porée et al., "Resonant x-ray spectroscopies on CrSBr: Probing the electronic structure through chromium *d*-*d* excitations", *Physical Review B* **112**, 125103 (2025)
DOI: 10.1103/pdvz-6cpg.

[78] M. C. Biesinger et al., "Resolving surface chemical states in XPS analysis of first row transition metals, oxides and hydroxides: Cr, Mn, Fe, Co and Ni", *Applied Surface Science* **257**, 2717 (2011)
DOI: 10.1016/j.apsusc.2010.10.051.

[79] G. H. Major et al., "Practical guide for curve fitting in x-ray photoelectron spectroscopy", *Journal of Vacuum Science & Technology A* **38**, 061203 (2020)
DOI: 10.1116/6.0000377.

[80] M. Schmid, H.-P. Steinrück, and J. M. Gottfried, "A new asymmetric Pseudo-Voigt function for more efficient fitting of XPS lines", *Surface and Interface Analysis* **46**, 505 (2014)
DOI: 10.1002/sia.5521.

[81] A. G. Shard, "Practical guides for x-ray photoelectron spectroscopy: Quantitative XPS", *Journal of Vacuum Science & Technology A* **38**, 041201 (2020)
DOI: 10.1116/1.5141395.

[82] R. Hesse et al., "Comparative study of the modelling of the spectral background of photoelectron spectra with the Shirley and improved Tougaard methods", *Journal of Electron Spectroscopy and Related Phenomena* **186**, 44 (2013)
DOI: 10.1016/j.elspec.2013.01.020.

[83] D. A. Shirley, "High-Resolution X-Ray Photoemission Spectrum of the Valence Bands of Gold", *Physical Review B* **5**, 4709 (1972)
DOI: 10.1103/PhysRevB.5.4709.

[84] W. Swiech et al., "Recent progress in photoemission microscopy with emphasis on chemical and magnetic sensitivity", *Journal of Electron Spectroscopy and Related Phenomena* **84**, 171 (1997)
DOI: 10.1016/S0368-2048(97)00022-4.

[85] J. Maklar et al., "A quantitative comparison of time-of-flight momentum microscopes and hemispherical analyzers for time- and angle-resolved photoemission spectroscopy experiments", *Review of Scientific Instruments* **91**, 123112 (2020)
DOI: 10.1063/5.0024493.

[86] C. Tusche, A. Krasyuk, and J. Kirschner, "Spin resolved bandstructure imaging with a high resolution momentum microscope", *Ultramicroscopy*, Special Issue: LEEM-PEEM 9 **159**, 520 (2015)
DOI: 10.1016/j.ultramic.2015.03.020.

[87] F. Schmitt et al., "Transient Electronic Structure and Melting of a Charge Density Wave in $TbTe_3$", *Science* **321**, 1649 (2008)
DOI: 10.1126/science.1160778.

[88] L.-P. Oloff et al., "Pump laser-induced space-charge effects in HHG-driven time- and angle-resolved photoelectron spectroscopy", *Journal of Applied Physics* **119**, 225106 (2016)
DOI: 10.1063/1.4953643.

[89] S. Ulstrup et al., "Ramifications of optical pumping on the interpretation of time-resolved photoemission experiments on graphene", *Journal of Electron Spectroscopy and Related Phenomena*, Special Anniversary Issue: Volume 200 **200**, 340 (2015)
DOI: 10.1016/j.elspec.2015.04.010.

[90] Y. Kim and J. Lee, "Time-resolved photoemission of infinitely periodic atomic arrangements: correlation-dressed excited states of solids", *npj Computational Materials* **6**, 132 (2020)
DOI: 10.1038/s41524-020-00398-0.

[91] F. Boschini et al., "Role of matrix elements in the time-resolved photoemission signal", *New Journal of Physics* **22**, 023031 (2020)
DOI: 10.1088/1367-2630/ab6eb1.

[92] J. K. Freericks, H. R. Krishnamurthy, and Th. Pruschke, "Theoretical Description of Time-Resolved Photoemission Spectroscopy: Application to Pump-Probe Experiments", *Physical Review Letters* **102**, 136401 (2009)
DOI: 10.1103/PhysRevLett.102.136401.

[93] P. Hein et al., "Momentum-resolved hot electron dynamics at the $2H$-MoS_2 surface", *Physical Review B* **94**, 205406 (2016)
DOI: 10.1103/PhysRevB.94.205406.

[94] W. Lee et al., "Time-resolved ARPES Determination of a Quasi-Particle Band Gap and Hot Electron Dynamics in Monolayer MoS2", *Nano Letters* **21**, 7363 (2021)
DOI: 10.1021/acs.nanolett.1c02674.

[95] S. Hellmann et al., "Vacuum space-charge effects in solid-state photoemission", *Physical Review B* **79**, 035402 (2009)
DOI: 10.1103/PhysRevB.79.035402.

[96] D. Kutnyakhov et al., "Time- and momentum-resolved photoemission studies using time-of-flight momentum microscopy at a free-electron laser", *Review of Scientific Instruments* **91**, 013109 (2020)
DOI: 10.1063/1.5118777.

[97] X. J. Zhou et al., "Space charge effect and mirror charge effect in photoemission spectroscopy", *Journal of Electron Spectroscopy and Related Phenomena* **142**, 27 (2005)
DOI: 10.1016/j.elspec.2004.08.004.

[98] S. Passlack et al., "Space charge effects in photoemission with a low repetition, high intensity femtosecond laser source", *Journal of Applied Physics* **100**, 024912 (2006)
DOI: 10.1063/1.2217985.

[99] S. Hellmann et al., "Vacuum space-charge effects in nano-ARPES", *Physical Review B* **85**, 075109 (2012)
DOI: 10.1103/PhysRevB.85.075109.

[100] R. Perea-Causin et al., "Exciton optics, dynamics, and transport in atomically thin semiconductors", *APL Materials* **10**, 100701 (2022)
DOI: 10.1063/5.0107665.

[101] J. Shah, *Ultrafast Spectroscopy of Semiconductors and Semiconductor Nanostructures*, red. by M. Cardona et al., Vol. 115, Springer Series in Solid-State Sciences (Springer, Berlin, Heidelberg, 1999),
DOI: 10.1007/978-3-662-03770-6.

[102] W. Schäfer and M. Wegener, *Semiconductor Optics and Transport Phenomena*, Advanced Texts in Physics (Springer, Berlin, Heidelberg, 2002),
DOI: 10.1007/978-3-662-04663-0.

[103] M. Kira and S. W. Koch, *Semiconductor Quantum Optics*, 1st ed. (Cambridge University Press, Cambridge, United Kingdom, 2011),
DOI: 10.1017/CBO9781139016926.

[104] A. Rustagi and A. F. Kemper, "Photoemission signature of excitons", *Physical Review B* **97**, 235310 (2018)
DOI: 10.1103/PhysRevB.97.235310.

[105] C. Trovatello et al., "The ultrafast onset of exciton formation in 2D semiconductors", *Nature Communications* **11**, 5277 (2020)
DOI: 10.1038/s41467-020-18835-5.

[106] S. Brem et al., "Exciton Relaxation Cascade in two-dimensional Transition Metal Dichalcogenides", *Scientific Reports* **8**, 8238 (2018)
DOI: 10.1038/s41598-018-25906-7.

[107] D. Christiansen et al., "Theory of exciton dynamics in time-resolved ARPES: Intra- and intervalley scattering in two-dimensional semiconductors", *Physical Review B* **100**, 205401 (2019)
DOI: 10.1103/PhysRevB.100.205401.

[108] E. Perfetto et al., "First-principles approach to excitons in time-resolved and angle-resolved photoemission spectra", *Physical Review B* **94**, 245303 (2016)
DOI: 10.1103/PhysRevB.94.245303.

[109] S. Dong et al., "Direct measurement of key exciton properties: Energy, dynamics, and spatial distribution of the wave function", *Natural Sciences* **1**, e10010 (2021)
DOI: 10.1002/ntls.10010.

[110] M. Weinelt et al., "Dynamics of Exciton Formation at the Si(100) c(4x2) Surface", *Physical Review Letters* **92**, 126801 (2004)
DOI: 10.1103/PhysRevLett.92.126801.

[111] H. Tanimura, K. Tanimura, and P. H. M. van Loosdrecht, "Dynamics of incoherent exciton formation in Cu_2O: Time- and angle-resolved photoemission spectroscopy", *Physical Review B* **100**, 115204 (2019)
DOI: 10.1103/PhysRevB.100.115204.

[112] M. K. L. Man et al., "Experimental measurement of the intrinsic excitonic wave function", *Science Advances* **7**, eabg0192 (2021)
DOI: 10.1126/sciadv.abg0192.

[113] J. Madéo et al., "Directly visualizing the momentum-forbidden dark excitons and their dynamics in atomically thin semiconductors", *Science* **370**, 1199 (2020)
DOI: 10.1126/science.aba1029.

[114] G. Meneghini et al., "Hybrid Exciton Signatures in ARPES Spectra of van der Waals Materials", *ACS Photonics* **10**, 3570 (2023)
DOI: 10.1021/acsphotonics.3c00599.

[115] L. Miaja-Avila et al., "Laser-Assisted Photoelectric Effect from Surfaces", *Physical Review Letters* **97**, 113604 (2006)
DOI: 10.1103/PhysRevLett.97.113604.

[116] J. C. Baggesen and L. B. Madsen, "Theory for time-resolved measurements of laser-induced electron emission from metal surfaces", *Physical Review A* **78**, 032903 (2008)
DOI: 10.1103/PhysRevA.78.032903.

[117] G. Saathoff et al., "Laser-assisted photoemission from surfaces", *Physical Review A* **77**, 022903 (2008)
DOI: 10.1103/PhysRevA.77.022903.

[118] L. Wenthaus et al., "Insights into the laser-assisted photoelectric effect from solid-state surfaces", *Physical Review B* **110**, 235406 (2024)
DOI: 10.1103/PhysRevB.110.235406.

[119] F. Mahmood et al., "Selective scattering between Floquet–Bloch and Volkov states in a topological insulator", *Nature Physics* **12**, 306 (2016)
DOI: 10.1038/nphys3609.

[120] M. Merboldt et al., "Observation of Floquet states in graphene", *Nature Physics* **21**, 1093 (2025)
DOI: 10.1038/s41567-025-02889-7.

[121] L. Kronik and Y. Shapira, "Surface photovoltage phenomena: theory, experiment, and applications", *Surface Science Reports* **37**, 1 (1999)
DOI: 10.1016/S0167-5729(99)00002-3.

[122] A. C. Kundmann, K. Becker, and F. E. Osterloh, "Surface photovoltage predicts open circuit voltage in GaP/PEDOT:PSS and GaP/CuSCN heterojunction solar cells", *RSC Applied Interfaces* **1**, 1426 (2024)
DOI: 10.1039/D4LF00225C.

[123] T. Yu et al., "Momentum-resolved electronic structure and band offsets in an epitaxial NbN/GaN superconductor/semiconductor heterojunction", *Science Advances* **7**, eabi5833 (2021)
DOI: 10.1126/sciadv.abi5833.

[124] R. Wang et al., "Tuning the Surface Electron Accumulation Layer of In_2O_3 by Adsorption of Molecular Electron Donors and Acceptors", *Small* **19**, 2300730 (2023)
DOI: 10.1002/smll.202300730.

[125] F. Roth et al., "Dynamical Nonlinear Inversion of the Surface Photovoltage at Si(100)", *Physical Review Letters* **132**, 146201 (2024)
DOI: 10.1103/PhysRevLett.132.146201.

[126] L. Rettig, P. S. Kirchmann, and U. Bovensiepen, "Ultrafast dynamics of occupied quantum well states in Pb/Si(111)", *New Journal of Physics* **14**, 023047 (2012)
DOI: 10.1088/1367-2630/14/2/023047.

[127] S.-i. Tanaka, "Utility and constraint on the use of pump-probe photoelectron spectroscopy for detecting time-resolved surface photovoltage", *Journal of Electron Spectroscopy and Related Phenomena* **185**, 152 (2012)
DOI: 10.1016/j.elspec.2012.06.003.

[128] L. L. Lev et al., "Impact of band-bending on the k-resolved electronic structure of Si-doped GaN", *Physical Review Research* **4**, 013183 (2022)
DOI: 10.1103/PhysRevResearch.4.013183.

[129] S. Ciocys et al., "Manipulating long-lived topological surface photovoltage in bulk-insulating topological insulators Bi_2Se_3 and Bi_2Te_3", *npj Quantum Materials* **5**, 16 (2020)
DOI: 10.1038/s41535-020-0218-4.

[130] S.-L. Yang et al., "Electron propagation from a photo-excited surface: implications for time-resolved photoemission", *Applied Physics A* **116**, 85 (2014)
DOI: 10.1007/s00339-013-8154-9.

[131] S. Ciocys et al., "Tracking surface photovoltage dipole geometry in Bi_2Se_3 with time-resolved photoemission", *Journal of Statistical Mechanics: Theory and Experiment* **2019**, 104008 (2019)
DOI: 10.1088/1742-5468/ab458a.

[132] D. Kühn et al., "The influence of x-ray pulse length on space-charge effects in optical pump/x-ray probe photoemission", *New Journal of Physics* **21**, 073042 (2019)
DOI: 10.1088/1367-2630/ab2f5c.

[133] A. Lévy et al., "Mitigating space charge in time-resolved photoelectron spectroscopy to study laser-heated copper dynamics in the high fluence regime", *Physical Review B* **109**, 174311 (2024)
DOI: 10.1103/PhysRevB.109.174311.

[134] A. Jürgensen, N. Esser, and R. Hergenröder, "Near ambient pressure XPS with a conventional X-ray source", *Surface and Interface Analysis* **44**, 1100 (2012)
DOI: 10.1002/sia.4826.

[135] K. J. Schiller et al., "Time-resolved momentum microscopy with fs-XUV photons at high repetition rates with flexible energy and time resolution", *Scientific Reports* **15**, 3611 (2025)
DOI: 10.1038/s41598-025-86660-1.

[136] F. Matsui et al., "Photoelectron Momentum Microscope at BL6U of UVSOR-III synchrotron", *Japanese Journal of Applied Physics* **59**, 067001 (2020)
DOI: 10.35848/1347-4065/ab9184.

[137] T.-H. Chuang et al., "Performance of a photoelectron momentum microscope in direct- and momentum-space imaging with ultraviolet photon sources", *Journal of Synchrotron Radiation* **31**, 195 (2024)
DOI: 10.1107/S1600577523009761.

[138] S. Ponzoni et al., "Dirac Bands in the Topological Insulator Bi_2Se_3 Mapped by Time-Resolved Momentum Microscopy", *Advanced Physics Research* **2**, 2200016 (2023)
DOI: 10.1002/apxr.202200016.

[139] L. Sternemann et al., "Fabrication of large-area 2D magnetic semiconductor films for low-temperature ARPES", *2D Materials* **12**, 035008 (2025)
DOI: 10.1088/2053-1583/add7ea.

[140] C. Bao et al., "Ultrafast time- and angle-resolved photoemission spectroscopy with widely tunable probe photon energy of 5.3–7.0 eV for investigating dynamics of three-dimensional materials", *Review of Scientific Instruments* **93**, 013902 (2022)
DOI: 10.1063/5.0070004.

[141] M. Heber et al., "Multispectral time-resolved energy–momentum microscopy using high-harmonic extreme ultraviolet radiation", *Review of Scientific Instruments* **93**, 083905 (2022)
DOI: 10.1063/5.0091003.

[142] B. Stadtmüller et al., "Strong modification of the transport level alignment in organic materials after optical excitation", *Nature Communications* **10**, 1470 (2019)
DOI: 10.1038/s41467-019-09136-7.

[143] R. Wallauer et al., "Intervalley scattering in MoS_2 imaged by two-photon photoemission with a high-harmonic probe", *Applied Physics Letters* **109**, 162102 (2016)
DOI: 10.1063/1.4965839.

[144] E. J. Sie et al., "Time-resolved XUV ARPES with tunable 24–33 eV laser pulses at 30 meV resolution", *Nature Communications* **10**, 3535 (2019)
DOI: 10.1038/s41467-019-11492-3.

[145] A. K. Mills et al., "Cavity-enhanced high harmonic generation for XUV time-resolved ARPES", *Review of Scientific Instruments* **90**, 083001 (2019)
DOI: 10.1063/1.5090507.

[146] J. Drs et al., "Intra-oscillator high harmonic source reaching 100-eV photon energy", *Optics Express* **32**, 17424 (2024)
DOI: 10.1364/OE.522104.

[147] R. Klas et al., "Ultra-short-pulse high-average-power megahertz-repetition-rate coherent extreme-ultraviolet light source", *PhotoniX* **2**, 4 (2021)
DOI: 10.1186/s43074-021-00028-y.

[148] F. Chen et al., "Time-resolved ARPES with tunable 12–21.6 eV XUV at 400 kHz repetition rate", *Review of Scientific Instruments* **94**, 043905 (2023)
DOI: 10.1063/5.0143485.

[149] M. Keunecke et al., "Time-resolved momentum microscopy with a 1 MHz high-harmonic extreme ultraviolet beamline", *Review of Scientific Instruments* **91**, 063905 (2020)
DOI: 10.1063/5.0006531.

[150] Y. Pfaff et al., "Nonlinear pulse compression of a thin-disk amplifier and contrast enhancement via nonlinear ellipse rotation", *Optics Express* **30**, 10981 (2022)
DOI: 10.1364/OE.455393.

[151] M. Kaumanns et al., "Multipass spectral broadening of 18 mJ pulses compressible from 13 ps to 41 fs", *Optics Letters* **43**, 5877 (2018)
DOI: 10.1364/OL.43.005877.

[152] A.-K. Raab et al., "Multi-gigawatt peak power post-compression in a bulk multi-pass cell at a high repetition rate", *Optics Letters* **47**, 5084 (2022)
DOI: 10.1364/OL.463960.

[153] E. Constant et al., "High order harmonic generation-based attosecond light sources and applications to quantum phenomena", *APL Photonics* **10** (2025)
DOI: 10.1063/5.0235171.

[154] H.-C. Bandulet et al., "High harmonic generation with a spatially filtered optical parametric amplifier", *Journal of Physics B: Atomic, Molecular and Optical Physics* **41**, 245602 (2008)
DOI: 10.1088/0953-4075/41/24/245602.

[155] D. Gérard and S. K. Gray, "Aluminium plasmonics", *Journal of Physics D: Applied Physics* **48**, 184001 (2014)
DOI: 10.1088/0022-3727/48/18/184001.

[156] R. Wallauer et al., "Tracing orbital images on ultrafast time scales", *Science* (2021)
DOI: 10.1126/science.abf3286.

[157] M. Lupo Pasini et al., "Two excited-state datasets for quantum chemical UV-vis spectra of organic molecules", *Scientific Data* **10**, 546 (2023)
DOI: 10.1038/s41597-023-02408-4.

[158] T. Zhu et al., "Highly mobile charge-transfer excitons in two-dimensional WS_2/tetracene heterostructures", *Science Advances* **4**, eaao3104 (2018)
DOI: 10.1126/sciadv.aao3104.

[159] SPECS, *UVS 300 - Duoplasmatron Discharge Light Source with Quartz Capillary*, URL: https://www.specs-group.com/specs/products/detail/uvs-300 (visited on 10/07/2025).

[160] R. Cucini et al., "Coherent narrowband light source for ultrafast photoelectron spectroscopy in the 17–31 eV photon energy range", *Structural Dynamics* **7**, 014303 (2020)
DOI: 10.1063/1.5131216.

[161] Y. Xie and D. Zhao, "2D materials: a wonderland for physical science", *National Science Review* **9**, nwab202 (2022)
DOI: 10.1093/nsr/nwab202.

[162] A. H. Castro Neto et al., "The electronic properties of graphene", *Reviews of Modern Physics* **81**, 109 (2009)
DOI: 10.1103/RevModPhys.81.109.

[163] J. C. Johannsen et al., "Direct View of Hot Carrier Dynamics in Graphene", *Physical Review Letters* **111**, 027403 (2013)
DOI: 10.1103/PhysRevLett.111.027403.

[164] I. Gierz et al., "Snapshots of non-equilibrium Dirac carrier distributions in graphene", *Nature Materials* **12**, 1119 (2013)
DOI: 10.1038/nmat3757.

[165] Q. H. Wang et al., "Electronics and optoelectronics of two-dimensional transition metal dichalcogenides", *Nature Nanotechnology* **7**, 699 (2012)
DOI: 10.1038/nnano.2012.193.

[166] Y.-C. Lin et al., "Recent Advances in 2D Material Theory, Synthesis, Properties, and Applications", *ACS nano* **17**, 9694 (2023)
DOI: 10.1021/acsnano.2c12759.

[167] J. Klein and F. M. Ross, "Materials beyond monolayers: The magnetic quasi-1D semiconductor CrSBr", *Journal of Materials Research* **39**, 3045 (2024)
DOI: 10.1557/s43578-024-01459-6.

[168] F. Reinert et al., "Direct measurements of the L-gap surface states on the (111) face of noble metals by photoelectron spectroscopy", *Physical Review B* **63**, 115415 (2001)
DOI: 10.1103/PhysRevB.63.115415.

[169] R. Gross and A. Marx, *Festkörperphysik*, 3rd ed. (De Gruyter, 2018),
DOI: 10.1515/9783110559187.

[170] B. Kim et al., "Spin and orbital angular momentum structure of Cu(111) and Au(111) surface states", *Physical Review B* **85**, 195402 (2012)
DOI: 10.1103/PhysRevB.85.195402.

[171] J. E. Nitschke et al., "Valence band electronic structure of the van der Waals antiferromagnet $FePS_3$", *Materials Today Electronics* **6**, 100061 (2023)
DOI: 10.1016/j.mtelec.2023.100061.

[172] M. Bianchi et al., "Paramagnetic electronic structure of CrSBr: Comparison between ab initio *GW* theory and angle-resolved photoemission spectroscopy", *Physical Review B* **107**, 235107 (2023)
DOI: 10.1103/PhysRevB.107.235107.

[173] Y. Huang et al., "Universal mechanical exfoliation of large-area 2D crystals", *Nature Communications* **11**, 2453 (2020)
DOI: 10.1038/s41467-020-16266-w.

[174] A. Castellanos-Gomez et al., "Deterministic transfer of two-dimensional materials by all-dry viscoelastic stamping", *2D Materials* **1**, 011002 (2014)
DOI: 10.1088/2053-1583/1/1/011002.

[175] P. Gant et al., "A system for the deterministic transfer of 2D materials under inert environmental conditions", *2D Materials* **7**, 025034 (2020)
DOI: 10.1088/2053-1583/ab72d6.

[176] M. D. Watson et al., "Giant exchange splitting in the electronic structure of A-type 2D antiferromagnet CrSBr", *npj 2D Materials and Applications* **8**, 1 (2024)
DOI: 10.1038/s41699-024-00492-7.

[177] M. Velický et al., "Mechanism of Gold-Assisted Exfoliation of Centimeter-Sized Transition-Metal Dichalcogenide Monolayers", *ACS Nano* **12**, 10463 (2018)
DOI: 10.1021/acsnano.8b06101.

[178] A. Grubišić-Čabo et al., "In-situ exfoliation method of large-area 2D materials", *Advanced Science*, 2301243 (2023)
DOI: 10.1002/advs.202301243.

[179] N. Vogel, J. Zieleniecki, and I. Köper, "As flat as it gets: ultrasmooth surfaces from template-stripping procedures", *Nanoscale* **4**, 3820 (2012)
DOI: 10.1039/C2NR30434A.

[180] E. A. Weiss et al., "Si/SiO2-Templated Formation of Ultraflat Metal Surfaces on Glass, Polymer, and Solder Supports: Their Use as Substrates for Self-Assembled Monolayers", *Langmuir* **23**, 9686 (2007)
DOI: 10.1021/la701919r.

[181] M. Capra et al., "Bottom-Up Realization of a Type-II Organic/Transition-Metal Dichalcogenides Heterointerface: Pentacene on Monolayer WS_2", *ACS Nano* **20**, 25410 (2026)
DOI: 10.1021/acsnano.6c07654.

[182] National Institute of Standards and Technology, *NIST X-ray Photoelectron Spectroscopy Database: NIST Standard Reference Database 20*, version 5.0 (Gaithersburg, MD, 2000),
DOI: 10.18434/T4T88K.

[183] M. Dendzik et al., "Substrate-induced semiconductor-to-metal transition in monolayer WS_2", *Physical Review B* **96**, 235440 (2017)
DOI: 10.1103/PhysRevB.96.235440.

[184] L. Bignardi et al., "Growth and structure of singly oriented single-layer tungsten disulfide on Au(111)", *Physical Review Materials* **3**, 014003 (2019)
DOI: 10.1103/PhysRevMaterials.3.014003.

[185] M. Dendzik et al., "Growth and electronic structure of epitaxial single-layer WS_2 on Au(111)", *Physical Review B* **92**, 245442 (2015)
DOI: 10.1103/PhysRevB.92.245442.

[186] C. J. Powell and A. Jablonski, "NIST Electron Inelastic-Mean-Free-Path Database - Version 1.2", *National Institute of Standards and Technology* (2010)
DOI: 10.18434/T48C78.

[187] M. Orlita and M. Potemski, "Dirac electronic states in graphene systems: optical spectroscopy studies", *Semiconductor Science and Technology* **25**, 063001 (2010)
DOI: 10.1088/0268-1242/25/6/063001.

[188] E. Fitzer et al., "Recommended terminology for the description of carbon as a solid (IUPAC Recommendations 1995)", *Pure and Applied Chemistry* **67**, 473 (1995)
DOI: 10.1351/pac199567030473.

[189] T. Suemoto et al., "Access to hole dynamics in graphite by femtosecond luminescence and photoemission spectroscopy", *Physical Review B* **87**, 224302 (2013)
DOI: 10.1103/PhysRevB.87.224302.

[190] M. Breusing, C. Ropers, and T. Elsaesser, "Ultrafast Carrier Dynamics in Graphite", *Physical Review Letters* **102**, 086809 (2009)
DOI: 10.1103/PhysRevLett.102.086809.

[191] G.-B. Liu et al., "Electronic structures and theoretical modelling of two-dimensional group-VIB transition metal dichalcogenides", *Chemical Society Reviews* **44**, 2643 (2015)
DOI: 10.1039/C4CS00301B.

[192] J. Xia, J. Yan, and Z. X. Shen, "Transition metal dichalcogenides: structural, optical and electronic property tuning via thickness and stacking", *FlatChem* **4**, 1 (2017)
DOI: 10.1016/j.flatc.2017.06.007.

[193] G. Wang et al., "Colloquium: Excitons in atomically thin transition metal dichalcogenides", *Reviews of Modern Physics* **90**, 021001 (2018)
DOI: 10.1103/RevModPhys.90.021001.

[194] R. Bertoni et al., "Generation and Evolution of Spin-, Valley-, and Layer-Polarized Excited Carriers in Inversion-Symmetric WSe2", *Physical Review Letters* **117**, 277201 (2016)
DOI: 10.1103/PhysRevLett.117.277201.

[195] H. Beyer et al., "80% Valley Polarization of Free Carriers in Singly Oriented Single-Layer WS_2 on Au(111)", *Physical Review Letters* **123**, 236802 (2019)
DOI: 10.1103/PhysRevLett.123.236802.

[196] V. Zatko et al., "Band-Gap Landscape Engineering in Large-Scale 2D Semiconductor van der Waals Heterostructures", *ACS Nano* **15**, 7279 (2021)
DOI: 10.1021/acsnano.1c00544.

[197] J. Á. Silva-Guillén, P. San-Jose, and R. Roldán, "Electronic Band Structure of Transition Metal Dichalcogenides from Ab Initio and Slater–Koster Tight-Binding Model", *Applied Sciences* **6**, 284 (2016)
DOI: 10.3390/app6100284.

[198] M. H. Naik and M. Jain, "Origin of layer dependence in band structures of two-dimensional materials", *Physical Review B* **95**, 165125 (2017)
DOI: 10.1103/PhysRevB.95.165125.

[199] L. Waldecker et al., "Rigid Band Shifts in Two-Dimensional Semiconductors through External Dielectric Screening", *Physical Review Letters* **123**, 206403 (2019)
DOI: 10.1103/PhysRevLett.123.206403.

[200] I. Tanabe et al., "Band structure characterization of WS_2 grown by chemical vapor deposition", *Applied Physics Letters* **108**, 252103 (2016)
DOI: 10.1063/1.4954278.

[201] C. Kastl et al., "Multimodal spectromicroscopy of monolayer WS2 enabled by ultra-clean van der Waals epitaxy", *2D Materials* **5**, 045010 (2018)
DOI: 10.1088/2053-1583/aad21c.

[202] G. H. Wannier, "The Structure of Electronic Excitation Levels in Insulating Crystals", *Physical Review* **52**, 191 (1937)
DOI: 10.1103/PhysRev.52.191.

[203] M. M. Ugeda et al., "Giant bandgap renormalization and excitonic effects in a monolayer transition metal dichalcogenide semiconductor", *Nature Materials* **13**, 1091 (2014)
DOI: 10.1038/nmat4061.

[204] J. Frenkel, "On the Transformation of light into Heat in Solids. I", *Physical Review* **37**, 17 (1931)
DOI: 10.1103/PhysRev.37.17.

[205] A. F. Rigosi et al., "Electronic band gaps and exciton binding energies in monolayer $Mo_xW_{1-x}S_2$ transition metal dichalcogenide alloys probed by scanning tunneling and optical spectroscopy", *Physical Review B* **94**, 075440 (2016)
DOI: 10.1103/PhysRevB.94.075440.

[206] A. Raja et al., "Coulomb engineering of the bandgap and excitons in two-dimensional materials", *Nature Communications* **8**, 15251 (2017)
DOI: 10.1038/ncomms15251.

[207] P. Cudazzo, I. V. Tokatly, and A. Rubio, "Dielectric screening in two-dimensional insulators: Implications for excitonic and impurity states in graphane", *Physical Review B* **84**, 085406 (2011)
DOI: 10.1103/PhysRevB.84.085406.

[208] Y. Jiang et al., "Interlayer exciton formation, relaxation, and transport in TMD van der Waals heterostructures", *Light: Science & Applications* **10**, 72 (2021)
DOI: 10.1038/s41377-021-00500-1.

[209] F. He et al., "Moiré Patterns in 2D Materials: A Review", *ACS Nano* **15**, 5944 (2021)
DOI: 10.1021/acsnano.0c10435.

[210] N. D. Mermin and H. Wagner, "Absence of Ferromagnetism or Antiferromagnetism in One- or Two-Dimensional Isotropic Heisenberg Models", *Physical Review Letters* **17**, 1133 (1966)
DOI: 10.1103/PhysRevLett.17.1133.

[211] S. Jenkins et al., "Breaking through the Mermin-Wagner limit in 2D van der Waals magnets", *Nature Communications* **13**, 6917 (2022)
DOI: 10.1038/s41467-022-34389-0.

[212] J.-F. Dayen et al., "Two-dimensional van der Waals spinterfaces and magnetic-interfaces", *Applied Physics Reviews* **7**, 011303 (2020)
DOI: 10.1063/1.5112171.

[213] W. Li, X. Qian, and J. Li, "Phase transitions in 2D materials", *Nature Reviews Materials* **6**, 829 (2021)
DOI: 10.1038/s41578-021-00304-0.

[214] Q. H. Wang et al., "The Magnetic Genome of Two-Dimensional van der Waals Materials", *ACS Nano* **16**, 6960 (2022)
DOI: 10.1021/acsnano.1c09150.

[215] D. Shcherbakov et al., "Raman Spectroscopy, Photocatalytic Degradation, and Stabilization of Atomically Thin Chromium Tri-iodide", *Nano Letters* **18**, 4214 (2018)
DOI: 10.1021/acs.nanolett.8b01131.

[216] D. L. Esteras et al., "Magnon Straintronics in the 2D van der Waals Ferromagnet CrSBr from First-Principles", *Nano Letters* **22**, 8771 (2022)
DOI: 10.1021/acs.nanolett.2c02863.

[217] H. Wang, J. Qi, and X. Qian, "Electrically tunable high Curie temperature two-dimensional ferromagnetism in van der Waals layered crystals", *Applied Physics Letters* **117**, 083102 (2020)
DOI: 10.1063/5.0014865.

[218] J. Beck, "Über Chalkogenidhalogenide des Chroms Synthese, Kristallstruktur und Magnetismus von Chromsulfidbromid, CrSBr", *Zeitschrift für anorganische und allgemeine Chemie* **585**, 157 (1990)
DOI: 10.1002/zaac.19905850118.

[219] E. J. Telford et al., "Layered Antiferromagnetism Induces Large Negative Magnetoresistance in the van der Waals Semiconductor CrSBr", *Advanced Materials* **32**, 2003240 (2020)
DOI: 10.1002/adma.202003240.

[220] W. Liu et al., "A Three-Stage Magnetic Phase Transition Revealed in Ultrahigh-Quality van der Waals Bulk Magnet CrSBr", *ACS Nano* **16**, 15917 (2022)
DOI: 10.1021/acsnano.2c02896.

[221] K. Yang et al., "Triaxial magnetic anisotropy in the two-dimensional ferromagnetic semiconductor CrSBr", *Physical Review B* **104**, 144416 (2021)
DOI: 10.1103/PhysRevB.104.144416.

[222] F. Marques-Moros et al., "Interplay between Optical Emission and Magnetism in the van der Waals Magnetic Semiconductor CrSBr in the Two-Dimensional Limit", *ACS Nano* **17**, 13224 (2023)
DOI: 10.1021/acsnano.3c00375.

[223] J. Cenker et al., "Reversible strain-induced magnetic phase transition in a van der Waals magnet", *Nature Nanotechnology*, 1 (2022)
DOI: 10.1038/s41565-021-01052-6.

[224] Y. J. Bae et al., "Exciton-coupled coherent magnons in a 2D semiconductor", *Nature* **609**, 282 (2022)
DOI: 10.1038/s41586-022-05024-1.

[225] K. Torres et al., "Probing Defects and Spin-Phonon Coupling in CrSBr via Resonant Raman Scattering", *Advanced Functional Materials* **33**, 2211366 (2023)
DOI: 10.1002/adfm.202211366.

[226] K. Lin et al., "Strong Exciton–Phonon Coupling as a Fingerprint of Magnetic Ordering in van der Waals Layered CrSBr", *ACS Nano* (2024)
DOI: 10.1021/acsnano.3c07236.

[227] G. M. Diederich et al., "Tunable interaction between excitons and hybridized magnons in a layered semiconductor", *Nature Nanotechnology* **18**, 23 (2023) DOI: 10.1038/s41565-022-01259-1.

[228] T. M. J. Cham et al., "Anisotropic Gigahertz Antiferromagnetic Resonances of the Easy-Axis van der Waals Antiferromagnet CrSBr", *Nano Letters* **22**, 6716 (2022) DOI: 10.1021/acs.nanolett.2c02124.

[229] I. WaveMetrics, *Igor Pro*, version 8.0, WaveMetrics, Inc., 2018.

[230] R. Wallauer et al., "Momentum-Resolved Observation of Exciton Formation Dynamics in Monolayer WS_2", *Nano Letters* **21**, 5867 (2021) DOI: 10.1021/acs.nanolett.1c01839.

[231] W. Chen et al., "Effect of trigonal warping on the Berry curvature and valley/spin Hall effects in monolayer MoS2", *Physics Letters A* **384**, 126344 (2020) DOI: 10.1016/j.physleta.2020.126344.

[232] D. W. Latzke et al., "Electronic structure, spin-orbit coupling, and interlayer interaction in bulk MoS_2 and WS_2", *Physical Review B* **91**, 235202 (2015) DOI: 10.1103/PhysRevB.91.235202.

[233] K. K. Kam and B. A. Parkinson, "Detailed photocurrent spectroscopy of the semiconducting group VIB transition metal dichalcogenides", *The Journal of Physical Chemistry* **86**, 463 (1982) DOI: 10.1021/j100393a010.

[234] D. Braga et al., "Quantitative Determination of the Band Gap of WS2 with Ambipolar Ionic Liquid-Gated Transistors", *Nano Letters* **12**, 5218 (2012) DOI: 10.1021/nl302389d.

[235] P. Majchrzak et al., "Spectroscopic view of ultrafast charge carrier dynamics in single- and bilayer transition metal dichalcogenide semiconductors", *Journal of Electron Spectroscopy and Related Phenomena* **250**, 147093 (2021) DOI: 10.1016/j.elspec.2021.147093.

[236] R. Oliva et al., "Strong Substrate Strain Effects in Multilayered WS_2 Revealed by High-Pressure Optical Measurements", *ACS Applied Materials & Interfaces* **14**, 19857 (2022) DOI: 10.1021/acsami.2c01726.

[237] A. Kunin et al., "Momentum-Resolved Exciton Coupling and Valley Polarization Dynamics in Monolayer WS_2", *Physical Review Letters* **130**, 046202 (2023) DOI: 10.1103/PhysRevLett.130.046202.

[238] A. Chernikov et al., "Population inversion and giant bandgap renormalization in atomically thin WS_2 layers", *Nature Photonics* **9**, 466 (2015) DOI: 10.1038/nphoton.2015.104.

[239] T. N. Lin et al., "Many-body effects in doped WS2 monolayer quantum disks at room temperature", *npj 2D Materials and Applications* **3**, 46 (2019) DOI: 10.1038/s41699-019-0129-z.

[240] N. F. Mott, "Metal-Insulator Transition", *Reviews of Modern Physics* **40**, 677 (1968)
DOI: 10.1103/RevModPhys.40.677.

[241] A. J. Graham et al., "Conduction Band Replicas in a 2D Moiré Semiconductor Heterobilayer", *Nano Letters* **24**, 5117 (2024)
DOI: 10.1021/acs.nanolett.3c04866.

[242] A. Grubišić Čabo et al., "Observation of Ultrafast Free Carrier Dynamics in Single Layer MoS_2", *Nano Letters* **15**, 5883 (2015)
DOI: 10.1021/acs.nanolett.5b01967.

[243] S. Aeschlimann et al., "Direct evidence for efficient ultrafast charge separation in epitaxial WS_2/graphene heterostructures", *Science Advances* **6**, eaay0761 (2020)
DOI: 10.1126/sciadv.aay0761.

[244] M. Bauer, A. Marienfeld, and M. Aeschlimann, "Hot electron lifetimes in metals probed by time-resolved two-photon photoemission", *Progress in Surface Science* **90**, 319 (2015)
DOI: 10.1016/j.progsurf.2015.05.001.

[245] K. F. Mak et al., "Atomically Thin MoS_2: A New Direct-Gap Semiconductor", *Physical Review Letters* **105**, 136805 (2010)
DOI: 10.1103/PhysRevLett.105.136805.

[246] D. Y. Qiu, F. H. da Jornada, and S. G. Louie, "Optical Spectrum of MoS_2: Many-Body Effects and Diversity of Exciton States", *Physical Review Letters* **111**, 216805 (2013)
DOI: 10.1103/PhysRevLett.111.216805.

[247] K. Wu et al., "Identification of twist-angle-dependent excitons in WS_2/WSe_2 heterobilayers", *National Science Review* **9**, nwab135 (2022)
DOI: 10.1093/nsr/nwab135.

[248] C. Jin et al., "Observation of moiré excitons in WSe_2/WS_2 heterostructure superlattices", *Nature* **567**, 76 (2019)
DOI: 10.1038/s41586-019-0976-y.

[249] H. Chen et al., "Ultrafast formation of interlayer hot excitons in atomically thin MoS_2/WS_2 heterostructures", *Nature Communications* **7**, 12512 (2016)
DOI: 10.1038/ncomms12512.

[250] C. H. Stansbury et al., "Visualizing electron localization of WS_2/WSe_2 moiré superlattices in momentum space", *Science Advances* **7**, eabf4387 (2021)
DOI: 10.1126/sciadv.abf4387.

[251] R. P. Xian et al., "An open-source, end-to-end workflow for multidimensional photoemission spectroscopy", *Scientific Data* **7**, 442 (2020)
DOI: 10.1038/s41597-020-00769-8.

[252] M. A. Aly et al., "Radiative pattern of intralayer and interlayer excitons in two-dimensional WS_2/WSe_2 heterostructure", *Scientific Reports* **12**, 6939 (2022)
DOI: 10.1038/s41598-022-10851-3.

[253] Y. Zhang et al., "Electronic Structure, Surface Doping, and Optical Response in Epitaxial WSe_2 Thin Films", *Nano Letters* **16**, 2485 (2016)
DOI: 10.1021/acs.nanolett.6b00059.

[254] N. R. Wilson et al., "Determination of band offsets, hybridization, and exciton binding in 2D semiconductor heterostructures", *Science Advances* **3**, e1601832 (2017)
DOI: 10.1126/sciadv.1601832.

[255] K. Wang et al., "Interlayer Coupling in Twisted WSe_2/WS_2 Bilayer Heterostructures Revealed by Optical Spectroscopy", *ACS Nano* **10**, 6612 (2016)
DOI: 10.1021/acsnano.6b01486.

[256] C. Zhang et al., "Engineering Point-Defect States in Monolayer WSe_2", *ACS Nano* **13**, 1595 (2019)
DOI: 10.1021/acsnano.8b07595.

[257] E. Mitterreiter et al., "The role of chalcogen vacancies for atomic defect emission in MoS_2", *Nature Communications* **12**, 3822 (2021)
DOI: 10.1038/s41467-021-24102-y.

[258] P. Merkl et al., "Ultrafast transition between exciton phases in van der Waals heterostructures", *Nature Materials* **18**, 691 (2019)
DOI: 10.1038/s41563-019-0337-0.

[259] V. R. Policht et al., "Time-domain observation of interlayer exciton formation and thermalization in a $MoSe_2/WSe_2$ heterostructure", *Nature Communications* **14**, 7273 (2023)
DOI: 10.1038/s41467-023-42915-x.

[260] J. E. Zimmermann et al., "Ultrafast Charge-Transfer Dynamics in Twisted MoS_2/WSe_2 Heterostructures", *ACS Nano* **15**, 14725 (2021)
DOI: 10.1021/acsnano.1c04549.

[261] C. Robert et al., "Exciton radiative lifetime in transition metal dichalcogenide monolayers", *Physical Review B* **93**, 205423 (2016)
DOI: 10.1103/PhysRevB.93.205423.

[262] L. Yuan et al., "Twist-angle-dependent interlayer exciton diffusion in WS_2–WSe_2 heterobilayers", *Nature Materials* **19**, 617 (2020)
DOI: 10.1038/s41563-020-0670-3.

[263] R. Sebait et al., "Sequential order dependent dark-exciton modulation in bilayered TMD heterostructure", *Nature Communications* **14**, 5548 (2023)
DOI: 10.1038/s41467-023-41047-6.

[264] G. Stefanucci and E. Perfetto, "From carriers and virtual excitons to exciton populations: Insights into time-resolved ARPES spectra from an exactly solvable model", *Physical Review B* **103**, 245103 (2021)
DOI: 10.1103/PhysRevB.103.245103.

[265] G. Moody et al., "Intrinsic homogeneous linewidth and broadening mechanisms of excitons in monolayer transition metal dichalcogenides", *Nature Communications* **6**, 8315 (2015)
DOI: 10.1038/ncomms9315.

[266] Y.-h. Chan et al., "Exciton thermalization dynamics in monolayer MoS_2: A first-principles Boltzmann equation study", *Physical Review B* **111**, 184305 (2025)
DOI: 10.1103/PhysRevB.111.184305.

[267] D. Yagodkin et al., "Probing the Formation of Dark Interlayer Excitons via Ultrafast Photocurrent", *Nano Letters* **23**, 9212 (2023)
DOI: 10.1021/acs.nanolett.3c01708.

[268] J. Hagel et al., "Exciton landscape in van der Waals heterostructures", *Physical Review Research* **3**, 043217 (2021)
DOI: 10.1103/PhysRevResearch.3.043217.

[269] J. Chen et al., "Twist-angle-dependent momentum-space direct and indirect interlayer excitons in WSe_2/WS_2 heterostructure", *RSC Advances* **13**, 18099 (2023)
DOI: 10.1039/D3RA02952B.

[270] A. R.-P. Montblanch et al., "Confinement of long-lived interlayer excitons in WS_2/WSe_2 heterostructures", *Communications Physics* **4**, 119 (2021)
DOI: 10.1038/s42005-021-00625-0.

[271] K. Chen et al., "Experimental evidence of exciton capture by mid-gap defects in CVD grown monolayer $MoSe_2$", *npj 2D Materials and Applications* **1**, 15 (2017)
DOI: 10.1038/s41699-017-0019-1.

[272] H. Fang et al., "Localization and interaction of interlayer excitons in $MoSe_2/WSe_2$ heterobilayers", *Nature Communications* **14**, 6910 (2023)
DOI: 10.1038/s41467-023-42710-8.

[273] Y. Hoshi et al., "Suppression of exciton-exciton annihilation in tungsten disulfide monolayers encapsulated by hexagonal boron nitrides", *Physical Review B* **95**, 241403 (2017)
DOI: 10.1103/PhysRevB.95.241403.

[274] T. Biktagirov et al., "Intrinsic defects as a source of n-type conductivity in CrSBr", *npj 2D Materials and Applications* **9**, 106 (2025)
DOI: 10.1038/s41699-025-00640-7.

[275] J. Klein et al., "Sensing the Local Magnetic Environment through Optically Active Defects in a Layered Magnetic Semiconductor", *ACS Nano* **17**, 288 (2023)
DOI: 10.1021/acsnano.2c07655.

[276] M. Weile et al., "Defect Complexes in CrSBr Revealed Through Electron Microscopy and Deep Learning", *Physical Review X* **15**, 021080 (2025)
DOI: 10.1103/PhysRevX.15.021080.

[277] E. J. Telford et al., "Coupling between magnetic order and charge transport in a two-dimensional magnetic semiconductor", *Nature Materials* **21**, 754 (2022) DOI: 10.1038/s41563-022-01245-x.

[278] M. Bianchi et al., "Charge transfer induced Lifshitz transition and magnetic symmetry breaking in ultrathin CrSBr crystals", *Physical Review B* **108**, 195410 (2023) DOI: 10.1103/PhysRevB.108.195410.

[279] S. Smolenski et al., "Large exciton binding energy in a bulk van der Waals magnet from quasi-1D electronic localization", *Nature Communications* **16**, 1134 (2025) DOI: 10.1038/s41467-025-56457-x.

[280] K. Mosina et al., "Electrochemical Intercalation and Exfoliation of CrSBr into Ferromagnetic Fibers and Nanoribbons", *Small Methods* **8**, 2300609 (2024) DOI: 10.1002/smtd.202300609.

[281] W. M. Linhart et al., "Optical markers of magnetic phase transition in CrSBr", *Journal of Materials Chemistry C* **11**, 8423 (2023) DOI: 10.1039/D3TC01216F.

[282] W. Shi et al., "Controllable Antiferromagnetic to Ferromagnetic Transition of CrSBr by Organic Cation Intercalation", *Advanced Electronic Materials* **11**, e2500125 (2025) DOI: 10.1002/aelm.202500125.

[283] H. Li et al., "Rapid and Reliable Thickness Identification of Two-Dimensional Nanosheets Using Optical Microscopy", *ACS Nano* **7**, 10344 (2013) DOI: 10.1021/nn4047474.

[284] W. Bennecke et al., "Disentangling the multiorbital contributions of excitons by photoemission exciton tomography", *Nature Communications* **15**, 1804 (2024) DOI: 10.1038/s41467-024-45973-x.

[285] L. Gierster, S. Vempati, and J. Stähler, "Ultrafast generation and decay of a surface metal", *Nature Communications* **12**, 978 (2021) DOI: 10.1038/s41467-021-21203-6.

[286] L. Hellbrück et al., "High-resolution MHz time- and angle-resolved photoemission spectroscopy based on a tunable vacuum ultraviolet source", *Review of Scientific Instruments* **95**, 033007 (2024) DOI: 10.1063/5.0179549.

[287] J. E. Nitschke et al., "Tracing the ultrafast buildup and decay of d-d transitions in $FePS_3$", *Newton* **1**, 100019 (2025) DOI: 10.1016/j.newton.2025.100019.

[288] J. E. Nitschke et al., "Electronic Structure Reorganization in MPS3 via d-Shell-Selective Alkali Metal Doping", *Advanced Science*, e10675 (2026) DOI: 10.1002/advs.202510675.

[289] D. M. Janas et al., “Metalloporphyrins on oxygen-passivated iron: Conformation and order beyond the first layer”, *Inorganica Chimica Acta* **557**, 121705 (2023)
DOI: 10.1016/j.ica.2023.121705.

List of publications

Main contribution

1. K. J. Schiller, L. Sternemann, M. Stupar, A. Omar, M. Hoffmann, J. E. Nitschke, V. Mischke, D. M. Janas, S. Ponzoni, G. Zamborlini, C. J. Saraceno, and M. Cinchetti, "Time-resolved momentum microscopy with fs-XUV photons at high repetition rates with flexible energy and time resolution", *Scientific Reports* **15**, 3611 (2025)
DOI: 10.1038/s41598-025-86660-1

2. T. Biktagirov, W. G. Schmidt, K. J. Schiller, M. Capra, J. E. Nitschke, L. Sternemann, M. S. Arndt, G. Zamborlini, A. Isaeva, and M. Cinchetti, "Intrinsic defects as a source of n-type conductivity in CrSBr", *npj 2D Materials and Applications* **9**, 106 (2025)
DOI: 10.1038/s41699-025-00640-7

As coauthor

1. J. E. Nitschke, D. L. Esteras, M. Gutnikov, K. Schiller, S. Mañas-Valero, E. Coronado, M. Stupar, G. Zamborlini, S. Ponzoni, J. J. Baldoví, and M. Cinchetti, "Valence band electronic structure of the van der Waals antiferromagnet $FePS_3$", *Materials Today Electronics* **6**, 100061 (2023)
DOI: 10.1016/j.mtelec.2023.100061

2. J. E. Nitschke, L. Sternemann, M. Gutnikov, K. Schiller, E. Coronado, A. Omar, G. Zamborlini, C. Saraceno, M. Stupar, A. M. Ruiz, D. L. Esteras, J. J. Baldoví, F. Anders, and M. Cinchetti, "Tracing the ultrafast buildup and decay of d-d transitions in $FePS_3$", *Newton* **1**, 100019 (2025)
DOI: 10.1016/j.newton.2025.100019

3. J. E. Nitschke, P. Bhumla, T. Willershausen, P. Merisescu, D. M. Janas, L. Sternemann, M. Gutnikov, K. Schiller, V. Mischke, M. Capra, M. S. Arndt, S. Botti, and M. Cinchetti, "Electronic Structure Reorganization in MPS3 via d-Shell-Selective Alkali Metal Doping", *Advanced Science*, e10675 (2026)
DOI: 10.1002/advs.202510675

4. D. M. Janas, A. Windischbacher, M. S. Arndt, M. Gutnikov, L. Sternemann, D. Gutnikov, T. Willershausen, J. E. Nitschke, K. Schiller, D. Baranowski, V. Feyer, I. Cojocariu, K. Dave, P. Puschnig, M. Stupar, S. Ponzoni, M. Cinchetti, and G. Zamborlini, "Metalloporphyrins on oxygen-passivated iron: Conformation and order beyond the first layer", *Inorganica Chimica Acta* **557**, 121705 (2023)
DOI: 10.1016/j.ica.2023.121705

5. L. Sternemann, D. M. Janas, J. E. Nitschke, K. Schiller, T. Willershausen, L. Becker, A. Isaeva, G. Zamborlini, S. Tappertzhofen, and M. Cinchetti, "Fabrication of large-area 2D magnetic semiconductor films for low-temperature ARPES", *2D Materials* **12**, 035008 (2025)
DOI: 10.1088/2053-1583/add7ea

6. M. Capra, C. S. Kern, M. S. Arndt, K. J. Schiller, M. Niederreiter, F. Presel, I. Di Bernardo, M. Gruenewald, T. Fritz, S. Tappertzhofen, M. Sterrer, P. Puschnig, M. Cinchetti, and G. Zamborlini, "Bottom-Up Realization of a Type-II Organic/Transition-Metal Dichalcogenides Heterointerface: Pentacene on Monolayer WS_2", *ACS Nano* **20**, 25410 (2026)
DOI: 10.1021/acsnano.6c07654

Declaration of the Use of Artificial Intelligence Tools

During the preparation of this thesis, I used ChatGPT (OpenAI) to enhance the quality of the writing by improving grammar, style, and clarity. In addition, I used Perplexity to support the literature search alongside standard academic search engines like Google Scholar and Web of Science. After using these tools, I have reviewed and edited the content as needed and take full responsibility for the final content of the thesis.

Acknowledgements

This work was supported financially for most of my PhD by TRR 142/3, project A08 (DFG project 231447078). I would like to express my sincere gratitude to all those who supported me throughout the course of this PhD.

My sincere thanks go to my PhD supervisor Prof. Mirko Cinchetti for giving me the opportunity to join his research group. Throughout my PhD, he supported and guided me with his scientific expertise, encouraged me through constructive and fruitful discussions, and provided access to state-of-the-art equipment. I also thank Prof. Christoph Lange for serving as the second examiner of this thesis.

I am deeply grateful to Dr. Mattia Stupar for his supervision and support during the commissioning of the trMM setup and the bulk WS_2 measurements. He shared both his expertise in developing such a state-of-the-art system and many practical insights for work in the laboratory. Beyond this, I greatly appreciated his collegial support throughout this time, the many stories he shared, and the different perspectives he brought to our discussions. I would also like to thank Dr. Giovanni Zamborlini for his supervision of the CrSBr project and for his general support in the laboratory, especially for teaching me the intricacies of the KREIOS MM. Many thanks also go to Dr. Stefano Ponzoni for his valuable support in both laser and photoemission-related matters, and to Dr. Michele Capra for his supervision of the XPS measurements.

My sincere thanks go to the many collaborators involved in the research projects addressed in this thesis. First, I thank the collaborators from the group of Prof. Clara Saraceno at Ruhr University Bochum, who designed and built the nonlinear pulse compression scheme. Special thanks go to Dr. Alan Omar, who taught me the working principle of MPCs and was always a pleasure to work with in the laboratory. Second, I thank Prof. Wolf Gero Schmidt and Dr. Timur Biktagirov from Paderborn for the fruitful collaboration on point-defect formation in CrSBr. Third, I would like to thank the group of Prof. Stefan Tappertzhofen for their expertise, support, and for providing equipment for the preparation of Au substrates for exfoliation, especially Philipp Czyba. Finally, special thanks also go to Dirk Schemionek from the preparation laboratory at TU Dortmund University for his help with sample preparation.

I would also like to thank everyone who took the time to carefully proofread parts of this thesis and helped improve it through their comments and corrections: Mira Arndt, Dr. Mattia Benini, Dr. Michele Capra, David Gutnikov, Dr. David Janas, Dr. Fabian Mertens, Dr. Valentin Mischke, Dr. Stefan Grisard, and Lasse Sternemann.

Many thanks go to everyone in the Cinchetti group for the friendly and enjoyable atmosphere, which greatly contributed to a productive working environment. I am

also grateful for the group activities outside academia that brought us together. I would like to mention in particular the other PhD students with whom I primarily worked with in the laboratory: Dr. Jonah Nitschke, Dr. Valentin Mischke, Lasse Sternemann, Dr. David Janas, and Mira Arndt.

I would also like to thank Patrick Mc Lelland for his technical support in the laboratory. In addition, I am grateful for the support of Michaela Wäscher, Nina Sesemann-Collette, and Lena Bobon in administrative matters.

Finally, I would like to thank my family and friends for their constant encouragement, patience, and support throughout this PhD. Without them, this work would not have been possible.